The University Of Sheffield.

Modelling and design optimisation of permanent magnet machines for electric vehicle traction applications

By:

Liang Chen

A thesis submitted in partial fulfilment of the requirements for the degree of Doctor of Philosophy

The University of Sheffield
Faculty of Engineering
Department of Electronic and Electrical Engineering

July 31 2016

Acknowledgements

First of all, I would like to express my deepest gratitude to Prof. Jiabin Wang, for always being a dedicated supervisor, enlightening advisor and trustworthy mentor throughout my doctoral period. I am greatly grateful for his valuable guide in knowledge and learning, work and life, from which I will still benefit in the future life.

I have been fortunate to carry out my doctoral studies in the Electrical Machine Group, with the energetic group of teachers, colleagues and fellows. I am sincerely grateful to Dr. Weiya Wang, who gave me lots of favourable advice, help and encouraging support, not only in machines. Special thanks to my friends Panagiotis Lazari, Dr. Xiao Chen, Dr. Vipulkumar Patel for your constructive criticisms, valuable views and ideas in many enthusiastic discussions and meetings. And also my sincere thanks to Mr. John Wilkinson, who provided expertise knowledge and strong backing during the experiments. I am very grateful to have Liu Bing, Dr. Bhaska Sen, Dr. Tian Fu, Bo Wang, Rongguang Hu, Sreeju Nair and Yanwen Shi as my genuine friends and cheering working mates, who are always there to offer help and support. Special thanks to Sreeju Nair, whom I joined with in a happy and productive co-operation in the last period of my doctoral studies. It is great memory to work with these wonderful persons.

My true gratitude from heart to all my close friends. Their accompanies and trust are precious elements in my life. Lastly, I would like to say a big thank you to my family. Their irreplaceable support, love and faith were and always are the endless sources of strength of my life.

Sheffield, 31 July 2016 Liang Chen

Contents

Abstract

While the fuel resource scarcity and the environment crisis are becoming two of the major problems for the human society in the new century, in the context that the on-road transport is the largest energy-consuming society sector, electrical vehicles (EVs) serving resource-sustainable environmentally-clean transport attract increasing attention. Permanent magnet (PM) traction machines with high torque and power densities, and high energy efficiency gain great interest from the engineer and industry communities.

Jointly with the chances, fresh challenges are brought by EVs to PM machine designers. In response to the vehicles' call for high speed, mighty acceleration, long range, safe and robust system, the engineers need to develop a powerful design platform that allows for multi-physic evaluations of machine designs over a large torque-speed range, especially for energy efficiency, PM health, and thermal-withstanding ability. More importantly, these evaluations must be against driving cycles rather than on a single rated operation point in catering to various real-world driving conditions. The complex and enormous computation efforts required necessitate new, effective and feasible design techniques.

In this work a set of modelling techniques for PM machines are developed, in order to establish a computationally-efficient yet accurate design and optimisation method for EV traction PM machines. Through the method, comprehensive machine multi-physics assessments against driving cycles are enabled; electro-thermally coupled evaluation is achieved; 3-dimensional eddy-current loss of PMs are accurately monitored in the context of PM protection; lastly with the techniques integrated together, a fast and effective optimisation method for EV traction PM machines is acquired.

To exploit the benefits of the proposed method, a design, optimisation and manufacture process of PM machines for a light-duty EV distributed traction system is formatted, which includes a quantity assessment of machine topologies, investigation of driving cycle influence on designs, optimisation of the selected 18-slot 8-pole interior PM machine against a series of EV machine design criteria, the subsequent prototype experiments, and optimisation of combinations and power split ratios of PM machines for the distributed traction system. Through the design process for the EV traction system and experiments, the effectiveness, computational efficiency, and accuracy of the proposed designing methods are exhibited and validated.

CHAPTER 1 Introduction

1.1 Energy, environment, electric vehicles

Energy and environment have increasingly been recognised as two of the most important issues since the world entered the new century. The well-being of mankind relies on sustainable and affordable energy, and clean environment. The researches on generations and applications of more secure, reliable and clean energy are receiving more and more interests.

Fossil fuel has been the major energy sources for human society for decades. Due to its limited natural storage and high demand to support booming economy development, the increase in price makes this kind of fuel less and less affordable. According to the EU's Energy Trends publications [1], the oil price is expected to increase by more than 130% in 2050 relative to the price in 2010, and the natural gas price to increase by 60%. Besides the trends of cut-down supply, at the same time, fossil fuel related emissions account for almost 80% of the EU's total greenhouse gas emissions [2].

Among the sectors of society covering households and services, agriculture, industry and transport, transport was responsible for 32% of EU final energy consumption (352 Mtoe) in 2012 [3]. Looking into total EU transport energy consumption [3], considering domestic, intra-EU and intercontinental traffic, road transport such as cars, buses and heavy-duty trucks accounts for by far 72% of the total which makes it the largest energy consumer. In the ranks after road transport are aviation (12%), international maritime transport (11%), rail transport (1.8%), and finally inland navigation (1.1%). On the other hand, EU Road transport depended on oil products for 94% of its energy use [3].

It is seen that road transport has the biggest energy saving potential among all the social sectors. Strong efforts would be required in the road transport area to drastically reduce the oil dependency, improve energy sustainability, increase the energy efficiency of the transport system, support clean urban mobility, as well as reduce greenhouse gas (GHG) emissions in the transport sector, in line with the goals put forward in the 2011 EU White Paper on Transport, i.e. a 20% reduction in the GHG emissions by 2030 relative to 2008 levels and a 60% reduction by 2050 relative to 1990 levels. Therefore the trend is to achieve a sustainable transportation: from oil source to renewable sources. Greener vehicles are pushed up by national and international strategies in recent years, i.e. the

European Commission integrated energy and climate action plan and the US Energy Independence and Security Act [4].

Electric vehicles (EV) including hybrid electric vehicles (HEV), plug-in hybrid electric vehicles (PHEV), and full electric vehicles (FEV) emerge in recent years as a very promising solution for the road transport revolution. An electric vehicle uses one or more electric motors for propulsion. The electric motors may be powered through a battery contained inside the vehicle (FEV) or through a generator to convert fuel to electricity (HEV or PHEV). Compared with fossil-fuel powered vehicles, the key advantages of EVs can be summarized as:

- Energy efficiency: the electric motors as the traction sources in EVs have higher energy efficiency in wide torque-speed operation range compared with internal combustion engine (ICE); EVs with battery can recover kinetic energy during braking; and the electric motors possess higher power density and torque density, thus saving the inside space of vehicles.
- Emissions reduction and energy sustainability: electric vehicles have less air pollution emission than ICE (HEV) or zero emission (FEV), and have drastically reduced dependence on oil energy. Full electric vehicles with the energy supplied by renewable sources such as wind power, hydropower and solar panels have no need of fossil fuel, thus could eliminate the emission of whole energy cycle system to zero.
- Driving performances: electric motors generate much less vibration in electric vehicles compared with ICE, thus ultra-low noise could be expected with EVs; due to high controllability of electric motors, EVs can adapt with intelligent drive or unmanned drive, and easily integrate into the intelligent traffic management.

Thanks to the significant advantages of electric vehicles in terms of energy, emission and control aspects, the research on electric vehicles receives great interest and making prominent progress in academic study and industrial application areas [5]-[7]. It is expected that by 2050, electric vehicles would take 52% share of passenger car stocks in EU, while the conventional cars using gasoline and diesel drop to 48% [1].

1.2 Motivation of the thesis

As discussed above, the design and optimisation of traction machine as the electric vehicle traction machine is one of important techniques in the studies of electric vehicles and their industry applications.

With high power density, high energy efficiency over wide torque-speed range, permanent magnet (PM) machines provide a very competitive solution for Electric vehicle (EV) tractions [5]-[8]. Among various PM machine topologies, Interior permanent magnet machines (IPM) which benefit from high torque and wide field weakening capability contributed by both PM torque and reluctance torque are particularly attractive [9][10]. Among other electrical machine technologies suitable for traction applications, induction machines have the potential for the lowest cost, a wide speed operation range, but they have a lower torque density and an inferior power factor and efficiency compared to permanent magnet machines. Switched reluctance machines (SRMs) are more robust than permanent magnet machines; however, beside the advantages of low torque/power density, they have a higher torque ripple, higher acoustic noise and vibration. And they have a poorer power factor which increases the inverter cost. Thus, in general, permanent magnet brushless machines are preferred for traction applications, where energy efficiency and power density are the most important attributes [11]-[13].

However, unlike the applications in industrial traction, electric vehicles bring highly demanding requirements on performances of electric traction machines particularly for permanent magnet machines, thus raising challenges in many aspects of machine design and optimisations.

- Energy efficiency: because an electric vehicle is a small power driven system relatively separated from the main electricity power supply network when running on the road, its power source mainly relies on the batteries. The energy efficiency of electric machine is extremely important. EV machine design engineers need to have accurate assessment of machine performance in order to choose an optimal design from numerous design candidates. Moreover, machine control strategies need to be applied to optimise the energy efficiency of electric machine at operations. All these aims are based on accurate electromagnetic models and accurate loss models of permanent magnet machines.

- While permanent magnet machines exhibit higher power density and higher efficiency compared to other candidate machine technologies, protection of permanent magnets from demagnetization is essential. The status of health of permanent magnets is of crucial concerns both in terms of machine performances and safety. Permanent magnets working under complex magnetic field and high temperatures are subject to high risk of demagnetisations especially at high speed operations. Therefore, the eddy current loss in permanent magnets needs to be accurately evaluated in order to assess the risk of high temperature for high speed electric machines.
- Thermal performances and withstand ability: since the temperatures of electric machines are varying according to machine performances at various driving conditions and machine performances are also dependent on the temperatures of machine windings and permanent magnets, electro-thermal coupled models are necessary for an accurate thermal and electromagnetic behaviour estimation.
- Complex driving conditions: the demands of torque and speed on the machine design candidates in the design process have to reflect the complex real-world driving conditions, rather than just centers around rated operation point as conventional method for industrial machine designs. This poses challenges to engineers because the performances over a vast torque-speed operations range need to be evaluated and this obviously largely increases the computation efforts.
- Traction system diversity: not restricted with using a signal traction machine in the power train system, an electric vehicle could choose to employ 2-4 traction machines to form a distributed traction system to improve the vehicle safety and traction performances. This system option induces the necessity of studies on the optimal co-operation strategy among the distributed tractions and their potential benefits.

Relating to the challenges illustrated above, the work of thesis is aimed to develop a set of comprehensive multi-physics, computationally-efficient, yet accurate machine modelling techniques and integrate them into an effective machine design/optimisation method for PM machines in electric vehicle traction applications. The brief review of the current state-of-the art and introductions of each part of study work are presented separately in the following sections.

1.3 High-fidelity modelling methods for Permanent Magnet Machines as EV traction Machines

A traction machine for EV applications requires high torque at low speeds, usually 3~4 times of the nominal value, in order to provide necessary acceleration and hill-climbing capability. Conversely, the machine has to exhibit peak power close to twice the rated value in medium to high speed range [5][14]-[16]. Thirdly, unlike conventional industrial machines which normally are designed and operate around the rated condition, the PM machines for EVs in real-life driving follow frequent change of torque and speed. Therefore, compared with industrial applications, EV traction machines are more likely to operate in extreme conditions with wide torque-speed variations in response to various driving conditions [17]. The high efficiency operating region of current state-of-the-art PM brushless machines for EV traction is typically designed around the rated operating point [18] or a few points around the rated point [19]. However, EV traction machines during a typical urban or suburb driving operate frequently in the low torque region where the efficiency is much lower, or in other frequent driving cases where EV cruises in the rural areas, high speed operations are the main working conditions of traction machines. Clearly the mismatch between the regions of high efficiency and high operating duty with the existing PM brushless traction drives results in a low overall efficiency, high energy consumption and reduced vehicle range. Therefore, it is important to develop a viable motor design method, allowing for minimizing the total energy loss over a driving cycle rather than at a few operating points [20]-[22]. The efficiency and other performance indicators should be evaluated for a given design against driving cycles, such as those defined in the Worldwide harmonized Light vehicles Test Procedures (WLTP), the New European Driving cycle (NEDC) and the Artemis Urban Driving Cycle (Artemis), etc.[23], rather than against a single operating point.

For each of operation points within the wide torque-speed range, multi-physical properties such as electrical, electromagnetic, thermal, mechanical and demagnetization withstanding are to be evaluated. This often involves repeated evaluations of thousands of operation points and requires tremendous computation effort in finite element analyses (FEAs), which are necessary to deal with nonlinearity and geometry complexity associated with Interior-embed Permanent Magnet Machines (IPMs) [17]. Since an optimization needs to evaluate a large number of trial designs in order to obtain the optimal design, the required computation time is prohibitively long even with the state-of-the art computing facilities and renders optimization by direct FEAs of

multi-physics fields not feasible [24]. High-fidelity yet computationally-efficient modelling methods for Permanent Magnet Machines as EV traction Machines are necessary due to the requirements of accurate evaluation of machine performances at various operations points over wide torque-speed range in multi-physics domains.

There are many literatures which developed analytical models with different fidelity to real physical features of PM machines to evaluate the EM performances [25]-[33]. With fidelity of the proposed methods increasing, the analytical models can finally make very accurate predictions of the machine EM performances such as the EM field or torque. However, firstly, these methods only apply for Surface-mounted Permanent Magnet Machine (SPM) designs due to the simple geometry of SPM topology. And also because of the relatively low level of saturation within SPM iron laminations, electromagnetic field in the iron could be assumed as linear in these analytical models. For IPM designs, the EM field is highly saturated and hence non-linear. And because the magnets are embedded inside the rotors of IPM machines, the IPM rotor geometries, with many variances such as the I-shape, V-shape, W-shape or multiple layers of magnets, are much more complex to modelled analytically than SPM. Secondly it is difficult for the analytical methods to predict iron loss within laminations.

To address the problems illustrated above, Chapter 2 of the thesis proposes a set of computationally efficient multi-physics modelling methods considering electromagnetic performances, energy loss predictions, thermal behaviours and mechanical stress constraints for PM traction machines' designs/optimisations and simulations. The proposed methods characterise multi-physics FEA models into mathematical functions based on the FEA results on typical geometrical and physical parameters, and thus greatly curtailing the machine performance evaluation time in FE, but yet all key physical effects, such as magnetic saturation, back electromotive force (EMF) harmonics, magneto-motive force (mmf) harmonics and the harmonics due slotting, etc. are captured.

1.4 3-D eddy current loss models for permanent magnets

A PM machine for electric vehicle traction is often required to operate at high power and high speed. The eddy current losses in the rotor magnets, due to slotting, space and time harmonics of the armature reaction field, may be significant, especially when the machine runs at high speed field weakening mode and the inverter operates with high frequency. If this loss is not appropriately assessed and reduced, excessive rotor

temperature may result which increases the risk of demagnetization. To reduce the eddy current losses, the magnets are usually segmented in circumferential and axial directions, which however increase manufacturing cost and magnet material waste because the rate of defective products would increase as more manufacturing steps are involved.

In order to evaluate the eddy current losses in the magnets, various methods have been reported in a large number in literatures. In general, evaluation of rotor eddy current losses requires simultaneous solutions for the governing equations of the magnetic and eddy current fields. For radial field machines, it is reasonable to assume that the machine magnetic field is predominantly 2-dimesional (2D). As for the eddy current distribution, if the axial length of the magnets is much greater that their width and thickness, it may be sufficient to assume that the eddy current only flows in the axial direction. Thus, 2D numerical methods such as transient finite element analysis (FEA) can be used to calculate the eddy current losses [34]-[37]. To reduce the computation time, a number of 2D analytical methods have been developed for quantifying rotor eddy current losses in SPM with varying degrees of accuracy [30]-[32][38]-[45]. While 2D evaluation of eddy current loss in PM machines can be performed in a computationally efficient manner by either FEA or analytically, its accuracy is compromised if the axial length of magnets is comparable to their other dimensions since the eddy current flow in the magnets may become predominantly 3-dimensional (3D).

In order to evaluate eddy current loss in magnets more accurately in PM machines which employ axial segmentations on the magnets as a means of reducing eddy current loss, 3D FEAs are usually applied [46]-[51]. However, 3D FEAs are usually complicated, and their solutions require large memory and enormous computation time. To circumvent this problem, 3D analytical methods for calculation of eddy current loss have received significant interest in research communities [52]-[60]. However, because of complex geometry and high level of magnetic saturation in IPMs, the reported 3D analytical methods are only restricted to SPMs, and require one or more simplifying assumptions, such as:

(1) Machine stator is slotless, and stator and rotor cores are infinitely permeable;

(2) Only radial flux densities exist in the magnets and air gap and they are independent of radial and angular positions;

(3) Radial component of eddy current and the boundary conditions perpendicular to the radial direction are neglected.

These assumptions will inevitably compromise the accuracy of the eddy current loss predictions, particularly if the frequency of eddy current is relatively high, or its wavelength is relatively short. Inaccurate eddy current loss calculation may cause underestimate of rotor temperatures, which in turn increases demagnetization risk. Therefore, an accurate and computationally-efficient solution for quantifying the eddy current losses is necessary.

The method of images is a classical solution method in solving electrostatic and magnetostatic field problems. It applies imaginary field sources (images) outside the calculated domain in the symmetrical positions to the original sources with respect to the boundaries. By using these images, the effect of the boundaries on the field could be equivalently reflected. This conception of the image method however has not been reported in literatures in solving eddy current field problems. Chapter 3 of the thesis proposes an analytical technique for 3D eddy current loss calculation based on the generalized image theory to account boundary conditions of 3D eddy current flow. This method can be easily integrated with accurate analytical models for predicting magnetic field distribution to account slotting effect [28]-[33][61]-[63], or with 2D FEAs to quantify 3D eddy current loss in IPMs with complex geometry and under heavy magnetic saturations. By employing generalised image method, the proposed analytical method gives fast and accurate predictions of 3-D eddy current losses at a given machine geometry design, magnet segmentations and electrical load. For a machine design with a given current load, the model takes ~10 seconds to calculate the eddy current loss in magnets on a PC with typical CPU and memory while the calculation error is less than 2% compared with time-step 3-D FE. This greatly reduces the computation efforts in the machine design and optimisation process.

1.5 Electro-thermally coupled model

Although permanent magnet machines are receiving prominent interest in electric vehicle (EV) traction applications due to their high torque/power density and high energy efficiency, the application of permanent magnets raises important concerns for machine robustness. Typical rare-earth permanent magnets such as NdFeB are subject to remanence loss under high temperatures which undermines the machine performances, or even to the risk of irreversible demagnetisation in extreme cases [64]-

[67]. Special studies are necessary to put on thermal response of PM machines under various working conditions.

Since the operation condition of a PM machine for EV traction varies frequently, its rotor (or magnets) temperature changes with ambient temperature, loads and driving conditions. Because the remanence of permanent magnets is considerably affected by temperature, the air gap flux density, the saturation level in the stator and rotor cores and harmonics in the stator flux linkage are all temperature-dependent. If the temperature effect were ignored, the voltage and current ratings for the torque-speed requirement and the magnet temperature and winding temperature would be underestimated when the machine operates at temperature higher than the designed value. Consequently, the machine would not be able to achieve the required torque, and risk partial irreversible demagnetization and a shorter life span due to higher temperatures. As the EV driving condition varies, at different torque command and different air-cooling speed (given the assumption that the EV traction machine is air cooled), temperature effect on the machine electromagnetic and thermal behaviours varies accordingly.

Therefore, an electromagnetic (EM) PM machine model coupled with machine thermal behaviour model is indispensable in an EV traction application. In order to solve the EM-thermal coupled problem, the most common method is to employ EM finite element (FE) analysis coupled with thermal simulation [68]-[72]. This method could obtain accurate machine performance predictions. However, although the thermal simuation (analytical or FE) may not take much time, since thermal time constant is much larger than electromagnetic time constant, for a thermal calculation at each time instant, a full electrical cycle of electromagnetic FE calculation needs to be implemented. The whole process is very time consuming due to enormous amount of FE calculations. Hence, it is not possible to employ such modelling techniques for simulation at system levels or for assessing machine performance over driving cycles.

The method proposed in Chapter 2 of the thesis builds high-fidelity electromagnetic analytical model for PM machines and requires much less computation time. It assumes the magnets have constant temperature (usually at the design limit of temperatures to evaluate machine performance in the worst thermal scenario) for machine design/optimisation process. Further from the method illustrated in Chapter 2, to capture the thermal influence on the electromagnetic models, a new technique is proposed in

Chapter 4. The temperature effect of the permanent magnets on the machine electromagnetic response is represented by an equivalent *d*-axis current which varies with temperature proportionally, thus greatly reduces calculation time for modelling and simulations. The temperature dependent electromagnetic model is combined with a lumped parameter thermal model to form a computationally efficient electro-thermally coupled model. The electro-thermal coupled model is simulated in various operations and validated by load experiments on a prototype machine.

1.6 Designing, building, and experiments on a prototype machine

As a case of study, Chapter 5 formulates a design, building and test process of permanent magnet machine for a light-duty electric vehicle traction system to exploit the benefits of advanced modeling techniques, which includes optimisation strategy and development of quantitative comparison among various PM machines, design/optimisation process of a selected 18-slot 8-pole IPM. And two prototype machines have been built and tested.

With the help of the machine analytical models presented in the previous chapters, a computationally-efficient optimisation technique for EV traction machine design is developed in this chapter. On the developed optimisation platform, wide range of PM machine topologies are optimised and investigated for the studied EV traction system. Finally, an IPM machine with 18 slots and 8 poles which shows high machine performance potentials and low magnet usage is employed, optimised and assessed in electromagnetic, thermal and mechanical aspects. On the other hand, a second machine using the same design but new type of magnets was also under investigation. The new magnets were developed with a technique which reduces dysprosium usage in the contents of magnets by 81% than conventional NdFeB, thus in the world's context of volatile rare earth material supply the PM machine's cost and reliance on rare-earth element is diminished. Prototypes of the two IPM machines are built, and the test on the machines' torque capability, energy efficiencies and thermal behaviours are carried out. Good agreement is found between the test results and the estimations made by the machine models in use, validating high accuracy of the proposed models.

1.7 Distributed traction system

The research work of Chapter 2 to Chapter 5 centers around PM machine modelling, design and optimisation. Chapter 6 further studies two special design concerns related to EV traction machine design:

(1). The influence of vehicle driving cycles on the machine designs;

(2). Possible benefits on the PM machine performances from EV distributed traction system.

1.7.1 The influence of driving cycles on the EV traction machine design

Driving cycles are developed by engineers in automobile industry to reflect the real-world driving conditions. The driving cycles are used for vehicle test procedures to acquire vehicle exhaust gas emission performance, energy efficiency and other vehicle properties. High energy efficiency capability of traction machines over driving cycles is a crucial design objective for machine designers. There are several commonly-used driving cycles among the regions such as Europe, USA and Japan. In Europe, the widely used driving cycles include New European Driving Cycles (NEDC), Common Artemis Driving Cycles (CADC) and the Worldwide Harmonized Light Vehicles Test Procedure (WLTP) [23]. These driving cycles demand different torque-speed output from the traction machines, requiring low, middle or high level of torque-speed capabilities. For example, a vehicle which runs during the NEDC cycle mainly needs low-torque but middle- to high- speed power output from the traction, yet when the vehicle is tested over the Urban schedule of CADC, it frequently requires high torque and low speed from its traction machine. Therefore, specifications of an EV traction machine should consider the requirements of driving cycles, and optimisations of machine design should target to maximise the energy efficiency during driving cycles. Subsequently, the machine designs are greatly affected by the driving cycles. Therefore, it is important to study the torque-speed features of different driving cycles and their influences on the machine designs in terms of geometry parameters, energy losses and efficiency characteristics. However, currently there are very few literatures which reports studies on this subject. The first part of Chapter 6 of the thesis will make use of a 12-slot 14-pole SPM machine and an 18-slot 8-pole IPM machine as two representative examples for SPM machine and IPM machine respectively to conduct optimisations against different driving cycles and investigate influences of the driving cycles on the optimal machine designs. The introduction of the 18-slot 8-pole IPM machine is given in Chapter 5. And since the EV application does not require machines to run at very high speed, the significance of the machine losses related to frequency is relatively small. Therefore, the 12-slot 14-pole SPM machine is chosen to reduce the back iron thickenss and increase the space for windings.

On the other hand, in order to assess the influence of driving cycles on the machine designs, the machine performances at each time instant of a driving cycle would have to be calculated. Taking the NEDC for an example, for a time interval of one second, the NEDC contains 600 operating points, excluding the 4 recurring ECE-15 city cycles. The computation time for the evaluation of machine performances of a single design would reach 200 hours assuming 20 minutes needed for FE calculation of each operating points. Thus the entire design/optimization process requires enormous amount of time and effort. A new technique is illustrated in Chapter 6 which characterises a driving cycle into tens of representative torque-speed operation points, thus greatly reduces the computation time in the machine design/optimisation process.

1.7.2 EV Distributed traction drive system

Distributed traction drive systems for electric vehicles employ two or more machines on the front and rear axles to provide traction forces. Compared with concentrated drive systems with a single traction machine, distributed traction systems benefit in terms of improved operational efficiency and safety [73]-[76]. The vehicle will have less tyre slip due to lower traction torque provided by the front and rear wheels than that of concentrated traction systems, and hence better efficiency performance. In term of safety concern, when one motor fails, with appropriate remedial actions, the remaining healthy motors can still provide traction forces and the vehicle is able to continue its operation, or at least stopped in a safe and controlled manner.

A further advantage of the distributed traction systems is that the torque from each wheel can be dynamically apportioned so that the vehicle may operate in high-efficiency regions over a wide torque-speed operation range. For example, in the 2-motor traction system, the front and rear machines could be designed purposely to locate their high efficiency regions in different areas within the torque-speed envelopes. The front motor is selected with a proper geometry and designed to have high efficiency at low-speed and high-torque operation regions, while the rear motor performs better in high-speed and low-torque region. It is reasonable to expect that the combined efficiency of the whole traction system would have higher efficiency over a wider torque-speed range, if the split ratios of the total traction power assigned to the front motor and to the rear motor are carefully selected according to the real torque-speed load conditions rather than being kept constant. For example, in an operation condition with high speed and low torque, the front motor could share more torque/power, while the rear motors may contribute less or just being switch off. In this way, both of them

would work in their best efficiency region, leading to a higher combined efficiency output from the traction system.

According to the work in [73], it is known that, in a traction system with front and rear axles coupled to two identical permanent magnet machines (PMM), the combined efficiency of the drive train with varying torque-split ratios would not be better than that with torque equal sharing, i.e., 50% to 50% split between the front and the rear because when one of the motor switches off with no power output, its iron loss which is significant at high speed still exists. Consequently, the combined efficiency will be lower. However, by employing PMa-SynRM (permanent magnet assisted synchronous reluctance machine) for the rear traction motors, this limitation has been avoided since a PMa-SynRM has very low iron loss at high speed. Therefore, a PM machine and a PMa-SynRM cooperating under selected power split ratios, higher efficiency is achievable.

For a complete investigation of the benefits of distributed traction systems, power split ratios for front and rear machines should be optimised together with machine geometric parameters at the same time. However, this very complex process requires 2 machine models to be evaluated simultaneously in optimisations, thus is difficult to realise using the current state-of-the art optimisation tool. In Chapter 6, studies on selection of appropriate power split ratios will be carried out after the optimisations of machine parameters to obtain basic knowledge on optimisations of electric vehicle traction systems with asymmetrical machine technologies, and distributed traction system with various machine topologies and their combinations are investigated.

1.8 Summary of contributions and publications

More comprehensive reviews of current state-of-the art associated with relevant topics are given in each chapter when the details of the technical issues and problems are addressed.

To the knowledge of the author, the main contribution of this thesis for the engineers and researchers in the efforts of addressing the challenges on the design and optimisation of permanent magnet machines for electric vehicle traction is:

(1). Computationally-efficient modelling techniques that allow accurate multi-physics performance evaluations of permanent magnet machines against driving cycles have been developed, greatly facilitating the machine

design/optimisations and subsequent machine simulations for electric vehicle traction applications.

(2). An analytical method, based on the generalized image theory, has been proposed which enables extremely computationally efficient and accurate prediction of 3-dimensional (3D) eddy current distributions in the magnets of permanent magnet machines and the resultant eddy current loss. And the proposed method is widely adaptable to a variety of permanent magnet machines with due account of complex machine geometry, various winding configurations and magnetic saturation.

(3). High-fidelity computationally-efficient electro-thermally coupled PM machine model has been proposed. Validated experimentally, the simulation results of the proposed model with remarkable temperature influence on the machine electromagnetic and thermal behaviours reveal high necessity of thermal-coupled models.

(4). Through a design, optimisation and test process of permanent magnet machine for a light-duty electric vehicle traction system, the computational efficiency, effectiveness and accuracy of the proposed analytical models is verified. Also as a worthy observation, the selected 18-slot 8-pole IPM topology exhibits very good overall performances especially in energy efficiency and cost for light-duty electric vehicles.

(5). Two special issues of electric traction system design are studied: the significant influence of driving cycles on the design and performance of PM machines; distributed traction system optimisation by using proper PM machine topologies and optimal power split ratios. The understandings acquired provide guidance that helps improve traction system in robustness, cost reduction and energy saving.

Several parts of the work of the thesis have been reported by the author during the course of his doctoral study in international conferences and journals. The publications are listed as follows:

Journal papers:

J1. L. Chen, D. Hopkinson, J. Wang, A. Cockburn, M. Sparkes and W. O'Neill, "Reduced Dysprosium Permanent Magnets and Their Applications in Electric Vehicle Traction Motors," in *IEEE Transactions on Magnetics*, vol. 51, no. 11, pp. 1-4, Nov. 2015.

J2. L. Chen, J. Wang and S. S. Nair, "An Analytical Method for Predicting 3-D Eddy Current Loss in Permanent Magnet Machines Based on Generalized Image Theory," in *IEEE Transactions on Magnetics*, vol. 52, no. 6, pp. 1-11, June 2016.

J3. S. S. Nair, L. Chen, J. Wang, R. Chin, I. Manolas, D. Svechkarenko, " Computationally Efficient 3D Analytical Magnet Loss Prediction in SPM Machines," accepted *to IET Transactions on Electric Power Application* for future publication

J4. P. Lazari, J. Wang and L. Chen, "A Computationally Efficient Design Technique for Electric-Vehicle Traction Machines," in *IEEE Transactions on Industry Applications*, vol. 50, no. 5, pp. 3203-3213, Sept.-Oct. 2014.

J5. S. Nair, J. Wang, L. Chen, R. Chin, I. Manolas, D. Svechkarenko, "Prediction of 3D High Frequency Eddy Current Loss in Rotor Magnets of SPM Machines," accepted to *IEEE Transactions on Magnetics for future publication*.

J6. S. S. Nair, J. Wang, L. Chen, R. Chin, I. Manolas, D. Svechkarenko, "Computationally Efficient 3D Eddy Current Loss Prediction in Magnets of Interior Permanent Magnet Machines," accepted to *IEEE Transactions on Magnetics for future publication.*

J7. S. S. Nair, J. Wang, L. Chen, R. Chin, I. Manolas, D. Svechkarenko, " Prediction of 3D Eddy Current Loss in Retaining Sleeve of Surface Mounted Permanent Magnet Machines," Submitted to *IEEE Transactions on Magnetics*

J8. S. S. Nair, J. Wang, R. Chin, L. Chen, T. Sun, " Analytical Prediction of 3D Magnet Eddy Current Losses in Surface Mounted PM Machines Accounting Slotting Effect," Submitted to *IEEE Transactions on Energy Conversion*

Conference papers:

C1. L. Chen, J. Wang, P. Lombard, P. Lazari and V. Leconte, "Design optimisation of permanent magnet assisted synchronous reluctance machines for electric vehicle applications," *Electrical Machines (ICEM), 2012 XXth International Conference on*, Marseille, 2012, pp. 2647-2653.

C2. L. Chen, J. Wang, P. Lazari and Xiao Chen, "Optimizations of a permanent magnet machine targeting different driving cycles for electric vehicles," *Electric Machines & Drives Conference (IEMDC), 2013 IEEE International*, Chicago, IL, 2013, pp. 855-862.

C3. L. Chen, P. Lazari and J. Wang, "Optimal power split ratio of a distributed electric vehicle traction system," *Power Electronics, Machines and Drives (PEMD 2014), 7th IET International Conference on*, Manchester, 2014, pp. 1-6.

C4. L. Chen, J. Wang and P. Lazari, "Influence of driving cycles on traction motor design optimizations for electric vehicles," *Transport Research Arena (TRA) 2014 Proceedings*, Paris, 2014, Accession number, 01540726

C5. L. Chen, X. Chen, J. Wang and P. Lazari, "A computationally efficient multi-physics optimization technique for permanent magnet machines in electric vehicle traction applications," *2015 IEEE International Electric Machines & Drives Conference (IEMDC)*, Coeur d'Alene, ID, 2015, pp. 1644-1650.

C6. P. Lazari, J. Wang and L. Chen, "A computationally efficient design technique for electric vehicle traction machines," *Electrical Machines (ICEM), 2012 XXth International Conference on*, Marseille, 2012, pp. 2596-2602.

C7. X. Chen, J. Wang, P. Lazari and L. Chen, "Permanent Magnet Assisted Synchronous Reluctance Machine with fractional-slot winding configurations," *Electric Machines & Drives Conference (IEMDC), 2013 IEEE International*, Chicago, IL, 2013, pp. 374-381.

C8. P. Lazari, J. Wang, L. Chen and X. Chen, "Design optimisation and performance evaluation of a rare-earth-free Permanent Magnet Assisted Synchronous Reluctance Machine for electric vehicle traction," *Power Electronics, Machines and Drives (PEMD 2014), 7th IET International Conference on*, Manchester, 2014, pp. 1-6.

C9. X. Chen, J. Wang, V. I. Patel, P. Lazari, L. Chen and P. Lombard, "Reluctance torque evaluation for interior permanent magnet machines using frozen permeability," *Power Electronics, Machines and Drives (PEMD 2014), 7th IET International Conference on*, Manchester, 2014, pp. 1-6.

C10. S. S. Nair, J. Wang, L. Chen, R. Chin, I. Manolas, and D. Svechkarenko, " Computationally efficent 3D rotor eddy current loss prediction in permanent magnet machines," *Electrical Machines (ICEM), 2016 XXIIth International Conference on*, Lausanne, 2016, pp. 1-7.

CHAPTER 2 Computationally efficient multi-physics models for permanent magnet machine design and optimisation in electric vehicle traction applications

This chapter describes computationally efficient modelling techniques that allow accurate multi-physics performance evaluations of permanent magnet machines in electric vehicle (EV) traction applications. It addresses multi-physics machine designs against driving cycles, including inverter-machine system electromagnetic performance, energy efficiency, thermal behaviours and mechanical stress in rotor lamination. To drastically reduce computation time of repeated finite element analysis (FE) of the non-linear electromagnetic field and mechanical stress in permanent magnet machines especially interior permanent magnet machines (IPM), a set of analytical machine models characterized from FE calculations are developed which lead to significant reduction in computation time without compromising accuracy for machine design/optimisations and subsequent machine simulations.

2.1 INTRODUCTION

Permanent magnet (PM) machines are increasingly employed in Electric Vehicle (EV) traction applications where high torque density and high energy efficiency are desirable. Especially for Interior Permanent Magnet Machines (IPM) which show promising potential in terms of high torque and wide field weakening capability that brought by both PM torque and reluctance torque, IPMs are receiving rapidly growing interest in the EV traction research community. As illustrated in Chapter 1, the challenge and complexity with design and optimization of an EV traction PM machine is the requirements for assessing multi-physical properties such as electrical, thermal, mechanical and demagnetization withstanding while achieving high energy efficiency over a wide torque-speed range. For a given machine design, these multi-physics performance evaluations should be carried out against driving cycles such as the Worldwide harmonized Light vehicles Test Procedures (WLTP), the New European Driving cycle (NEDC) and the Artemis Urban Driving Cycle (Artemis), etc., rather than against a single operating point with rated torque and speed. However, a driving cycle usually consists of thousands of torque-speed operation points, and for each operation point, finite element analyses (FEAs) are usually needed to implement machine performance evaluations, due to the necessity of dealing with nonlinearity and geometry complexity associated with IPMs. The consequence is that the evaluation process over a whole driving cycle for a single machine design requires tremendous computation effort. On the other hand, the design and optimization of a PM machine needs to evaluate a large number of trial designs in order to find the optimal design. Therefore, the required

computation time for an optimisation of a PM machine for EV traction is enormously huge even with the state-of-the art computing facilities and renders optimization by direct FEAs of multi-physics fields not feasible.

This chapter proposes a set of computationally efficient multi-physics modelling methods considering electromagnetic, thermal performances and mechanical stress constraints for designs/optimisations and simulations of PM traction machines especially IPM machines. The proposed methods characterise multi-physics FEA models into mathematical functions based on the FEA results on typical geometrical and physical parameters, and thus greatly curtailing the machine performance evaluation time in FE.

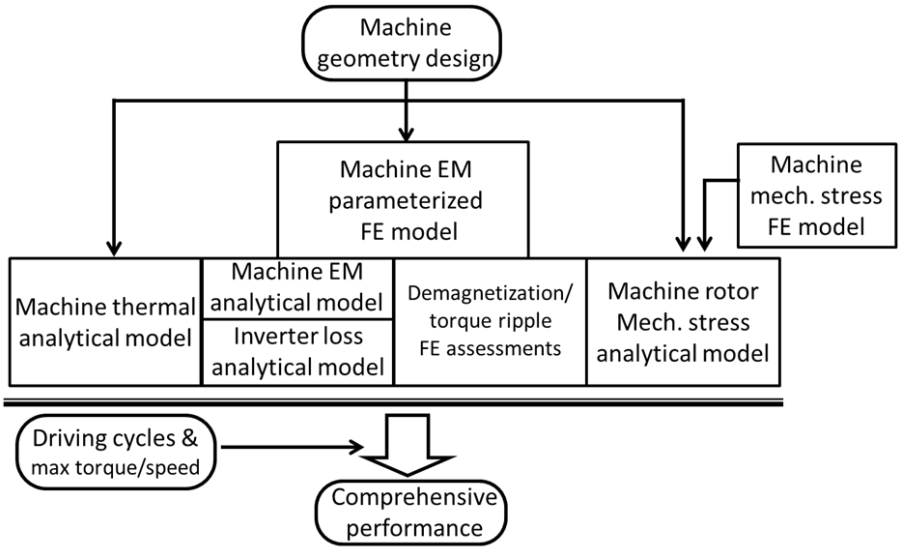

Figure 2.1. Comprehensive evaluation process of Machine performances employing multi-physics modelling method

2.1.1 FE-based multi-physical models

Figure 2.1shows the characterization process of these proposed analytical models. For a machine design sample, a flux linkage model, an iron loss model and magnet loss model are extracted from its electromagnetic (EM) FEA model. Accurate assessments on the demagnetization and torque ripple in the worst-case scenarios are also obtained during the process. The three models together with the analytical inverter loss model are used to predict the machine performance, such as Voltage-Current (VA) ratings over the peak torque-speed profile, power factor and energy loss of the system (inverter and machine). An analytical rotor mechanical stress model, defined as a function of rotor parameters is

established. Several mechanical FE calculations are used to calibrate the polynomial coefficients in the stress analytical model. It evaluates the maximum stress occurring in the rotor laminations at high speeds for a given rotor design. An analytical thermal model employs a lumped parameter circuit to predict the machine temperature rise under various operations. In addition, by using the techniques proposed in [77], a driving cycle is also characterized into a finite number of representative operation points, based on which the energy loss evaluation over the cycle could be performed with great reduction of computation without compromising accuracy.

It should be noted that the proposed models are applied for machines in light-duty electric vehicle applications, and the number of pole pairs is below 7. The maximum speeds are around 5000 rpm, maximum frequency is around 500 Hz for a 7-pole-pair machine. Thus the winding resistance and the copper loss are marginally affected by the frequency since the proximity effect is quite minor and the skin depth of the wires at the maximum speed is far greater than the wire diameter. For the applications with the maximum speed above 15000 rpm and the number of pole pairs above 14, the AC resistance associated with the frequency variation should be calculated by a proper FE winding model.

2.1.2 IPM Machine design example

In order not to lose generality of method, between the two major kinds of rotor topologies of PM machines: surface mounted PM (SPM) machines and IPM machines, due to the complexity of IPM machine geometry and its modelling techniques, an IPM machine is employed as an example in the following explanation. However the modelling method to be illustrated is also compatible to SPM with due simplifications and other permanent machine topologies such as synchronous reluctance machine (SynRM) or PM-assisted SynRM with modifications accordingly.

In terms of slots-poles combinations, compared with distributed winding configurations, fractional-slot windings benefit in reduced resistance and volume, high winding factor and inductance for field weakening, low cogging torque and easy manufacturing. But its high space harmonic content in the air-gap magnetic field brings disadvantages such as higher iron loss and eddy current loss in the magnets, higher risk of demagnetisation, and also noise and vibration. With the fractional slots and high harmonic contents, the benefit of reluctance torque in IPMs also diminishes as the saliency ratio is greatly reduced.

In the efforts of overcoming the disadvantages of fractional slot windings, a new low-harmonic-content fractional-slot winding configuration with 18 slots and 8 poles or 10 poles is proposed and studied [78][114] recently. As shown in Figure 2.4 (a), the 18-slot 8-pole winding configuration employs 2 sets of identical coils which are displaced in space of 9 slots for each phase. This arrangement of windings benefit from reduced harmonics of magneto-motive force (MMF), thus has improved performances on eddy current loss and reluctance torque [78][105]. The magnets are embedded in a V-shape slot inside the rotor core, thus protected by the lamination from the demagnetizing field. In the following illustrations of this chapter, the 18-slot 8-pole IPM machine is used as an example, and it will be studied against specifications for a small sized EV traction application. And in Chapter 5, this IPM machine will be studied and compared with other potential PM machine topology candidates.

Table 2.1 lists the machine design specifications and constraints. Two typical European driving cycles as shown in Figure 2.2: the NEDC driving cycle and the Artemis driving cycle are used as the target cycles against which the machine designs are particularly investigated. Figure. 2.3 shows the peak and continuous torque-speed envelopes with the representative operation points of the NEDC and Artemis. The typical operation points such as peak torque at base speed, continuous torque at base speed, peak torque at maximum speed, continuous torque at maximum speed are abbreviated as T_{pk}, T_r, T_m and T_{rm} respectively. Figure 2.4 (b) shows the 18-slot 8-pole IPM machine geometry with the six independent leading design parameters, including rotor radius (*Rr*), turn number per coil (*TN*), back iron width (*BW*) and tooth width (*TW*) in the stator, the ratio of the magnet depth to rotor radius (*RMR*) and the magnet opening angle (*BetaM*). Based on the specifications listed in Table 2.1, the IPM machine is designed and its basic geometric and characteristic parameters are listed in Table 2.2.

Table 2.1 Machine Design Specifications

Base speed	1350 rpm
Maximum cruise speed	4500 rpm
Maximum speed	5050 rpm
Peak torque below and at base speed	70 Nm
Continuous(rated) torque below and at base speed	35.5 Nm
Peak Power	9.9 kW
Continuous Power	5 kW

Peak Power at maximum cruise speed	7 kW
Continuous Power at maximum cruise speed	4.7 kW
Maximum current limit	170 A
Nominal DC link Voltage	120 V
Peak line-to-line voltage at maximum speed	<240 V
Stator outer diameter	150 mm
Stack length	118 mm
Demagnetization withstand ability (150^{o}C)	B >0.6 T
Magnet/ winding temperature limit (wind cooling)	120 ^{o}C/150 ^{o}C
Torque ripple (peak to peak) limit (percentage to average peak torque)	10%
Lamination mechanical stress limit	450 MPa

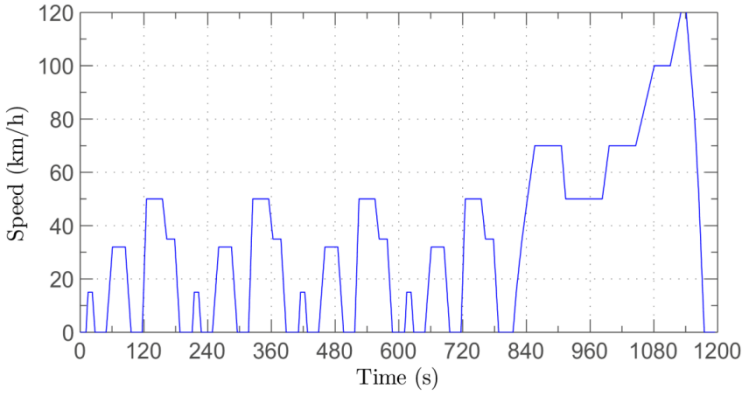

(a)

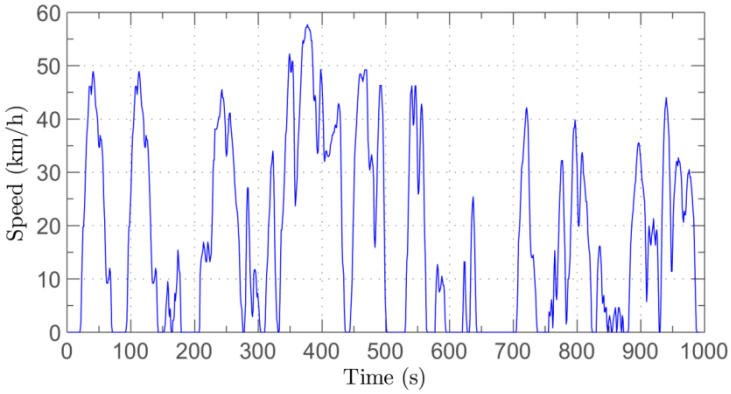

(b)

Figure 2.2. Vehicle speed during (a) the NEDC cycle and (b) the Artemis cycle

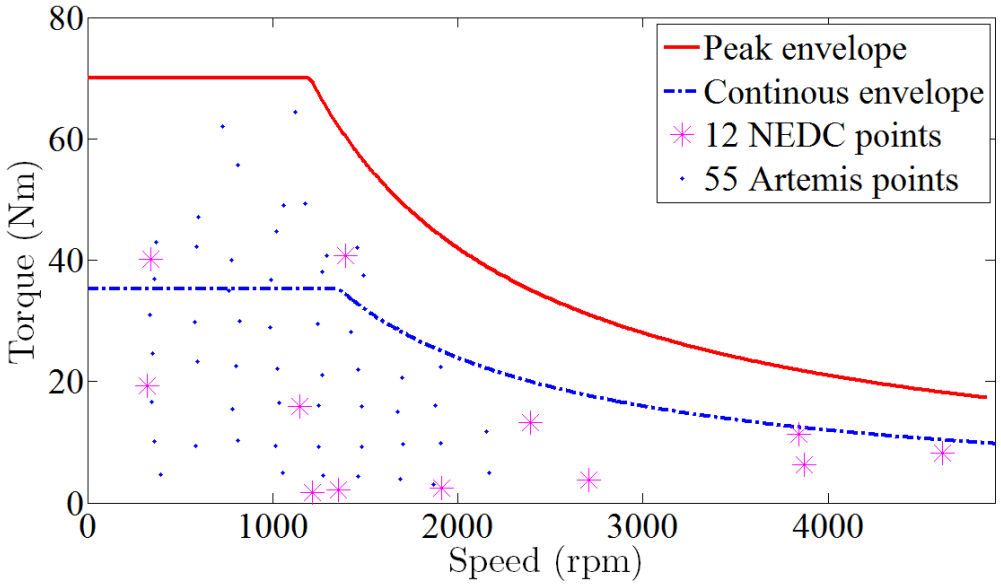

Figure. 2.3. Peak power and continuous power torque-speed envelopes with driving cycle representative points.

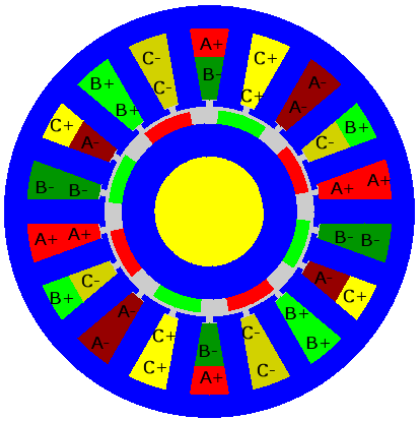

(a)

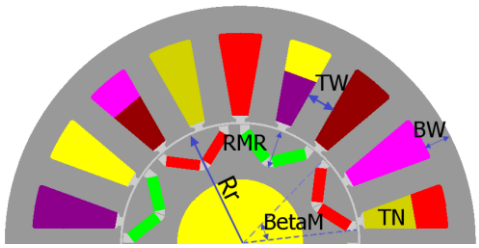

(b)

Figure 2.4. 18-slot 8-pole IPM machine (a) winding configuration, (b) design parameters to be optimised.

Table 2.2 Basic geometric and charateristic parameters of the 18-slot 8-pole IPM machine

	Unit			Unit	
Stator outer radius	mm	75	Coil number per phase	-	6
Rotor outer radius	mm	36.45	Turn number per coil	-	6
Air gap	mm	0.5	Phase resistance	ohm	0.0349
Shaft radius	mm	20	D-axis inductance	mH	0.622
Stack length	mm	118	Q-axis inductance	mH	1.25
Stator slot number	-	18	Saliency ratio	-	2.01
Pole pair number	-	4	Magnet flux linkage (phase)	wb	0.0633
Phase number	-	3	Torque constant	Nm/A	0.45

2.2 Machine electromagnetic model

2.2.1 Flux linkage model

The machine's EM property is characterized as analytical flux linkage models, which relate *d*-axis and *q*-axis flux linkages ψ_d, ψ_q to current i_d, i_q in the *d*-*q* system. The flux linkage models are used to predict the current needed for a given torque-speed demand, thus providing the basis for the other performance evaluations. In the models, ψ_d, ψ_q are expressed as polynomial functions of the variables(i_d, i_q).

$$\psi_d(i_d, i_q) = \sum_{n=0}^{N} a_n \cdot i_d^n \cdot i_q^{N-n} \tag{2.1}$$

$$\psi_q(i_d, i_q) = \sum_{n=0}^{N} b_n \cdot i_d^n \cdot i_q^{N-n} \tag{2.2}$$

where *N* is the polynomial order number.

The polynomial coefficients a_n and b_n are calculated by curve-fitting the output flux linkages, which are obtained from static electromagnetic (EM) FEA of a given design excited by a group of (i_d, i_q) current samples. The average flux linkages over one electric period are used in the modelling process. Figure 2.5 shows the d-axis flux linkage variation with rotor position for a given (i_d, i_q). As can be seen, it contains

high order space harmonics with the dominant 6th order. In order to save FE computations, only two rotor positions θ_a and θ_b, which is shifted by half wavelength of the dominant harmonic are calculated, as shown in Figure 2.5. The mean values from the two positions are used as the average flux linkages.

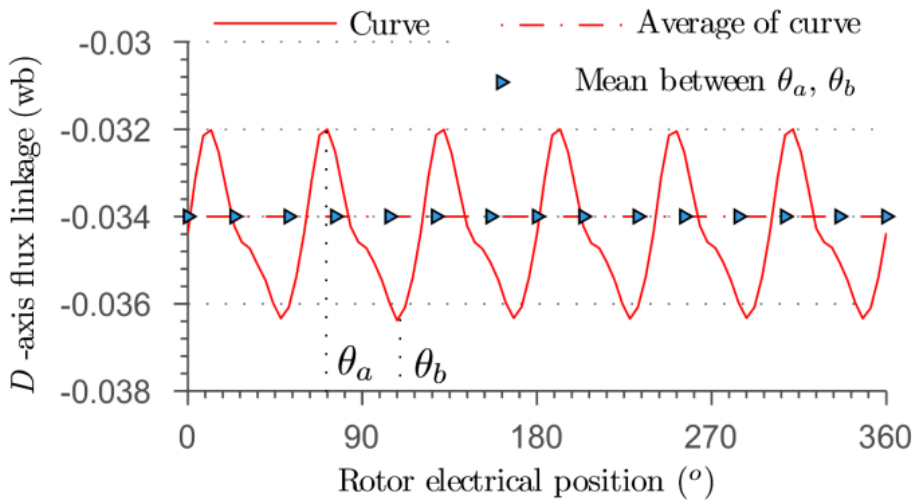

Figure 2.5. D-axis flux linkage curve with varying rotor positions obtained from FE.

By way of example, Figure 2.6 compares the *d*-axis and *q*-axis flux linkage maps of the 5th order polynomial derived from 20 current samples (4 i_d × 5 i_q) with that obtained from discreet FE analyses. It can be seen that the analytical model fits the FE predicted flux linkage very well. It only takes ~20 mins to implement these static FE calculations and to build the analytical model for a given machine geometry design.

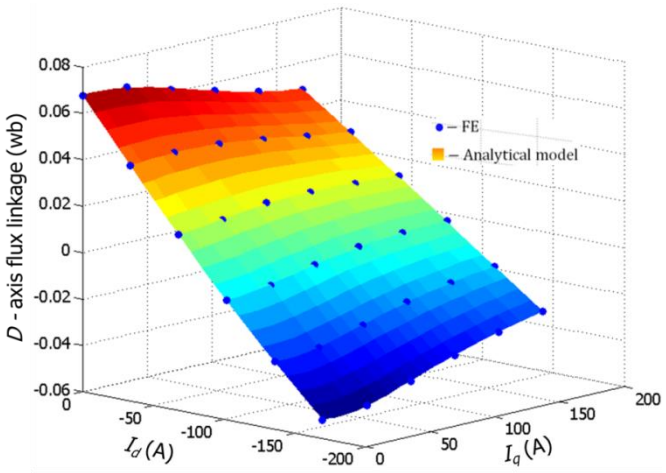

(a)

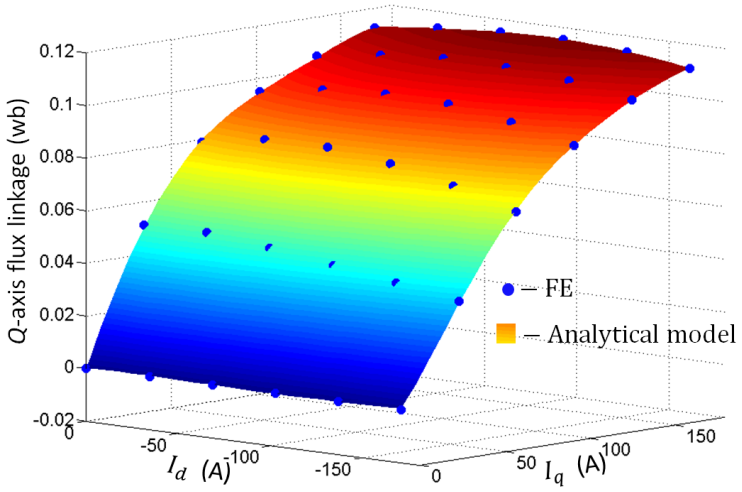

(b)

Figure 2.6. (a). D-axis flux linkage, (b) Q-axis flux linkage from analytical model and FE.

2.2.2 Torque and voltage models

Thereafter the average torque $T_{em}(i_d, i_q)$ and phase voltage $V(i_d, i_q)$ functions of the machine in steady state could be obtained by:

$$T_{em}(i_d, i_q) = \frac{m}{2} P \left[\psi_d(i_d, i_q)\, i_q - \psi_q(i_d, i_q)\, i_d\right] \tag{2.3}$$

$$V_d(i_d, i_q) = R_s i_d - \omega_e \psi_q(i_d, i_q) \tag{2.4}$$

$$V_q(i_d, i_q) = R_s i_q + \omega_e \psi_d(i_d, i_q) \tag{2.5}$$

$$V(i_d, i_q) = \sqrt{V_d^2(i_d, i_q) + V_q^2(i_d, i_q)} \tag{2.6}$$

where m is the phase number, P is the pole pair number and ω_e is the electrical radiant speed.

Figure 2.7 compares the electromagnetic torque map over (i_d, i_q) variations of the 5th order polynomial torque function with that obtained from discreet FE analyses. Figure

2.8 shows the prediction error of the analytical model. The FE results are average torque values over an electrical cycle. It can be seen that the analytical results have good agreements with the FE model and the maximum prediction error is 2.5%.

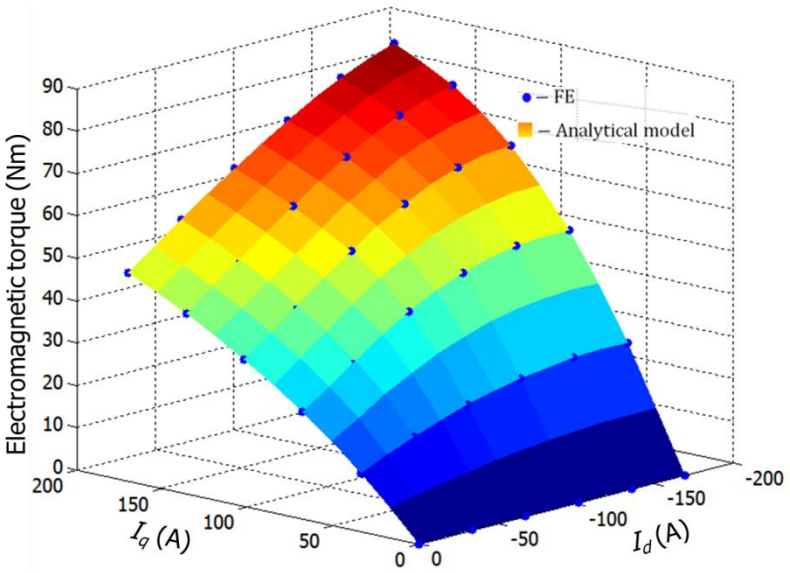

Figure 2.7. Electromagnetic torque map predicted using analytical model and FE.

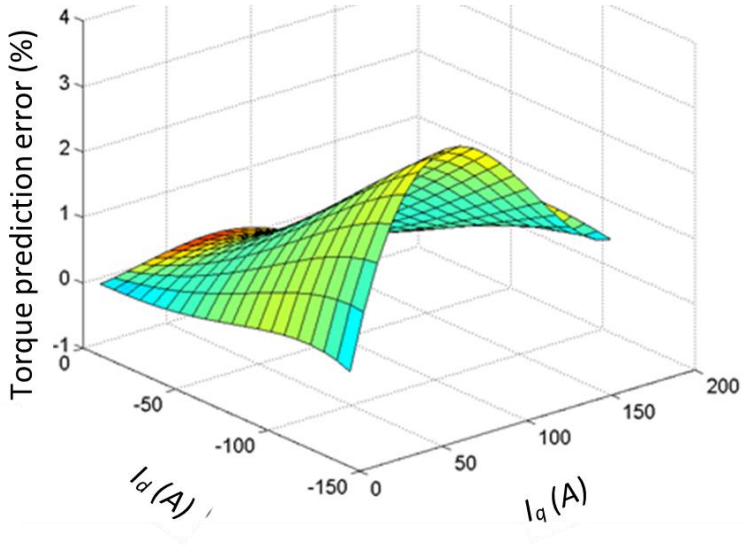

Figure 2.8. Electromagnetic torque prediction error between analytical model and FE model.

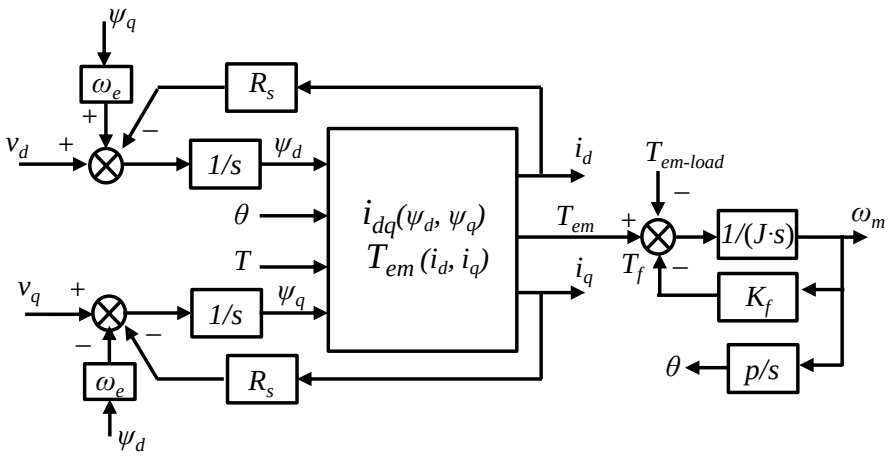

Figure 2.9. Machine model based on analytical inverse flux linkage model

The derived analytical models $\psi_d(i_d, i_q)$, $\psi_d(i_d, i_q)$, $T_{em}(i_d, i_q)$ could also be used in transient electromagnetic simulations of machines based on the equations given in (2.7), (2.8) and (2.9). To avoid the differential computation in the simulations, the *d*- and *q*-axis currents may be expressed as functions of *d*- and *q*-axis flux linkages, i.e., $i_d(\psi_d, \psi_q)$ and $i_q(\psi_d, \psi_q)$ by inverting of $\psi_d(i_d, i_q)$and $\psi_q(i_d, i_q)$. The method for the inverse is described in [79]. The simulation model is described in Figure 2.9.

$$V_d = \frac{d\psi_d}{dt} + R_s i_d - \omega_e \psi_q \tag{2.7}$$

$$V_q = \frac{d\psi_q}{dt} + R_s i_q + \omega_e \psi_d \tag{2.8}$$

$$T_{em} = \frac{m}{2} p[\psi_d i_q - \psi_q i_d] \tag{2.9}$$

2.3 Current control modelling method

Based on the derived analytical models $\psi_d(i_d, i_q)$, $\psi_d(i_d, i_q)$, $T_{em}(i_d, i_q)$ and $V(i_d, i_q)$, an algorithm is developed by employing the Bisection method or the Newton-Raphson method to search for the d- and q-axis currents $I_d(T_{em}, n)$ and $I_q(T_{em}, n)$ which produce the required torque T_{em} at a given speed n with minimum power loss under current and voltage limits. At low speeds, the machines should operate on so called Maximum Torque per Ampere (MTPA) trajectory to minimise the current and, hence,

the copper loss. At high speeds, the back-EMF of a PM machine may become larger than the supply voltage and consequently field weakening is needed to keep the motor peak line-to-line voltage below the inverter DC voltage limit. The processes searching for the control current $I_d(T_{em}, n)$ and $I_q(T_{em}, n)$ at the MTPA and field weakening operations are described as below respectively.

2.3.1 MTPA point

Figure 2.10 shows typical variations of copper loss, total loss and the line-to-line voltage with the *d*-axis current I_d for a given torque at low speeds. As can be seen, the minimum copper loss point (MPTA) virtually coincides with the minimum total loss point since at low speeds copper loss is dominant. Thus, for computation convenience, I_d and I_q are selected to realise the MTPA point.

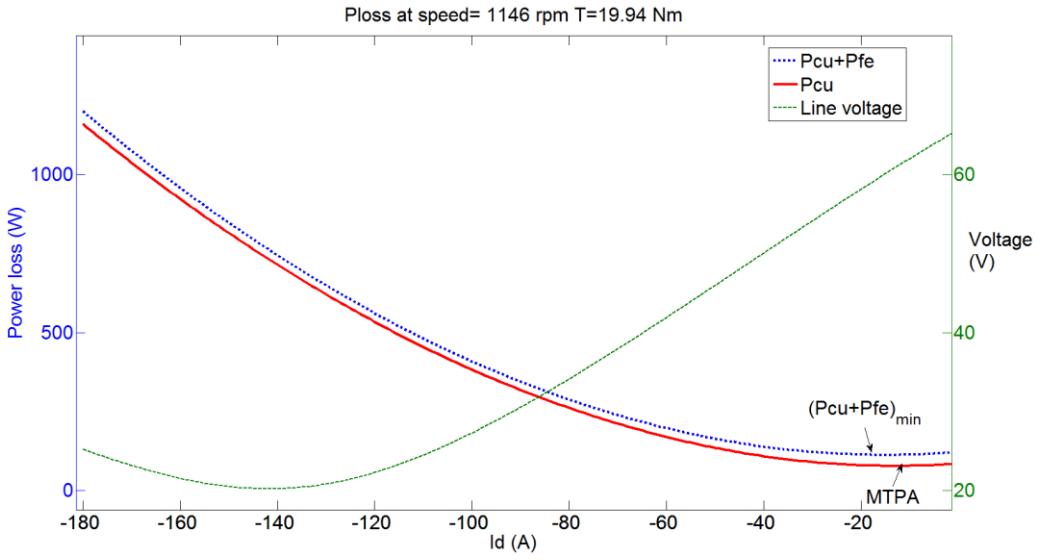

Figure 2.10. Power loss and voltage curves with changing i_d and constant torque 19.94 Nm at low speed 1146 rpm

2.3.2 Field-weakening point

When machines operate at high speeds, the voltage becomes higher and a large negative i_d deviating away from the MTPA has to be selected in order to weaken the magnetic field and, hence, to reduce the voltage. As shown in Figure 2.11, the copper loss (slash line) and the total loss (solid line) increase with the increase of the negative i_d. The gap between the two lines shows the iron loss. It can be seen that in the increasing process of the negative i_d , the iron loss first decreases due to the magnet flux is weakened, then it turns to increase as 1) the iron loss component due to the harmonics are increased; 2) the sign of *d*-axis flux is changed due to the further increasing of i_d. The variation of the

iron loss is minor because during the process the torque is kept the same, thus while i_d is increased, i_q has to be decreased which has some cancelling effect on the variation of the total iron loss.

i_d is chosen to satisfy the DC-link voltage limit at 120V with the minimum loss. This is indeed the *d*-axis current which yields the peak line-to-line voltage equal to the inverter DC-link voltage.

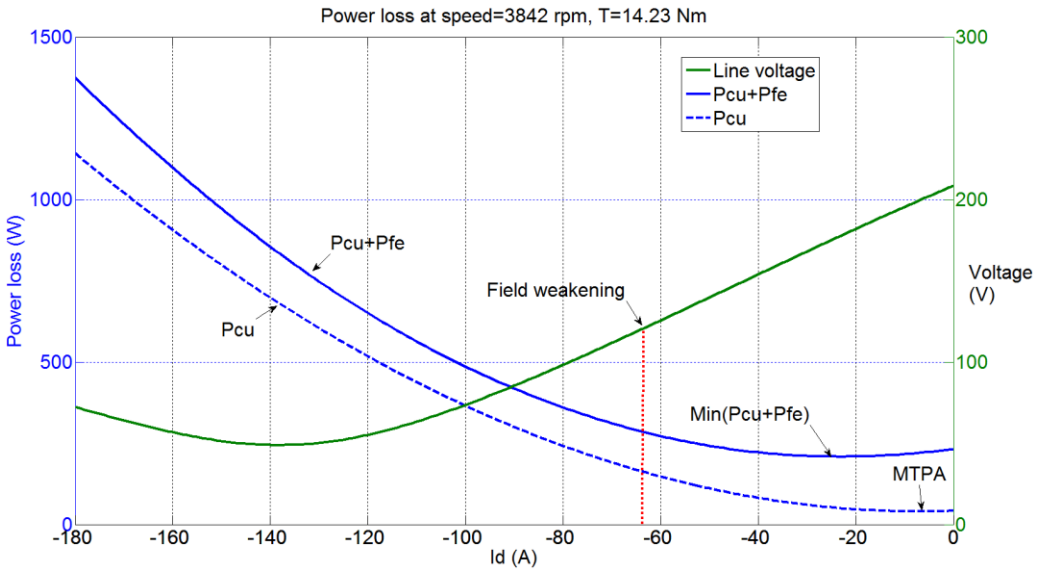

Figure 2.11. Power loss and voltage curves with changing i_d and constant torque 14.23 Nm at high speed 3842 rpm

2.3.3 Controlled current over torque-speed envelope

Figure 2.12 (b) shows the i_d and i_q selections on an iso-torque map to realise the torque-speed envelope shown in Figure 2.12 (a) for the studied machine. The torque-speed envelope could be separated into 3 sections. In section A, the *d* and *q*-axis currents are determined by the minimum power loss operation (MTPA) and are restricted by the maximum current limit. In section B, the motor operates in field weakening mode. The highest torque productions at every speed are constrained by the current limit line. In section C, as speed goes higher, the maximum achievable torque is on the tangential intersection of the iso-torque curves and the voltage limiting ellipses.

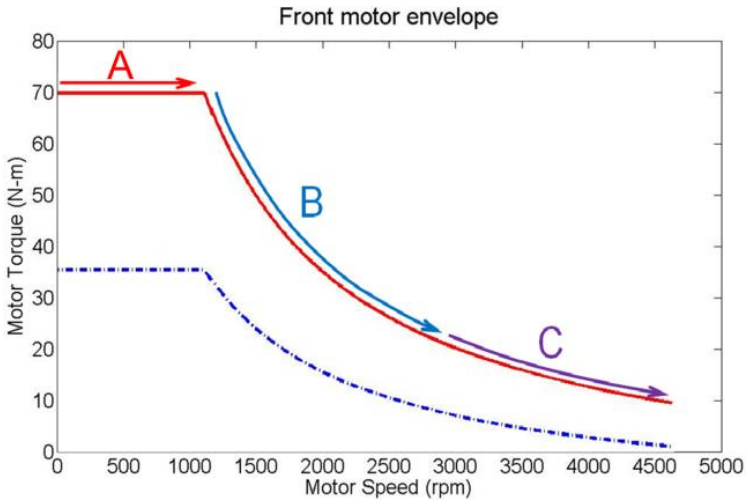

(a)

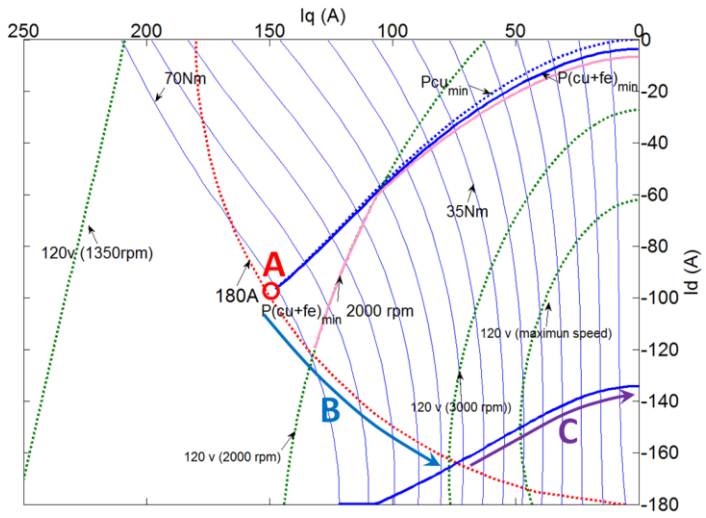

(b)

Figure 2.12. (a) Torque-speed envelopes; (b) i_d-i_q selection over the machine torque-speed envelope

Figure 2.13 shows the calculated the *d*-axis and *q*-axis control current maps over the torque-speed envelope of the studied machine. The obtained current at a given torque-speed operation point are used in machine performance evaluations such as the VA ratings, energy efficiency, thermal and demagnetisations.

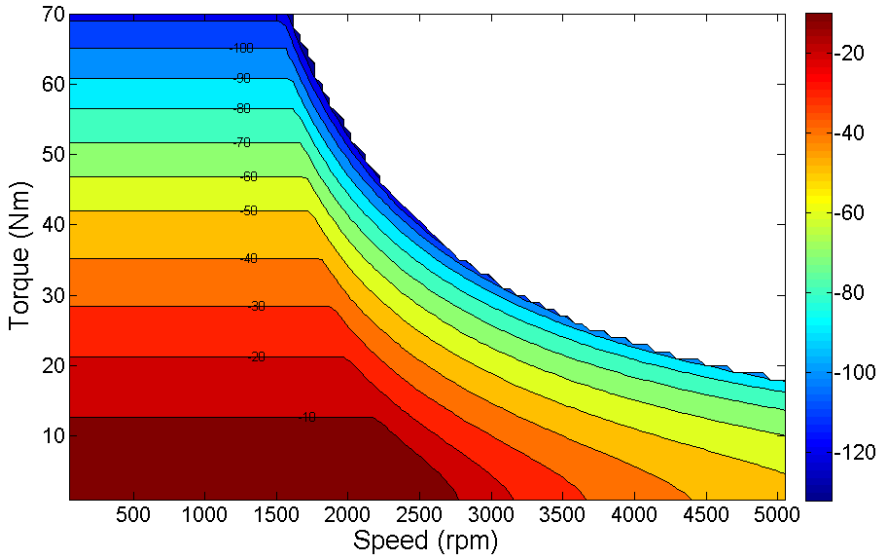

(a)

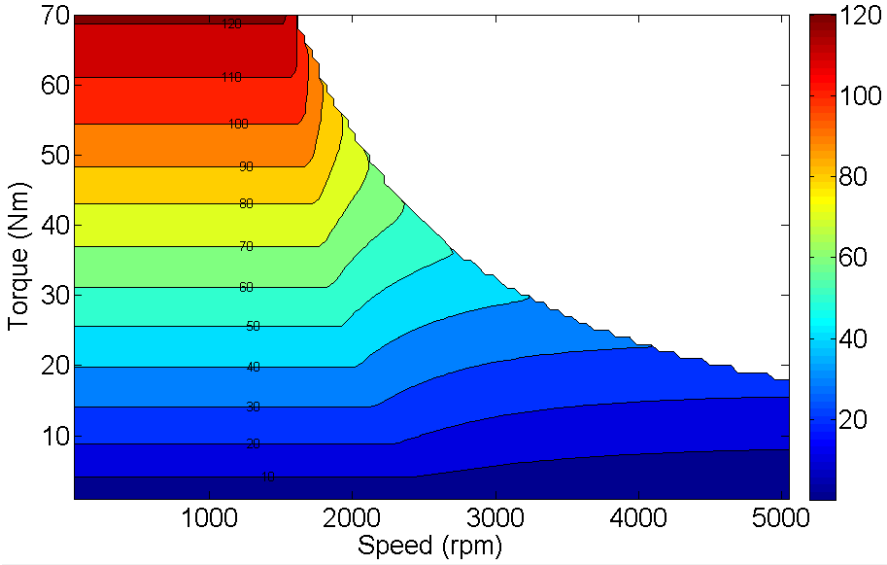

(b)

Figure 2.13. (a) *d*-axis, (b) *q*-axis control current maps over the machine torque-speed envelope

2.4 Analytical iron loss models

An electric vehicle drives across a wide speed range, and often operates at high cruising speed in rural areas. The high speed performance of a permanent magnet machine is important in the overall design criteria as a traction machine. The evaluation of machine performances at high speed, such as energy efficiency and thermal behaviours, relies heavily on an accurate iron loss model.

However there are several modelling challenges for the iron loss evaluation: (1). hysteresis loss mechanism within magnetic domains is very complex. The hysteresis BH loop is not only dependent on the fundamental flux density variation amplitude and frequency, but also considerably affected by the minor loops due to the space and time harmonics and magnetisation orientation direction variation as a result of the flux density vector changes; and (2) although the complexity of the iron loss mechanism model in magnetic domains could be averted by the final calibration of the machine iron loss predictions against typical iron loss experiment results such as at open circuit operation, the accumulated iron loss over the machine's stator and rotor laminations varies significantly with drive conditions when the torque and speed or input current amplitude, phase and frequency change. Because of saturation of iron material property and complex machine geometry such as slotted laminations in stator and irregular IPM rotor topologies, electromagnetic FE calculations with calibration are necessary for a given load. That indicates enormous computation time in FE for various load conditions which inhibits realistic machine optimisations and dynamic simulations with FE.

This section first discusses state-of-art iron loss models on the scale of an individual magnetic domain and on the scale of a whole machine. Then to substitute enormous FE calculations, an improved accurate analytical machine iron loss model is proposed for applications which require high accuracy level such as performance evaluations and dynamic simulations after machine optimisations. Finally for EV traction machine optimisations which have high demand for computation efficiency, a simplified analytical machine iron loss model is developed.

2.4.1 Iron loss mechanism models of magnetic domains

A classical iron loss model of magnetic domains includes three loss components: hysteresis loss P_h, eddy current loss P_e and excess eddy current loss P_x. According to Bertotti iron loss model, the iron loss equation within a magnetic domain or an FE element is given by:

$$P_{fe} = P_h + P_e + P_x \tag{2.10}$$

$$P_{fe} = k_h f (B_m)^2 + k_e \{\sum_{v=1}^{\infty} [B_v vf]^2\} + k_x \{\sum_{v=1}^{\infty} [B_v vf]^{1.5}\} \tag{2.11}$$

B_m is the peak flux density within the studied element over one electrical cycle, B_v is the amplitude of the v-th harmonic component of the flux density, k_h, k_e and k_x are the hysteresis, eddy current and excess eddy current loss coefficients respectively, f is the electrical frequency.

The classical Bertotti iron loss model is an ideal analytical model describing the iron loss generating effect. It does not consider many complexities such as the material property nonlinearity, harmonic effect on hysteresis BH loops and orientation variation. Much work has been done since to improve iron loss models in terms of considering the iron loss coefficients' dependence on the local flux density and frequency [80]-[83] and the minor hysteresis loops due to the space and time harmonics [84]-[88]. These modification methods render the model closer to the reality and gain higher accuracy over wide electromagnetic field situations. In a summary the modified iron loss models for a magnetic domain element is governed by:

$$P_{fe} = \sum_{v=1}^{\infty} k_h(B_1)B_v^{\alpha} vf + k_e(B_1)k_{ef}(f)[B_v vf]^2 + k_x(B_1)[B_v vf]^{1.5} \tag{2.12}$$

In the equation, hysteresis loss is also expressed with combined effect of all the flux density harmonics to account for the minor loops. The coefficients k_h, k_e and k_x for the hysteresis, eddy current and excess losses respectively are functions of flux density associated with the fundamental harmonic. For the eddy current loss, another coefficient k_{ef} as a function of frequency is added to consider the skin effect. In an FE calculation of the whole machine at a given electric loading and frequency, the flux density in each element is Fourier analysed in time domain, then (2.12) is used to calculate the iron loss. At last the iron loss of all the elements are accumulated together to obtain the machine's total iron loss.

2.4.2 Machine iron loss model based on open-circuit and short-circuit FEs

According to [89], each iron loss component of a machine under a given operation can be estimated approximately using its values obtained in open-circuit and short-circuit conditions, together with phase voltage V_m using (2.7) and a virtual voltage V_{id} relevant to the d-axis current. This method greatly reduces the calculation work when examining the iron losses of a machine over a wide torque-speed operation region as only two time-step FE calculations are needed. The iron loss function is given as:

$$P_h = P_h^{oc} \times f_m + P_e^{oc} \times {f_m}^2 + P_x^{oc} \times {f_m}^{1.5} + P_h^{sc} \times f_d + P_e^{sc} \times {f_d}^2 + P_x^{sc} \times {f_d}^{1.5} \tag{2.13}$$

$$f_m = \frac{V_m}{V_{oc}}, \qquad f_d = \frac{V_{i_d}}{V_{oc}}, \qquad V_{i_d} = |\omega_e(\psi_d - \psi_m)|$$

where $P_h^{oc}, P_e^{oc}, P_x^{oc}$ and $P_h^{sc}, P_e^{sc}, P_x^{sc}$ are the hysteresis, eddy current and excess losses on the open-circuit and short-circuit points respectively, V_{oc} is the open-circuit back-EMF, ω_e is the electrical angular speed, ψ_d is the d-axis flux linkage, and ψ_m is the magnet flux linkage.

The accuracy of the method is examined when it is employed to predict the iron loss of the studied IPM machine. Figure 2.14 shows relative error map of method (2.13) compared to FE prediction over the machine torque-speed envelope while control modes such as MTPA and field weakening are implemented. The relative errors are against the FE predicted iron loss of 114 W at the point of maximum speed 4500 rpm and continuous power. Figure 2.15 shows a similar relative error map of the method (2.13) where the errors are calculated against FE predicted iron loss at a given torque-speed load point.

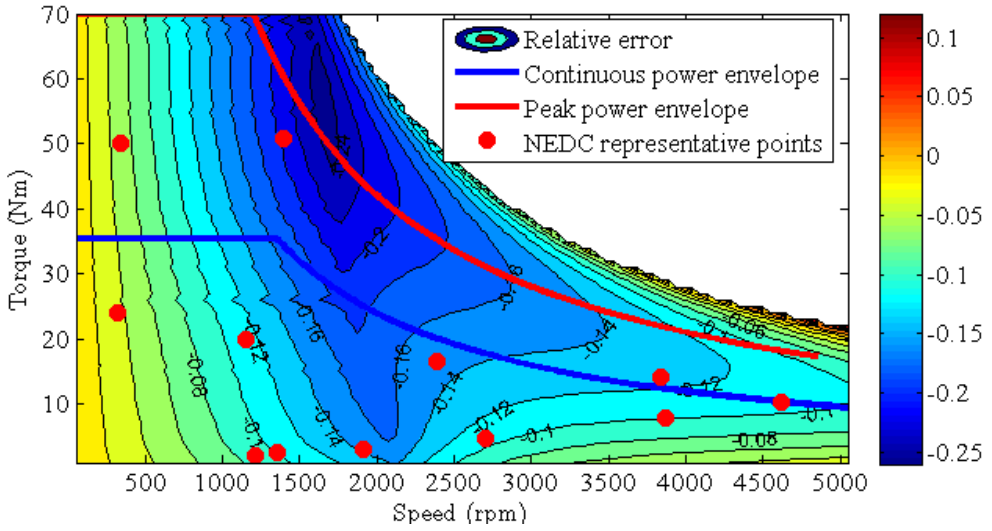

Figure 2.14. Relative error of method (2.13) compared to FE prediction over the machine torque-speed envelope normalised against FE predicted iron loss of 114 W at the maximum speed 4500 rpm and continuous power)

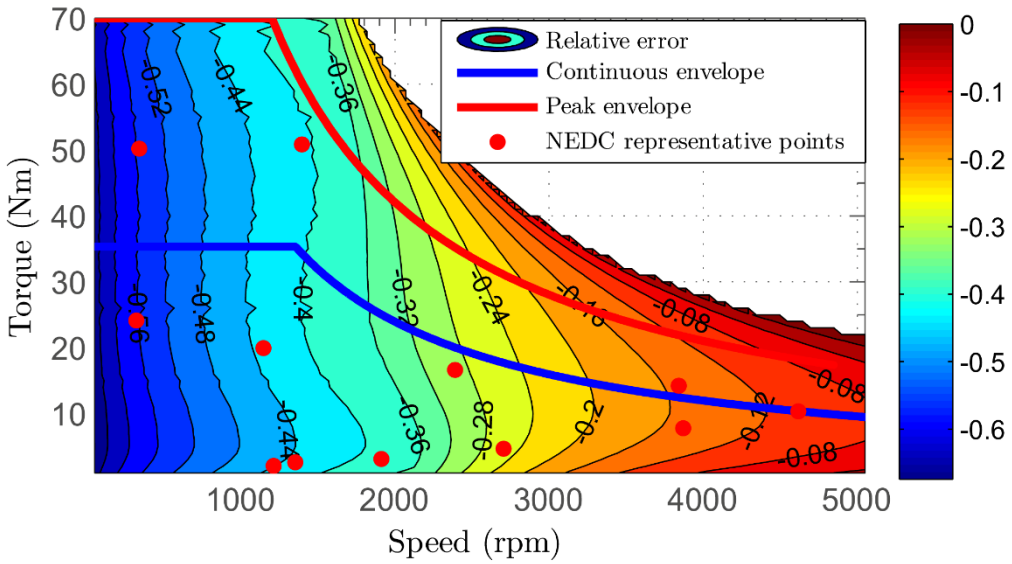

Figure 2.15. Relative error of method (2.13) compared to FE prediction over the machine torque-speed envelope against FE predicted iron loss at each load point

It can be seen from Figure 2.14 that when the speed is low or torque is small, the error is below 5%. However the error is up to 10%-16% in the middle of the torque-speed range of the envelope, where the machine continuously operates and majority of the NEDC representative points locate in this area. From Figure 2.15 where the relative errors are plotted against FE results at each load point, the iron loss model (2.13) generates much greater errors which are up to 30%-40%. The large error would affect the accuracy of the predictions of machine energy efficiency and thermal performances, especially when the machine operates in the low torque or high speed regions where the iron loss is a significant part compared with the copper loss.

2.4.3 High-fidelity iron loss model for simulations

A new iron loss prediction model is developed and presented in this section. The model aims to give accurate iron loss predictions over various torque-speed operation scenarios.

Investigating the classical Bertotti iron loss model and state-of-art iron loss models, the iron loss associated with every FE element could be expressed as two separable parts: one as a function of current (i_d, i_q) representing the influence of flux density; the other as a function of frequency f or rotational speed ω_e representing the rate of change of electromagnetic field. In a time-step FE calculation over an electrical cycle with current (i_d, i_q) variations and given frequency f_1, the equation for the iron loss of the machine P_{1fe} may be expressed by:

$$P_{1fe} = \sum_{i=1}^{N}\sum_{v=1}^{\infty} k_h(B_{1,i})B_{v,i}(i_d, i_q)^{\alpha} v f_1 + k_e(B_{1,i})k_{ef}(f_1)\left[B_{v,i}(i_d, i_q) v f_1\right]^2 + k_x(B_{1,i})\left[B_{v,i}(i_d, i_q) v f_1\right]^{1.5} \tag{2.14}$$

where N is the total number of the elements in the FE model, $B_{1,i}$ and $B_{v,i}$ are the amplitudes of the fundamental flux density and v-th harmonic components, respectively, over an electrical cycle within the i-th element. Flux density $B_{1,i}$, $B_{v,i}$ and coefficient k_h, k_e, k_x are all functions of current (i_d, i_q), regardless of the frequency. Subsequently the equation (2.14) could be rewritten as:

$$P_{1fe} = P_{1h}(i_d, i_q) + P_{1e}(i_d, i_q) + P_{1x}(i_d, i_q) \tag{2.15}$$

where P_{1h}, P_{1e} and P_{1x} are the hysteresis loss, eddy current loss and excess eddy current loss of the whole machine at the frequency f_1 respectively. The three components are also functions of current (i_d, i_q).

Based on (2.14), the variable f could be decoupled from the current (i_d, i_q) in the iron loss function. Thus for other operating points with the same current (i_d,i_q) but different frequency f, the total iron loss P_{fe} could be derived based on the result P_{1h}, P_{1e} and P_{1x}, obtained at f_1, and is given by:

$$P_{fe} = P_{1h}(i_d, i_q)k_f + P_{1e}(i_d, i_q)k_{sf}k_f^2 + P_{1x}(i_d, i_q)k_f^{1.5}$$
$$k_f = \frac{f}{f_1}, \qquad k_{sf} = \frac{k_{ef}(f)}{k_{ef}(f_1)} \tag{2.16}$$

Equation (2.16) implies that if the functions $P_{1h}(i_d, i_q)$, $P_{1e}(i_d, i_q)$ and $P_{1x}(i_d, i_q)$ of the three iron loss components at a reference frequency f_1 are constructed, the iron loss of the machine at arbitrary frequency f could be calculated.

In order to represent the influence of the flux density saturation and machine geometry on the total iron loss, time-step FEs at several (i_d, i_q) current samples and reference frequency f_1 could be performed to acquire the iron loss values at these current samples. Thereafter the functions $P_{1h}(i_d, i_q)$, $P_{1e}(i_d, i_q)$ and $P_{1x}(i_d, i_q)$ could be established using curve fitting method based on the FE results.

As a case study on the studied IPM machine, 20 time-step FEs over one electrical cycle with 4×5 (i_d, i_q) combination samples at the base speed 1350 rpm are implemented. Thereafter the 20 samples of iron information are curve-fitted as polynomial functions of hysteresis, eddy current and excess eddy current loss given by:

$$P_{1h} = \sum_{i=0}^{4} \sum_{j=0}^{i} a_{i,j} \cdot i_d^j \cdot i_q^{i-j}$$

$$P_{1e} = \sum_{i=0}^{4} \sum_{j=0}^{i} b_{i,j} \cdot i_d^j \cdot i_q^{i-j}$$

$$P_{1x} = \sum_{i=0}^{4} \sum_{j=0}^{i} c_{i,j} \cdot i_d^j \cdot i_q^{i-j} \quad (j \leq 3) \tag{2.17}$$

where $a_{i,j}$, $b_{i,j}$ and $c_{i,j}$ are the polynomial coefficients for three iron loss components, respectively. Thus the complete the iron loss model with the current (i_d, i_q) and frequency f is given by:

$$P_{fe} = \sum_{i=0}^{4} \sum_{j=0}^{i} a_{i,j} i_d^j \cdot i_q^{i-j} k_f + b_{i,j} \cdot i_d^j \cdot i_q^{i-j} k_{sf} k_f^2 + c_{i,j} \cdot i_d^j \cdot i_q^{i-j} k_f^{1.5}, (j \leq 3) \tag{2.18}$$

The proposed iron loss model (2.18) is examined over variations of current (i_d, i_q) and machine speed by comparing the prediction results with FE calculations. Figure 2.16 compares the predicted iron losses and the three loss components when the machine is excited with the MTPA currents (i_d=-39A,i_q=66A) at the rated-torque 35 Nm and 1350rmp over the speed range of 450 rpm to 4050 rpm. Figure 2.17 shows similar comparison when the machine is excited with the field weakening current (i_d=-59A, i_q=16A) at the maximum-speed 4500 rpm andcontinuous-power point. Good agreements of the prediction results with FE could be observed in the wide speed range.

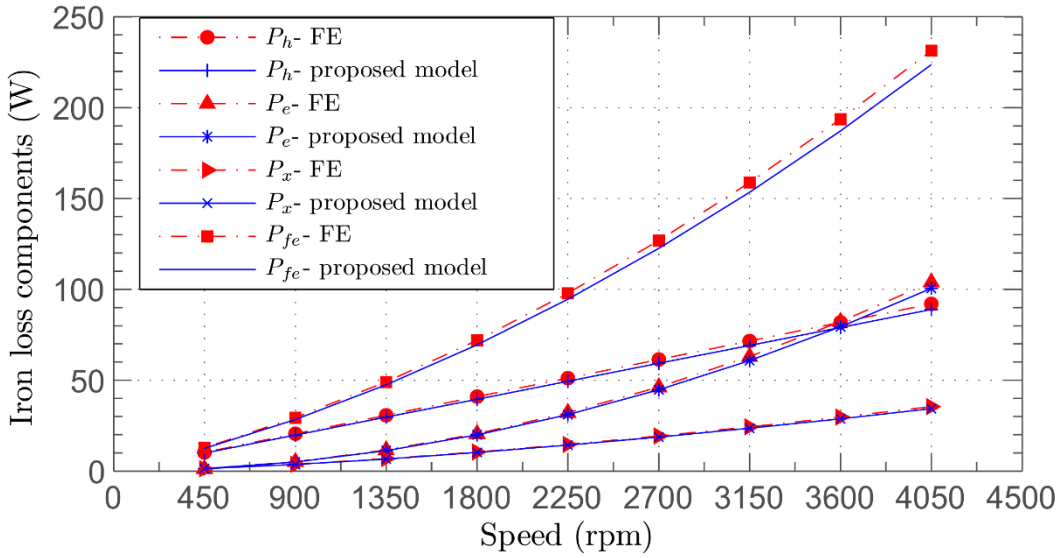

Figure 2.16. Iron loss variations with speed at rated currents (i_d=-39A, i_q=66A) predicted by the proposed model and FE

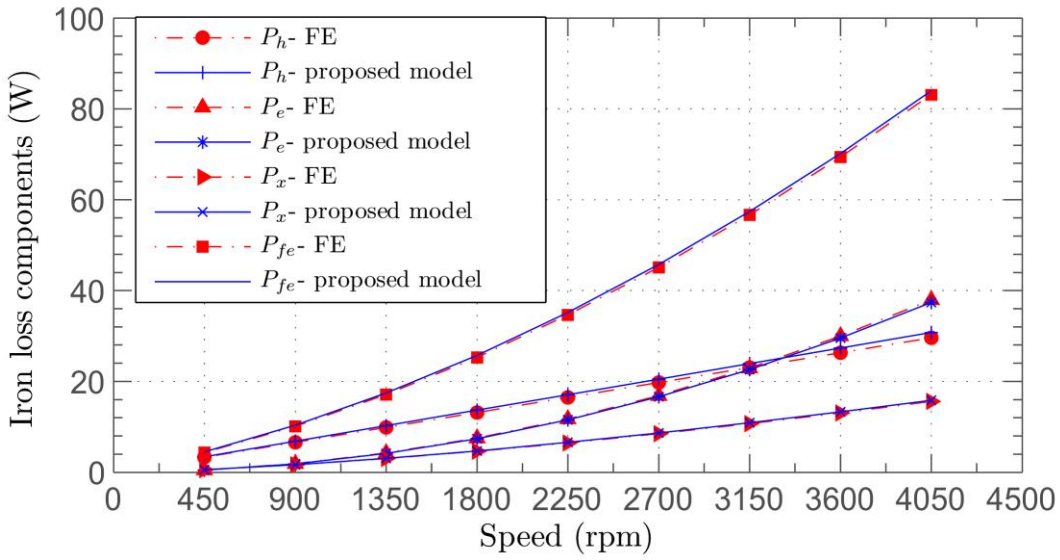

Figure 2.17. Iron loss variations with speed at (i_d=-59A, i_q=16A) predicted by the proposed model and FE

The accuracy of the iron loss model (2.18) is also examined when the current (i_d, i_q) varies. Figure 2.18 shows the iron loss over the available (i_d, i_q) range predicted by the model and FE at the speed of 2300 rpm. Figure 2.19 shows the relative errors of the proposed model compared to the FE results at each current combination. It can be seen that over the whole (i_d, i_q) range, the relative error is below 4%.

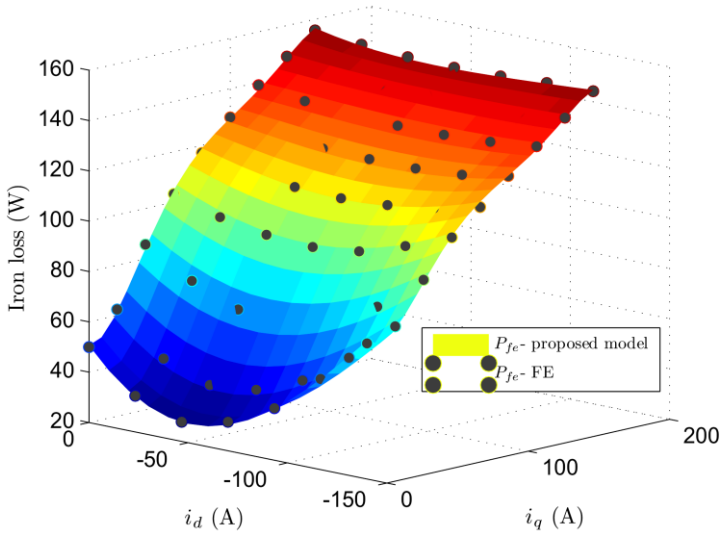

Figure 2.18. Iron loss variation at 2300 rpm with (i_d, i_q) predicted by the proposed model and FE

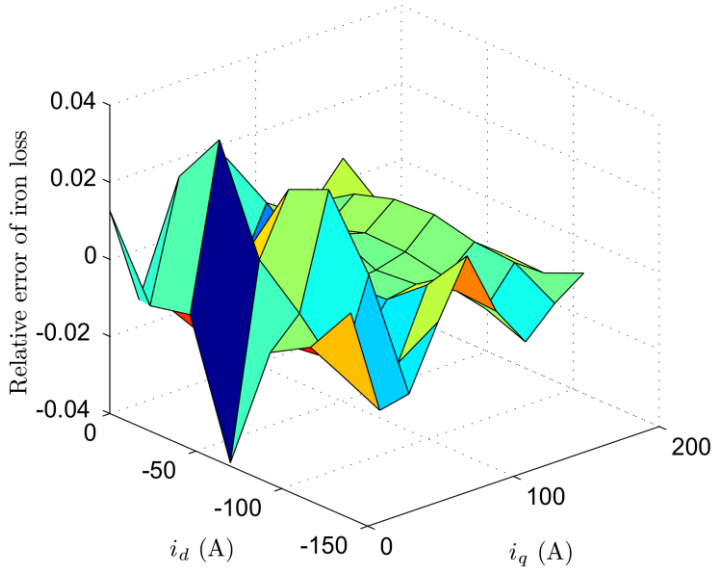

Figure 2.19. Relative iron loss error variation at 2300 rpm with (i_d, i_q) between proposed model and FE

Compared to time-step FE, the proposed model provides an analytical method that allows efficient calculation of iron loss with high accuracy over wide torque and speed operations, thus facilitates the machine design performance evaluations and simulations after geometry optimisations. Because the building of the model for a given machine design requires several FE sample calculations that take about 3.5 hours on a PC with normal CPU and memory, it would not be suitable to be integrated in a optimisation

process. A simplified model developed for the design optimisation platform will be developed in Section 2.4.4.

It should be noted that the FE calculations which are used to build and validate the proposed method employ the classical Bertortti iron loss model. However, when the FE can utilise improved iron loss models for magnetic domains, as long as the frequency is a separable variable in the models, as shown in (2.14), the proposed modelling method in this section could be applied.

The proposed model should also be calibrated against iron loss experiment results by applying a building factor on the iron loss predictions before being applied in relevant machine performance evaluations and simulations. The building factors usually vary around 1.5~2.0 depending on the machine geometries, materials and building method. They also vary with speed and load current for a given machine theoretically. However the variations are difficult to be obtained from experiment results, in practicaly constant building factors are used regardless of speed and current.

2.4.4 Simplified iron loss model for optimisations

The model proposed in Section 2.4.3 could predict iron accurately, but it needs to calculate dozens of load sample points in FE which take long time up to 3.5 hours in order to build the model for a given machine design. Therefore, it is not suitable for iron loss estimations during machine optimisation in which a number of machine design trial samples are to be assessed. This section proposed a simplified iron loss model specifically for the optimisations that allows the model building process as short as 20 mins. The model also facilitates the optimisation process by providing optimisation constraint information such as torque ripple and demagnetisation in the worst scenarios for a given machine design.

The simplified iron loss model is based on the method (2.13). However, the parameters of the model is established from FE computations of iron loss at the peak operating points, such as the peak torque at base speed T_{pk}, and the peak power at the maximum speed T_m, instead of FE prediction of iron loss at open-circuit and short-circuit. This is because when checking the machine's design constraints for torque ripple and permanent magnets demagnetisation for a given machine trial design in an optimisation, the worst scenarios for the two performance indicators often occur at the two peak power points. Therefore time-step FE calculations on the two points over an electrical cycle could be used to provide not only the characteristic iron losses to build iron loss

model, but also the torque ripple and demagnetisation constraint information. Thus the computation time on a trial machine design in the optimisation is greatly reduced. Further, these two points are more close to the machine operation conditions than the open-circuit and short-circuit. The iron loss at a given operation point with phase voltage V_m and *d*-axis voltage V_d calculated using the iron loss P_{pk} at the peak torque T_{pk} and the base speed, and the iron loss P_m at the peak torque T_m and the maximum speed is given as:

$$P_h = a \times f_m + b \times {f_m}^2 + c \times {f_m}^{1.5} + d \times f_d + e \times {f_d}^2 + g \times {f_d}^{1.5}$$

$$a = \frac{f_d^{pk} P_h^m - f_d^m P_h^{pk}}{f_d^{pk} f_m^m - f_d^m f_m^{pk}} \quad d = \frac{f_m^{pk} P_h^m - f_m^m P_h^{pk}}{f_m^{pk} f_d^m - f_m^m f_d^{pk}}$$

$$b = \frac{(f_d^{pk})^2 P_e^m - (f_d^m)^2 P_e^{pk}}{\left(f_d^{pk}\right)^2 (f_m^m)^2 - (f_d^m)^2 \left(f_m^{pk}\right)^2} \quad e = \frac{\left(f_m^{pk}\right)^2 P_e^m - (f_m^m)^2 P_e^{pk}}{\left(f_m^{pk}\right)^2 (f_d^m)^2 - (f_m^m)^2 \left(f_m^{pk}\right)^2}$$

$$c = \frac{(f_d^{pk})^{1.5} P_x^m - (f_d^m)^{1.5} P_x^{pk}}{\left(f_d^{pk}\right)^{1.5} (f_m^m)^{1.5} - (f_d^m)^{1.5} \left(f_m^{pk}\right)^{1.5}} \quad g = \frac{\left(f_m^{pk}\right)^{1.5} P_x^m - (f_m^m)^{1.5} P_x^{pk}}{\left(f_m^{pk}\right)^{1.5} (f_d^m)^{1.5} - (f_m^m)^{1.5} \left(f_m^{pk}\right)^{1.5}} \tag{2.19}$$

$$f_m^{pk} = \frac{V_m^{pk}}{V_{oc}}, \qquad f_d^{pk} = \frac{V_d^{pk}}{V_{oc}}, \qquad f_m^m = \frac{V_m^m}{V_{oc}}, \qquad f_d^m = \frac{V_d^m}{V_{oc}},$$

$$f_m = \frac{V_m}{V_{oc}}, \qquad f_d = \frac{V_d}{V_{oc}}$$

where $P_h^{pk}, P_e^{pk}, P_x^{pk}$ and P_h^m, P_e^m, P_x^m are the hysteresis, eddy current and excess eddy current losses at the T_{pk} and T_m points, respectively; V_m^{pk}, V_d^{pk} and V_m^m, V_d^m are the phase voltage and *d*-axis voltage at the T_{pk} and T_m points, respectively.

Figure 2.20 and Figure 2.21 show the relative error maps of the proposed method (2.19) compared to FE over the machine torque-speed envelope. The relative errors are computed against FE predicted iron loss of 114 W at the maximum speed 4500 rpm and continuous power in Figure 2.20, and computed against FE predicted iron loss at each torque-speed point in Figure 2.21.

From the two maps, it is seen that the relative errors of the predictions are lower than that of method (2.13) by -10% ~ -15% in the region where the machine continuously operates. This is because the iron loss model of (2.19) is derived from the operation

points closer to the machine real operations than those represented by open or short circuits.

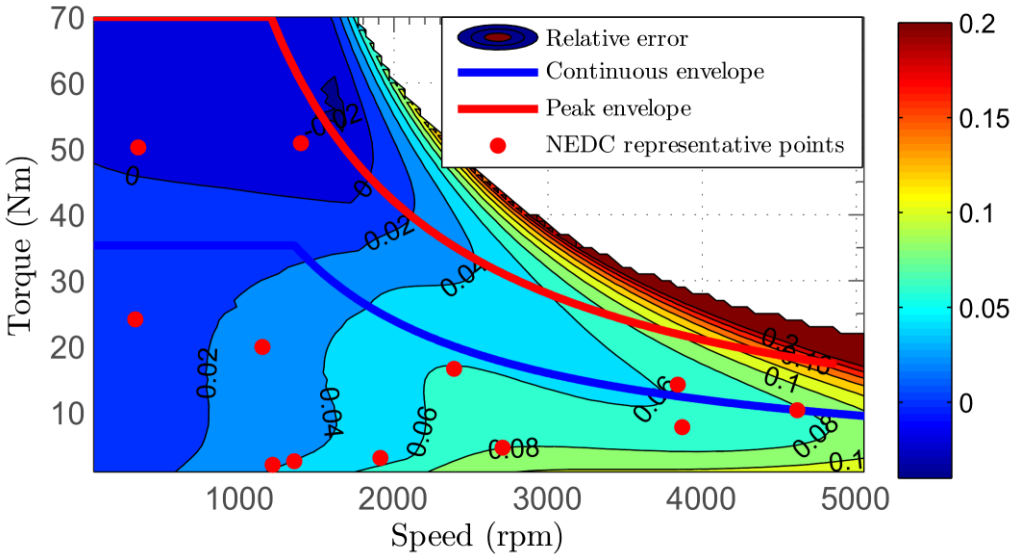

Figure 2.20. Relative error map between method (2.19) and FE prediction normalised against FE predicted iron loss of 114 W at 4500 rpm and continuous power)

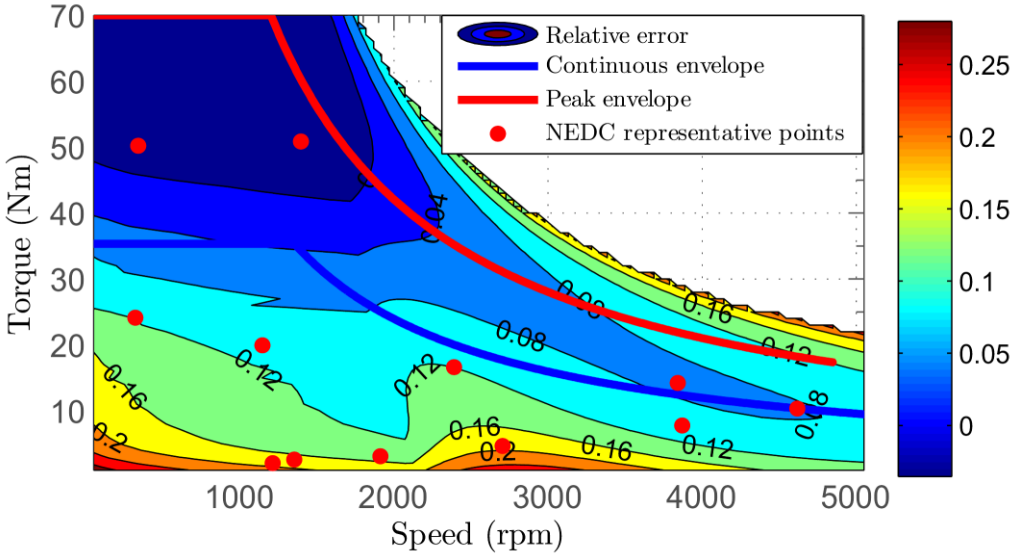

Figure 2.21. Relative error map between method (2.19) and FE prediction over torque-speed range against FE predicted iron loss at each torque-speed load points

2.5 Analytical eddy current loss model for permanent magnets

The eddy current loss in permanent magnets is important for permanent magnet machines because at high speeds, a large eddy current loss may lead to high temperature rise and subsequently great risk of demagnetisation. The calculation of eddy current loss in magnets is complex due to the existence of time and space harmonics and 3-D end effect of magnets. The solution of the eddy current field and loss in 3-D domain within the permanent magnets is discussed and a 3-D analytical eddy current loss model is developed in Chapter 3. By employing generalised image method, the proposed analytical method gives fast and accurate predictions of 3-D eddy current losses at a given machine geometry design, magnet segmentations and electrical load. For a machine design with a given current load, the model takes ~10 seconds to calculate the eddy current loss in magnets using Matlab on a PC with typical CPU and memory while the calculation error is less than 2% compared with time-step 3-D FE. However in an optimisation and the subsequent investigations of the optimised design, there would be a large number of operation points to be evaluated for driving cycles and transient simulations. Hence, computation time for predicting eddy current loss at each operation point needs to be further reduced.

Without considering the eddy current reaction on electromagnetic field, for a given machine design, the eddy current loss in permanent magnets is governed by:

$$P_{\mathrm{edd}} = \left[\mathrm{F}(i_d, i_q) f\right]^2 \tag{2.20}$$

where F is a function representing influence of the flux density field which varies with current load (i_d, i_q). Because the frequency f could be separated from the flux density function of F in a resistance-limited mode, similar modelling process as in iron loss model could be implemented.

By employing the 3-D analytical model to calculate eddy current loss on several current samples, for example, ($4\times i_d$, $5\times i_q$) with a reference frequency f_1, eddy current loss $P_{1\mathrm{edd}}$ as a polynomial function of (i_d, i_q) could be established. Therefore the eddy current loss with arbitrary current load and frequency could be calculated using:

$$P_{edd} = \sum_{i=0}^{4}\sum_{j=0}^{i} a_{i,j} \cdot i_d^j \cdot i_q^{i-j} k_f^2, \quad (j \le 3), \qquad k_f = \frac{f}{f_1} \tag{2.21}$$

2.6 Converter loss model

Because converter loss is a significant part of the total loss of converter-machine drive system, it should be included in the machine design and optimisation process. The total converter loss P_{lc} of a voltage source converter includes three components: P_{cond} – the conduction loss of switching devices and diodes, P_{sw} – the switching loss, and P_{rrevc} – the reverse recovery loss. The converter losses associated with high frequency are considered in the switching loss and the reverse recovery loss. The three loss can be calculated using the equations as follows [91]:

$$
\begin{aligned}
P_{lc} &= P_{cond} + P_{sw} + P_{rrevc} \\
P_{cond} &= \frac{6V_{ton}I_m}{2\pi}\left[1+\frac{\pi}{4}m_d\cos(\varphi)\right] + \frac{6R_{ton}I_m^2}{2\pi}\left[\frac{\pi}{4}+\frac{2}{3}m_d\cos(\varphi)\right] \\
&\quad + \frac{6V_{don}I_m}{2\pi}\left[1-\frac{\pi}{4}m_d\cos(\varphi)\right] + \frac{6R_{don}I_m^2}{2\pi}\left[\frac{\pi}{4}-\frac{2}{3}m_d\cos(\varphi)\right] \\
P_{sw} &= \frac{6V_{dc}t_{rn}f_sI_m^2}{8I_{cn}} + 6V_{dc}t_{fn}f_sI_m\left[\frac{1}{3\pi}+\frac{1}{24}\frac{I_m}{I_{cn}}\right] \\
P_{rrevc} &= 6V_{dc}f_s\left\{\left[0.28+\frac{0.38I_m}{\pi I_{cn}}+0.015\left(\frac{I_m}{I_{cn}}\right)^2\right]Q_{rnn}+\left(\frac{0.8}{\pi}+0.05\frac{I_m}{I_{cn}}\right)I_mt_{rnn}\right\}
\end{aligned}
\tag{2.22}
$$

where

V_{ton} on-state voltage drop of power switch;
R_{ton} on-state resistance of power switch;
V_{don} on-state voltage drop of diode;
R_{don} on-state resistance of diode;
I_m peak line current of machine;
f_s switching frequency;
m_d modulation ratio of converter;
I_{cn} rated device current;
t_{rn} rated rise time;
t_{fn} rated fall time;
Q_{rnn} rated recovery charge;
t_{rnn} rated reverse recovery time

These parameters can be obtained from manufacturer's device datasheet. The peak motor current, I_m, is determined according to operation conditions.

2.7 Demagnetisation constraint evaluation

In machine design and optimisations, the magnet material should operate with the field above the coercivity H_c all over the torque-speed envelope to avoid irreversible demagnetisation. Figure 2.22 shows the *d*-axis current variation with torque along the MTPA and the peak power envelope for the studied IPM machine. Because the highest

demagnetising field is usually generated at peak power point where the negative *d*-axis current is very high, the flux densities at T_{pk} and T_m points are checked.

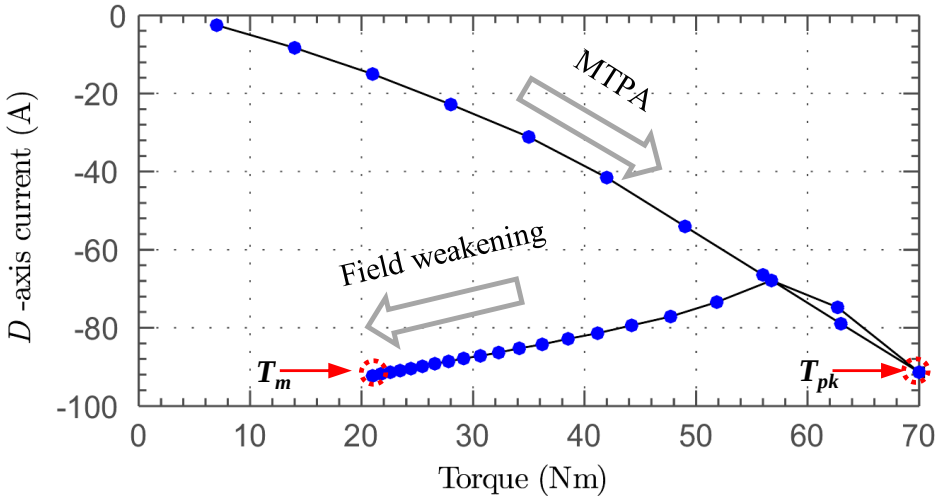

Figure 2.22. *D*-axis current variation with torque along the MTPA and the peak power envelope

On the other hand, demagnetisation level of the permanent magnets is determined by the flux density distribution within the magnets. It is not possible to evaluate such distribution using a lumped-parameter analytical model. Therefore FE is usually necessary. In a comprehensive optimisation process, time-step FEs at T_{pk} and T_m over one electrical cycle will be performed as a part of the iron loss model derivation.

It should be noted that the effective flux density in demagnetisation evaluation is not the amplitude of the flux density but the flux density vector component B_{ori} projected on the magnetisation direction. B_{ori} needs to be above the knee point value in the *BH* curve of the magnet material to avoid irreversible demagnetisation at the machine's highest operating temperature. Figure 2.23 shows the *BH* curves of the magnets employed in the IPM machine under study at different temperatures.

For the studied IPM, since the i_d at the peak torque, T_{pk}, and the base speed is larger than the static short-circuit current, the demagnetization under this condition is at the highest risk. During the time-step FE at the T_{pk} point, the flux densities in the magnetising direction at the corner points of the square magnets of each pole are monitored. These points are most vulnerable to demagnetisation field because they are close to bridges which provides flux paths for the negative *d*-axis current. Figure 2.24 shows 64 curves

of flux density at the corner points over one electrical cycle at T_{pk} point at 150°C. According to the *BH* curves of the magnet material shown in Figure 2.23, the knee point of the magnets is about 0 T at the maximum operation temperature of $150^{o}C$. The minimum flux density of the magnet sample points is 0.32 T, which safely withstands against the worst demagnetization.

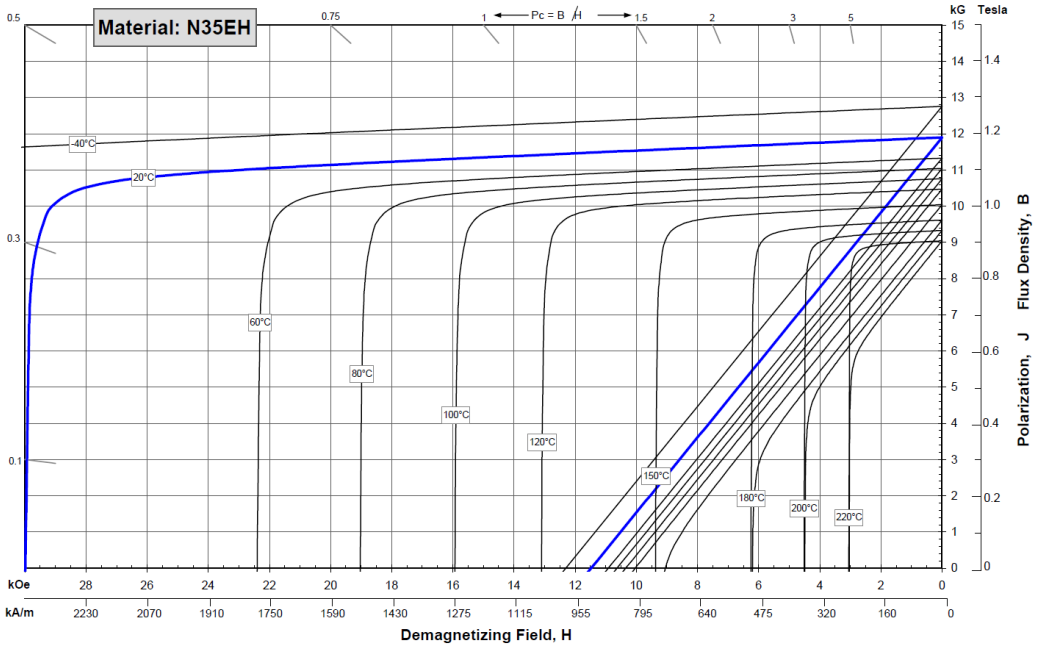

Figure 2.23. BH curves of permanent magnet at different temperatures

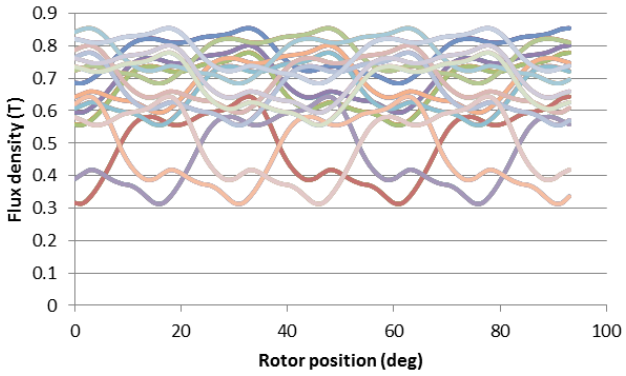

Figure 2.24. Flux density waveform of 64 sample points in magnets at peak torque

2.8 Torque ripple constraint evaluation

In a machine design and optimisation, the highest torque ripple over torque-speed envelope should be maintained under a design constrain value, e.g. 10% defined by the ratio of peak-peak torque variation to the average value. For an IPM machine, the highest torque ripple usually occurs at peak power points such as T_{pk} and T_m. This is because at these points, the main flux is weakened by a large negative i_d, the effect of the harmonic flux in the torque ripple production becomes more pronounced. Due to the

geometry complexity and saturation of IPM machines, time-step FE at T_{pk} and T_m are necessary to acquire accurate torque ripple constraint information.

2.9 Analytical mechanical stress model

Besides the evaluations of machine designs in the electromagnetic domain in the design process, machine performances with respect to mechanical issues need also be assessed, especially the mechanical stress within rotors. When the rotor is rotating, the centrifugal force will cause tangential or radial mechanical stress in the rotor. The mechanical stress in the rotor at the worst scenario, usually at the speed with additional margin to the maximum machine speed, need to be evaluated against material strength so as to ensure the rotor mechanical integrity. Hence a rotor mechanical stress loss model must be integrated in the machine design/optimisation platform, particularly for high-power and high-speed machines.

For surface-mounted permanent magnet (SPM) machines, the maximum stress usually arises within the glass-fibre or carbon-fibre sleeves that bind around the rotor to retain magnets mounted on the rotor surface. Due to the relatively simple geometry of SPM machine rotor topology, the sleeve mechanical stress model could be analytically deduced and has been widely reported [92]-[94]. For IPM machines, because the magnets are installed inside the rotor laminations, leaving narrow strips or "bridges" of lamination around the magnets to support or retain them, the maximum stress is usually generated in the bridges. Because the rotors of IPM machines have complex geometries and diverse topology variants, the evaluations of mechanical stress for IPM machines usually have to rely on FE analyses. Since there will be numerous machine design samples to be evaluated during a IPM machine design and optimisation process, it would be necessary to find an alternate method which could greatly curtail the evaluation computation time but without compromising the accuracy. An FE-based mechanical stress analytical model which is developed for IPM machines to predict the maximum stress in the bridges is illustrated in this section, employing the IPM machine aforementioned in the previous sections as study example.

Figure 2.25 shows the close-up figure of the V-shape rotor within one pole of the studied IPM. Ideally, in order to predict the maximum stress in the bridges at the worst case i.e. 1.5 times of maximum cruise speed, the mathematical model of stress should be a function of all the leading geometric parameters of the rotor, and also the bridge parameters: b_u of the top bridge width and b_m of the bottom bridge width, as shown in

Figure 2.25. To reduce the number of parameters thus the complexity of model, a new parameter m_{eqv} of equivalent mass of rotor pole which is retained by the bridges is used. It is defined by:

$$m_{eqv} = \rho_i A_{fi} + \rho_m A_m \tag{2.23}$$

in which, ρ_i is the rotor lamination density, and ρ_m is the permanent magnet density; A_m is the area of the magnets per pole, and A_i is the area of the lamination per pole held by the bridges. Using b_u , b_m and m_{eqv} as parameters, the maximum stress in the top bridge $S_{u\max}$ and the maximum stress in the bottom bridge $S_{m\max}$ could be analytically modelled applying three-variable polynomial functions as shown in (2.24) and (2.25), with the help of function coefficients C_{u0}, C_{u1}, C_{u2}, C_{m0}, C_{m1}, and C_{m2}.

$$S_{u\max} = m_{eqv}\left[C_{u0} + C_{u1}\frac{1}{b_u} + C_{u2}\left(\frac{1}{b_u}\right)^2\right] \tag{2.24}$$

$$S_{m\max} = m_{eqv}\left[C_{m0} + C_{m1}\frac{1}{b_m} + C_{m2}\left(\frac{1}{b_m}\right)^2\right] \tag{2.25}$$

To quantify the coefficients, stress values with samples of different bridge width variables and equivalent mass variable have to be acquired. Then by curve fitting stress samples into (2.24) and (2.25), the coefficients could be decided. In order to obtain accurate values of the maximum stress, an IPM machine rotor FE model in mechanical domain is employed to reflect complex rotor geometries and material's mechanical non-linearity. The FE model is calculated at 7575 rpm, 1.5 times of maximum speed with different settings of geometry parameters to get the maximum stress in the bridges. Figure 2.26 shows the stress values with variation of bridge width predicted by the proposed analytical model for the studied IPM machine. It is seen that the model predictions have good agreements with FE results when the bridge widths change.

Beside the variation of bridge width, the proposed model is checked against FE results with different equivalent mass m_{eqv} when the leading geometrical parameters change. As an example of validation, two different rotor designs are evaluated by the analytical

model and FE. Their geometrical parameters are listed in Table 2.3. Design 1 is the reference rotor design whose mechanical stress is checked as in Figure 2.26. Design 2 is the new rotor design with m_{eqv} increased by 31% compared with Design 1. Figure 2.27 shows the mechanical stress distribution for the two rotor designs calculated by FE. The stress predictions for Design 2 are compared between the analytical model and FE calculations in Table 2.3. From Design 1 to Design 2, although the leading geometrical parameters of the rotor differ by 15%, the equivalent mass m_{eqv} differs by 31%, and the bridge thicknesses b_u , b_m differ by 50%, the stress predictions applying the analytical model to to Design 2 still agree well with the FE results, with 3% relative error in the top bridge and 5% in the bottom bridge.

Theoretically the coefficients in (2.24) and (2.25) should change when the rotor geometry changes, however the model developed based on the reference rotor geometry design is verified to possess good accuracy when the rotor leading parameters differ in the range of ± 15% and the equivalent mass in the range of ± 40% in the machine design and optimisation process.

It should be noted that although the proposed model is based on the single-layer V-shape IPM machine, the modelling method employing the equivalent mass and polynomial functions in the model is also adaptable to other IPM machine rotor design, for example I-shape rotor, double-layer V-shape rotor or PM-assisted Synchronous Reluctance Machine, with due account of the rotor topology modifications.

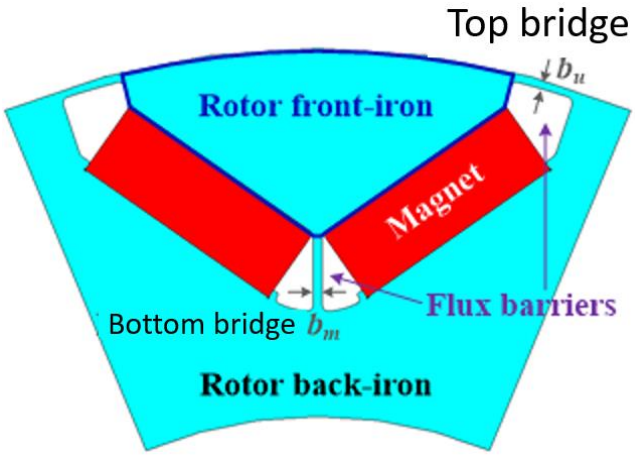

Figure 2.25. Rotor cross-sectional picture of a single-layer V-shape IPM machine.

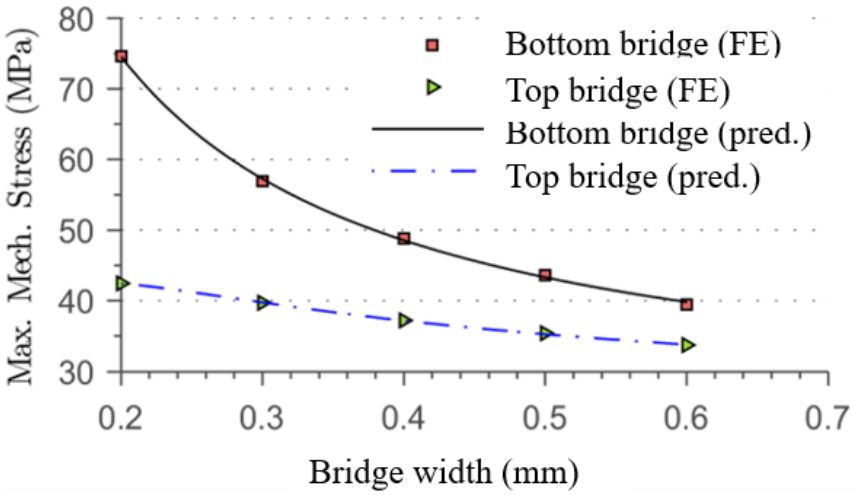

Figure 2.26. Maximum mechanical stress in the rotor predicted by the analytical model in comparison with FE calculation results

Table 2.3 Mechanicals stress prediction for rotor design with geometrical changes

Item	Unit	Design 1	Design 2	Variation ratio
Rad1	mm	36.45	40	9.7%
BetaM	°	147.8	160	8.3%
Magnet depth	mm	8.26	9.6	16.2%
Magnet thickness	mm	3.5	3	-14.3%
m_{eqv}	kg/m	0.596	0.78	30.9%
b_u	mm	0.4	0.6	50.0%
b_m	mm	0.4	0.6	50.0%
Pred./FE /Error (S_{umax})	MPa	-	44.3 / 43.1 / 2.7%	-
Pred./FE /Error (S_{mmax})	MPa	-	52.1 / 55.0/-5.2%	-

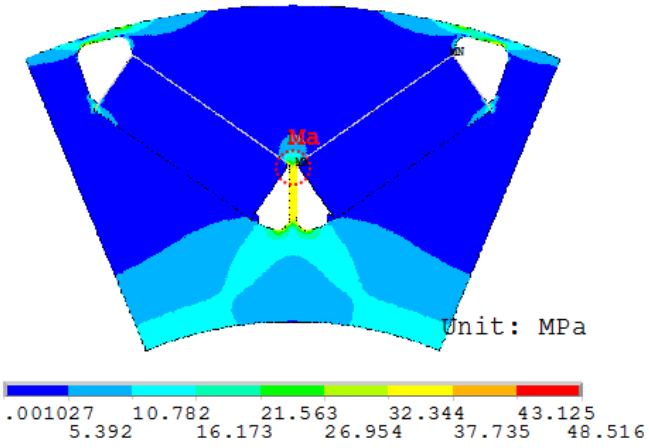

(a)

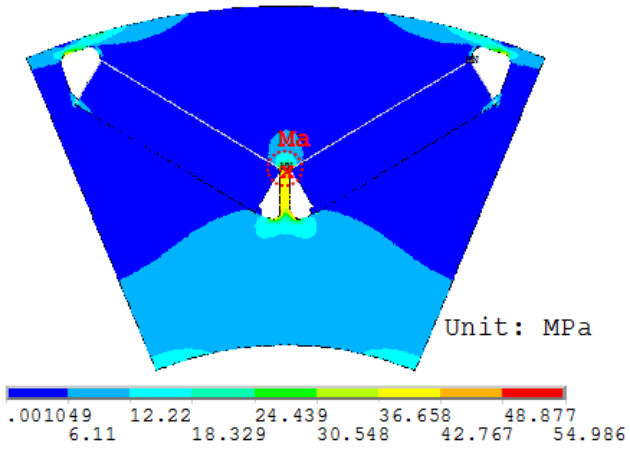

(b)

Figure 2.27. Von Mises mechanical stress distributions in the rotors of (a) Design 1. (b) Design 2, respectively.

It is important to note that the lamination elongation under the centrifugal force at the high speed is also necessary to check. Because even a small amount of lamination elongation would be comparable to the length of air gap, it is possible that the deformed rotor lamination touches the internal circular surface of stator while rotating. Generally speaking, the main body of rotor lamination has marginal level of stress compared to the yield stress of lamination material. Therefore, the total elongation of rotor is determined by the stress level and elongation in the top bridge area, and if the calculated top bridges' stress is far below the yield stress, the bridges' elongation would be within safe region, considering the bridges' original length is small and their elongation is linearly proportional to the stress. Taking Figure 2.27 as an example, the top bridge thickness is 0.4 mm, and the average stress in the top bridges is around 30 MPa. According to the datasheet of the lamination material M270-35A, the lamination's elongation rate is 23% at its yield stress 354 MPa. Proportionally, the absolute elongation of the bridge (i.e. the total elongation of rotor) is estimated as 0.0078 mm, and the elongation in the radial direction is smaller. It can be seen that the elongation is 1.6% of the 0.5mm air gap, thus should be within the safe limit.

When the maximum stress level is close to the yield stress, accurate estimation of elongation is needed. Theoretically, similar to the modelling method of the mechanical stress, the elongation could be modelled as mathematical functions based on FE

calculations on typical geometric parameters. However it is not studied in the thesis.

2.10 Analytical steady-state thermal model

Temperatures of the windings and the magnets in steady state are predicted by a lumped parameter thermal model. Although with some simplifications for use in the optimization process, the model has sufficient accuracy validated by dedicated tools, such as Motor-CAD and experiments.

The extreme points on the continuous operation envelope such as, the rated torque T_r at the base speed, and the rated torque T_{rm} at the maximum speed, as well as the average temperatures over representative operation points (weighted by durations on the points) of driving cycles are to be monitored against the design constraints. Some simplifications are made to the thermal circuit model:

- Axial heat transfer is neglected. The temperature is assumed to distribute evenly in the axial direction.

- The two magnets in the V-shape in one pole are rotated to form a horizontal bar shape which is perpendicular to the radial heat flow direction. Therefore, the shapes of rotor yoke and pole become cylindrical making it easy to calculate thermal resistances.

- The heat transfer path from the end windings to the external frame via the internal air is not considered.

- Because the convection resistance of internal air is very large compared to the thermal resistances within the machine stack, the accuracy of the temperature predictions is not affected significantly by neglecting the resistance.

Figure 2.28 shows the thermal circuit used for the studied IPM machine. Its sources, i.e., the copper loss P_{cu}, iron loss P_{fe} and magnet loss P_{mag}, are calculated using the analytical electromagnetic models described previously. The thermal resistances are calculated based on the machine geometry parameters and material thermal properties of a given design.

While only one layer of heat source and resistance for the windings is shown in Figure 2.28 for the sake of illustration, the windings in a slot are separated into several (5-8) layers for the accurate prediction of average and hot-spot temperature in the windings. Each layer has its own heat source P_{cu}, conduction resistance R_{w-top} connected on its top and R_{w-side} connected to the sides. R_0 represents the equivalent natural or force convection using air cooling or liquid cooling between the external frame and the ambient environment. It is determined using Motor-CAD [95]. In machine design/optimization processes where the machine diameter and stack length are fixed at the design limits, the frame can be pre-designed and the resistance of the frame needs only to be calibrated with the machine speed. In other cases, where the machine's space ratio is varying, R_0 needs to be calibrated according to the ratio as well. The conduction resistance of the assembly gap between the stator stack and the frame is also included in R_0.

The magnets and winding temperatures predicted by the proposed thermal model is 2-5 ^{o}C different from that calculated by Motor-CAD over wide torque/speed operations. The model accuracy is also validated by thermal load tests on a prototype machine which are to be shown in Chapter 5.

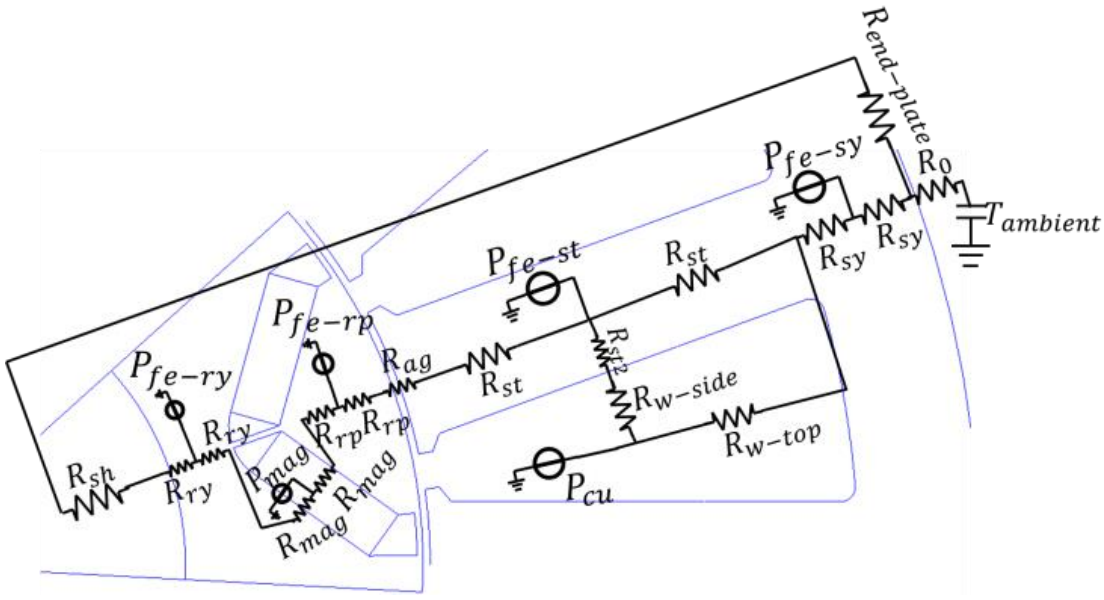

Figure 2.28. Static thermal model of IPM machines used in optimization process

CHAPTER 3 Three-dimensional eddy current loss prediction in permanent magnet machines

This chapter investigates the calculation method of the eddy current loss in the magnets of permanent magnet machines and proposes an analytical method, based on the generalized image theory, for accurate prediction of 3-dimensional (3D) eddy current distributions in the rotor magnets of permanent magnet machines and the resultant eddy current loss. Then the proposed method is validated by 3D time-stepped transient finite element analysis (FEA). It is shown that the proposed method is extremely computationally efficient, accurate and widely adaptable to a variety of permanent magnet machines with due account of complex machine geometry, various winding configurations and magnetic saturation.

3.1 Introduction

The significant negative influence of eddy current loss within magnets on permanent magnet machines are introduced in the Chapter of Introduction. Major disadvantages of the state-of-art methods (FE or analytical) of calculating eddy current loss for SPM machines and IPM machines are also discussed in the Chapter of Introduction. In order to overcome the disadvantages, this chapter proposes an analytical technique for 3D eddy current loss calculation based on the generalized image theory to account boundary conditions of 3D eddy current flow. This method can be easily integrated with accurate analytical models for predicting magnetic field distribution to account slotting effect, or with 2D FEAs to quantify 3D eddy current loss in IPMs with complex geometry and under heavy magnetic saturations.

The rest of this chapter is organized as follows. Section 2 describes the governing equations and boundary conditions for 3D eddy current field. Section 3 develops imaging techniques for accounting the boundary conditions of the eddy current field in rectangular magnets. Section 4 presents analytical solutions for 3D eddy current distribution and expression for quantifying the eddy current loss in magnets. Section 5 illustrates the process of implementing the proposed 3D eddy current evaluation technique. Section 6 validates the proposed technique on a SPM by comparison with 3D FEAs. Section 7 summarizes the findings in conclusions. Appendix I in the end of the thesis provides a rigorous proof of the generalize image theory when applied to 3D current field problem, and lists the developed expressions for eddy current densities and eddy current losses.

3.2 Field description for eddy current in rectangular magnets

From Faraday's induction law and neglecting eddy current reaction, the eddy current density distribution $\boldsymbol{J}$ in magnets at a given time instant is dependent on the rate of change of flux density $\boldsymbol{B}$ with time which can be seen as a source distribution denoted by $\boldsymbol{S}$. Their relation is expressed as (3.1).

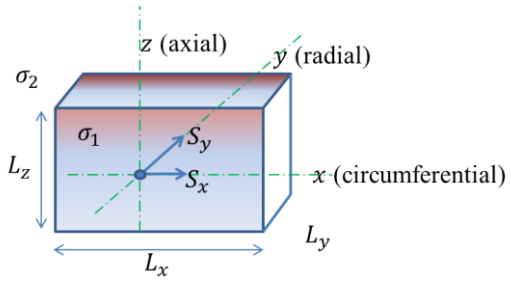

Figure 3.1. A rectangular magnet in a permanent magnet machine with eddy current field excited by 2D magnetic field

$$\boldsymbol{\nabla} \times \boldsymbol{J} = \boldsymbol{\sigma S}$$

$$S_x = -\frac{\partial B_x}{\partial t}, S_y = -\frac{\partial B_y}{\partial t}, S_z = -\frac{\partial B_z}{\partial t} \tag{3.1}$$

where σ is the conductivity of magnets. According to the continuity law of the eddy current density, $\nabla \cdot \boldsymbol{J} = 0$, $\boldsymbol{J}$ may be expressed as the curl of a current vector penitential $\boldsymbol{A}$ in (3.2).

$$\nabla \times \boldsymbol{A} = \boldsymbol{J} \tag{3.2}$$

And using the Coulomb gauge $\nabla \cdot \boldsymbol{A} = 0$, it can be shown that the current vector potential $\boldsymbol{A}$ satisfies:

$$\nabla^2 \boldsymbol{A} = -\sigma \boldsymbol{S} \tag{3.3}$$

For radial field machines, it is reasonable to assume that the machine magnetic field has no axial component with negligible error in the results [96]-[99], and thus is predominantly 2-dimesional (2D), i.e. in radial and circumferential dimensions. Figure 3.1 indicates a magnet in a PM machine in which the eddy current field is induced by 2D time-varying magnetic field. The magnet is approximated in rectangular shape by neglecting any curvature effect. The circumferential direction is denoted as $\boldsymbol{x}$, radial direction as $\boldsymbol{y}$ and axial direction as $\boldsymbol{z}$. The flux density has x and y components which is independent of z. Thus, the source vector $\boldsymbol{S}$ only has two components S_x and S_y. The dimensions of the magnets in the three directions are denoted as L_x, L_y and L_z, respectively.

Since the conductivity outside the magnet is zero, the boundary conditions on the 6 magnet surfaces, namely, two parallel *x*-*z* planes, two *y*-*z* planes and two *x*-*y* planes, are given by:

$$n_v \cdot \boldsymbol{J} = 0 \tag{3.4}$$

where n_v denotes the normal vectors of the magnet surfaces. However, analytical solution which satisfies (3) and (4) has not been established in literature because of the 3D nature and complexity of the problem.

For 2D static magnetic field problems with regular boundaries, image method has been used [101]-[103]. But the applications of the image method in the eddy current field are rarely reported in literatures. Paper [104] uses the conception of image to account for the 2D boundary conditions of a conducting plate in an eddy current damper. The images leads to a reduction of the calculation error of eddy current loss compared with the originally-solved eddy current field which assumes a 2D infinite conductor. However, because the subject which is imaged in the method is the originally-solved eddy current field, it is equivalent to adding extra sources (flux density) inside the solving area that no longer satisfy the Poisson Equations, thus may incur error.

Regarding the applications of the image method in 3D problems of eddy current field, none published literatures has been discovered. Appendix I establishes the generalized image theory and the rules for 3D eddy current field. Based on these rules, the eddy current field in permanent magnets with 6 boundaries is analyzed below.

3.3 Image Method Solution for 3D Eddy Current Field within a Rectangular Magnet

3.3.1 Image sources created for boundary conditions in two x-z planes

The eddy current field sources $\boldsymbol{S}_1(x, y, t)$ within the magnet boundaries ($0 < x \leq L_x, 0 < y \leq L_y, 0 < z \leq L_z$) maybe determined analytically or by 2D FEAs. According to the rule derived in Appendix I, to represent the effect of the right *x*-*z* boundary on the eddy current field, as shown in Figure 3.2, the boundary is removed and an extra image source, denoted as $\boldsymbol{S}_2$, is placed in the symmetrical position with respect to the boundary plane. The three vector components of the image have the same amplitude. The vector component whose direction is perpendicular to the boundary plane will have the same sign as that of the source, while the other two vector components change their signs. However, only two components need to be considered if the magnetic field is two-dimensional. The combined equivalent source $\boldsymbol{G}_{1D}(x, y, t)$of the original and image

sources after the first reflection on the right *x*-*z* plane is expressed in (3.5). $\boldsymbol{K}_y$ is a vector constant used to represent the sign changes of the image vector components. *i* and *j* are the unit vectors in the *x* and *y* direction, respectively.

$$\boldsymbol{G_{1D}(x,y,t)} = \begin{cases} \boldsymbol{S_1(x,y,t)}, & \boldsymbol{0 < y \le L_y} \\ \boldsymbol{K_y S_1(x, 2L_y - y, t)}, & \boldsymbol{L_y < y \le 2L_y} \end{cases}$$
$$0 < x \le L_x, 0 < z \le L_z \qquad (3.5)$$
$$\boldsymbol{K_y} = -i + j$$

It should be noted that $\boldsymbol{K_y S_1}$ denotes component wise product of the two vectors, i.e., $\boldsymbol{K_y S_1} = -S_{1x} i + S_{1y} j$. Further, $\boldsymbol{G}_{1D}(x,y,t)$ will be reflected by the left *x*-*z* plane as shown in Figure 3.2 and have the second image, denoted as $\boldsymbol{S}_3$ and $\boldsymbol{S}_4$. The process of the reflections between the two parallel *x*-*z* planes continues, resulting in an infinite sequence of equivalent sources. Figure 3.2 shows an arbitrary source $\boldsymbol{S}_1$ and its images after three reflections. Table 3.1 lists the positions and signs of the original and image sources up to 5 reflections. It can be found that the original source $\boldsymbol{S}_1$ and its first image source $\boldsymbol{S}_2$ form a pair expressed in (3.5), and all the images repeat the pattern of the pair every $2L_y$ in $\pm$ *y* directions. Therefore the resultant equivalent sources $\boldsymbol{S}_{1D}(x,y,t)$ representing the combined effect of the source and the two *x*-*z* planes are expressed in the one dimensional periodic form given in (3.6).

$$\boldsymbol{S_{1D}(x,y,t)} = \boldsymbol{G_{1D}(x, y - 2nL_y, t)},$$
$$2nL_y < y \le 2(n+1)L_y, \quad n = 0, \pm 1, \pm 2, \ldots \qquad (3.6)$$
$$0 < x \le L_x, 0 < z \le L_z$$

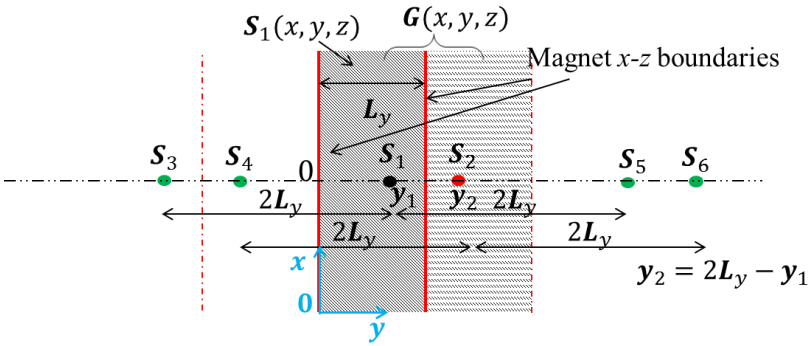

Figure 3.2. Image sources created for boundary conditions on two *x*-*z* planes

Table 3.1 Co-ordinates and Signs of the Original source and images

Source and images	*y-coordinate*	*Source signs*	
		k_x	k_y
…	…	…	…
$\boldsymbol{S}_7$	$y_1 - 4L_y$	+1	+1
$\boldsymbol{S}_8$	$y_2 - 4L_y$	+1	-1
$\boldsymbol{S}_3$(second image on the left)	$y_1 - 2L_y$	+1	+1
$\boldsymbol{S}_4$ (second image on the left)	$y_2 - 2L_y$	+1	-1
$\boldsymbol{S}_1$ (original source)	y_1	+1	+1
$\boldsymbol{S}_2$ (first image on the right)	$y_2 = 2L_y - y_1$	+1	-1
$\boldsymbol{S}_5$	$y_1 + 2L_y$	+1	+1
$\boldsymbol{S}_6$	$y_2 + 2L_y$	+1	-1
$\boldsymbol{S}_9$	$y_1 + 4L_y$	+1	+1
$\boldsymbol{S}_{10}$	$y_2 + 4L_y$	+1	-1
…	…	…	…

3.3.2 Image sources created for boundary conditions on the x-z and y-z planes

When the boundaries on the two y-z planes are also considered, as shown in Figure 3.3, the sequence of images of the original source $\boldsymbol{S}_1$ derived for the two *x*-*z* planes will be further reflected between the two parallel *y*-*z* planes. The consecutive reflections of the sequence form a 2D pattern which has periodicities of $2L_x$ and $2L_y$ in the *x* and *y* directions, respectively. The repeated pattern is a set of the source and images denoted as $\boldsymbol{S}_{1,}\, \boldsymbol{S}_{2,}\, \boldsymbol{S}_{12}$ and $\boldsymbol{S}_{22}$ after the first reflection on the right *x*-*z* plane and the subsequent first reflection on the top *y*-*z* plane. Their analytical expression is given in (3.7).

$$\boldsymbol{G_{2D}}(\boldsymbol{x},\boldsymbol{y},\boldsymbol{t}) = \begin{cases} \boldsymbol{S_1}(\boldsymbol{x},\boldsymbol{y},\boldsymbol{t}), \boldsymbol{0} < \boldsymbol{y} \le \boldsymbol{L_y}, \boldsymbol{0} < \boldsymbol{x} \le \boldsymbol{L_x} \\ \boldsymbol{K_y S_1}(\boldsymbol{x}, \boldsymbol{2L_y} - \boldsymbol{y}, \boldsymbol{t}), \boldsymbol{L_y} < \boldsymbol{y} \le \boldsymbol{2L_y}, \boldsymbol{0} < \boldsymbol{x} \le \boldsymbol{L_x} \\ \boldsymbol{K_x S_1}(\boldsymbol{2L_x} - \boldsymbol{x}, \boldsymbol{y}, \boldsymbol{t}), \boldsymbol{0} < \boldsymbol{y} \le \boldsymbol{L_y}, \boldsymbol{L_x} < \boldsymbol{x} \le \boldsymbol{2L_x} \\ \boldsymbol{K_x K_y S_1}(\boldsymbol{2L_x} - \boldsymbol{x}, \boldsymbol{y}, \boldsymbol{t}), \boldsymbol{L_y} < \boldsymbol{y} \le \boldsymbol{2L_y}, \boldsymbol{L_x} < \boldsymbol{x} \le \boldsymbol{2L_x} \end{cases} \quad (3.7)$$

$$0 < z \le L_z$$

$$\boldsymbol{K}_x = +i - j$$

The resultant equivalent sources $\boldsymbol{S}_{2D}(x, y, t)$ representing the combined effect of the original source and the boundary conditions on the four planes are expressed in the two dimensional periodic form of (3.8).

$$\begin{gathered} \boldsymbol{S_{2D}}(\boldsymbol{x},\boldsymbol{y},\boldsymbol{t}) = \boldsymbol{G_{2D}}(\boldsymbol{x} - \boldsymbol{2mL_x}, \boldsymbol{y} - \boldsymbol{2nL_y}, \boldsymbol{t}), \\ 2mL_x < x \le 2(m+1)L_x, \;\; 2nL_y < y \le 2(n+1)L_y, \\ 0 < z \le L_z, \qquad m, n = 0, \pm 1, \pm 2, \ldots \end{gathered} \quad (3.8)$$

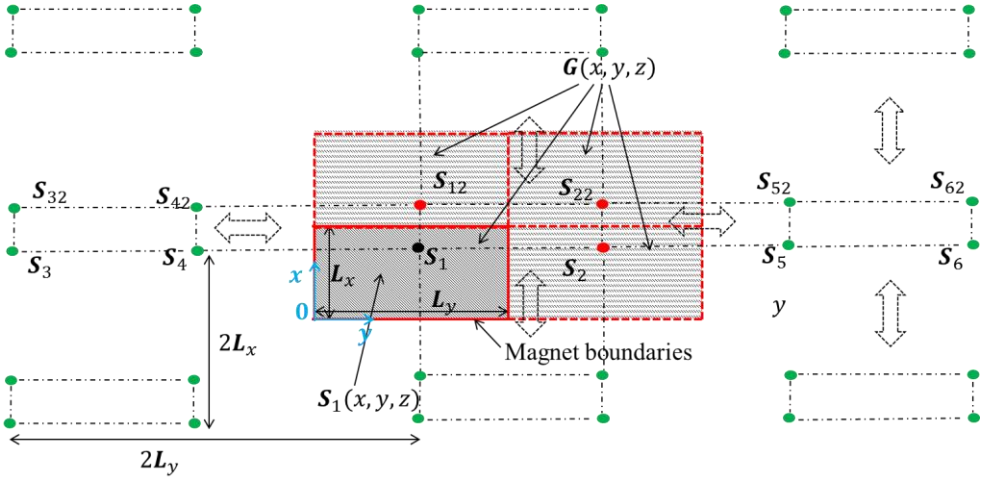

Figure 3.3. Image sources created for boundary conditions on two x-z planes and two y-z planes

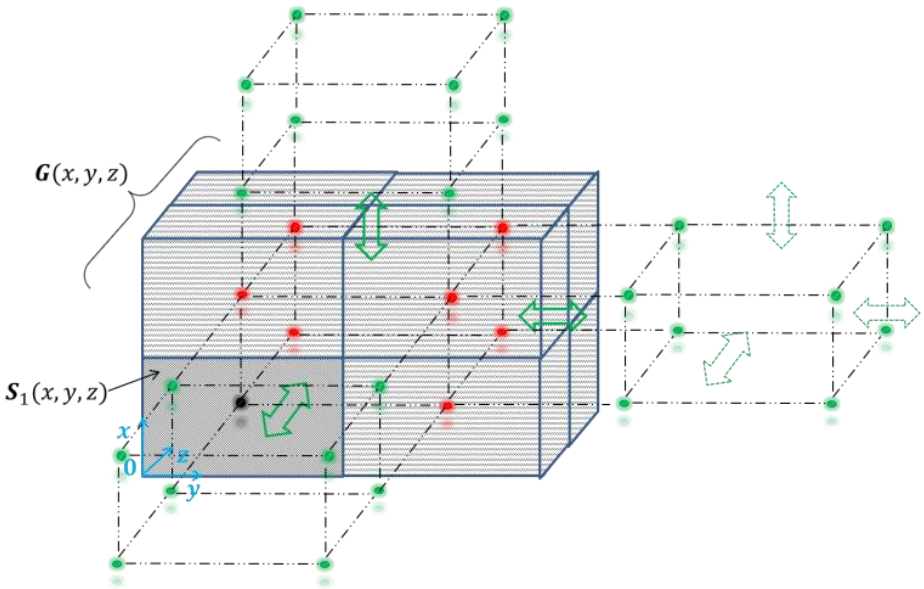

Figure 3.4. Image sources created for boundary conditions on all the six planes

3.3.3 Image sources created for boundary conditions in y-z, x-z and x-y planes

Following the same process, when the two x-y plane boundaries are introduced, the 2D pattern of the source and images will be extended into infinite 3D volume, as seen in Figure 3.4. The image distribution is periodic in all the *x*, *y* and *z* directions. The source and images to be repeated are formed from the first reflection with respect to the right *x*-*z* plane, followed by the first reflection with respect to the top *y*-*z* plane and the subsequent first reflection with respect to the front *x*-*y* plane. The group of the original

source and 7 images, denoted by $\boldsymbol{G_{3D}}(x,y,t)$, is defined in the region: $0 < x \leq 2L_x, 0 < y \leq 2L_y, 0 < z \leq 2L_z$ and given by (3.9):

$$\boldsymbol{G_{3D}}(\boldsymbol{x},\boldsymbol{y},\boldsymbol{t}) = \begin{cases} \boldsymbol{S_1}(\boldsymbol{x},\boldsymbol{y},\boldsymbol{t}), & \in \boldsymbol{r_1} \\ \boldsymbol{K_y S_1}(\boldsymbol{x},\boldsymbol{2L_y}-\boldsymbol{y},\boldsymbol{t}), & \in \boldsymbol{r_2} \\ \boldsymbol{K_x S_1}(\boldsymbol{2L_x}-\boldsymbol{x},\boldsymbol{2L_y}-\boldsymbol{y},\boldsymbol{t}), & \in \boldsymbol{r_3} \\ \boldsymbol{K_x K_y S_1}(\boldsymbol{2L_x}-\boldsymbol{x},\boldsymbol{2L_y}-\boldsymbol{y},\boldsymbol{t}), & \in \boldsymbol{r_4} \\ \boldsymbol{K_z S_1}(\boldsymbol{x},\boldsymbol{2L_y}-\boldsymbol{y},\boldsymbol{t}), & \in \boldsymbol{r_5} \\ \boldsymbol{K_z K_y S_1}(\boldsymbol{x},\boldsymbol{2L_y}-\boldsymbol{y},\boldsymbol{t}), & \in \boldsymbol{r_6} \\ \boldsymbol{K_z K_x S_1}(\boldsymbol{2L_x}-\boldsymbol{x},\boldsymbol{y},\boldsymbol{t}), & \in \boldsymbol{r_7} \\ \boldsymbol{K_z K_y K_x S_1}(\boldsymbol{2L_x}-\boldsymbol{x},\boldsymbol{2L_y}-\boldsymbol{y},\boldsymbol{t}), & \in \boldsymbol{r_8} \end{cases} \tag{3.9}$$

$$\boldsymbol{K_z} = -i - j$$

where,

$$\begin{aligned} r_1&: \ 0 < x \leq L_x, 0 < y \leq L_y, 0 < z \leq L_z \\ r_2&: \ 0 < x \leq L_x, L_y < y \leq 2L_y, 0 < z \leq L_z \\ r_3&: \ L_x < x \leq 2L_x, 0 < y \leq L_y, 0 < z \leq L_z \\ r_4&: \ L_x < x \leq 2L_x, L_y < y \leq 2L_y, 0 < z \leq L_z \\ r_5&: \ 0 < x \leq L_x, 0 < y \leq L_y, L_z < z \leq 2L_z \\ r_6&: \ 0 < x \leq L_x, L_y < y \leq 2L_y, L_z < z \leq 2L_z \\ r_7&: \ L_x < x \leq 2L_x, 0 < y \leq L_y, L_z < z \leq 2L_z \\ r_8&: \ L_x < x \leq 2L_x, L_y < y \leq 2L_y, L_z < z \leq 2L_z \end{aligned} \tag{3.10}$$

The final resultant equivalent source $\boldsymbol{S}_{3D}(x,y,\mathrm{z},t)$ representing the combined effect of the original source and the boundary conditions on all the six planes are expressed in the three dimensional periodic form of (3.11):

$$\begin{aligned} \boldsymbol{S_{3D}}(\boldsymbol{x},\boldsymbol{y},\boldsymbol{z},\boldsymbol{t}) &= \boldsymbol{G_{3D}}(\boldsymbol{x}-\boldsymbol{2mL_x},\boldsymbol{y}-\boldsymbol{2nL_y},\boldsymbol{z}-\boldsymbol{2kL_z},\boldsymbol{t}), \\ 2mL_x < x &\leq 2(m+1)L_x, \\ 2nL_y < y &\leq 2(n+1)L_y, \\ 2kL_z < z &\leq 2(k+1)L_z, \\ m,n,k &= 0,\pm 1,\pm 2,\ldots \end{aligned} \tag{3.11}$$

It follows that by employing the generalized image technique, the combined effect of the source $\boldsymbol{S}_1(x,y,t)$ and the boundary conditions can be represented by $\boldsymbol{S}_{3D}(x,y,z,t)$ which is periodical in *x*, *y*, *z* directions. It may be further expressed as a 3D Fourier series given in (3.12)-(3.14).

$$a(m,n,k) = \frac{8}{L_x L_y L_z} \iiint_{(0,0,0)}^{(2L_x,2L_y,2L_x)} G_{3Dx}(x,y,t) e^{-j2\pi(mx+ny+kz)} dxdydz$$

$$b(m,n,k) = \frac{8}{L_x L_y L_z} \iiint_{(0,0,0)}^{(2L_x,2L_y,2L_x)} G_{3Dy}(x,y,t) e^{-j2\pi(mx+ny+kz)} dxdydz \quad (3.12)$$

where $m, n, k = 0, 1, 2, \ldots$

$$S_{3Dx} = \sum_{m=1}^{\infty}\sum_{n=1}^{\infty}\sum_{k=1}^{\infty} a_{(m,n,k)} cos\left(m\frac{\pi}{L_x}x\right) sin\left(n\frac{\pi}{L_y}y\right) sin(k\frac{\pi}{L_z}z) \quad (3.13)$$

$$S_{3Dy} = \sum_{m=1}^{\infty}\sum_{n=1}^{\infty}\sum_{k=1}^{\infty} b_{(m,n,k)} sin\left(m\frac{\pi}{L_x}x\right) cos\left(n\frac{\pi}{L_y}y\right) sin(k\frac{\pi}{L_z}z) \quad (3.14)$$

$a_{(m,n,k)}$ and $b_{(m,n,k)}$ are the coefficients of the $(m, n, k)^{th}$ harmonic for the x and y components of the equivalent sources respectively. They are easily calculated using fast Fourier transform (FFT) once the original source is known.

3.4 Eddy Current Distribution and Total Eddy Current Loss

For each harmonic $S_{x(m,n,k)}$ and $S_{y(m,n,k)}$, the source is distributed sinusoidally within an infinite isotropic 3-dimensional space. Hence, the solution to (3.3) may be found by the method of variable separation for each harmonic of the order (m, n, k). The resultant current vector potential is obtained in (3.15) and (3.16)

$$A_x = \sum_{m=1}^{\infty}\sum_{n=1}^{\infty}\sum_{k=1}^{\infty} c_{(m,n,k)} cos\left(m\frac{\pi}{L_x}x\right) sin\left(n\frac{\pi}{L_y}y\right) sin(k\frac{\pi}{L_z}z) \quad (3.15)$$

$$A_y = \sum_{m=1}^{\infty}\sum_{n=1}^{\infty}\sum_{k=1}^{\infty} d_{(m,n,k)} sin\left(m\frac{\pi}{L_x}x\right) cos\left(n\frac{\pi}{L_y}y\right) sin(k\frac{\pi}{L_z}z) \quad (3.16)$$

The eddy current density is derived from (2) as:

$$J_x = \sum_{m=1}^{\infty}\sum_{n=1}^{\infty}\sum_{k=1}^{\infty} e_{(m,n,k)} sin\left(m\frac{\pi}{L_x}x\right) cos\left(n\frac{\pi}{L_y}y\right) cos(k\frac{\pi}{L_z}z) \quad (3.17)$$

$$J_y = \sum_{m=1}^{\infty}\sum_{n=1}^{\infty}\sum_{k=1}^{\infty} h_{(m,n,k)} cos\left(m\frac{\pi}{L_x}x\right) sin\left(n\frac{\pi}{L_y}y\right) cos(k\frac{\pi}{L_z}z) \quad (3.18)$$

$$J_z = \sum_{m=1}^{\infty}\sum_{n=1}^{\infty}\sum_{k=1}^{\infty} q_{(m,n,k)} cos\left(m\frac{\pi}{L_x}x\right) cos\left(n\frac{\pi}{L_y}y\right) sin(k\frac{\pi}{L_z}z) \quad (3.19)$$

Since each harmonic is orthogonal, the total eddy current loss at a given time instant is the sum of the losses associated with each harmonic component:

$$P_{eddy} = \sum_{m=1}^{\infty}\sum_{n=1}^{\infty}\sum_{k=1}^{\infty} P_{(m,n,k)}$$

$$= \sum_{m=1}^{\infty}\sum_{n=1}^{\infty}\sum_{k=1}^{\infty} \frac{1}{8}\int_0^{2L_x}\int_0^{2L_y}\int_0^{2L_z} \frac{1}{\sigma}\cdot\left[J_{x(m,n,k)}{}^2 + J_{y(m,n,k)}{}^2 + J_{z(m,n,k)}{}^2\right]dxdydz \quad (3.20)$$

$$= \sum_{m=1}^{\infty}\sum_{n=1}^{\infty}\sum_{k=1}^{\infty}\left\{p_{1(m,n,k)} + p_{2(m,n,k)} + p_{3(m,n,k)} + p_{4(m,n,k)} + p_{5(m,n,k)}\right\}$$

The coefficients, $c_{(m,n,k)}$, $d_{(m,n,k)}$, $e_{(m,n,k)}$, $h_{(m,n,k)}$, $q_{(m,n,k)}$ for the current vector potential and eddy current densities, and $p_{1(m,n,k)}$ - $p_{5(m,n,k)}$ for the total eddy current loss are all arithmetic functions of the harmonic order and magnet dimensions. They are summarized in Appendix II.

3.5 Method of implementation

3.5.1 Computation process

The process of computing 3D eddy current loss in rotor magnets employing the analytical technique described in sections 3 and 4 is illustrated in the flowchart of Figure 3.5. The 2D magnetic field as the source function may be calculated analytically using the more accurate subdomain model [100] with due account of slotting effect. Alternatively, the magnetic field distribution may be obtained from 2D FE in which case complex geometry and heavy magnetic saturation often seen in IPMs can also be easily dealt with. If the 2D FEA includes eddy current effect, the reaction field of the eddy current is, to some extent, approximated in the 3D evaluation [46]. In addition, if the magnetic field solver can take eddy current distribution as its input, the resultant eddy current density from the image method may be fed back to the magnetic solver. The iterations repeat until convergence is achieved. However, this is not studied in the chapter.

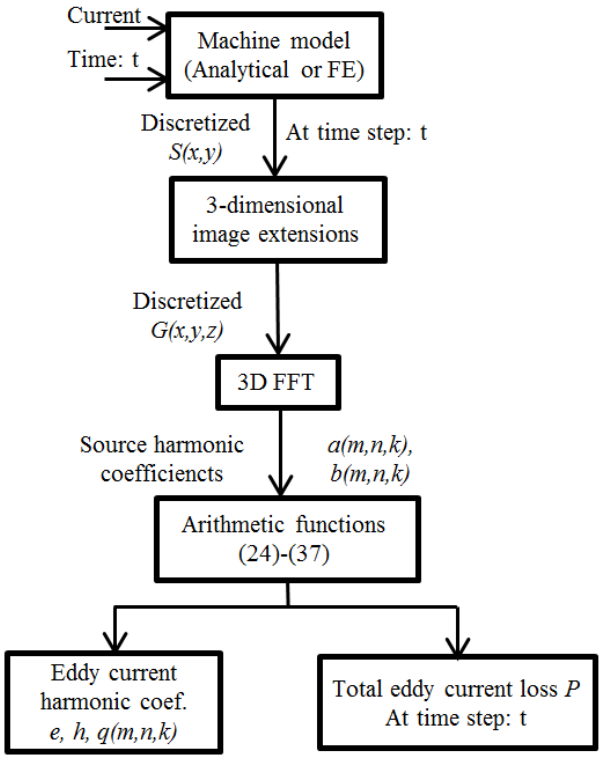

Figure 3.5. Flowchart of 3D eddy current calculation using generalized image method

Due to the periodicity, the infinite combined sources of the original and imaged sources are represented by 3D sinusoidal harmonic functions defined all over the space. In order to perform FFT of the combined sources, the magnetic field distribution obtained from analytical or FE prediction need to be discretized in the *x*, *y*, *z* dimensions. Therefore the accuracy of the sources and their resultant eddy current field depends on the harmonic numbers ($m \times n \times k$) that are considered in the calculations, namely depends on the number of samples of the magnetic field in the *x*-*y*-*z* dimensions which are used in FFT. To account for the space harmonics caused by winding configuration, slotting, magnetic saturation and step change of the image sources across the boundaries, the number of discretization samples should be sufficiently large. In order to facilitate the speed of FFT, the sample numbers are chosen as the integer power of 2. It is shown by checking the eddy current loss when using different sample numbers, that the loss already converges with 32 × 32 × 32 samples. When calculating the eddy current loss at the rated current, max speed with 6 axial segments and none circumferential segments for the studied machine, the relative differences of the results with 32 × 32 × 32 samples and 64 × 64 × 64 samples, compared with the results with 128 × 128 × 128 samples, are 0.212% and 0.0429%, respectively.

The eddy current distribution is calculated at each time step. Because time varying eddy current densities usually repeat 6 or 12 times in a fundamental electric period, it is necessary to calculate the eddy current loss at least for one sixth or one twelfth of the electrical period to obtain the average value.

Since the calculations are performed in 3-dimensional space for each harmonic, matrix operations are used to facilitate efficient calculations of (3.9) - (3.20). When the magnetic field within the magnets are sampled with 64 × 64 × 64 points in the *x-y-z* directions, which means the harmonic orders *(m, n, k)* are also accounted up to 64 × 64 × 64, the whole calculation time, including implementations of the analytical machine magnetic field and the eddy current loss calculations, is ~10 seconds using Matlab. As a comparison, in order to perform 3D time-step FEs, apart from the geometry and physical model construction and meshing process, the time consumption on the solving and post-processing processes, on a 3.10 GHz, 32.0 GB PC, could be up to from 82 hours for the case of non-axial-segmentation to 7.5 hours for the case of 18 axial segmentations.

3.5.2 Magnetic 3-D end effect and magnet curvature effect

Because of the influence of the end windings and the fringe effect, the flux density field due to the armature winding and magnets decreases as it approaches to the axial ends of the machine lamination stack. Plenty of works have been done to examine the phenomenon analytically [96][97] and 3D FE [98][99]. It is shown in these works that the affected length of the air gap in the axial direction (e.g. ‘’affected’’ here defined as that the flux density drops below 99% of the value that exists in the middle of the axial length) is approximately equal to the radial thickness of the equivalent air gap (considering the height of magnets also as part of air gap). And at the end of the axial length, the flux density is 80% - 70% (depending on the equivalent air gap thickness) of the value in the middle. On account of this, as for the SPM machine studied in the chapter, the length of magnets affected by the magnetic 3D end effect makes ~5% of the total stack length, and its effect on the eddy current loss should be negligible. However for the other SPM machine designs with short stack lengths compared to the air gap thicknesses, the end effect on the magnetic field and the eddy current loss should not the neglected. Thus the proposed method based on the 2D magnetic field sources may give large errors. The above discussion is for SPM machines. For IPM machines, because the magnet is shielded in the lamination, the end effect of the armature reaction on the field

within magnets would be much smaller, and the end effect on the eddy current loss calculations could be negligible.

As for the circular-shaped magnets, a conventional process approximating the arc shapes to rectangular shapes should be applied. It should be noted that the curvature effect becomes prominent when the magnets have large opening angles and large radial thickness, the calculation error using the proposed method would increase accordingly.

3.6 Validations by 3D FEAs

The proposed method for analytical predicting 3D eddy current loss in PM machines has been validated by 3D FEAs. As aforementioned, the proposed method overcomes the disadvantages of the state-of-art methods both in the case of SPM machine applications and also in the case of IPM machine applications. In this section, an 18-slot 8-pole SPM machine is employed as an example to illustrate the calculation process with details. In the next section, a study case of an 18-slot 8-pole IPM will be briefly presented.

3.6.1 Machine topology and design parameters

The proposed method is applied to a 5kW 18-slot 8-pole SPM machine as shown in Figure 3.6, for evaluation of the eddy current loss in the rotor permanent magnets. The magnets are binded on the rotor surface using fibre. The machine employs winding design features [105] to reduce space harmonics and hence rotor eddy current loss, while retaining the merits of fractional slot per pole machine topology. The key geometrical and physical parameters and specifications are listed in Table 3.2.

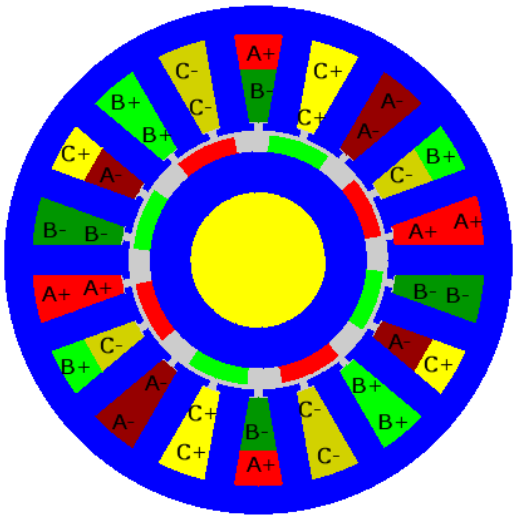

Figure 3.6. Cross-sectional schematic of 18-slot 8-pole SPM machine

•

Table 3.2 Machine Parameters

Items	*Value*
Rotor radius	32.5 mm
Magnet outer radius	37.5 mm
Stator inner radius	38.45 mm
Stack length	118 mm
Magnet resistivity	$1.8 \times 10^{-6}\ \Omega \cdot m$
Rated Ampere turns per coil	513.5
Max. speed	4500 r/mim
Rated current	80 A
Rated torque	35 Nm

3.6.2 2D FE for field source validations

2D magnetic field distributions of the machine are obtained analytically as described in [38] and the resultant time derivations of flux density distributions form the source for the eddy current calculation. For simplicity, magnetic saturation and effect of slotting are neglected. This will not lead to large error when the machine runs at the Maximum Torque per Ampere (MTPA) mode [37].

Figure 3.7 to Figure 3.10 compare the analytically and 2D FE predicted variations of the magnetic flux density components with the spatial circumferential positions and their time derivatives at a given time instant of $\omega t = 15^{o}$ (elec.) when the machine operates at the maximum speed of 4500 r/min and rated current, where ω is the fundamental electric angular frequency of the operation. It can be seen that the analytical predictions agrees very well with those obtained from the 2D FEAs. This ensures the accuracy of the source of excitation of the eddy current distribution to be analytically predicted by the proposed method.

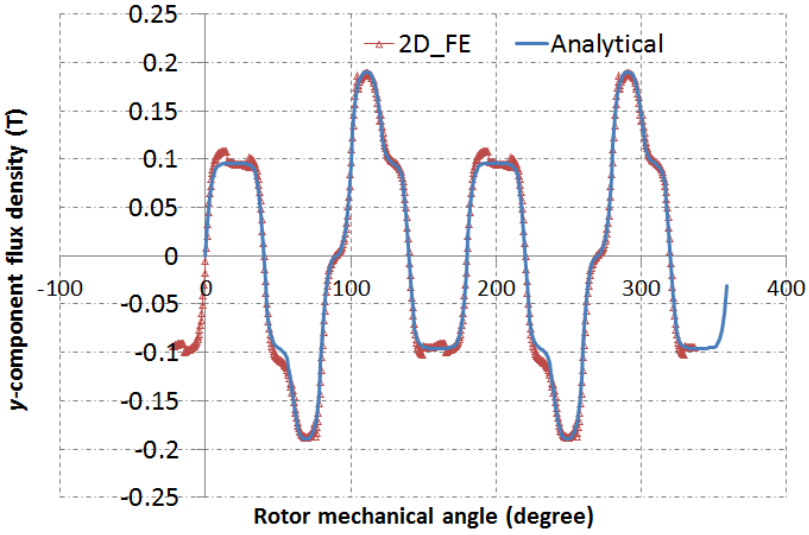

Figure 3.7. variation of the *y*-component flux density with spatial circumferential positions along the mean radius of magnets at $\omega t = 15^{o}$ (elec.)

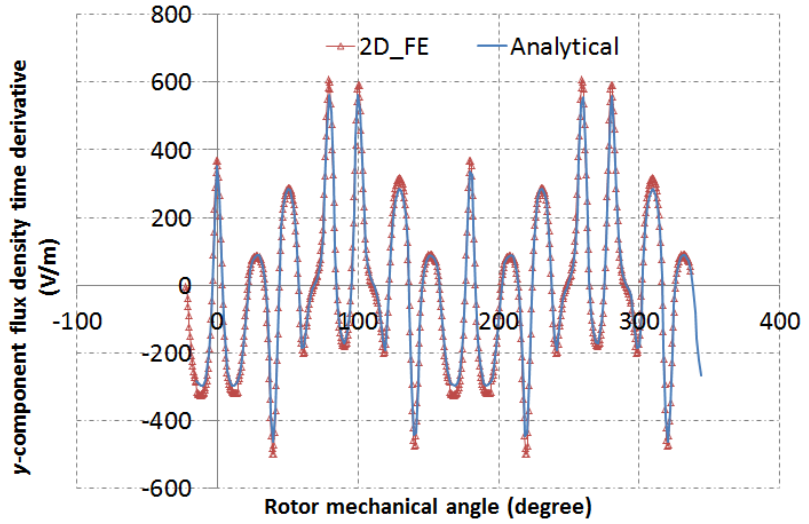

Figure 3.8. variation of *y*-component flux density time-derivative with spatial circumferential positions along the mean radius of magnets at $\omega t = 15^{o}$ (elec.)

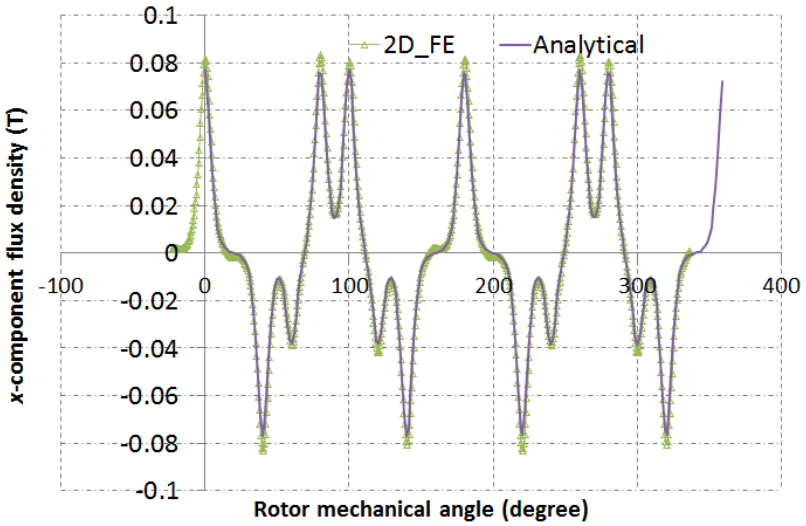

Figure 3.9. variation of *x*-component flux density with spatial circumferential positions along the mean radius of magnets at ωt = 15^{o} (elec.)

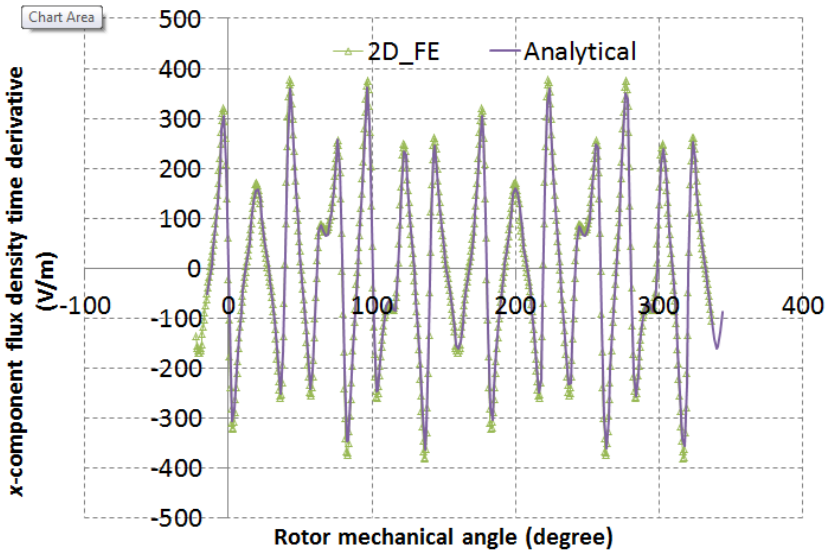

Figure 3.10. variation of *x*-component flux density time-derivative with spatial circumferential positions along the mean radius of magnets at ωt = 15^{o} (elec.)

3.6.3 Comparisons of eddy current distribution and eddy current loss with 3D FEAs

A 3D FE model of the machine, as shown in Figure 3.11, has been built to predict the 3D eddy current distribution and resultant eddy current loss induced in the magnets.

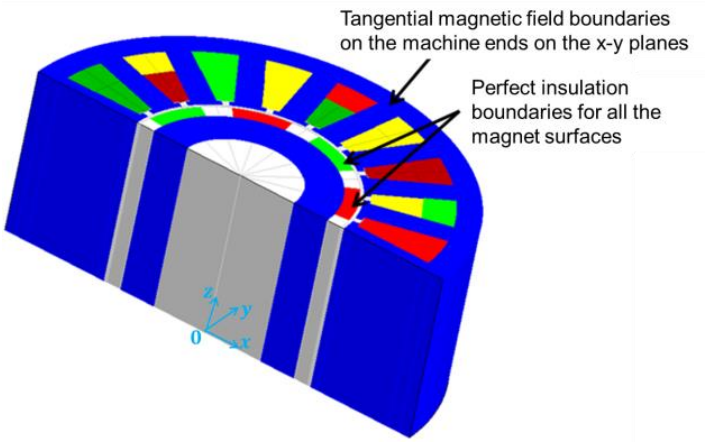

Figure 3.11. 3D FE machine model

Since the machine employs fractional slot per pole topology, circumferential symmetry exits only over 180 mechanical degrees. Thus, a quarter of the machine has to be modelled in 3D FEAs. Tangential magnetic field boundary condition is imposed on the two end surfaces perpendicular to the axial direction. Consequently, the magnetic field will be confined in the 2D *x-y* plane. This implies that the end (3D) effect of magnetic field distribution is neglected. In addition, perfect insulation boundaries are applied to the end surfaces of the magnets. The time-step 3D FEs consider the BH curves of the real iron laminations. The field in the conducting parts of magnets is governed by:

$$\nabla \times (\nabla \times A_m/\mu) = -\sigma(\partial A_m/\partial t + \nabla\phi) \tag{3.21}$$

$$J_e = \sigma(\partial A_m/\partial t + \nabla\phi) \tag{3.22}$$

in which A_m, μ and ϕ are the magnetic vector potential, permeability and electric scalar potential respectively. The model is meshed to make sure the calculated eddy current loss achieved convergence. The total number of the nodes for the model without axial segmentation is approximately 2×10^6.

Figure 3.12 compares analytically and 3D FE predicted z-component eddy current density distributions at $\omega t = 15^o$ (elec.) on the surface (defined by $y = 0.5L_y$, $0 < x < L_x$, $0.5L_z < z < L_z$) of the second magnet piece on the right in Figure 3.11 when the machine operates at the maximum speed and rated current. Each magnet per pole is segmented into 2 pieces circumferentially and 14 pieces axially.

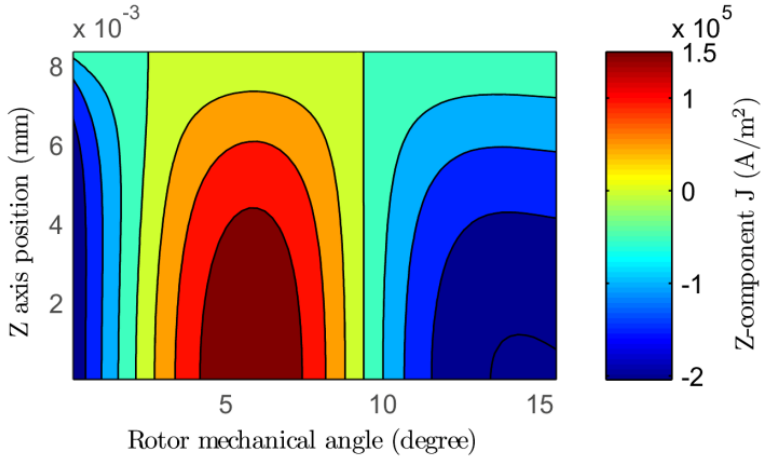

(a)

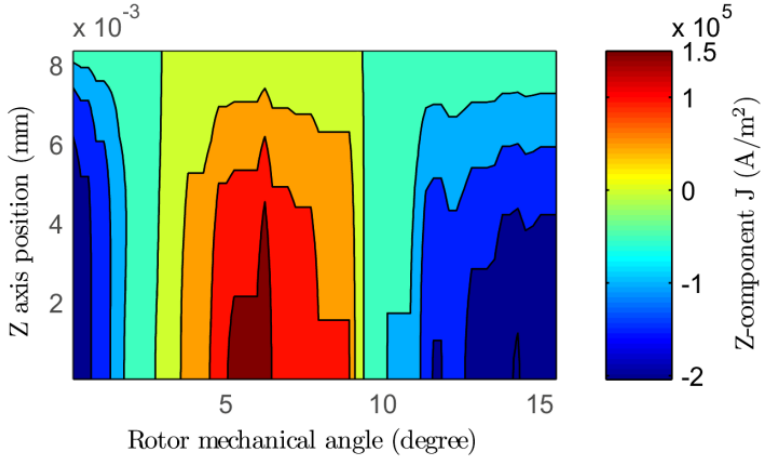

(b)

Figure 3.12. *Z*-component eddy current density contours on the surface defined by (y = 0.5L_y, 0 < x < L_x and 0.5L_z < z < L_z) at ωt = 15^o (elec.): (a): Analytical; (b): 3D FE

Figure 3.13 compares analytically and 3D FE predicted variations of z-component eddy current density with circumferential position (x) at ωt = 15^o (elec.) y = 0.5L_y and z = 0.75L_z. Good agreement between the two can be observed albeit the effect of mesh discretization is clearly visible in the 3D FE predictions.

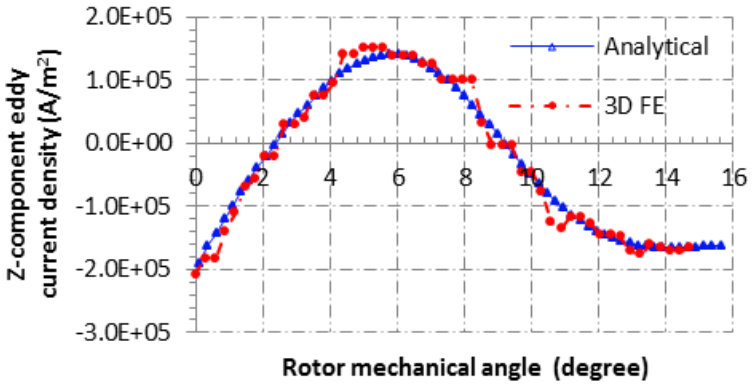

Figure 3.13. Variations of analytically and 3D FE predicted *z*-component eddy current density with circumferential position *x* at ωt = 15^{o} (elec.), $y = 0.5L_y$ and $z = 0.75L_z$.

Figure 3.14 compares analytically and 3D FE predicted total eddy current loss variations with time when the machine operates at the maximum speed and rated current with each magnet per pole segmented by 2 circumferentially. Figure 3.15 compares analytically and 3D FE predicted eddy current loss variations with number of axial and circumferential segments per pole. It can be seen that in all cases, good agreements are obtained between the 3D FE and analytical results. Owing to neglect of the magnet curvature effect, the analytical results deviate slightly from the FE predictions when the magnets in each pole are not circumferentially segmented (SC=1).

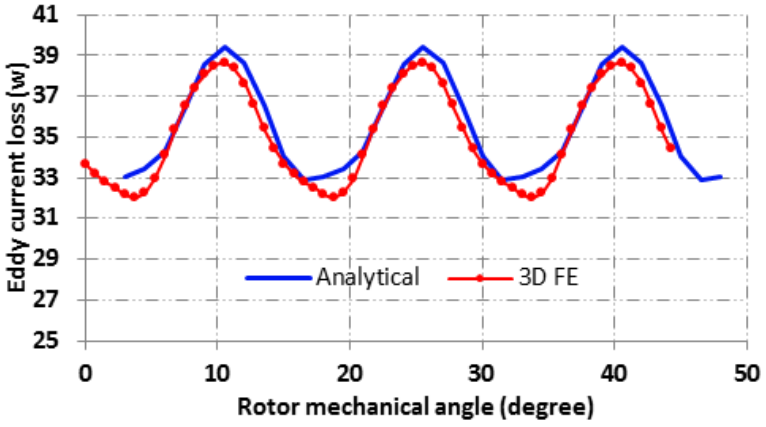

Figure 3.14. Comparison of 3D FE and analytically predicted total eddy current loss variations with time when machine operates at the maximum speed and rated current with each magnet per pole segmented by 2 circumferentially

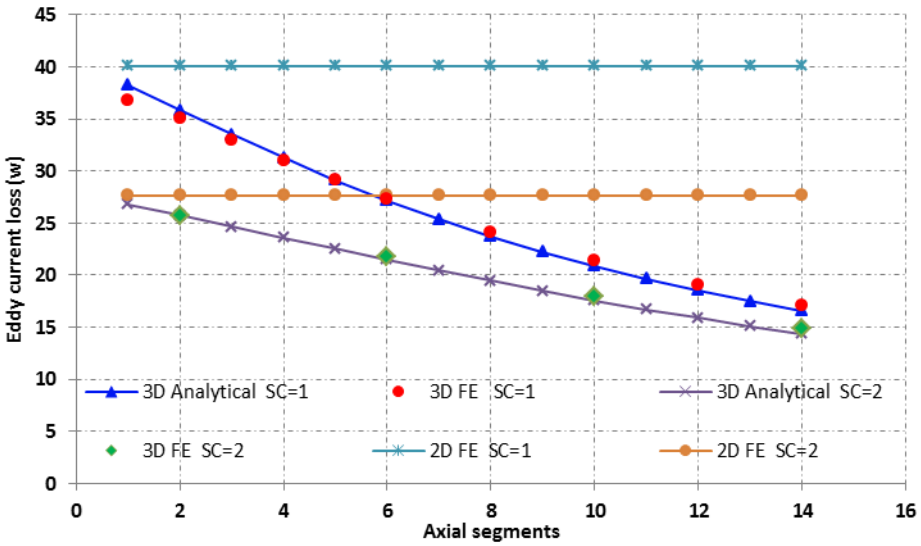

Figure 3.15. Analytically and 3D FE predicted eddy current loss variations with the number of axial and circumferential segments. The number of circumferential segments is denoted by SC

Figure 3.15 also shows the eddy current loss results calculated using the 2D FE method aforementioned in the introduction which neglects the circumferential and radial components of eddy current. The 2D results are 40.06 w and 27.63 w in the case of 1 circumferential segment (SC=1) and the case of 2 circumferential segments (SC=2) respectively. While the magnet has only one axial segment, the 2D results are not far from 3D FE which are 36.76 w (SC=1) and ~26.80 w (SC=2). But with more axial segments are employed, the 2D FE calculation error becomes increasingly larger. In particular, with 10 axial segments where the axial length of each magnet segment is close to its circumferential length, the 2D FE error is 87.8% higher for SC equal to 1 and 53.8% higher for SC equal to 2, compared with 3D FE results.

3.7 The image method applied for IPM machines

The image method is also applied to the eddy current loss calculation for an 18-slot 8-pole IPM, and verified by 3D FE calculations. The work on the IPM application has been published in a journal paper (J6, publication list). The IPM machine is designed with the same power size, rated current and the outer dimensions as the SPM studied in this chapter. Figure 3.16 (a) shows the machine geometry; Figure 3.16 (b) shows the mesh grids constructed on one of magnets for the eddy current field calculations (not for electromagnetic FE calculations). Following the procedures illustrated in Figure 3.5, the

eddy current field sources Sx and Sy are obtained from electromagnetic FE calculations, and then image method is applied to calculate the eddy current field within the magnets.

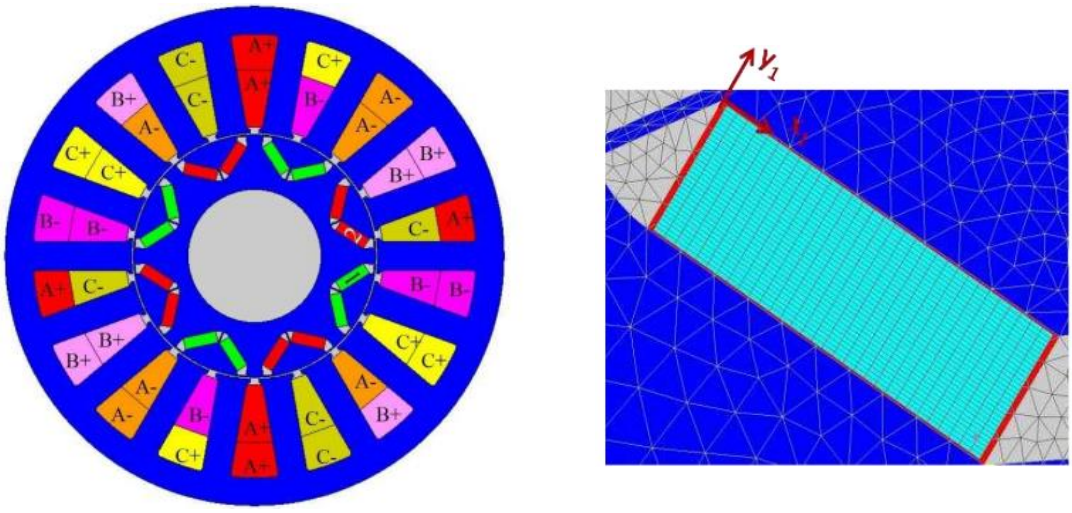

(a) (b)

Figure 3.16. (a) Geometry of the 18-slot 8-pole IPM machine, (b) Mesh grids constructed on one of magnets in arrangement for eddy current field calculations

The eddy current loss is evaluated and compared with 3D FE and 2D FE results when the machine runs at 4500 rpm with rated current 61.17 Arms. Figure 3.17 shows the comparison with variation of the number of axial segments when the circumferential segments are 1 and 2 respectively. It can be seen that a very good agreement is achieved between the results of image method and 3D FE. And 2D FE results differ quite significantly when the number of axial segments is increased. Moreover, similarly to the comparison shown from Figure 3.12 to Figure 3.14 for the SPM machine, the eddy current field distribution in 3 dimensions and the instantaneous eddy current loss of the IPM machine are also checked against the 3D FE results, and good agreements have been observed.

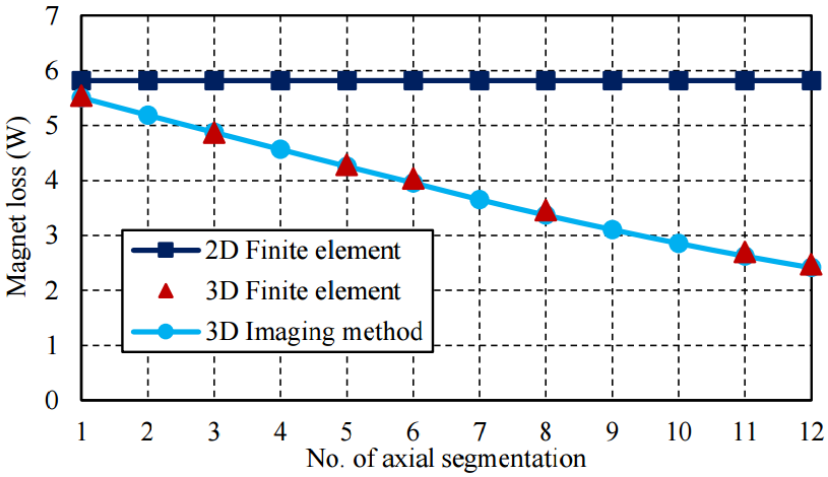

(a)

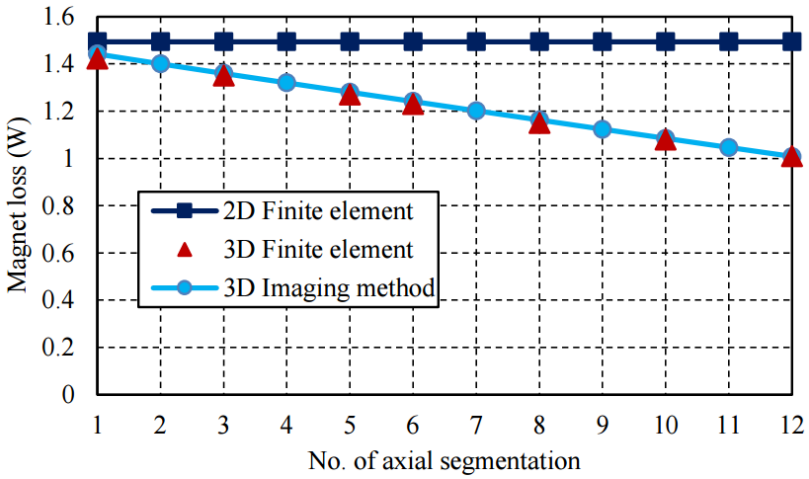

(b)

Figure 3.17. Comparison of eddy current loss calculation results with variation of the number of axial segments when the circumferential segments: (a) SC = 1 and (b) SC = 2

3.8 Conclusions

A computationally efficient and accurate means for predicting 3D eddy current loss in rotor magnets of PM machines has been developed based on the generalized image theory. The developed method has been validated by 3D FEAs on an 18-slot, 8-pole SPM machine. It has been shown that the developed method only takes about 10 seconds for computing 3D eddy current loss in contrast to more than 24 hours of computation time required by 3D FEA, representing computational efficiency improvement by 5 orders of magnitude.

Although the effectiveness of the developed method is only demonstrated on a SPM machine in the chapter, the method can be used to evaluate 3D eddy current loss in a variety of PM machines which have complex geometry and exhibit high level of magnetic saturation, e.g. IPM, when it is combined with 2D FE analysis of the magnetic field distributions. The method is also applicable to PM machines in which the magnets are placed on the stator, such as flux-switching PM machines, etc.

Moreover, the developed method provides a very efficient and effective tool for assessing the influence of axial and circumferential segmentations of magnets on eddy current loss as a part of design optimization process.

CHAPTER 4 Electro-thermally coupled model for permanent magnet machines

This chapter develops an accurate and computationally-efficient modelling method that considers the effect of temperature variation on the electromagnetic behaviours of IPM machines. The temperature influence is accounted conveniently on a machine high-fidelity model established at a reference temperature, by employing an equivalent d-axis current offset which varies linearly with temperature. No extra model building calculations are required while the effect of saturation and space harmonics are represented. The proposed machine model is combined with a lumped-parameter state-space thermal model to form an electro-thermal coupled machine model. The proposed model is validated with experiments on a prototype IPM machine.

4.1 Introduction

The method proposed in Chapter 2 of the thesis builds high-fidelity electromagnetic analytical model for PM machines. With magnets' and winding temperatures assumed at the design limits, this high-fidelity model can be used in machine design/optimisation process to evaluate machine performances at the worst thermal scenarios.

However, unlike the conventional machines used in industrial traction applications, the working conditions of PM machines used in EV traction don't center around rated point, but varies widely with driving conditions in the torque-speed range, thus the machine temperatures would change accordingly. Since the remanences of permanent magnets are affected significantly by the temperature of magnets, the air gap flux density, the saturation level in the stator and rotor cores and harmonics in the stator flux linkage are all temperature-dependent, hence the electromagnetic analytical models of PM machines should change as a result. Consequently, the iron loss of machine iron cores and copper loss of stator windings would also change with temperature, and in return influence the machine thermal behaviour.

If the temperature effect were ignored, the voltage and current ratings for the torque-speed requirement and the magnet temperature and winding temperature would be underestimated when the machine operates at temperature higher than the designed value. Consequently, the machine would not be able to achieve the required torque, and risk partial irreversible demagnetization and a shorter life span due to higher temperatures.

Therefore, an electromagnetic (EM) PM machine model coupled with machine thermal behaviour model is indispensable in an EV traction application. Although employing

EM finite element analysis coupled with thermal simulation, as most of the literatures do, could obtain accurate machine performance predictions, it is not possible to employ such modelling techniques for simulation at system levels or for assessing machine performance over driving cycles due to enormous time consumption on FE calculations.

Further from the method illustrated in Chapter 2, to capture the thermal influence on the electromagnetic models, a new technique is proposed in this chapter. The temperature effect of the permanent magnets on the machine electromagnetic response is represented by an equivalent *d*-axis current which varies with temperature proportionally, thus greatly reduces calculation time for modelling and simulations. The temperature dependent electromagnetic model is combined with a lumped parameter thermal model to form a computationally efficient electro-thermally coupled model. The electro-thermal coupled model is simulated in various operations and validated by load experiments on a prototype machine. Beside the temperature effect on the machines' EM models, as for the thermal model used for the coupling simulations, the heat transfer coefficients between the housing surface and the environment is also temperature dependant, however this is not studied in this chapter, and an average coefficient will be used to approximate the effect.

The rest of the chapter is organized as follows. Section 4.2 describes a high fidelity electromagnetic model of IPM machines and illustrates the effect of temperature on the machine flux linkage and torque. Section 4.3 introduces the concept for accounting the temperature effect. Section 4.4 presents the detailed modelling process and section 4.5 assesses the accuracy of the proposed model. The temperature dependent electromagnetic model is combined with a lumped parameter thermal model to form a computationally efficient electro-thermally coupled model in section 4.6. The utility and significance of the model are evaluated by simulation studies. Section 4.7 presents experimental results that validate the developed model and Section 4.8 draws conclusion.

4.2 Electromagnetic model and the temperature effect

4.2.1 Machine model at a constant temperature

The *d*-*q* axis model given in (4.1)-(4.3) is widely used for modelling permanent magnet machines

$$V_d = L_d \frac{di_d}{dt} + R_s i_d - \omega_e L_q i_q \tag{4.1}$$

$$V_q = L_q \frac{di_q}{dt} + R_s i_q + \omega_e(\psi_m + L_d i_d) \tag{4.2}$$

$$T_{em} = \frac{m}{2} p[\psi_m i_q + (L_d - L_q) i_d i_q] \tag{4.3}$$

where $v_d, v_q$are the *d*- and *q*-axis voltages, $i_d, i_q$are the *d*- and *q*-axis current, ψ_m is the permanent magnets flux linkage, $L_d, L_q$are the *d*- and *q*-axis inductances. R_s is the phase resistance, p is the number of pole-pairs, m is the number of phases, $\omega_e$is the electric angular frequency and T_{em} is the electromagnetic torque. While the effect of magnetic saturation may be accounted by variations of $L_d, L_q$and $\psi_m$as functions of i_d and i_q, the classic *d*-*q* axis model given in (4.1)-(4.3) neglects back-emf harmonics, stator mmf harmonics and slotting effect. Consequently, the resultant phase voltage and current are sinusoidal in steady state, and the electromagnetic torque is smooth without any ripple.

In order to accurately represent IPM machine behaviour, the saturation effect which varies with the current and the space harmonics which varies with the rotor positon need to be taken into account. In Chapter 1 the machine electromagnetic model characterising the average flux linkage over one electrical cycle considering the saturation effect is established. However in order to facilitate the calculation of design and optimisation process, the model does not include the effect of the rotor position changes. This effect was accounted for in a high-fidelity machine model proposed in [106]. The model represents the characteristics of an IPM machine by expressing its *d*- and *q*-axis flux linkages, $\psi_d(i_d, i_q, \theta)$ and $\psi_q(i_d, i_q, \theta)$, as functions of *d*- and *q*-axis currents, and rotor position θ. The governing equations of the machine are given in (4.4)-(4.6). The ψ_d and ψ_q functions are analytical expressions or discrete look-up tables extracted from FEA calculations. Since the cogging torque is not included in (4.6), the look-up table of torque as a function of currents and rotor position $T_{em}(i_d, i_q, \theta)$ is also extracted from FEA to give an accurate torque model.

$$V_d = \frac{d\psi_d}{dt} + R_s i_d - \omega_e \psi_q \tag{4.4}$$

$$V_q = \frac{d\psi_q}{dt} + R_s i_q + \omega_e \psi_d \tag{4.5}$$

$$T_{em} = \frac{m}{2} p[\psi_d i_q - \psi_q i_d] \tag{4.6}$$

Without loss of generality, two IPM machines shown in Figure 4.1 are used for studies in this chapter. One is a fractional-slot IPM machine with 18 slots and 8 poles [105] and

the other is a 36-slot, 6-pole IPM machine with distributed windings [110]. Both machines have 10kW peak power and are designed for distributed traction of a small sized EV. Figure 4.2 shows a surface of ψ_q versus (i_d, i_q) calculated using FEA at a given rotor position of $\theta = 7.5$ degree and magnet temperature = 120 ^{o}C in the high fidelity model of the 18-slot 8-pole IPM. It is evident that the flux varies with the currents in a highly non-linear fashion.

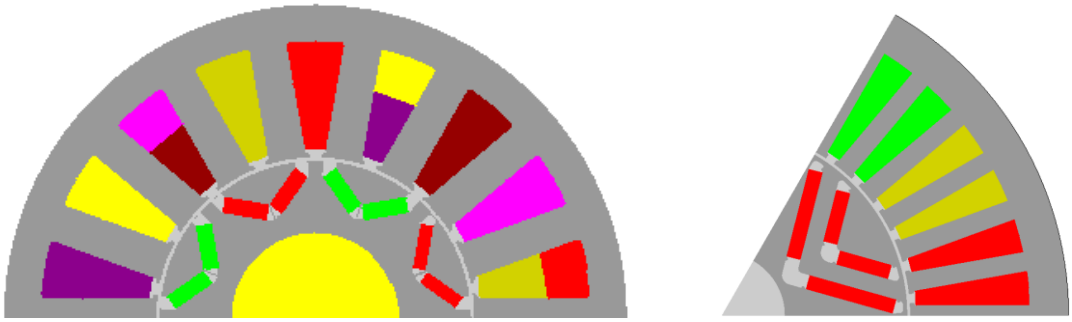

(a) (b)

Figure 4.1. (a) 18-slot 8-pole IPM geometry; (b) 36-slot 6-pole IPM geometry

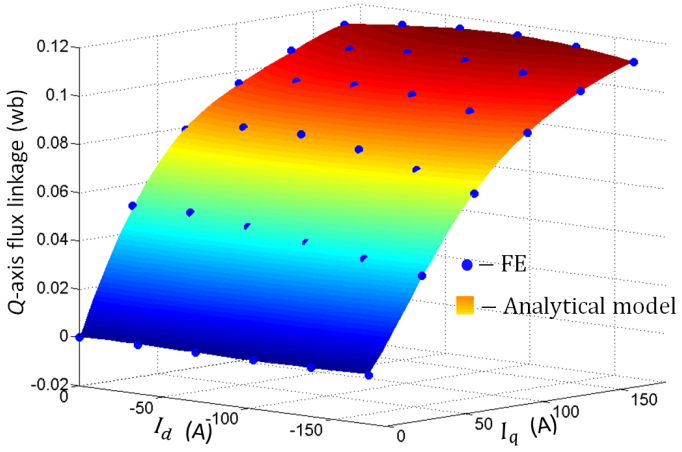

Figure 4.2. 18-slot 8-pole IPM q-axis flux linkage from analytical model and FE and magnet temperature 120 ^{o}C

4.2.2 Temperature effect on the machine high-fidelity EM model

In addition to current and rotor position, temperature also affects the flux linkages of a machine and hence its performance, since the remanence B_r of the permanent magnets varies with the temperature T linearly, characterized by the temperature coefficient α as:

$$B_{r2}(T_2) = B_r(T_1) \times [1 + \alpha \times (T_2 - T_1)] \tag{4.7}$$

where B_{r2} and B_{r1} represent the remanence at the temperature of T_2 and T_1, respectively. Figure 4.3 shows the FE predicted d-axis flux linkage ψ_d variation of the

18-slot, 8-pole machine over *d*- and *q*-axis current ranges when the magnet temperature changes from 120°C to 20°C, normalized to the flux-linkage due to permanent magnets at 120 °C. As can be seen, the increase in flux linkage due to the temperature reduction is up to 18%. Thus, this will significantly affect the torque capability and energy efficiencies. It is also evident in Figure 4.3 that the increase in the flux is not uniform in the range of *d*- and *q*-axis currents, and varies in the region of 10%-18%. The non-uniformity makes accurate modelling of the temperature effect difficult. Due the nonlinearity of the magnetic field, the effect of temperature and remanence change on the flux linkages of windings cannot be simply represented by a linear factor inside the machine model.

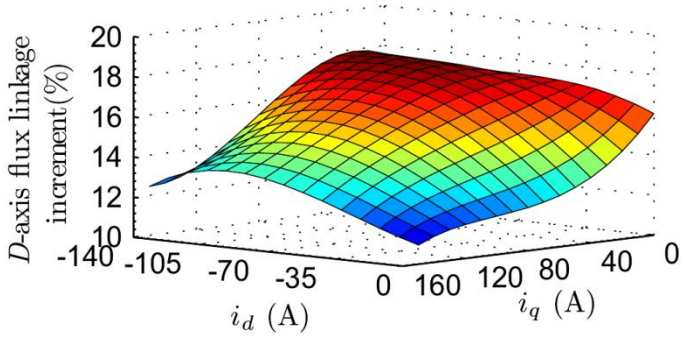

Figure 4.3. *D*-axis flux linkage increment over *d*-, *q*-axis current ranges when temperature decreases from 120°C to 20°C (percentage with respect to permanent magnet flux linkage), at rotor position =7.5 degree

Figure 4.4 shows the similar *q*-axis flux linkage ψ_q variation when the permanent magnet temperature changes from 120°C to 20°C normalized to ψ_q at the max i_q and $i_d = -56\ A$ at the temperature 120°C. The percentage change is very small, around 1-3%. This implies that neglecting the temperature effect on the *q*-axis flux linkage does not incur large error.

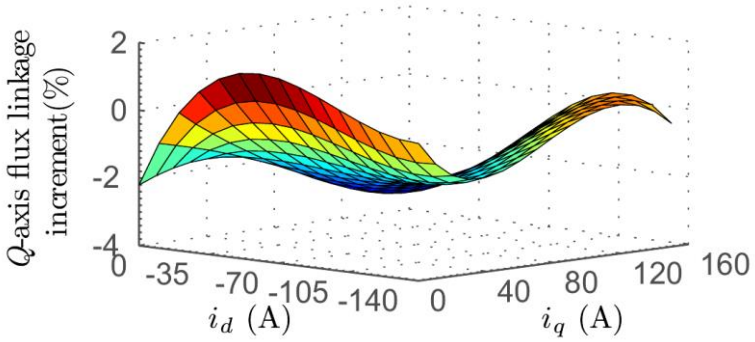

Figure 4.4. *Q*-axis flux linkage increment over *d*-, *q*-axis current ranges when temperature decreases from 120°C to 20°C (percentage with respect to ψ_q at max i_q), at rotor position = 7.5 degree

Figure 4.5 shows FE predicted open-circuit *d*-axis flux linkage ψ_d variation with magnet temperature. Due to saturation effect, ψ_d varies not strictly linear with temperature.

In order to represent the temperature effect accurately, the flux linkage under every *d*- and *q*- axis current and each rotor position need to be computed for a given temperature. If this is performed by FE analysis, enormous amount of computation time will be required, which makes it impossible to perform system simulations and design optimizations over driving cycles.

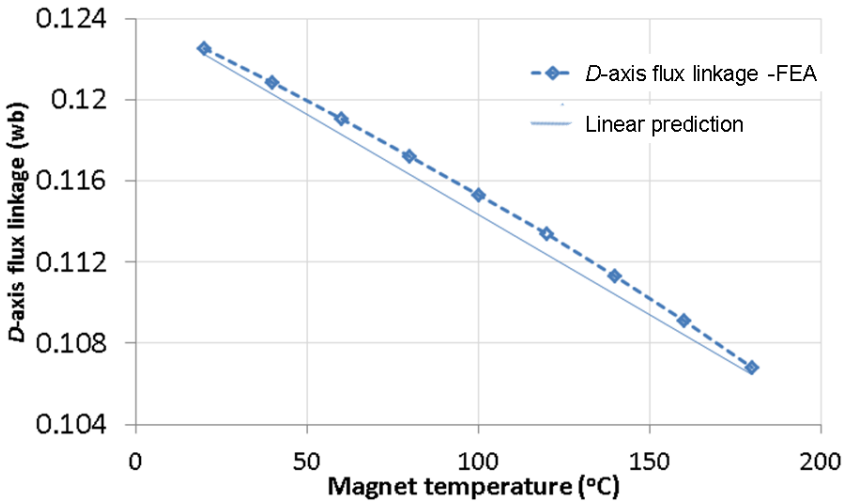

Figure 4.5. *D*-axis flux linkage (open-circuit) versus temperature variation

4.3 Equivalent *d*-axis current representing temperature effect

4.3.1 Temperature effect on machine flux circuit

The magnetic field produced by the permanent magnets may be represented by a virtual winding on the rotor aligned with the *d*-axis and carrying an excitation current. Figure 4.6 shows a schematic *d*-axis magnetic flux path of a spoke-type IPM rotor where *d*-axis armature current i_d and equivalent magnet current i_M together produce the d-axis flux linkage in the stator winding through the equivalent reluctances of the laminations and air gap. $R_{sB}, R_{st}, R_{ag}, R_{rt}, R_{mg}, R_{sl},$ and R_{rl} denote the reluctances of the stator back iron, the stator tooth iron, the air gap, the rotor tooth, the magnet, the stator slot leakage and the rotor bridge leakage, respectively. The equivalent current i_M representing the effect of the permanent magnets may be transposed to the stator side as i_m in the circuit shown in Figure 4.7. Therefore the total equivalent excitation current in the *d*-axis seen by the stator windings is $i_d + i_m$.

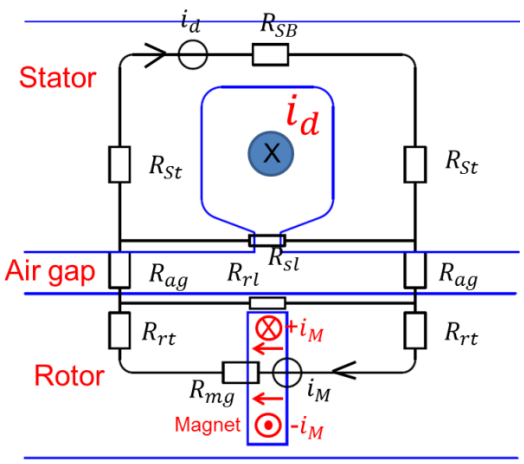

Figure 4.6. Magnetic flux path

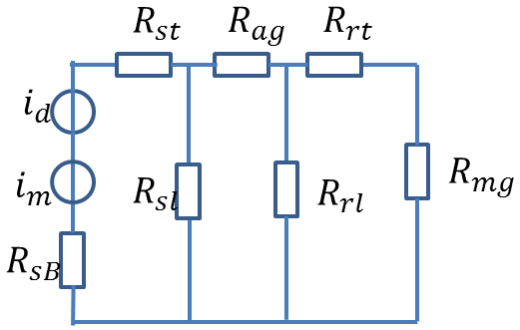

Figure 4.7. Magnetic circuit with transposed equivalent magnet *d*-axis current

When the magnet temperature varies, its remanence and equivalent current i_m changes proportionally to the temperature variation, resulting in the variation of *d*-axis and *q*-axis flux linkages, as shown in Figure 4.8, where the horizontal coordinate is the total equivalent *d*-axis excitation current, and i_{m1} and i_{m2} are the equivalent currents of permanent magnets at temperatures, $T_1$and T_2, respectively.

The machine flux linkages models using the total equivalent *d*-axis excitation current as the variable at the reference temperature T_1 may be expressed as:

$$\psi_d(i_d, i_q, T_1) = \psi_D(i_d + i_{m1}, i_q) \tag{4.8}$$

$$\psi_q(i_d, i_q, T_1) = \psi_Q(i_d + i_{m1}, i_q) \tag{4.9}$$

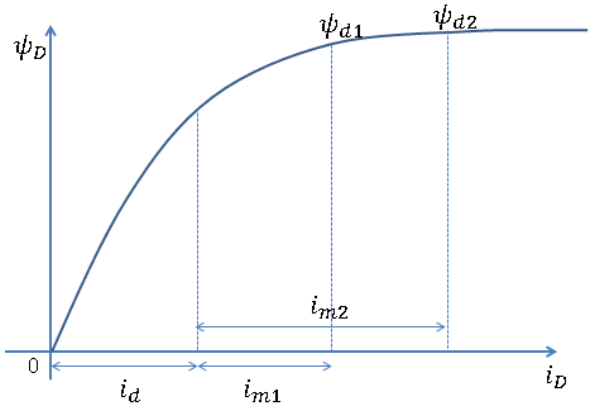

Figure 4.8. *D*-axis flux with equivalent magnet *d*-axis current

Similarly, the flux linkages at a new temperature T_2 are:

$$\psi_d(i_d, i_q, T_2) = \psi_D(i_d + i_{m2}, i_q) \tag{4.10}$$

$$\psi_q(i_d, i_q, T_2) = \psi_Q(i_d + i_{m2}, i_q) \tag{4.11}$$

From (4.8) and (4.10), it can be derived that

$$\begin{aligned}\psi_d(i_d, i_q, T_2) &= \psi_D(i_d + i_{m1} + i_{m2} - i_{m1}, i_q) \\ &= \psi_d(i_d + (i_{m2} - i_{m1}), i_q, T_1) = \psi_d(i_d + i_{mc}, i_q, T_1)\end{aligned} \tag{4.12}$$

$$\psi_q(i_d, i_q, T_2) = \psi_q(i_d + i_{mc}, i_q, T_1)$$

$$i_{mc} = i_{m2} - i_{m1} \tag{4.13}$$

Therefore the flux linkages at a new temperature T_2 can be predicted using the model at the reference T_1 with its *d*-axis current displaced by a constant i_{mc}, which is equal to the magnet equivalent current difference between the two temperatures. The *q*-axis current is kept the same.

When the rotor position θ changes, the position dependent *d*- and *q*- axis flux linkages can also be expressed as:

$$\psi_d(i_d, i_q, \theta, T_2) = \psi_d(i_d + i_{mc}, i_q, \theta, T_1) \tag{4.14}$$

$$\psi_q(i_d, i_q, \theta, T_2) = \psi_q(i_d + i_{mc}, i_q, \theta, T_1) \tag{4.15}$$

If the saturation effect in the rotor bridge region is neglected, i_{mc} varies linearly with the temperature difference given by:

$$i_{mc} = i_{m2} - i_{m1} = i_{m1} \times \alpha \times (T_2 - T_1) \tag{4.16}$$

Based on the equivalent circuit concept in Figure 3.9, the resultant d-axis flux linkage is zero if $i_d = -i_m$. Thus, the equivalent current i_{m1} at the reference temperature T_1 is equal to the short circuit current, i_{d-sc1}, i.e., $i_{m1} = -i_{d-sc1}$ and can be obtained by a short-circuit FE calculation since

$$\psi_D(i_{d-sc1} + i_{m1}, 0) = \psi_d(i_{d-sc1}, 0, T_1) = 0 \tag{4.17}$$

Once i_{m1} has been determined from the FE simulation of the short-circuit condition at the reference temperature T_1, the i_{mc} at any given temperature T_2 is obtained from (4.16).

4.3.2 Conventional model considering temperature effect

The above concept can be applied to the conventional PM machine model given in (4.1)-(4.3) to account the effect of magnet temperature variation. The PM flux linkage ψ_m, d-axis and q-axis inductances L_d, L_q at temperature T_2 can be expressed as:

$$\psi_m(0, i_q, T_2) = \psi_{m1}(i_{mc}, i_q, T_1) \tag{4.18}$$

$$\begin{aligned} L_d(i_d, i_q, T_2) &= L_{d1}(i_d + i_{mc}, i_q, T_1) \\ L_q(i_d, i_q, T_2) &= L_{q1}(i_d + i_{mc}, i_q, T_1) \end{aligned} \tag{4.19}$$

where ψ_{m1}, L_{d1}, and L_{q1} are the PM flux linkage and d- and q- axis inductances at the reference temperature T_1. The electromagnetic torque at T_2 is given by:

$$\begin{aligned} T_{em}(i_d, i_q, T_2) &= 1.5p \times [\psi_d(i_d, i_q, T_2) i_q - \psi_q(i_d, i_q, T_2) i_d] \\ &= T_{em}(i_d + i_{mc}, i_q, T_1) + 1.5p \times \psi_q(i_d + i_{mc}, i_q, T_1) i_{mc} \end{aligned} \tag{4.20}$$

It should be noted that an addition term $1.5p \times \psi_q(i_d + i_{mc}, i_q, T_1) i_{mc}$ is necessary to account the temperature effect on torque. It follows that by introducing the equivalent current i_{mc} the machine flux linkages ψ_d, ψ_q and torque T_{em} at any temperature can be obtained from their values computed at a reference temperature.

4.4 Machine Models Considering Temperature Effect

4.4.1 Equivalent current constant based on two FEAs

Because the reluctance R_{rl} shown in Figure 4.7, representing the effect of the leakage flux in the rotor bridge is affected by saturation, the equivalent current i_m is slightly influenced by temperature, and hence needs to be corrected by two short-circuit FE calculations at two reference temperatures T_1 and T_3 respectively.

The equivalent currents at the two reference temperatures can be expressed as:

$$i_{m1} = -i_{d-sc1},\ \psi_d(i_{d-sc1}, 0, T_1) = 0 \tag{4.21}$$

$$i_{m3} = -i_{d-sc3},\ \psi_d(i_{d-sc3}, 0, T_3) = 0 \tag{4.22}$$

the equivalent current, i_{mc}, at a new temperature T can be obtained by:

$$i_{mc} = i_m - i_{m1} = \frac{i_{m3} - i_{m1}}{T_3 - T_1}(T - T_1) = k(T - T_1) \tag{4.23}$$

Thus, the modified *d*-axis current $i_d + i_{mc}$ can be used obtain to the flux linkages and torque at any temperature T based on their values computed at the reference temperature T_1.

4.4.2 Machine simulation models considering temperature variations

By employing the equivalent current i_{mc}, the *d*-and *q*- axis flux linkages and electromagnetic torque which account the temperature effect can be used to form a complete machine model as shown in Figure 4.9. However, this model contains differential operator which may be sensitive to numerical error and slow down transient simulations. To circumvent this problems, the d- and q- axis currents may be expressed as functions of d- and q-axis flux linkages, i.e., $i_d(\psi_d, \psi_q, \theta)$ and $i_q(\psi_d, \psi_q, \theta)$ by inverting of $\psi_d(i_d, i_q, \theta)$and $\psi_q(i_d, i_q, \theta)$. The method for the inverse is described in [106]. To account for the temperature effect, the *d*-axis current at any temperature, T, can be obtained by the d-axis current from the inverse at the reference temperature T_1 minus i_{mc} as given in (4.24), while the q-axis current is not affected as given in (4.25):

$$i_d(\psi_d, \psi_q, \theta, T) = i_{d1}(\psi_d, \psi_q, \theta, T_1) - k(T - T_1) \tag{4.24}$$

$$i_q(\psi_d, \psi_q, \theta, T) = i_{q1}(\psi_d, \psi_q, \theta, T_1) \tag{4.25}$$

Figure 4.10 shows the inverse flux linkage model with temperature effect and Figure 4.11 shows the complete machine model employing the inverse flux linkage model, in which differential operators are avoided.

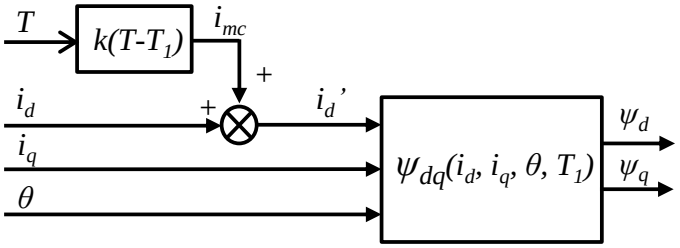

(a)

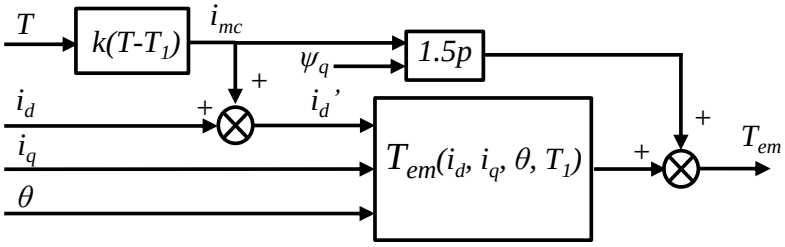

(b)

Figure 4.9. IPM machine model with temperature effect (a) Flux linkage model; (b) Torque model.

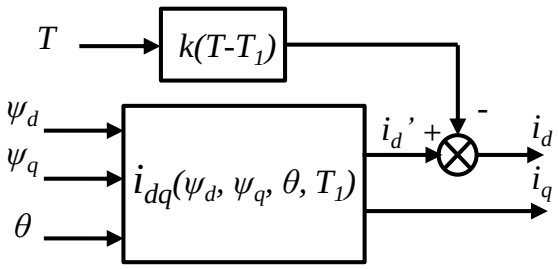

Figure 4.10. Inverse flux linkage model with temperature effect

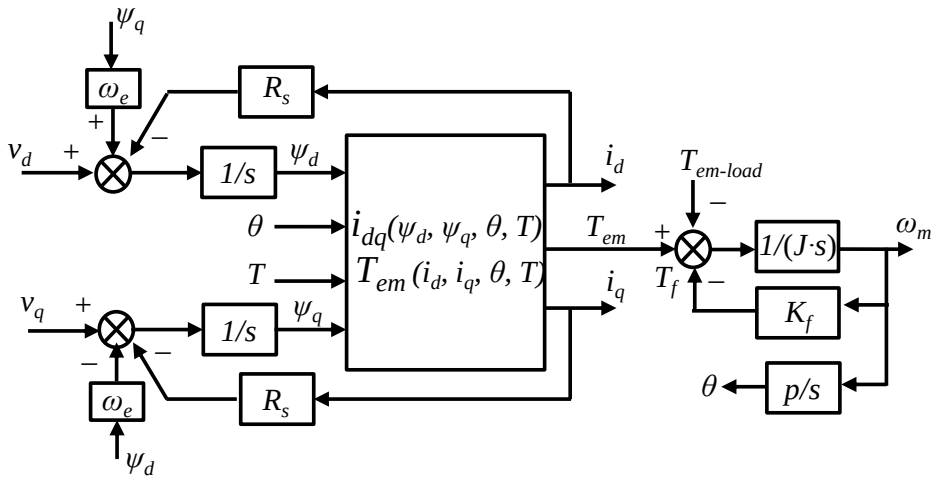

Figure 4.11. Machine model with temperature effect based on inverse flux linkage model

It should be noted that in the machine model, the temperature effect on the stator winding phase resistance R_s is considered as described in (4.26):

$$R_s(T) = R_s(T_1) \times [1 + \alpha_R(T - T_1)] \tag{4.26}$$

in which R_s (T_1) is the winding resistance at the reference temperature T_1; α_R is the winding resistivity temperature coefficient.

It should be noted that when the temperature varies, the d- and q-axis currents for maximum torque per Ampere (MTPA) operation or for field weakening operation have to be adjusted. The control strategy for such adjustments is not covered in this chapter.

4.5 Assessment of Model Accuracy

4.5.1 Accuracy of flux linkage and torque models

The accuracy of the proposed flux linkage model, $\psi_d(i_d, i_q, \theta, T)$, $\psi_q(i_d, i_q, \theta, T)$, and the torque model $T_{em}(i_d, i_q, \theta, T)$, which account for temperature effect, is assessed by two case studies. The machine flux linkage and torque models are extracted from FEA for the 18-slot 8-pole IPM machine at the reference temperature T_1 = 100°C and for the 36-slot 6-pole IPM at the reference temperature T_1 = 70°C. The equivalent magnet currents i_{mc} for the two machines are acquired through two short-circuit FEAs at two different temperatures, 20 °C and 70 °C, respectively, according to (4.23). To assess the proposed model accuracy, the flux linkages and torque at a given temperature T are also computed directly by FEA, and they are denoted as "FE" in the subsequent figures. The flux linkages and torque obtained from the proposed model is denoted as "T-model".

Figure 4.12 shows the variation of the average *d*-axis flux linkage over one electric period with temperature for the 36-slot 6-pole IPM predicted by both FEA and the proposed model when operating at 35Nm and 1350 rpm. In the FE predictions, the flux linkage is computed at each temperature with the *d*- and *q*-axis currents adjusted to produce the rated torque under MTPA condition. With the proposed model, the *d*-axis flux linkage at a given temperature is calculated based on its map computed at the reference temperature of 100°C and the currents adjusted for MTPA operation. A good agreement with the FE prediction is observed.

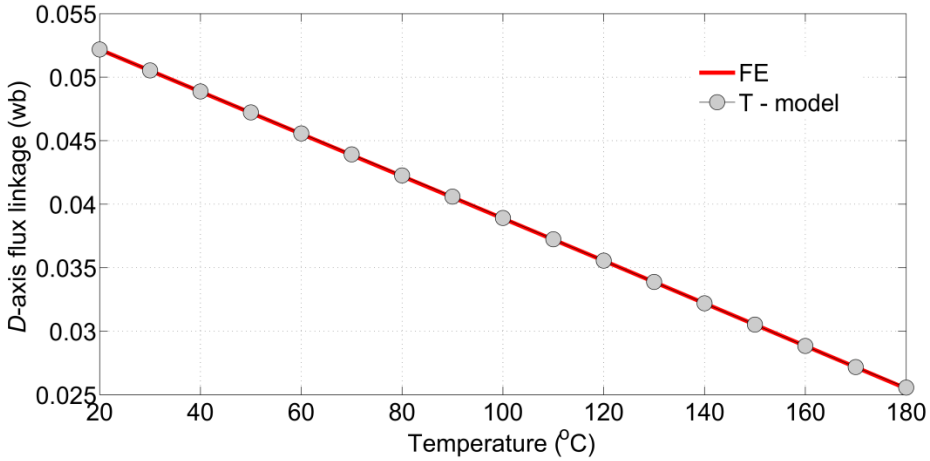

Figure 4.12. *d*-axis flux linkage versus temperature at rated torque of 35Nm and base speed of 1350 rpm

The accuracies of the average flux linkages, inductances and torque over an electric period predicted by the proposed model are investigated for the 18-slot 8-pole machine with varying *d*-, *q*-axis currents when the magnet temperature is changed from the reference 100°C to 20°C. Figure 4.13 and Figure 4.14 show the relative *d*- and *q*- flux linkage errors defined as $(\psi_{FE} - \psi_M)/\psi_{FE}\%$, where ψ_{FE} and ψ_M denote the average *d*- or *q*-axis flux linkages predicted by FE and the proposed model at 20°C, respectively. It is observed that over a wide *d*- and *q*-axis current range, the model predicted flux linkages have good accuracy in that the *d*-axis flux linkage error is below 0.6% and the *q*-axis error below 2%. Table 4.1 lists RMS errors of the flux linkages, inductances and torque over the i_d and i_q range. It is shown that the proposed model gives accurate prediction especially for ψ_d, ψ_m, L_d and T_{em} which increase by around 11%, 9%, 3% and 5%, respectively, when the magnet temperature varies from 100°C to 20°C. The proposed model follows the changes accurately with the error around 1%-1.5% except for L_q.

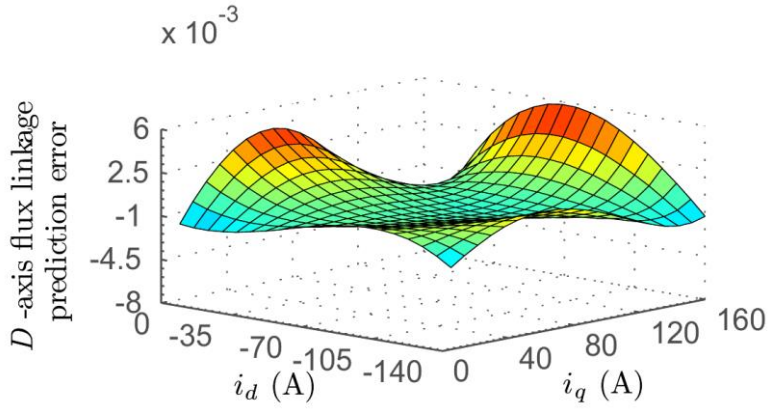

Figure 4.13. Variation of relative error of *d*-axis flux linkage with i_d and i_q

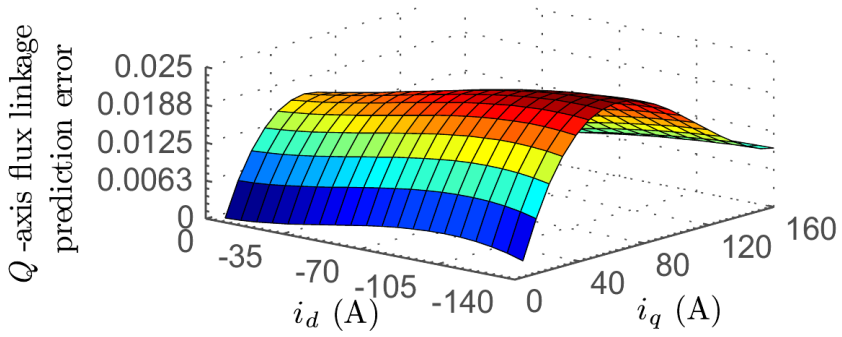

Figure 4.14. Variation of relative error of *q*-axis flux linkage with i_d and i_q

Table 4.1 RMS Errors Over id-iq Range at 20°C with 100°C as the Reference

Variables	% change (from 100 **°C** to 20 **°C)**	Relative error of proposed model
ψ_d	10.82%	1.41%
ψ_q	1.45%	1.51%
ψ_m	8.98%	1.28%
L_d	3.05%	1.54%
L_q	1.90%	2.65%
T_{em}	4.66%	0.98%

The accuracy of predicted flux linkage and torque variations with rotor positions is also assessed. Figure 4.15 and Figure 4.16 compare the model and FE predicted *d*-axis flux linkage and electromagnetic torque at 120°C for the 36-slot 6-pole IPM when operating

at the rated torque and base speed, and at the peak torque and maximum speed, respectively. It can be seen that in all the representative operating conditions, the model predicted variations of the flux linkages and torque with rotor position match very well the FE results.

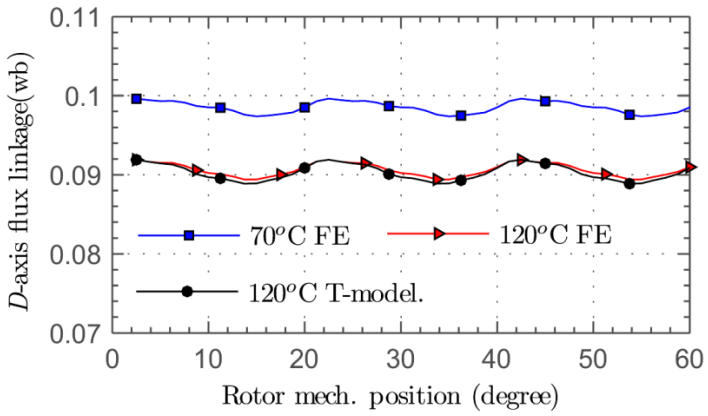

(a)

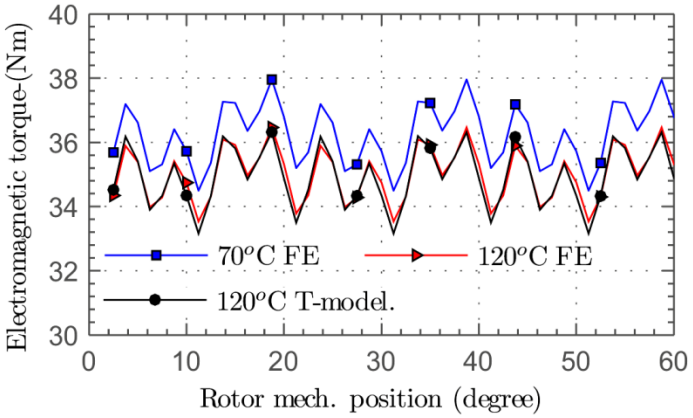

(b)

Figure 4.15. Variations of *d*-axis flux linkage and electromagnetic torque with rotor position predicted by FE and proposed model at rated torque of 35Nm and base speed of 1350 rpm (a): *d*-axis flux linkage; (b): electromagnetic torque

It should be noted that in the field weakening region the temperature effect on electromagnetic torque is less significant, as evident in Figure 4.16. This is because as temperature increases, the permanent magnet flux linkage decreases, which tends to reduce the torque. However, the decrease in permanent magnet flux linkage leads to less d-axis current required for field weakening, and hence for the same current magnitude, the q-axis current can be increased, which increases the torque. The two effects cancel each other, resulting in a less significant change in torque for a given current magnitude.

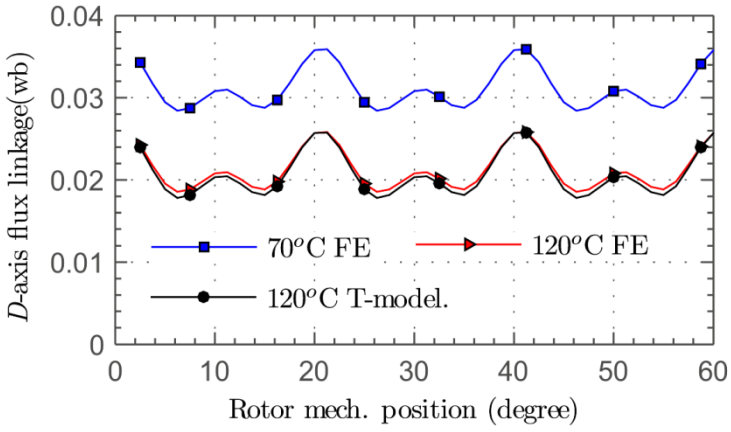

(a)

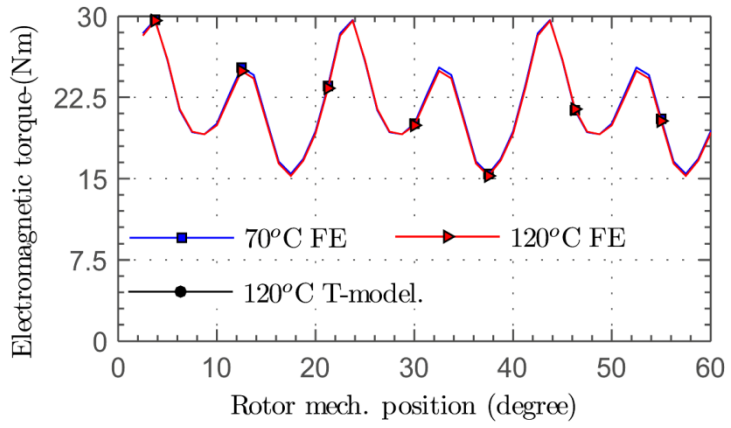

(b)

Figure 4.16. Variations of *d*-axis flux linkage and electromagnetic torque with rotor position predicted by FE and proposed model at peak torque of 21Nm and maximum speed of 4500 rpm (a): *d*-axis flux linkage; (b): electromagnetic torque

4.5.2 Accuracy of inverse flux linkage models

The accuracies of the inverse flux linkage models are also examined. By way of example, Figure 4.17 shows the relative *d*- axis current errors between the FE predictions and proposed model predictions normalized to the rated current of 79.9 A over the ψ_d and ψ_q range for the 36-slot 6-pole IPM at 120°C. Similar error distribution of the *q*-axis current is shown in Figure 4.18.

As can be seen, good agreements are obtained when comparing the results predicted by the proposed model and by FE over the *d*- and *q*-axis flux-linkage operating range at the magnet temperature of 120°C. Comparisons at different magnet operating temperatures were made and similar agreements were observed.

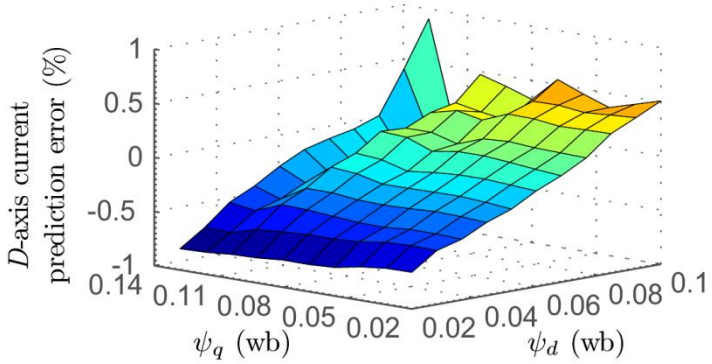

Figure 4.17. Relative prediction errors compared to the FEA for *d*-axis current over ψ_d-ψ_q range (averaged over rotor positions) using the machine reverse flux linkage model considering temperature effect at 120 ^{o}C

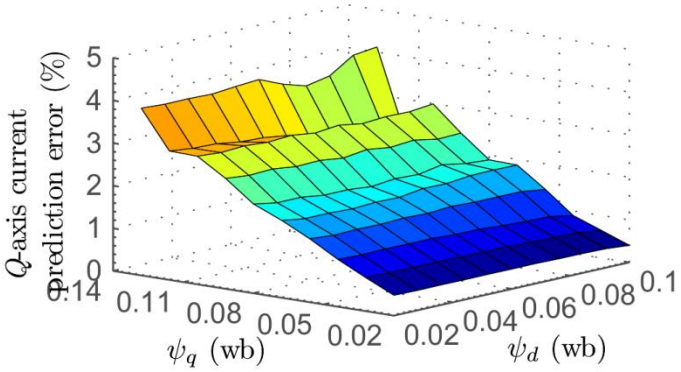

Figure 4.18. Relative prediction errors compared to the FEA for *q*-axis current over ψ_d-ψ_q range (averaged over rotor positions) using the machine reverse flux linkage model considering temperature effect at 120 ^{o}C

4.6 Electric-thermally coupled Model

For a machine in the real time operation, its electrical and thermal performances are dependent on each other. In order to accurately predict the machine behaviors, the proposed machine model considering the temperature effect needs to be combined with its thermal model.

Figure 4.19 shows the proposed schematic of the electro-thermally coupled model. The electromagnetic machine model, denoted as "machine model" for notational convenience, calculates the current and flux linkages at a given load condition based on the predicted magnet and winding temperatures from the thermal model. As described in Section 4.4.2, both the flux linkages, torque and the phase winding resistance vary with temperatures in the machine model.

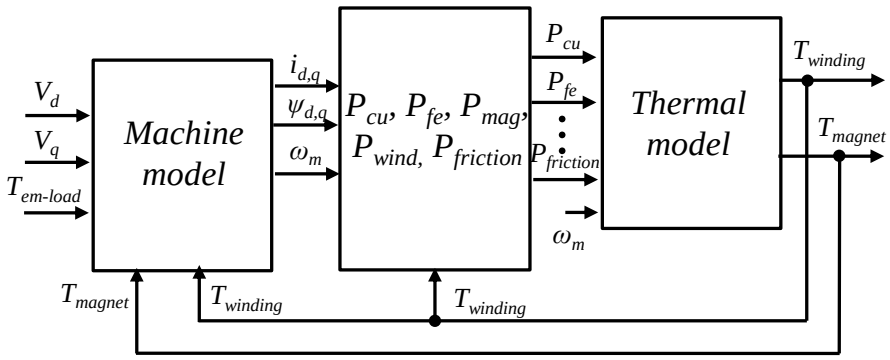

Figure 4.19. Schematic of electro-thermally coupled model of an IPM machine

With the predicted current and flux linkages from the machine model as inputs, analytical machine loss models are used to predict the copper loss, iron loss, windage and bearing friction loss. These losses are then fed into the machine transient thermal model in the form of state-space equation as section 4.6.3. The output of the thermal model, namely, the temperatures of the windings and magnets are fed back to the machine model and the loss models to close the coupling loop.

4.6.1 The machine model for electro-thermally coupled simulations

In an ideal electro-thermally coupled simulation, both electrical and thermal transients should be accurately captured. However for a traction system to reach its thermal steady state in real operation or over a driving cycle, it usually takes a few hours. This implies that, in order to represent both the electrical and thermal transient behaviors, enormous amount of computational time and data storage capacity are required, since the simulation time step has to be sufficiently smaller than the minimum electrical time constant.

Since the thermal time constants of an IPM machine are typically a few orders of magnitude higher than its electrical time constants, the current and flux linkage would reach their steady state for a given load operation long before temperature changes. Therefore, the machine model shown in Figure 4.20, which is simplified from the model in Figure 4.11, may be used in the electro-thermally coupled simulations, where only steady-state values of current, torque, flux linkages and voltages are calculated. The voltage integrations which represent the electrical transients are removed and the reverse flux linkage functions $i_{dq}(\psi_d, \psi_q, \theta, T)$ and torque function $T_{em}(i_d, i_q, \theta, T)$ are

also changed to $i_{dq}(\psi_d, \psi_q, T)$ and $T_{em}(i_d, i_q, T)$, respectively, by averaging the current, flux linkage and torque values over an electrical cycle. The flux linkages fed to $i_{dq}(\psi_d, \psi_q, T)$ can be calculated by:

$$\psi_d = (V_q - R_s i_q)/\omega_e \tag{4.27}$$

$$\psi_q = -(V_d - R_s i_d)/\omega_e \tag{4.28}$$

The current and flux linkage inputs for the loss models are also steady-state averaged values over an electrical cycle.

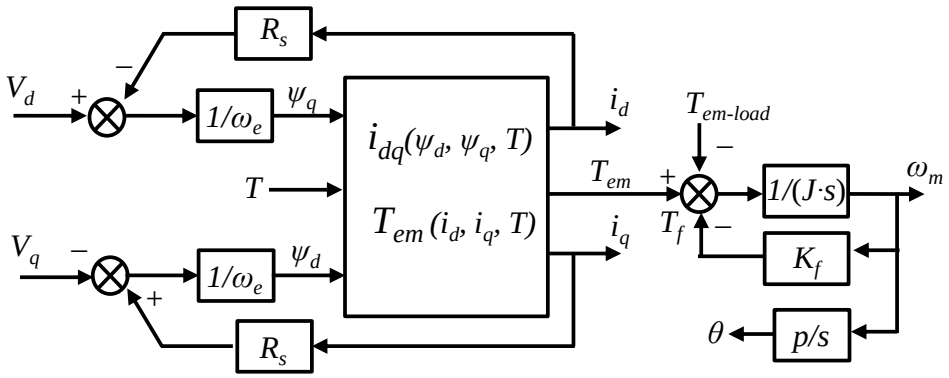

Figure 4.20. The schematic of the steady-state machine model used in the electro-thermally coupled simulation for an IPM machine

Following the above method, the simulation time step can be increased to represent the thermal transients and the variations of averaged voltages, currents and flux linkages with time. Thus the time durations of the simulations are greatly reduced. It takes ~5 seconds on a typical PC to perform a ~5.6 hour electro-thermally coupled simulation using Matlab/Simulink.

After the system reaches the thermal steady state, the machine electrical transients including the position-dependent effect could be simulated with the full model shown in Figure 4.11 if detailed electrical transient and harmonic behaviors are to be studied.

4.6.2 Machine loss models

In Chapter 1, an improved model for the analytical model for the Bertotti iron loss calculation based on [107] and the analytical model proposed in [108] for eddy current loss in the magnets are illustrated. The two loss models are employed in the electro-

thermally coupled simulations. The parameters of the loss models are obtained by performing 2 FE simulations at the peak power, rated speed point and the peak power, maximum speed point respectively, and the iron loss model can be calibrated with measured losses in no-load tests. Therefore, for a given current and flux linkage input, the iron losses and magnet loss could be predicted automatically.

The combined windage and friction loss is modeled as a polynomial function of speed by curve-fitting based on measured no-load loss at different speeds with a dummy rotor.

4.6.3 Thermal model

A steady-state thermal model predicting the machine temperatures at continuous operations are proposed in Chapter 1. In order to predict the transient thermal behaviours, a transient thermal model of the machine is employed based on the thermal network [109] in a set of state-space equations. The thermal network contains 48 nodes, including the housing, end-plate, end-cap, stator tooth, stator back-iron, 18 winding layers, end-windings, air gap, rotor pole, rotor back-iron, magnets, shaft, and bearings, etc. The thermal behaviours on each node are governed by the heat transfer equations given by:

$$C_i \frac{dT_i}{dt} = P_i - \sum_j \frac{1}{R_{i,j}} \left(T_i - T_j \right) \tag{4.29}$$

where T_i is the temperature of i-th node (i=1, 2, ⋯, 48), C_i is the heat capacitance (thermal mass), P_i is the loss input, and $R_{i,j}$ is the thermal resistance between i-th and j-th nodes (j=1, 2, ⋯, 48, $j \neq i$). The resistance and capacitance on each node could be derived from the dedicated thermal simulation software such as Motor-CAD [109].

The copper loss, iron losses of different iron components (stator tooth, stator back iron, rotor pole and rotor back iron), magnet loss, and windage and bearing friction loss are expressed as a loss vector u on the 48 nodes and fed into the thermal network. The temperatures on the 48 nodes form an output vector y. They could be expressed as:

$$u = \begin{bmatrix} P_1 \\ P_2 \\ \vdots \\ P_{48} \end{bmatrix}, \qquad y = \begin{bmatrix} T_1 \\ T_2 \\ \vdots \\ T_{48} \end{bmatrix} \tag{4.30}$$

Therefore, according to (4.29), the state-space equations are described as:

$$x' = Ax + Bu$$
$$y = Cx + Du \tag{4.31}$$

where x is the state vector of temperatures and is chosen as $x=y$, and A, B, C and D are coefficient matrixes whose dimensions are all 48×48 in this model.

Matrixes A and B representing the networks of thermal resistances and capacitances, are expressed by (4.32) and (4.33) respectively. The matrixes C and D are unit and null matrixes respectively. The matrix A also includes the resistance between the ambient environment and the housing, which is determined by the cooling conditions.

$$A = \begin{bmatrix} C_1 & 0 & \cdots & 0 \\ 0 & C_2 & \cdots & \vdots \\ \vdots & \vdots & \ddots & 0 \\ 0 & \cdots & 0 & C_{48} \end{bmatrix}^{-1} \begin{bmatrix} -\sum_{j\neq 1}\frac{1}{R_{1,j}} & \frac{1}{R_{1,2}} & \cdots & \frac{1}{R_{1,48}} \\ \frac{1}{R_{2,1}} & -\sum_{j\neq 2}\frac{1}{R_{2,j}} & \cdots & \vdots \\ \vdots & \vdots & \ddots & \frac{1}{R_{47,48}} \\ \frac{1}{R_{48,1}} & \cdots & \frac{1}{R_{48,47}} & -\sum_{j\neq 48}\frac{1}{R_{48,j}} \end{bmatrix} \tag{4.32}$$

$$B = \begin{bmatrix} C_1 & 0 & \cdots & 0 \\ 0 & C_2 & \cdots & \vdots \\ \vdots & \vdots & \ddots & 0 \\ 0 & \cdots & 0 & C_{48} \end{bmatrix}^{-1} \tag{4.33}$$

The output vector y solved from the state space functions are actually the temperature rises on the 48 nodes and, thus, should be added with the ambient temperature. The average winding temperature and magnet temperature are fed back to the temperature dependent machine model for accounting the temperature effect.

4.6.4 Simulation results

To investigate the influence of the temperature variations on the machines' electrical and thermal performances, electro-thermally coupled simulations are carried out on the 36-slot 6-pole IPM when the machine is speed-controlled at base speed 1350 rpm with the rated load 35Nm. The ambient temperature and initial temperature is set to 45^{o}C. The simulation time duration lasts for 20,000s until the machine reach thermal steady state.

To illustrate the temperature influence, two other simulations are also performed. First, the simulation is repeated without temperature feedback to the machine flux linkage

model and the winding resistance. Thus the temperature effect is not considered. The temperature of the flux linkage model is set to the rated temperature of 120°C. In the subsequent simulation, the winding resistance variation with temperature is accounted using (4.26) while the temperature of the machine flux linkage model is still kept at 120 °C. Thus only the winding temperature is fed back to the machine model and the loss models. The results obtained are referred to as the "R_s temp. effect" in the subsequent illustrations.

Figure 4.21 and Figure 4.22 show, respectively, the temperature variations of the magnets and windings during the three simulations. Table 4.2 lists the machine electrical and thermal performances when the machine reaches the thermal steady states after the three simulations.

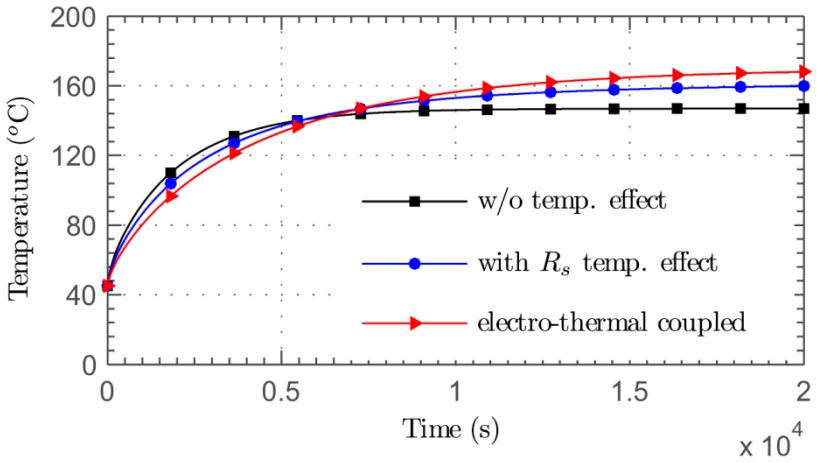

Figure 4.21. Temperature variation in armature windings when the 36-slot 6-pole IPM operates at 35 Nm, 1350 rpm.

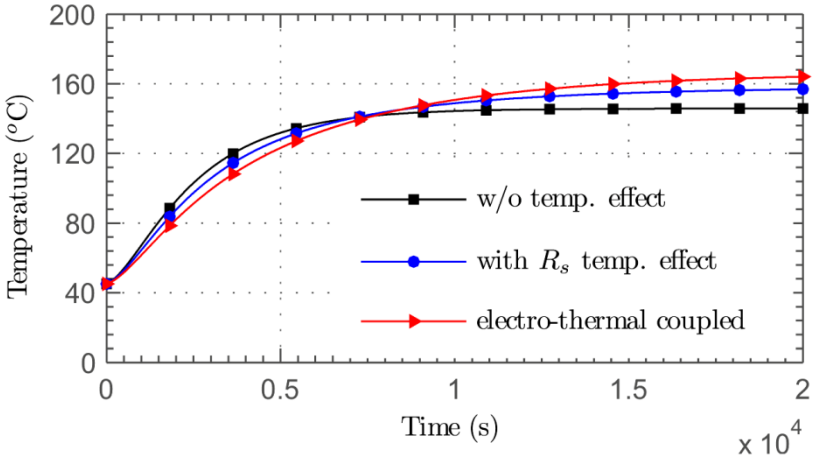

Figure 4.22. Temperature variation in magnets when the 36-slot 6-pole IPM operates at 35 Nm, 1350 rpm.

Table 4.2 Machine Performance Comparison with and without Temperature Effect at 35 nm and 1350 rpm

Performances	Without temp. effect	With only *Rs* temp. effect	Electro-thermal coupled	Difference against w/o temp. effect	Difference against *Rs* temp. effect
d-axis current (A)	-37.9	-37.9	-41.4	9.29%	9.29%
q-axis current (A)	53.0	53.0	53.5	0.94%	0.94%
d-axis voltage (V)	-45.9	-46.5	-49.1	6.87%	5.51%
q-axis voltage (V)	34.1	34.6	30.3	-11.06%	-12.44%
Resistance (Ω)	0.0624	0.0701	0.0717	14.93%	2.32%
Copper loss (W)	397.2	446.2	492.3	23.93%	10.33%
Iron loss (W)	67.9	67.7	72.6	7.00%	7.27%
Winding temperature (^{o}C)	148.9	159.4	169.4	13.82%	6.32%
Magnet temperature (^{o}C)	146.7	156.3	164.8	12.36%	5.45%

It can be observed from Figure 4.21 and Figure 4.22 that the machine model which does not account the temperature effect underestimates the steady-state temperatures. The predicted winding and magnet temperatures are 148.9 ^{o}C and 146.7 ^{o}C, respectively, being ~20 ^{o}C lower than those predicted by the electro-thermal coupled model. Although the machine model which accounts the temperature effect on the winding resistance yields better results, the predicted steady-state winding and magnet temperatures of 159.4 ^{o}C and 156.3 ^{o}C, respectively, are still ~10 ^{o}C lower than those predicted by the electro-thermally coupled model.

The underestimations due to neglecting the temperature effect could be explained by the steady state electrical performances listed in Table 4.2. Compared to the machine model which assumes a fixed temperature at 120 ^{o}C, the machine flux linkages predicted by the electro-thermally coupled model is reduced when the machine temperature rises above 120 ^{o}C. In order to maintain the torque and speed, the current is increased by around 10% as seen in the Table 4.2. Therefore, the copper loss and iron loss are increased by around 20% and 10%, respectively. This means the resultant temperatures are significantly higher.

On the other hand, when the machine temperature is below the designed temperature of 120 ^{o}C, for example, during the transient when t < 5,000 s in Figure 4.21 and Figure 4.22, the predicted temperatures by the electro-thermally coupled model are lower than those predicted by other two, because the currents and flux linkages required by the proposed model for the same load condition are lower.

The temperature underestimations resulting from the conventional machine models which neglect temperature effect, or only account temperature effect of winding resistance may have a serious consequence. First the permanent magnets may have a higher risk of irreversible demagnetization at some demanding operations than they are designed. Secondly the designed lifespan of winding insulation materials could be significantly reduced since the lifetime is halved by every 10°C increase in temperature. Therefore, an electro-thermal coupled machine model is essential for minimizing demagnetization risk and for lifetime estimation.

4.7 Experiment Validation

In order to validate the proposed machine model, various tests are performed on a prototype 36-slot 6-pole IPM machine. No-load back-EMF test at different temperatures are performed to calibrate the remanence and the remanence temperature coefficient of the permanent magnets for the construction of the proposed model. Thereafter load tests are undertaken to verify the electro-thermally coupled model. Figure 4.23 shows the test rig, including the prototype machine, dynamometer and the cooling fan to condition the thermal environment of the experiments. The machine was designed with air cooling condition. With the experiments at the rated torque and base speed, the air flow rate to reproduce the rate during driving conditions is given to simulate the reality and for operation safety, although the addition of cooling fan make the thermal validation more difficult.

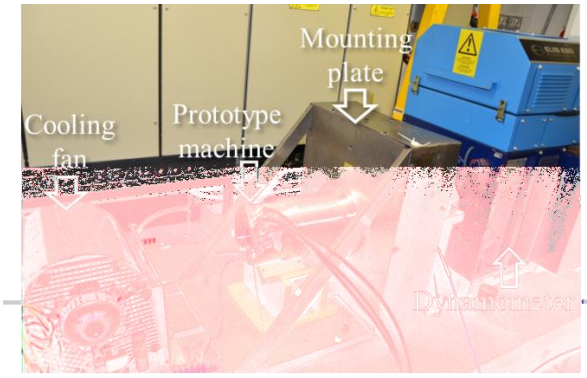

Figure 4.23. Prototype machine test rig

4.7.1 No-load back-EMF test

The no-load back-EMF test is carried out. A calibration coefficient onto the remanence of the magnets in FE models is obtained by matching the open-circuit fundamental back-EMF amplitude with the test result. Figure 4.24 compares the measured and predicted back-EMF at the room temperature measured as 20 °C, following a calibration process in the 2-D FE model. As can be seen, a good agreement between the prediction and measurement is achieved. The proposed electro-thermally coupled machine model is built based on the calibrated 2-D FE model.

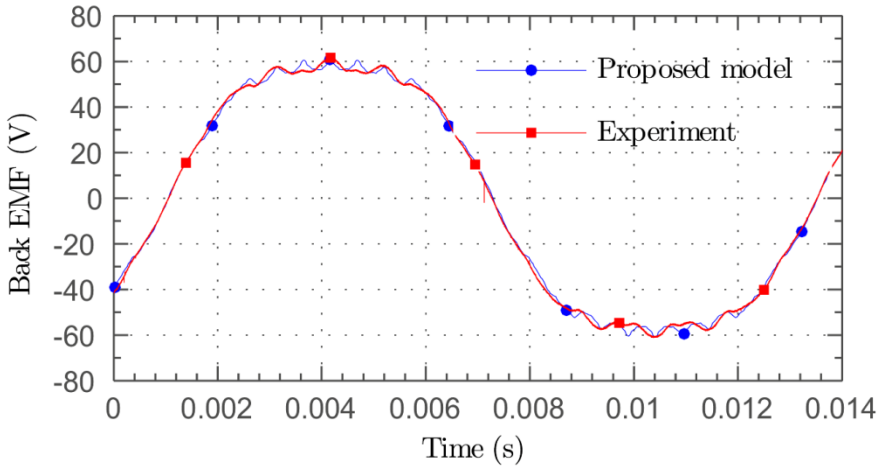

Figure 4.24. Back EMF (open-circuit) at 1600 rpm, 20^{o}C

4.7.2 Temperature coefficient test at thermal steady states

The remanence temperature coefficient α of permanent magnets in (4.7) is measured by experiments. The prototype machine is placed in an environmental chamber in which the temperature is set at 20°C and thereafter 70°C, each time lasting for 3 hours until the machine reaches thermal equilibrium. The machine is driven at a given speed when the back-EMF is tested at 20°C and 70°C respectively. The back-EMF coefficient is 0.381 V.s/rad at 20°C and 0.371 V.s/rad at 70°C. The resultant magnet temperature coefficient is -0.056%/°C. Its value is much lower than the value -0.12%/°C given by the datasheet, It is reasonable because the datasheet value is the worst case value the magnet manufacturer aim to guarantee.

4.7.3 Load test in generator mode

In the load test, without introducing uncertainties from inverter and controller, the prototype machine is operated in the generator mode with a three-phase resistive load while driven by the dynamometer at a constant speed.

With the load resistance set at 0.71 Ω and driven by the dynamometer at the base speed 1350 rpm, the machine runs through a thermal transient, starting from the room temperature 20^{o}C until it reaches a thermal steady state. The whole process lasts for more than 5 hours during which the air-flow measured a wind gauge is 8.65 m/s. The measured winding average temperature in steady-state is 65.5^{o}C. The measured air flow rate is used in the Motor-CAD to generate the state space thermal model.

The temperatures of three phase windings are measured with the thermocouples. Figure 4.25 shows the measured and predicted transient temperatures. It is seen that phase B and C have very similar temperature curves, and the predicted winding temperature matches reasonably well the measurements in phases B and C. The temperature in phase A is clearly different, which may be caused by the uneven air flow distribution and/or dislocated thermocouple in phase A not in good contact with the winding.

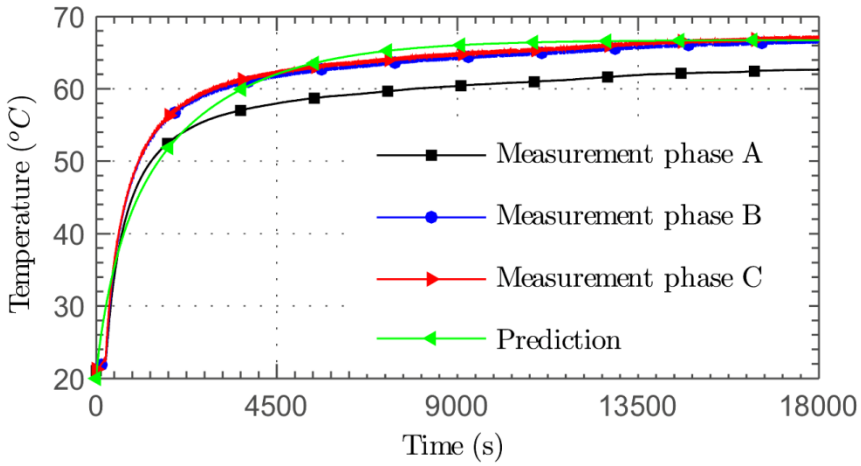

Figure 4.25. Predicted and measured winding temperature transient during the load test.

When the machine reaches the thermal steady state, the phase current and voltage waveforms and average current and voltages are obtained respectively. Although a difference of Phase A temperature exist, the current and voltage waveforms of three phases are still balanced as it is reasonable that the magnet temperature should be even among the poles without being affected by the uneven cooling. Figure 4.26 compares

the measured and predicted voltage and current of one phase The measured and predicted fundamental phase voltage and current, the torque and the winding steady-state temperatures are compared in Table 4.3 together with the relative errors between the predictions and measurements. It can be seen that the proposed model gives results that agree well with the measurements with the errors below 5%.

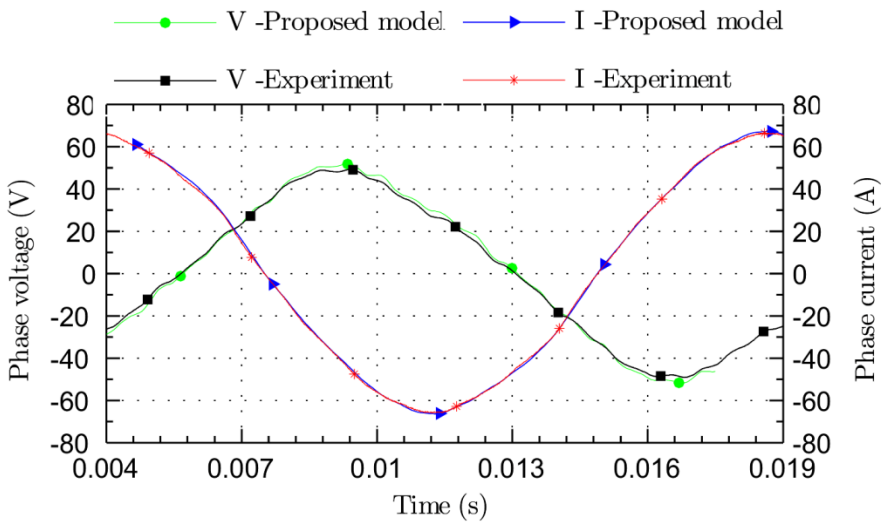

Figure 4.26. Phase voltage and phase current from prediction and measurement at the thermal steady state

Table 4.3 Measured and Predicted Machine Performances at Thermal Steady-State with 0.71Ohm Load at 1350 rpm

	Measurement	Simulation	Error
Steady-state winding temp. (^{o}C)	65.5	66.7	1.8%
Fundamental phase voltage (V)	46.2	47.4	2.5%
Fundamental phase current (A)	65.1	65.4	0.5%
Average torque (Nm)	-35.5	-36.3	2.6%

4.8 Conclusions

A high fidelity, computationally efficient model for IPM machines with due account of temperature effect has been established. The temperature dependency of flux linkages due to magnet remanence variation with temperature is quantified by employing an equivalent *d*-axis current offset. The temperature dependent model is combined with a state-space lumped parameter thermal model to form an electro-thermally coupled

model. The developed model facilitates more accurate assessments of the electromagnetic and thermal performance of IPM machines.

Simulation studies have shown that the temperatures of the windings and magnets may be underestimated by 10-20^{o}C if the temperature effect on the machine is neglected or if only the temperature effect on the winding resistance is considered. It is therefore essential to use electro-thermally coupled model for designs and for performance predictions in order to minimize the risk of partial demagnetization and reduced lifetime due to underestimation of winding temperatures. The developed model has been validated by measurements on the prototype IPM machine.

CHAPTER 5 Design, prototype and experiments of an IPM for light-duty EV traction

As a case of study, this chapter formulates a design process of permanent magnet machine for a light-duty electric vehicle traction system to exploit the benefits of advanced modeling techniques. A computationally-efficient optimisation technique for EV traction machine design is developed. With the aid of the machine analytical models presented in the previous chapters, a wide range of PM machine topologies are assessed and optimised for the application in the EV traction system. Finally an IPM machine with 18 slots and 8 poles is selected and optimised in terms of electromagnetic performance under thermal and mechanical constraints. In addition, the performance of a second machine employing the same design but with new dysprosium-reduced magnets is assessed in order to reduce the reliance on the rare-earth element. The prototypes for the two machines are built and tested for their torque capability, energy efficiencies and thermal behaviours. The test results show a good agreement with the predictions, validating high accuracy of the analytical models.

5.1 EV traction system and traction machine requirements

The traction machines described in this section are designed and developed for the distributed power train of a micro-size electric vehicle, as shown in Figure 6.6 with three independent drives. The front axle is driven by the front motor through the mechanical transmission with gear ratio of 4. Two identical machines with different design from the front motor are connected to the two rear wheel drive shafts by two separate transmissions with gear ratio of 7. The power split ratios among the three machines are designed as 40% : 30% : 30% .

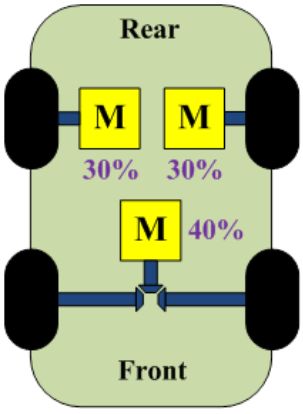

Figure 5.1. Three-motor traction system

Table 5.1 lists relevant physical parameters of the studied vehicle. The NEDC cycle is employed as a reference cycle to define the traction machines' torque-speed

specifications. Figure 5.2 shows the torque speed envelopes and trajectory of the front motor over the NEDC. Table 5.2 and Table 5.3 list the derived machine design specifications and constraints for the front motor and the rear motor respectively.

Table 5.1. Vehicle Data

Parameter (Unit)	Value
Tyre size	165/50 R15
Radius of wheels (m)	0.273
Vehicle mass (kg)	800
Gravitational acceleration (m/s^2)	9.807
Rolling resistance	0.007
Product of drag coefficient and front area (m^2)	0.35
Air density (kg/m^3)	1.25
Efficiency of differential	0.980

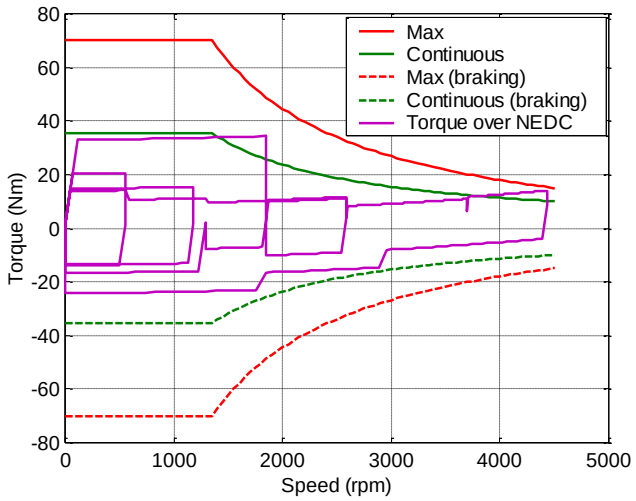

Figure 5.2 Torque speed envelope and trajectory over NEDC

Table 5.2 Front Motor design specifications and constraints

Base speed	1350 rpm
Maximum cruise speed	4500 rpm

Maximum speed	5050 rpm
Peak torque below and at base speed	70 Nm
Continuous(rated) torque below and at base speed	35.5 Nm
Peak Power	9.9 kW
Continuous Power	5 kW
Peak Power at maximum cruise speed	7 kW
Continuous Power at maximum cruise speed	4.7 kW
Maximum current limit	170 A
Nominal DC link Voltage	120 V
Peak line-to-line voltage at maximum speed	<240 V
Stator outer diameter	150 mm
Stack length	118 mm
Cooling	Air -cooled

Table 5.3 Rear motor design specifications and constraints

Base speed	2100 rpm
Maximum speed	8200 rpm
Peak torque below and at base speed	30.0 Nm
Continuous(rated) torque below and at base speed	17.0 Nm
Peak Power	6.6 kW
Continuous Power	3.75 kW
Peak Power at maximum cruise speed	6.35 kW
Continuous Power at maximum cruise speed	3.53 kW
Maximum current limit	120 A
Nominal DC link Voltage	120 V
Peak line-to-line voltage at maximum speed	<240 V
Stator outer diameter	120 mm
Stack length	105 mm
Cooling	Air -cooled

As can be seen, for the front motor, the continuous and peak power ratings are 5 kW, and 9.9 kW, respectively; for the rear motor, the continuous and peak power ratings are 3.75 kW and 6.6 kW respectively. Due to the different gear ratios for the front and the rear motor, the rear motor maximum speed is ~2 times as the front one. Therefore, reduction of iron loss at high speed would be important for the rear motor topology selection and design optimisation. Because that the front motor is required to exert relatively more torque, and that the rear motors are required to run at high speed, the torque capability at low-middle speed and the performance at high speed of the candidate PM machine topologies will be investigated in the following section for a topology selection guideline. For ease of mechanical integration, stator outer diameter, shaft radius and stack length are kept constant in the design process. Likewise, current and voltage limits should be imposed together with thermal constraints during the design process.

5.2 Quantitative comparisons on PM machine topologies for light-duty EV traction

As illustrated in the Chapter of introduction, Permanent Magnet (PM machines) Machines have greater advantages than other competing machine technologies, in terms of efficiency and torque density, especially in EV traction applications with relatively small power ratings. State-of-art techniques targeting fault tolerance and reliability of PM machines could be applied to address safety issues. Thus, applications of PM machine in EV traction systems will be the main focus of this study. On the other hand, to reduce losses in high speeds, synchronous reluctance machine (SynRM) or PM-assisted SynRM, might also be a very competitive candidate in the distributed power train studied in the thesis, particularly when the different characteristics of the front and rear motors can be exploited to minimise the total loss. In order to obtain quantitative information for machine topology selection and optimisation, preliminary designs of SPM, IPM, SynRM, PMa-SynRM and Variable-Flux PM Flux Switching Machine, with different winding and pole pair configurations, are carried out against the EV power train specifications shown in Table 5.2. The main comparison will focus on the machines' torque capabilities and energy efficiencies over driving cycles. The geometry designs employing these topologies underwent initial optimisations before their performances are compared. The optimisation method will be illustrated in the next section.

5.2.1 Fractional-slot SPM machines

Fractional-slot winding configuration has shown its significant advantages over conventional distributed winding in SPM design, in terms of resistance reduction and high torque capability, which are particularly attractive for automotive applications. This winding configuration is not suitable for IPM design since not much reluctance torque can be gained while the rotor iron loss will be significantly higher due to the presence of high order space harmonics [105][114]. Although SPM machines are known for relatively high back EMF and low field weakening capability at high speed, considering that the studied EV traction application only requires low and middle speed operations (up to 4500 rpm) and pursue high torque and efficiency performances, and that the fractional-slot SPM machines have high torque capability, the fractional-slot SPM machines are still investigated as machine candidates. An SPM with typical fractional-slot 12-slot 14-pole winding configuration is designed and optimised against 6 parameters illustrated in Figure 5.3. Since only middle speeds are required, the 14-pole rotor design is a good choice as it brings a relatively thinner back iron compared with 8-pole or 10-pole rotors. Table 5.4 (a) and (b) shows the optimised parameters and performances of the 12-slot 14-pole SPM. Due to short end winding, the SPM design has high torque density and higher efficiency at the rated torque point, peak torque point and over NEDC. The following machine topologies under comparison will be examined taking the performance of the 12-slot 14-pole SPM as reference.

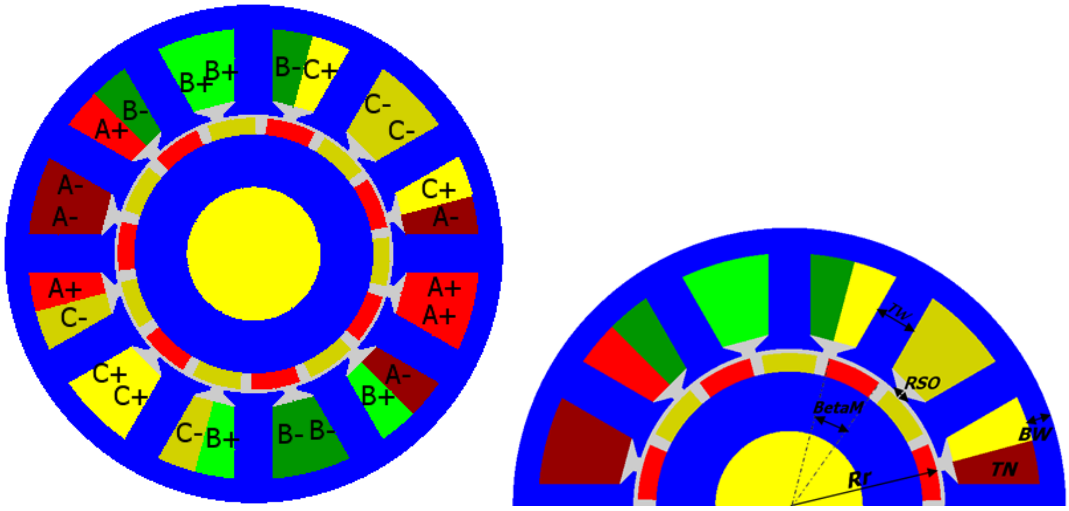

(a) (b)

Figure 5.3. (a). Optimised geometry of 12-slot 14-pole SPM; (b). six parameters optimised in the optimisation process for the SPM machine

Table 5.4 (a). Parameters optimised for the 12-slot 14-pole SPM

TW	Tooth width	10.88 mm
BW	Back iron width	6.52 mm
RSO	Slot opening width	2.12 mm
TN	Number of turns per coil	8
Air gap	Air gap thickness	1.0 mm
BetaM	Angle span of magnets	132.6 degree
Rr	Rotor radius	38.0 mm

(b). Performances of 12-slot 14-pole SPM

Current at rated torque (35 Nm)	78.9 A
Efficiency at rated torque (35 Nm)	95.2%
Current at peak torque (70 Nm)	163.0 A
Efficiency at peak torque (70 Nm)	91.3%
Efficiency for NEDC	94.4%

5.2.2 Variable-Flux PM Flux Switching Machine

Suitability of variable–flux PM flux switching machine (PMFSM) for EV tractions is assessed. By way of example, Figure 5.4 and Figure 5.5 show the geometries and magnetic field distributions of variable-flux PMFSM with three different slot-pole combinations [111]-[113].

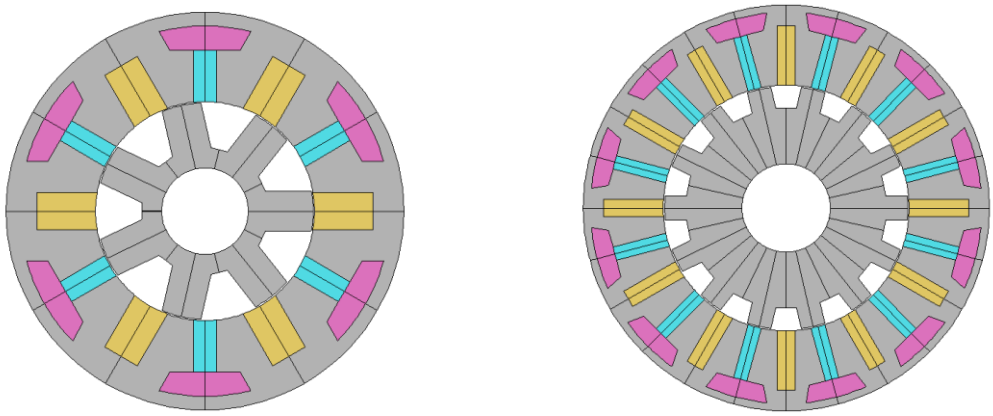

(a) (b)

Figure 5.4. Geometries of (a) 6-slot 7-pole PMFSM and (b) 12-slot 14-pole PMFSM

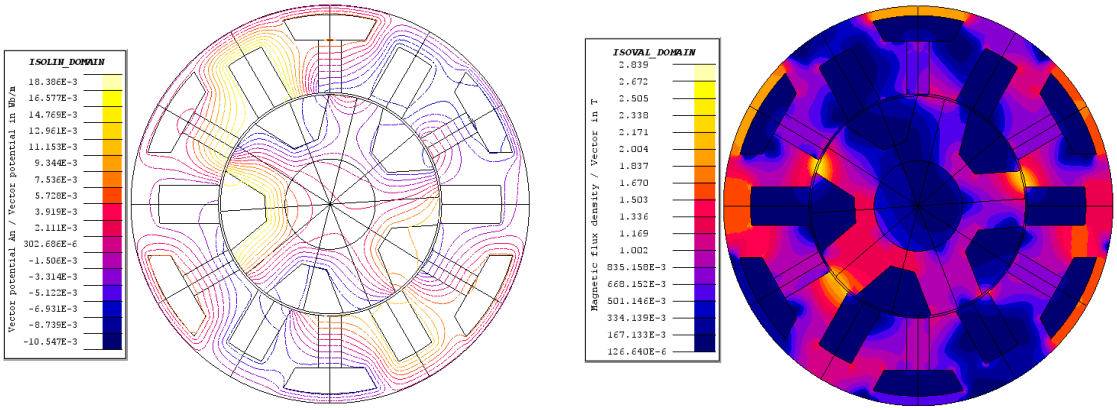

(a) (b)

Figure 5.5. (a) Flux lines and (b) flux density contour of 6-slot 5-pole PMFSM

Variable-flux permanent magnet flux switching machine (PMFSM) is a variant of flux switching PM machine. For the purpose of easily modifying flux linkage and increasing torque production, a DC excitation winding is added in the stator. The armature winding

flux can be increase or weakened to increase the torque capability at low speeds or to extend constant power operation at high speeds. However, the DC excitation coils, armature windings and magnets compete against each other for space in the stator, resulting in high level of saturation in the stator core and hence restricting peak power capability. Moreover, due to high operating frequency, rotor iron loss for this kind of machines is clearly higher than that of SPM and IPM counterparts. Consequently, the efficiency at both high torque region and high speed region become much poor. Both machines are optimised against their leading design parameters shown in Figure 5.4 and their performances are compared with the SPM in Table 5.5. It can be seen that the efficiency over the NEDC of both the variable-flux PMSFM is much lower than that of the SPM candidate. Another fact has also been observed that the torque ripple of the variable-flux PMFSM is higher than the typically acceptable level of 5%, and measures should be employed to address this problem.

Table 5.5 Performance comparison of PMFSM

Machine topology	12-slot 14-pole SPM	6-slot 7-pole PMFSM	12-slot 14-pole PMFSM
Air gap	1.0 mm	0.5 mm	0.5 mm
Current at rated torque (35 Nm)	78.9 A	90.5 A	93.6 A
DC Current at rated torque	-	0	0
Efficiency at rated torque (35 Nm)	95.2%	92.4%	94.4%
Current at peak torque (70 Nm)	163.0 A	181.7 A	89.1 A
DC Current at peak torque	-	115 A	111 A
Efficiency at peak torque (70 Nm)	91.3%	78.4%	80.3%
Efficiency for NEDC	94.4%	93.5%	92.3%

5.2.3 SynRM and PM-assisted SynRM

A 36-slot, 6-pole SynRM and a 36-slot, 4-pole PM-assisted SynRM, both with distributed windings, are designed and optimised against the leading design parameters, as shown in Figure 5.6. The torque production of the former is purely and that of the latter is mainly relies on good reluctance characteristics. Ferrite magnets are embedded into the rotor of PMa-SynRM just as an additional flux source to improve the efficiency. Therefore, as can be observed in Table 5.6, both the machines exhibit good efficiency in the low-torque high-speed region and over the NEDC, but relatively low efficiency in

the high torque region because of their higher phase resistances and higher current. Considering their lower cost (without rare earth magnets), the machine topologies may be suitable as a complementary part of the distributed power train for high speed operations.

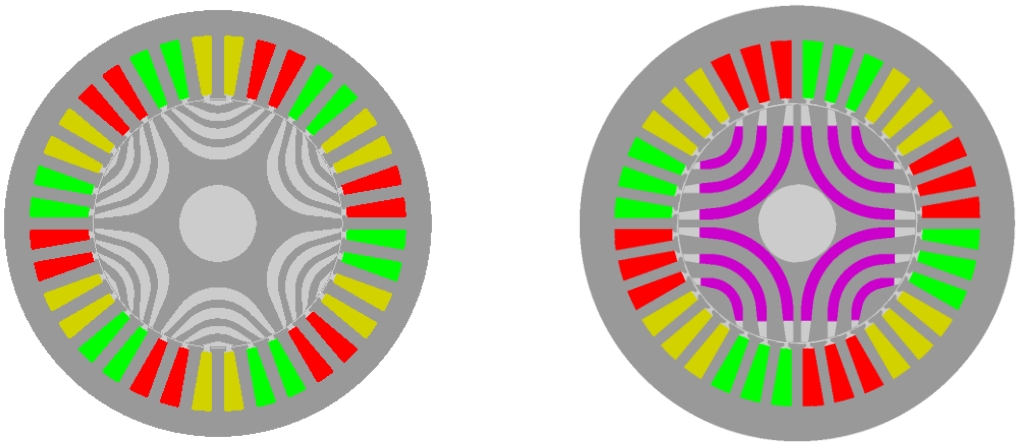

(a) (b)

Figure 5.6. Geometries of (a) 36-slot 6-pole SynRM and (b) 36-slot 4-pole PMa-SynRM

Table 5.6 Performance comparison of the SynRM and PMa-SynRM

Machine topology	12s 14p SPM	36s 6p SynRM	36s 4p PMa-SynRM
Air gap	1.0 mm	0.5 mm	0.5 mm
Current at rated torque (35 Nm)	78.9 A	56.0 A	86.2 A
Efficiency at rated torque (35 Nm)	95.2%	91.1%	90.7%
Current at peak torque (70 Nm)	163.0 A	120.0 A	172 A
Efficiency at peak torque (70 Nm)	91.3%	83.9%	84.0%
Efficiency for NEDC	94.4%	93.4%	92.8%

5.2.4 Selection of suitable machine topologies

The performances of the studied candidate machine designs are summarised in Table 5.7. Specifically, the low-speed performances which are determined by the torque capabilities of the candidates are reflected by their energy efficiencies at the rated torque or peak torque, and base speed operations; the middle-high speed performances which are determined by the field weakeaning capability and iron loss of the candidates

are reflected by their energy efficiencies over the NEDC driving cycle, since the NEDC requires machine's energy mostly consumed at middle-high speed operations.

It is found that on the power level and the speed range for light-duty EV machines, SPM with fractional slots shows well-balanced performances both for the torque production at low speed and field weakening during the NEDC. As regards PMFSM, it has fairly good torque capability around the rated torque operation and good field weakening capability during the NED, the high saturation at high torque operations, and the high iron loss in the stator and the rotor at high speed operations lead to low efficiency at peak torque as well as over the NEDC. This prevents them in such traction applications as the light-duty vehicles. SynRM and PMa-SynRM show relatively high efficiency over the NEDC due to the low iron loss at high speed, although their efficiency at rated torque are relatively low compared with the SPM and the PMFSMs.

In the respect of cost, while the NdFeB magnet cost could be more than half of the total machine cost, the NdFeB magnet usages of the machines are the qualitative cost indicators. The SPM machines and the two PMFSMs have used similar amount NdFeB magnets, thus their cost would be close to one another; the PMa-SynRM has used only ferrite magnets, and the SynRM doesn't have magnets, thus the machines' cost would be much lower.

It can be seen that the number of pole pairs and the frequency of the machines quite differ from one another, therefore beside the influence of the frequency on the iron loss which has been accounted in the performance calculation, the copper loss component associated with frequency need also be checked. Among the candidate machines, the 12-slot 14-pole PMFSM has the highest frequency 1050 Hz at the maximum speed 4500 rpm. According to the skin depth equation, the skin depth of the wires at 1050Hz is 1.55mm which is ~3 times of the wire diameter. It follows that for the candidate machines, the copper loss would only be marginally affected by the different pole pairs.

In the summary, further study will focus on exploration of SPM or IPM topologies as the main traction machine in the vehicle with improved fractional-slot configurations. SynRM and PMa-SynRM are competitive candidates as part of the traction system for their quite low cost and good efficiency at high speed.

Table 5.7 Performance comparison of machine topologies

Machine topology	12s 14p SPM	6s 7p PMFSM	12s 14p PMFSM	36s 6p SynRM	36s 4p PMa-SynRM
Air gap (mm)	1.0	0.5	0.5	0.5	0.5
Rated Current (A)	78.9	90.5	93.6	56.0	86.2 A
Rated Efficiency (%)	95.2	92.4	94.4	91.9	90.7%
Peak Current (A)	163.0	181.7	89.1	120.0	172 A
Peak Efficiency (%)	91.3	78.4	80.3	83.9	84.0%
NEDC Efficiency (%)	94.4	93.5	92.3	93.4	92.8%

5.3 Low-harmonic-content fractional slot winding configurations

Compared with distributed winding configurations, fractional-slot windings provide permanent magnet machines with many benefits, such as reduced resistance and volume, high winding factor and inductance for field weakening, low cogging torque and easy manufacturing. However fractional slots brought about high space harmonic content in the air-gap magnetic field. This leads to increased iron loss and eddy current loss in the magnets, higher risk of demagnetisation, and also causes noise and vibration problems. With the fractional slots and high harmonic contents, the benefit of reluctance torque in IPMs also diminishes as the saliency ratio is greatly reduced.

A new low-harmonic-content fractional-slot winding configuration with 18 slots and 8 poles or 10 poles is proposed and studied [78][114] recently. As seen in Figure 5.7 for the 18-slot 8-pole winding configuration, the new windings employ two identical sets of three-phase windings whose positions are shifted by 9 slots, the odd (or even for 18-slot 10-pole) order of space harmonics are removed thus the total harmonic contents are greatly reduced. It should be noted that each of the 18-slot 8-pole coil end windings only overlaps one of the other coil sides. Therefore the negative influence of its relatively longer end winding on copper loss and on manufacturing processes are not significantly increased compared with conventional fractional slot winding configurations.

Since the 12-slot 14-pole winding is the convectional fractional winding configuration and its good performance investigated in the previous section has shown it is suitable candidate for the studied EV application, the benefits of 18-slot 8-pole windings are assessed against the 12-slot 14-pole winding in this section. Although the 12-slot 8-pole

winding configuration also has less harmonic content compared with the 12-slot 14-pole, it is not selected as the EV traction machine due to its problem of high cogging torque.

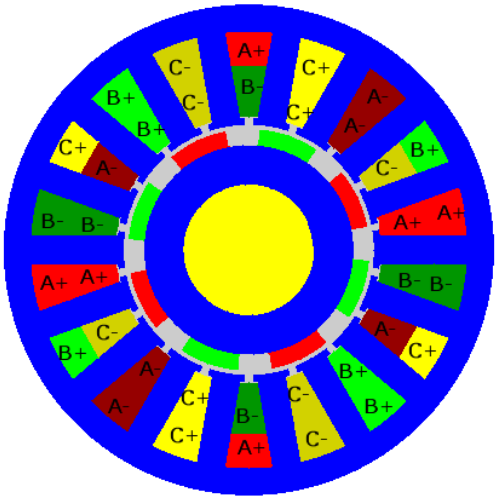

Figure 5.7. 18-slot 8-pole winding configuration

5.3.1 Eddy current loss evaluation for 18-slot 8-pole SPM

5.3.1.1 Harmonic analysis

To illustrate the merits of the new 18-slot 8-pole fractional slot PM machine topology, the SPM design variant shown in Figure 5.7 is designed and optimised against the EV traction machine specifications. The eddy current loss in the rotor magnets of the machine is assessed and compared with that of the 12-slot 14-pole SPM described in the previous section.

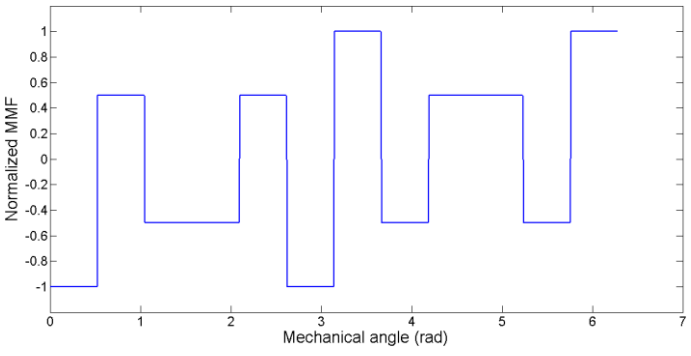

Figure 5.8. MMF waveform of 12-slot 14-pole winding

Figure 5.9 and Figure 5.11 show the MMF distribution and its harmonic spectrum of the 18-slot 8-pole SPM, respectively. Figure 5.8 and Figure 5.10 shows the MMF distribution and its spectrum of the 12-slot 14-pole SPM. The harmonic amplitudes

shown in the figures are normalised against their fundamental component respectively. It is seen that the spectrum of the 18-slot 8-pole SPM has much less harmonics.

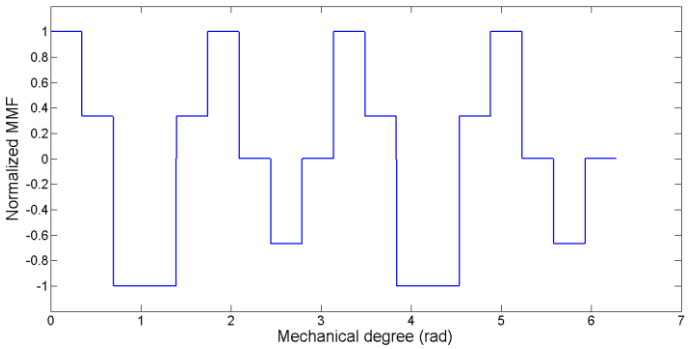

Figure 5.9. MMF waveform of 18-slot 8-pole winding

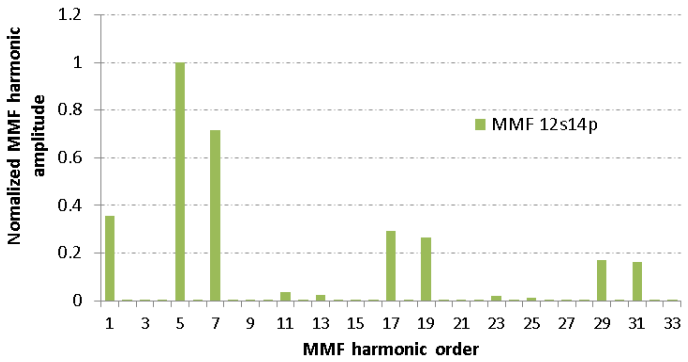

Figure 5.10. Normalize harmonic distribution of 12-slot, 14-pole PM machine

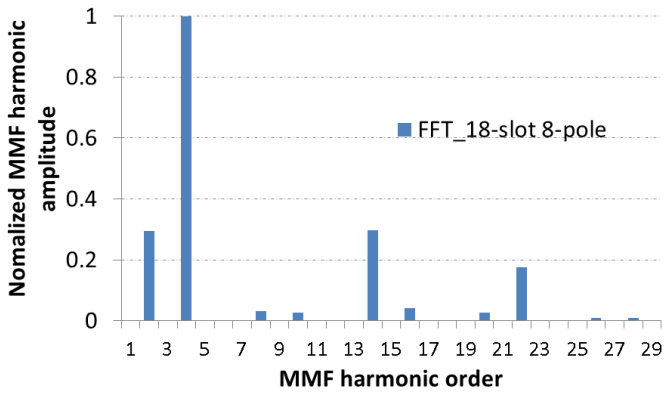

Figure 5.11. Normalize harmonic distribution of 18-slot, 8-pole PM machine

5.3.1.2 Eddy current loss comparison

Using the method illustrated in Chapter 3, the 3-dimensional eddy current losses within magnets are calculated for the 12-slot, 14-pole SPM and 18-slot, 8-pole SPM respectively.

Figure 5.12 shows the eddy current loss waveforms of the two machines in one electrical cycle at the maximum speed and with the rated current of 85 A. Figure 5.13 (a) and (b) shows the loss time harmonics of the two SPMs, respectively. The major loss component of 12-slot 14-pole is the 12^{th} which is created by the 5^{th} MMF and 19^{th} harmonics. The major loss component of 18-slot 8-pole is the 18^{th} which is created by the 14^{th} MMF harmonic and the 22th MMF harmonic.

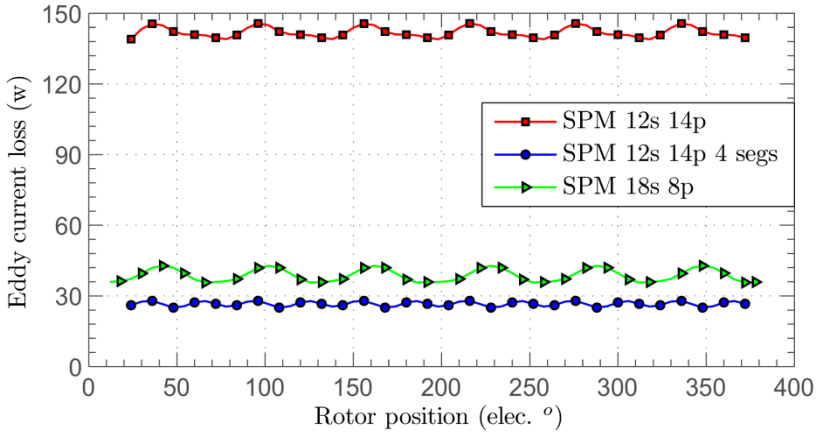

Figure 5.12. Eddy current loss for two SPM designs at maximum speed and rated currents

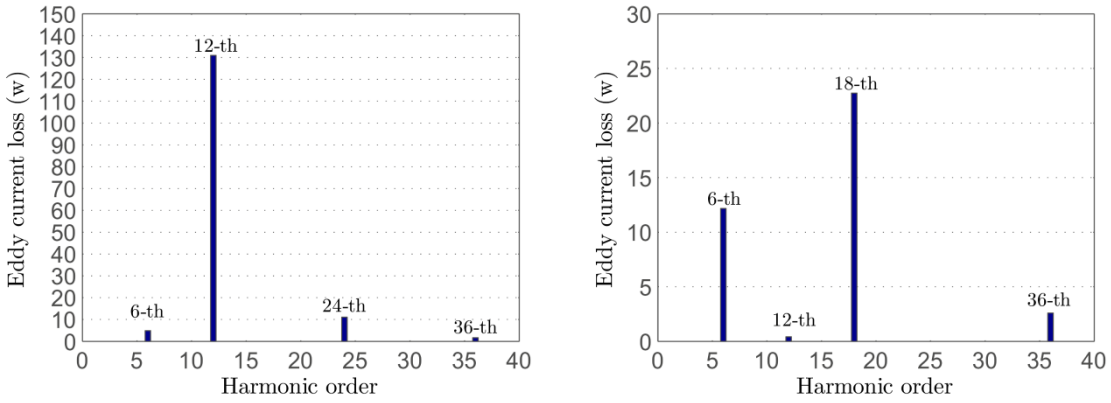

(a) 12-slot, 14-pole (b) 18-slot, 8-pole

Figure 5.13. Loss harmonics of the two SPMs at the maximum speed and rated current

It is seen that without segmentations on the magnets, the 12-slot 14-pole SPM has the average rotor eddy current loss 148 W, while the loss associated with 18-slot 8-pole is only 38 w. The reduction around 75% is gained. Even considering that the two machines have different operating frequencies and the square of frequency ratio 4/7 is applied, the loss with 18-slot 8-pole is still 42% less. Only when the magnets of the 12-slot 14-pole machine are segmented circumferentially into 4 pieces per pole, its loss can be reduced to the similar level of the 18-slot 8-pole SPM, as shown in Figure 5.12. It should be noted that the segmentation of the rotor magnets in the 12-slot, 14-pole design is necessary in order to ensure the rotor is not overheat. Segmentation of rotor magnets significantly increases production cost and also wasters more precious materials due to cutting.

5.3.2 Quantitative comparison of 18-slot, 8- or 10 -pole SPMs and IPMs

In order to compare the torque and efficiency performances of the machines with the new winding configurations, four different machine designs are optimised. They are two 18-slot SPM machines with 10 poles or 8-pole, denoted as SPM 18s 10p and SPM 18s 8p; and two 18-slot IPM machines with the same number of poles denoted as IPM 18s 10p and IPM 18s 8p. Figure 5.14 shows the geometries of the optimised designs.

By analysing the machine d- and q-inductances, it is found that the achievable saliency ratio of the IPM 18s 8p is 1.8~2.2, therefore its reluctance torque contributes 30~50% of the total torque. This is a great improvement considering the typical fractional-slot IPM with 12 slots 10 poles only has a saliency ratio of 1.2-1.4, and 5~10% reluctance torque.

Table 5.8 compares the energy losses, efficiencies and magnet usages as well as torque ripples of the four machines. The PM usage of the four machines are given as percentages with respect to the 12s 14p SPM design. It shows that two IPM machines use about 20%~30% less magnets due to the contribution of reluctance torque than the SPMs. Consequently they have ~15% less NEDC loss, thus yielding 0.5-1% higher efficiency at the rated point, and peak point and over NEDC. Comparing the two IPMs, the 18s 10p IPM exhibits relatively lower saliency ratio than 18s 8p, partially due to the lower ratio of slot number to pole number. It also has slightly higher iron loss at high speed due to its higher number of poles. As a result, its efficiency over the NEDC is 0.48% lower.

In summary, the IPM with 18 slots and 8 poles shows great improvements on torque capability and energy efficiency compared with conventional fractional-slot IPMs It also reduced magnet usage and yield competitive efficiency compared with the conventional fractional-slot SPMs. It is employed as the main traction machine in the vehicle power train. Further optimisation of the machine design and its performance assessment are carried out.

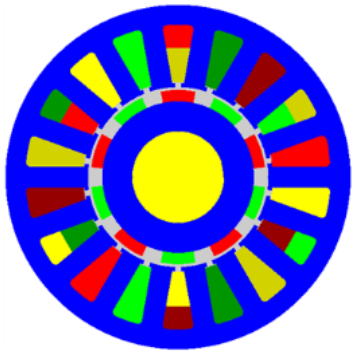

(a)

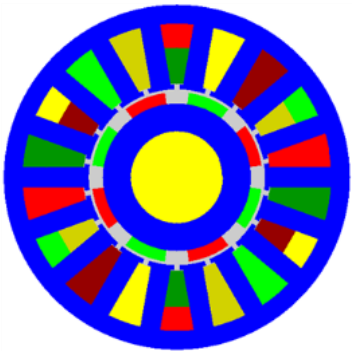

(b)

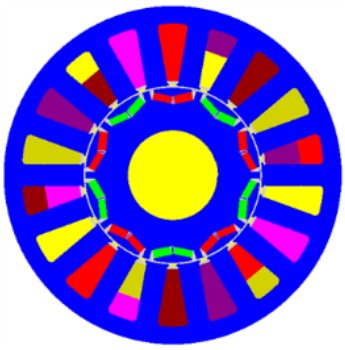

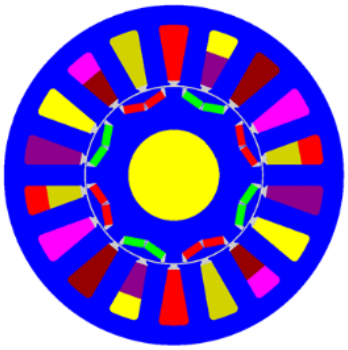

(c) (d)

Figure 5.14. Geometries of (a) SPM 18s 10p, (b) SPM 18s 8p, (c) IPM 18s 10p and (d) IPM 18s 8p

Table 5.8 Comparisons on performances of four optimised motors

	SPM 18s 10p	SPM 18s 8p	IPM 18s 10p	IPM 18s 8p
Loss $_{(NEDC)}$ (kJ)	73.92	72.62	67.09	61.33
Eff_{NEDC} (%)	93.58	93.69	94.14	94.62
Eff_{rated}, Eff_{peak} (%)	92.28, 84.30	92.05, 84.02	93.29, 86.31	92.98, 85.85
PM usage (%)	78.40	78.40	59.03	50.38
NEDC Max Current (A)	79.95	76.85	78.98	80.46

5.4 Optimisation technique for permanent magnet machines in EV traction applications

With the help of the FE-based analytical machine models, a comprehensive multi-physic optimisation technique against driving cycles for electric vehicle traction machine designs with high computational efficiency is developed. Without loss of generality, the process of the optimisation of the 18-slot 8-pole IPM is presented. Although the illustration takes the IPM machine as an example, it could also be applied to other PM machines such as SPM, PMa-SynRM or flux switching machines.

5.4.1 Optimisation strategy

5.4.1.1 Problem definition of a machine design optimisation

For a machine geometry design, it has a number of geometric parameters which can be adjusted freely within available ranges. The geometric parameters could be taken as variables $(g_1,g_2,\ldots,g_m)$ defined in the variable ranges $(G_1,G_2,\ldots,G_m)$, which can be expressed as:

$$(g_1,g_2,\ldots,g_m) \in (G_1,G_2,\ldots,G_m), \quad g_i \in G_i \tag{5.1}$$

g_i is the i-th geometric variable. m is the number of geometric variables.

For a given machine design $(g_1,g_2,\ldots,g_m)$, it exhibits performance in various aspects, such as the driving cycle efficiency, maximum winding temperature in continuous operations, torque ripple, etc. These performance indicators could be taken as a set of functions of the geometric variables as in:

$$p(g_1,g_2,\ldots,g_m),\ p=\{p_1,p_2,\ldots,p_n\} \tag{5.2}$$

p_i is the i-th performance function. n is the number of performances to be assessed.

Therefore for all the available geometery designs within the range $(G_1,G_2,\ldots,G_m)$, the variable range $(G_1,G_2,\ldots,G_m)$ are mapped to the performance function range $(P_1,P_2,\ldots,P_n)$, which can be expressed as in:

$$\begin{gathered}(G_1,G_2,\ldots,G_m) \rightarrow (P_1,P_2,\ldots,P_n) \\ (p_1,p_2,\ldots,p_n) \in (P_1,P_2,\ldots,P_n),\ \ p_i \in P_i\end{gathered} \tag{5.3}$$

In a optimisation problem, if one of the performance function e.g. p_1 is chosen as the objective function, and for the rest of the performances $(p_2,p_3,\ldots,p_n)$, design constraints values $(C_2,C_3,\ldots,C_n)$ are applied. Thus, the optimisation problem could expressed as: searching inside the variable ranges $(G_1,G_2,\ldots,G_m)$ for the optimal design $(g_1^*,g_2^*,\ldots,g_m^*)$ with the performances $(p^*=\{p_1^*,p_2^*,\ldots,p_n^*\})$ which satisfy the conditions expressed as in:

$$p_1^*=\max(P_1),\ \text{and}\ p_i^* \leq C_i\ \ (i \geq 2) \tag{5.4}$$

Multi-objectives can be similarly evaluated by introducing weighting factors or by plotting the resultant objective functions in the Pareto graphs for aid of selection.

5.4.1.2 Selection of optimisation variables and performances for EV traction PM machines

5.4.1.2.1 Selection of geometric variables

The leading geometric parameters which can significantly affect machine performances such as torque, efficiency and thermal should be optimised in the optimisation process. For a PM machine, the leading parameters include the stack length, stator diameter, rotor diameter, dimensions of tooth and back iron in the stator, dimensions of magnets as well as the turn number. Figure 5.15 shows the 18-slot 8-pole IPM topology and six geometric variables to be optimised. The stack length and stator diameter are already fixed by the design specifications. Table 5.9 lists the ranges of the six variables in the optimisation.

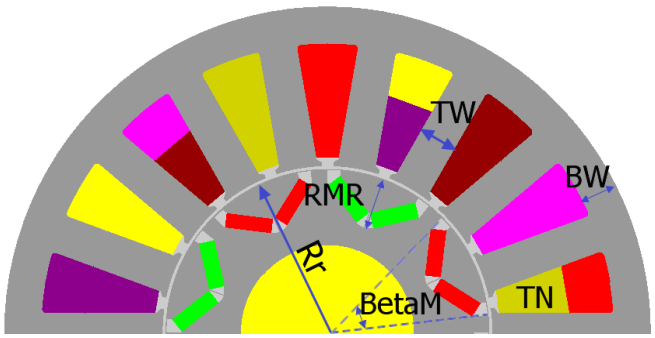

Figure 5.15. IPM geometry for optimization.

Table 5.9 Geometric variable ranges in the optimisation for 18-slot 8-pole IPM

Geometric variables	Unit	Definition	Range
Rr	mm	Rotor radius	35-45
BetaM	°	Magnet opening angle	120-175
RMR	-	Ratio of magnet depth to rotor radius	0.1-0.4
TW	mm	Stator tooth width	7-10
BW	mm	Back iron width	7-10
TN	turn	Number of turns per coil	4-6

5.4.1.3 Selection of performance to be evaluated in optimisations

In order to evaluate a PM machine in an EV application, two challenges have to be addressed. First the performances evaluation should cover multi-physics aspects over electrical, electromagnetic, thermal and mechanical domains. Secondly, unlike conventional machine designs for industrial drives, for traction machines in EV applications, performances should be evaluated when machines operate over wide torque-speed range especially through predefined driving cycles rather than evaluated only on the rated operation point.

Table 5.10 lists performances evaluated in the optimisation for EV traction machines. The multi-physics analytical models illustrated in Chapter 2, 3 and 4 are used as the performance evaluation functions $p(g_1,g_2,\ldots,g_m)$. For each operation (T_i, n_i) point, control current model $i_{dq}(T_i, n_i)$ is used to calculate the i_d, i_q to realise the MTPA or field weakening control. Then voltage, copper loss, iron loss including eddy current loss in the rotor magnets and static thermal performances are derived from the i_d, i_q inputs.

To estimate the performances in the worst thermal scenario, the temperature of magnets is applied as the design limit 150°C in the analytical models. And the design limit 120°C is used to calculate the winding resistances. The mechanical stress model is established as a function of geometric variables for V-shape IPM topology before the optimisation.

As illustrated in Chapter 2, for a given design sample $(g_1,g_2,\ldots,g_m)$, only 20 static FE calculation plus 2 time-step FE calculations are needed. Thus total time consumed in one design evaluation is just around 30 mins.

Table 5.10 Performances evaluated in the optimisation for EV traction machines

Performances	Definitions	Analytical models	Requirements
Energy efficiency over NEDC	Machine and inverter energy efficiency over NEDC driving cycle	$i_{dq}(T_i, n_i)$ $P_{cu,\,fe,\,mag}(i_d,i_q)$	To optimise
VA rating	Maximum voltage and current that occur on the peak power envelope	$i_{dq}(T_{pk}, n_{base})$ $i_{dq}(T_{pk}, n_{max})$ $V(i_d,i_q)$	≤ 120V, 170A
Maximum back-EMF	Maximum back-EMF at the maximum speed 5050 rpm	$V(i_d=0,i_q=0)$	≤ 240V
Torque ripple	Peak-peak torque ripple percentage of peak torque against the average	- (from time-step FE at T_{pk} or T_m)	≤ 5%
Demagnetisation	Magnet flux density compared against the knee point on BH curve at	- (from time-step FE at T_{pk} or T_m)	≥ 0.6 T
Winding and magnet temperatures	Winding and magnet maximum temperature over continuous operation range	$i_{dq}(T_i, n_i)$ $T_{emp}(i_d,i_q)$	≤ 120°C, 150°C
Mechanical stress	Maximum mechanical stress in rotor at 1.5 times maximum speed 5050 rpm	$S_{stress}(g_1,g_2,..g_5)$	≤ 150 MPa

* The performances are all evaluated with magnets at 150°C

For the IPM design in the study, the energy efficiency over driving cycles is taken as the only optimisation objective. The other performances are considered by applying design constraints, as shown in Table 5.10. This is because the machine efficiency will significantly affect the size and cost of the batteries.

In other optimisation scenarios, multiple optimisation objectives such as the torque ripple or the magnet usage may be used in addition to the energy efficiency. In those

cases, the Pareto front technique may be used to broaden optimum choices for trade-off studies [115][116]. Alternatively, weighting factors can be used to combine multiple objectives into a single one. In the consideration of number of k objectives p_1, p_2, ..., p_k, the combined objective p_o can be expressed as:

$$p_o = w_1 p_1 + w_2 p_2 + \ldots + w_k p_k \tag{5.5}$$

where w_1, w_2, ..., w_k are weight ratios.

Due to the importance of driving cycles in the machine design and optimisation, typical driving cycles including the Worldwide Harmonized Light Vehicles Test Procedures (WLTP), the New European Driving cycle (NEDC) and the Artemis Urban Driving Cycle (Artemis), etc. are specifically analysed in Chapter 6. The influence of different driving cycles on the machine optimisation is also investigated. According to the findings in Chapter 6, in order for balanced machine performances, the NEDC is selected as the target against which the energy efficiency is to be optimised.

5.4.1.4 Optimisation algorithm

In order to efficiently search within the available geometric variable range $(G_1, G_2, \ldots, G_m)$ for the optimum design $(g_1^*, g_2^*, \ldots, g_m^*)$, response surfaces (RS) algorithm widely applied in the machine design optimization [117][118] is employed in the optimisations. The algorithm is realized in the GOT-It software developed by Cedrat [119].

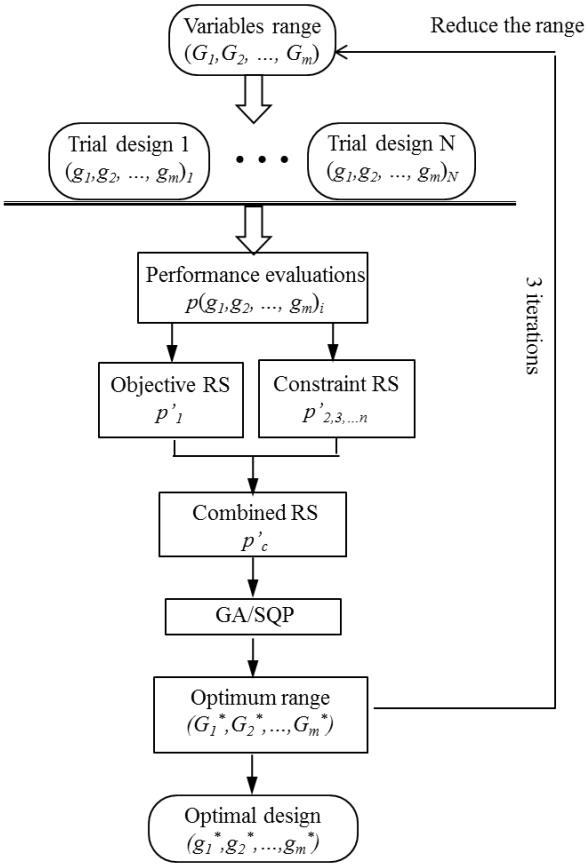

Figure 5.16 Flow chart of optimisation algorithm using Response Surface method

Figure 5.16 shows the scheme of the optimisation algorithm. First according to the initial variable range $(G_1, G_2, \ldots, G_m)$, it selects a number of trial designs $(g_1, g_2, \ldots, g_m)_i$ and evaluates their performances by using the functions $p_{1,2,..,n}(g_1, g_2, \ldots, g_m)$, where n is the number of performance evaluation functions used in the optimisation. Based on the evaluation results, the algorithm builds a polynomial RS of the objective function p'_1 and the RSs of the design constraints functions $p'_{2,3,..,n}$. Subsequently, the objective RS and the constraint RSs are combined into a single objective function p'_c as in:

$$p'_c = p'_1 + \sum_{i=2}^{n} k_i \cdot \max(0, C_i - p'_i) \quad (5.6)$$

where k_i is the penalty coefficient for the i-th constraint function if it exceeds the design limit.

By applying the Genetic Algorithm (GA) and Sequential Quadratic Program (SQP) on the combined objective function p'_c, a sub-range $(G_1^*, G_2^*, \ldots, G_m^*)$ of geometric variables which has a better value of p'_c is located. As a result, the algorithm repeats the

process using the new sub-range, and begins a new iteration of performance evaluation and range shrinking process. As the iteration goes on, the polynomial response surfaces of the objective and constraints will converge to the real optima of machine designs. Usually the process converges in 3 iterations and the optimum geometry design $(g_1^*, g_2^*, \ldots, g_m^*)$ could be searched out.

5.4.2 Optimisation platform and work flow

The optimisations are conducted on Flux&GOT-It coupled platform developed by CEDRAT. Flux is an electromagnetic FE tool providing parameterised geometry building and programmable control in Python language for FE modelling, solving and post-processing. GOT-It is an optimisation tool addressing different types of optimisation problems, such as Genetic, Sequential Quadratic Program, and Sequential Surrogate Optimizer.

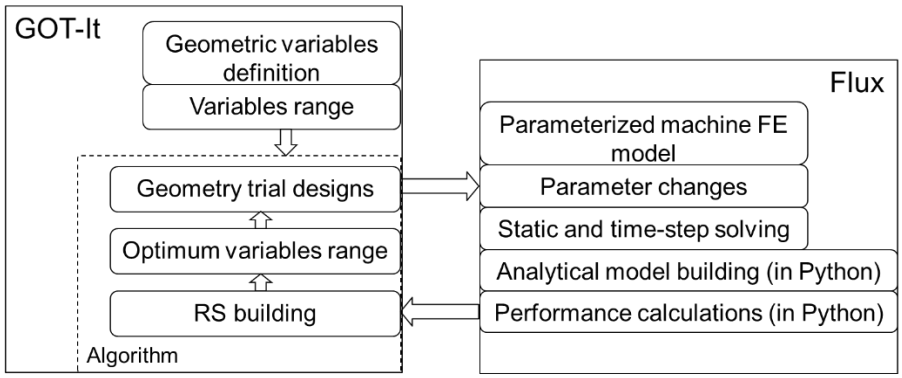

Figure 5.17 The work flow using the optimisation platform

Figure 5.17 shows the work flow using the optimisation platform. When GOT-It couples with Flux, the Flux FE model works as a server. A parameterised FE model is first built in FE ready to be called by GOT-It. In GOT-It, the geometric variables and variable ranges are defined. The algorithm chooses parameters, and sends them to Flux. Flux implements the geometry changes and runs static and time-step FE calculations. Then analytical machine multi-physics models including the EM, thermal and mechanical models are built using Python. The calculated performances are fed back to GOT-It optimisation algorithm, in which response surfaces are built and used to optimise the variable ranges. A sub-range will be selected and sent to FE for another iteration of performance evaluations.

5.4.3 Optimisation process

After 3 iterations of geometric variables optimisation, the final optimised design is achieved. Figure 5.18 shows the evolutions of the design parameters and objective in

the optimization. Figure 5.19 shows the evolutions of the constraint performances respectively of the maximum current that occurs on the peak power envelope and the torque ripple on the peak-torque point.

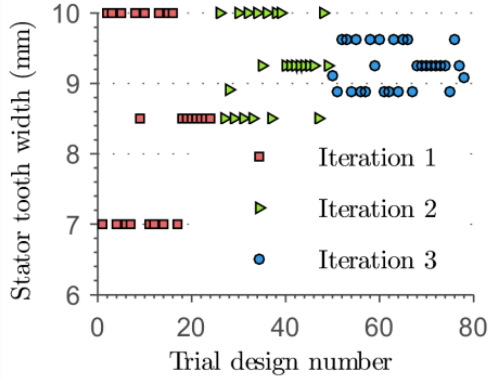

(a)

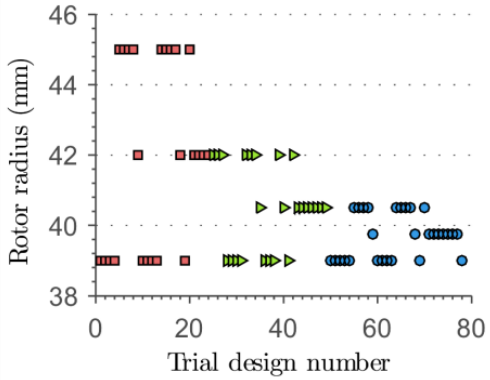

(b)

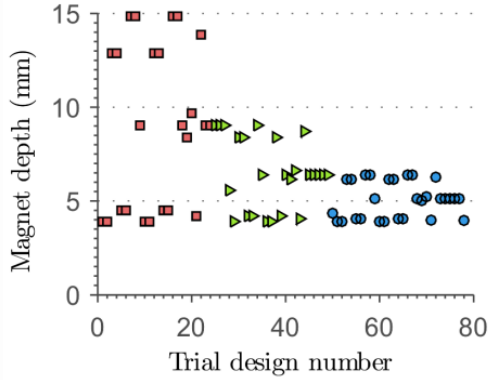

(c)

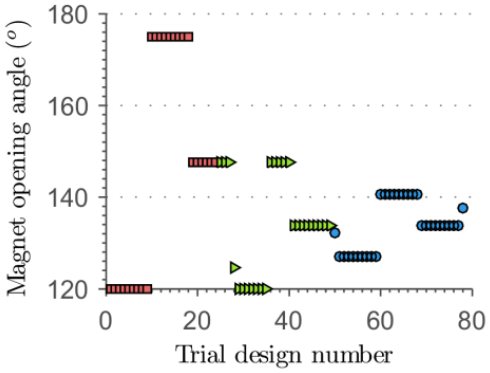

(d)

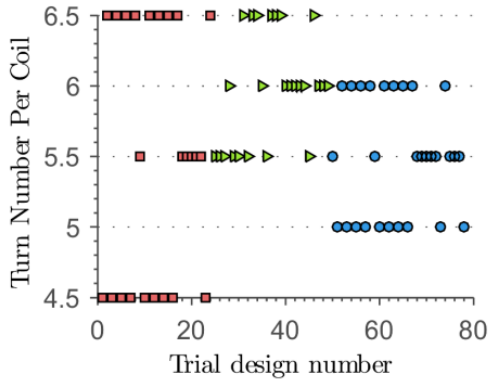

(e)

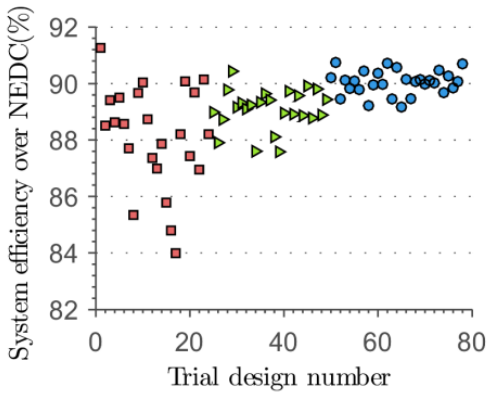

(f)

Figure 5.18 Parameter convergence during 3 iterations of optimization: (a). stator tooth width, (b). rotor radius, (c). magnet depth, (d). magnet opening angle, (e). number of turns per coil, and (f). system efficiency over NEDC.

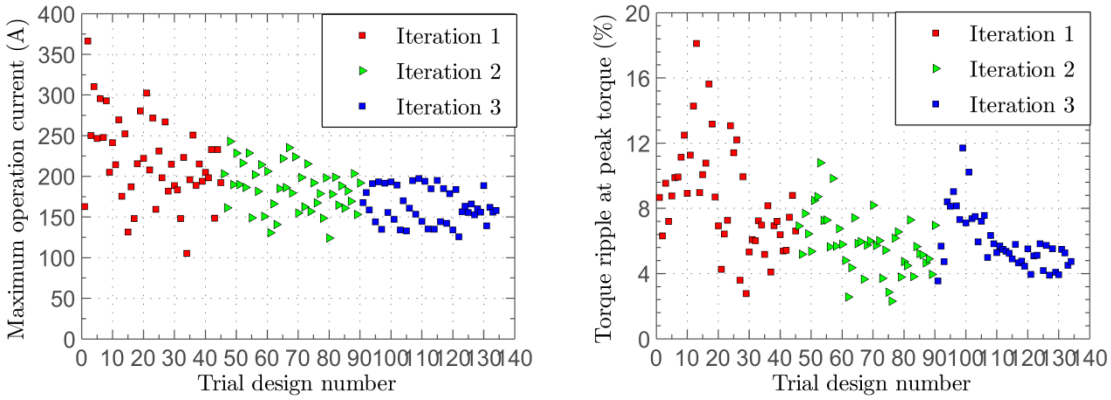

(a) (b)

Figure 5.19 Constraints convergence during 3 iterations of optimisation: (a) Maximum current on peak power envelope; (b) Torque ripple (peak-peak value against average)

The inverter-machine system efficiencies over the NEDC in the third iteration vary only within 0.5%, indicating the designs have converged to the optimum efficiency performance. And the maximum current and torque ripple are also gradually constrained below the design limits.

The optimisation process explored the geometric variables range using 85 design samples in total before searching out the optimum machine design. Each design sample takes around 30 min in the performance evaluations. The whole optimisation consumes 43 hours or less than 2 days on a person computer with typical configurations. The computation efficiency is quite high considering there are 6 parameters optimised together and multiple aspects of performances against a driving cycle are assessed in the optimisation.

5.5 Machine geometry and mechanical design

5.5.1 Machine geometry design

The final machine geometry design of the IPM after the optimisation process is shown in Figure 5.20. The geometric parameters of the stator and rotor are shown in Table 5.11. Table 5.12 lists the materials used in the motor. Non-oriented electrical steel M270-35A with the thickness of 0.35 mm and maximum loss 2.70 w/kg at 1.5 T and 50

Hz is selected for the stator and rotor laminations. The sintered Neodymium-Iron-Boron (NdFeB) N35EH is used for the magnets. Figure 5.21 gives a 3-dimensional view of the stator assembly with end windings. As it is shown in Figure 5.21, the machine has 18 coils in total. Each coil has 6 turns and each turn incorporates 21 strands of 0.75 mm diameter wire, which give a packing factor around 0.43.

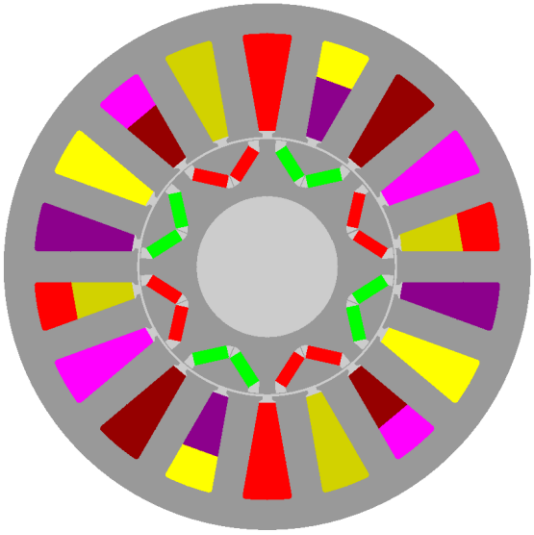

Figure 5.20 Cross-sectional picture of the optimised machine design

Table 5.11 Basic geometry parameters

	Unit			Unit	
Stator outer radius	mm	75	Stator slot number	-	18
Rotor outer radius	mm	36.45	Pole pair number	-	4
Air gap	mm	0.5	Phase number	-	3
Shaft radius	mm	20	Coil number per phase	-	6
Stack length	mm	118	Turn number per coil	-	6

Table 5.12 Materials used in the front motor

	Type	Usage
Laminations	M270-35A	9.58 kg
Magnets	N35EH	0.49 kg
Windings	Round copper wires (bare copper diameter: 0.75 mm)	3.7 kg

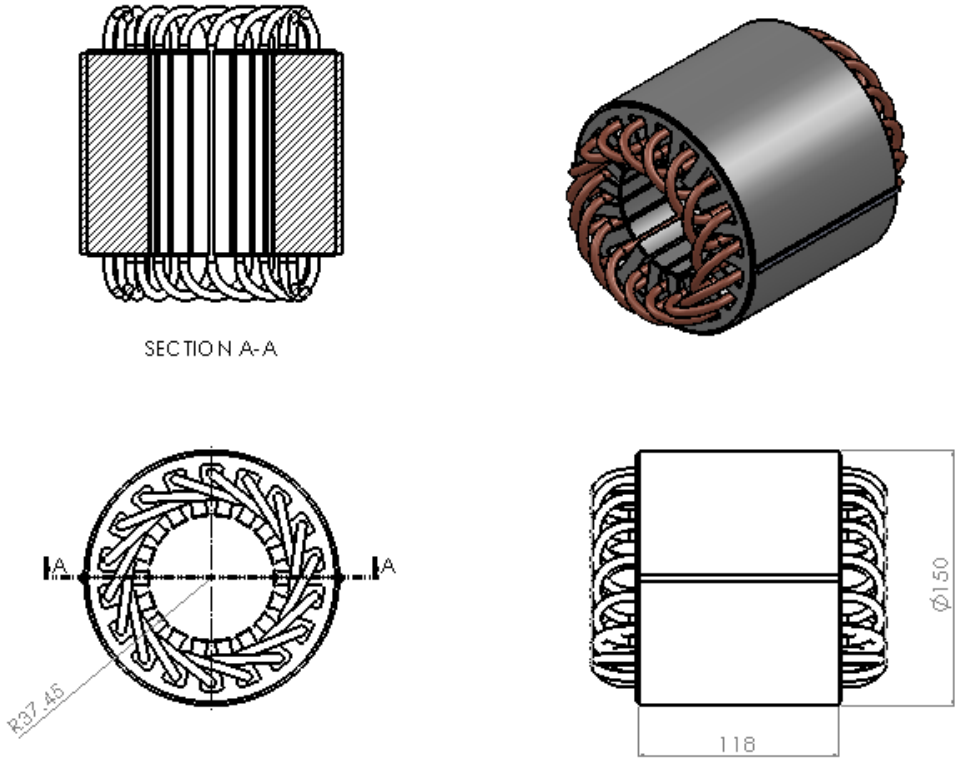

Figure 5.21. The stator assembly with view of end windings

5.5.2 Mechanical design and cooling arrangements

The mechanical design is also performed for the machine's outer enclosure, shaft and connection box for the purpose of prototype building and test in the later stage. Figure 5.22 shows the assembly of the stator, rotor, enclosure and connection box. With the machine's cooling condition set as air-cooled, by using the thermal simulation tool Motor-CAD, the enclosure is designed with 14 heat ventilation fins for the best heat dissipation capability, which increase the diameter of the machine to 190 mm. The 4 ports on the connection box are for the armature windings, speed sensor signal connector and thermal signal connectors.

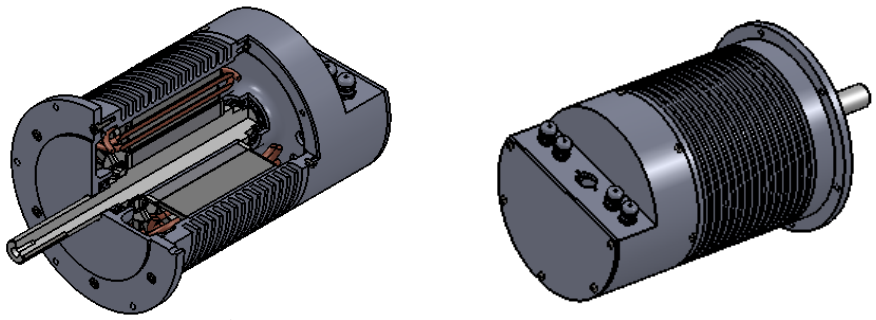

Figure 5.22. Complete machine assembly

5.6 Performance evaluation using analytical models

The electromagnetic parameters and multi-physics performances of the machine design are investigated by employing the analytical models developed in the previous chapters. The prediction results includes 1) the characteristic parameters of magnet flux linkage and *d/q*- axis inductances; 2) electromagnetic performances: VA ratings, energy efficiencies at typical continuous/peak power points and driving cycles, torque ripples, demagnetisation assessment of rotor laminations at high speed; 3) static and transient thermal behaviours, and 4) maximum mechanical stress. Correspondent experiments on a prototype machine shown in the next section validates the performance predictions of the analytical models.

It should be noted that, to consider the worst scenarios of thermal conditions, the electromagnetic parameters and performances are evaluated at the thermal design limits, in which the temperature of windings are set at 120, and the temperature of magnets are set at 150.

5.6.1 Electromagnetic parameters

Flux linkage modelling method $\psi_d(i_d,i_q)$, $\psi_q(i_d,i_q)$ described in (2.1) and (2.2) of Chapter 2 is built for the IPM machine and used to acquire classic characteristic parameters such as the *d*- and *q*- axis inductances L_d and L_q, permanent magnet flux linkage ψ_m. The derivation equations are given by (5.7). The parameter values are averaged over one electrical cycle to neglect their dependency on rotor position θ.

$$\begin{aligned} &\psi_m(i_q) = \psi_d(0, i_q) \\ &L_d(i_d, i_q) = \frac{\psi_d(i_d, i_q) - \psi_m(i_q)}{i_d}, L_q(i_d, i_q) = \frac{\psi_q(i_d, i_q)}{i_q} \end{aligned} \tag{5.7}$$

Table 5.13 lists the resistance of one phase winding R_s, *d*-axis inductance L_d and *q*-axis inductance L_q, as well as the flux linkage from the magnets ψ_m and torque constant K_A

at three typical operation points: peak-torque base-speed point, continuous-power base-speed point (or rated-torque base-speed point) and continuous-power maximum-speed point. The torque constant at the continuous-power base-speed point is 0.45 Nm/A, while it is reduced slightly to 0.42 Nm/A at the peak-torque base-speed point due to saturation in laminations. The torque constant becomes very low as 0.16 Nm/A at the continuous-power maximum speed point as field-weakening currents are used at this operation point.

Table 5.13 Basic machine parameters

	Unit	Peak torque & Base speed	Rated Torque & Base speed	Continuous power & Max speed
R_s	ohm	0.0349	0.0349	0.0349
L_d	H	4.97E-04	6.22E-04	7.34E-04
L_q	H	8.81E-04	1.25E-03	1.83E-03
$(L_d - L_q) * P$	H	1.53E-03	2.50E-03	4.39E-03
L_d/L_q	-	1.77	2.01	2.50
$\psi_m * P$	Vs	0.211	0.253	0.269
Torque constant: K_A	Nm/A	0.42	0.45	0.16

* P is the pole pair number.

Figure 5.23 and Figure 5.24 display the flux linkages and inductances as functions of *d*-axis and *q*-axis currents, respectively. Clear saturation effect on both *d*- and *q*-axis inductances caused by increase in the *q*-axis current can be observed. Besides the saturation effect due to the mutual coupling between *d*- and *q*- axis can also be perceived.

Particular attention should be paid to the saliency ratio L_d/L_q. From Figure 5.24 (c) ratio varies within 1.8~2.3 in a large current loading region. Especially in the slight saturated or unsaturated situations such as at the rated-torque base-speed point and continuous-power maximum-speed point, the ratio reaches 2.5. The well-maintained saliency with this IPM makes reluctance torque a significant contribution to the total torque output.

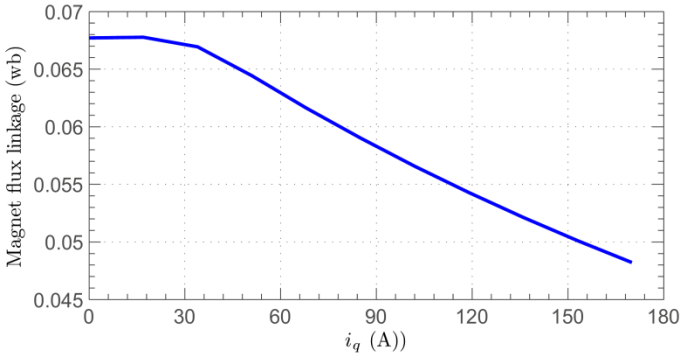

Figure 5.23 *D*-axis flux linkage variation with i_q at $i_d = 0$

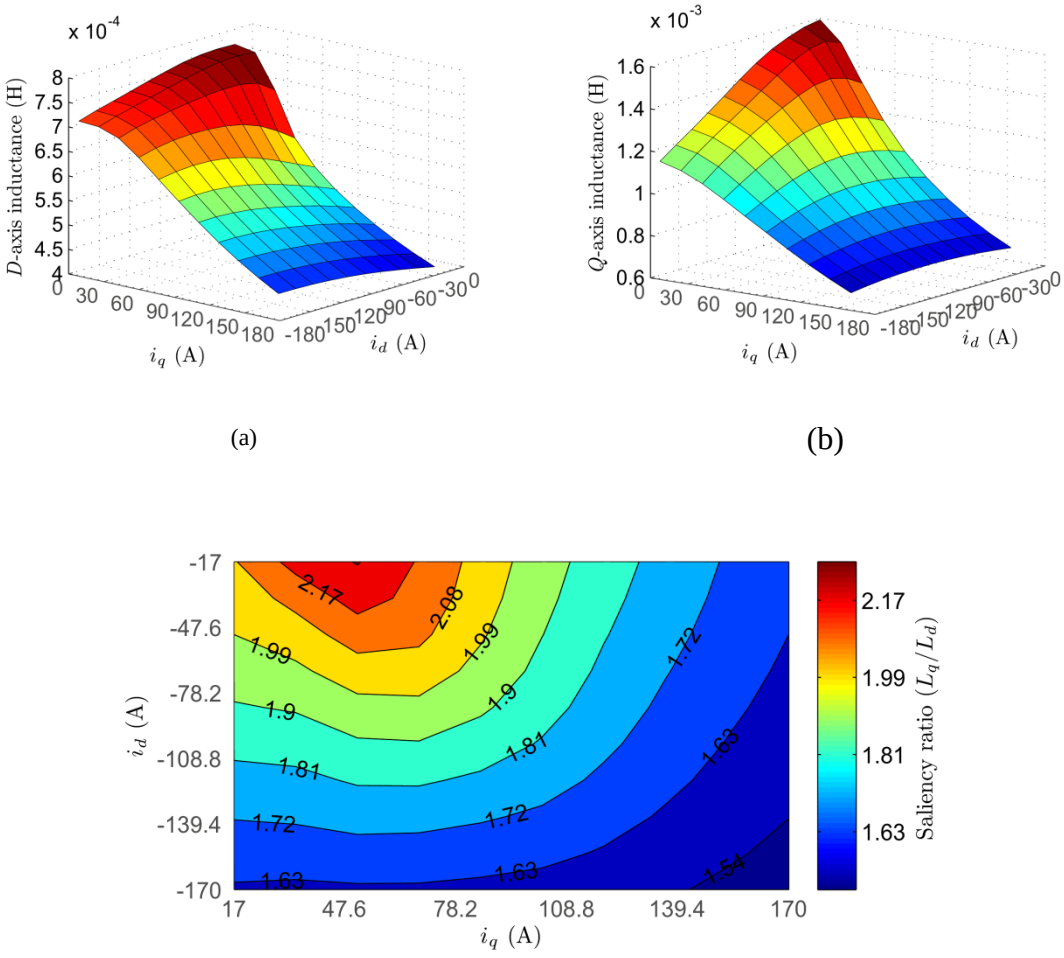

Figure 5.24 (a). *d*-axis inductance, (b). *q*-axis inductance, and (c). saliency ratio with i_d and i_q variations

5.6.2 Electromagnetic performances

5.6.2.1 Performances on typical operation points

Making use of the models illustrated in Chapter 2 for calculating flux linkage, control current, and losses for given torque-speed operation points, machine electromagnetic performances on arbitrary load points can be estimated. The converter loss is also calculated using typical converter parameters. Table 5.14 lists the machine performances on the three typical operation points. For the peak power points, the voltage limit 120 V and current limit 170 A are well satisfied. The torque ripple value shown in the table is the ratio of peak-peak value of the torque variation over one electrical cycle to the average value of the peak torque, and it is within the design limit 5% at the two continuous power operation points.

Because of a high level of saturation with the IPM design, the machine current at the peak torque and based speed is relatively higher. The machine efficiency at this operation is 87%, being relatively low due to large copper loss. However the efficiency at continuous-power maximum speed point is increased to as high as 94%. This is partly because IPM machines have high field weakening capability thus they need relatively low current to meet the voltage constraint at high speed. More importantly the designed machine benefits in high-speed torque capability from the considerable saliency ratio. The resultant reluctance torque contributes 29% of the total torque at the rated-torque base-speed point and 38% with the field-weakening currents at the continuous-power maximum-speed point.

Table 5.14 Performance at typical operation points

	Unit	Peak torque & Base speed	Rated Torque & Base speed	Continuous power & Max speed
Torque	Nm	70	35	10
Speed	rpm	1350	1350	4500
Current	A	165.89	77.30	56.80
Current density (rms)	A/mm^2	13.08	6.09	4.48
Voltage (line)	V	108.84	91.66	109.51
Mechanical output	W	9756.74	4969.79	4216.96
Copper loss	W	1439.8734	312.5791	168.7673
Iron loss	W	64.33	48.62	92.48

Iron loss (rotor)	W	10.58	7.71	31.26
Iron loss (stator)	W	53.75	40.92	61.22
Magnet loss	W	2.22	0.32	2.59
Efficiency (w/o P_{conv})	%	86.63%	93.22%	94.11%
Converter loss P_{conv}	W	506.17	194.52	138.49
Efficiency (with P_{conv})	%	82.90%	89.94%	91.29%
Torque ripple	%	5.81%	3.00%	2.79%
Reluctance torque %	%	44.31%	29.07%	38.21%
Power factor	-	0.71	0.85	0.85

5.6.2.2 Reluctance torque contribution

As shown in Table 5.14, the reluctance torque of the machine contributes 29% of the total torque at the rated-torque base-speed point and 38% at the continuous-power maximum-speed point.

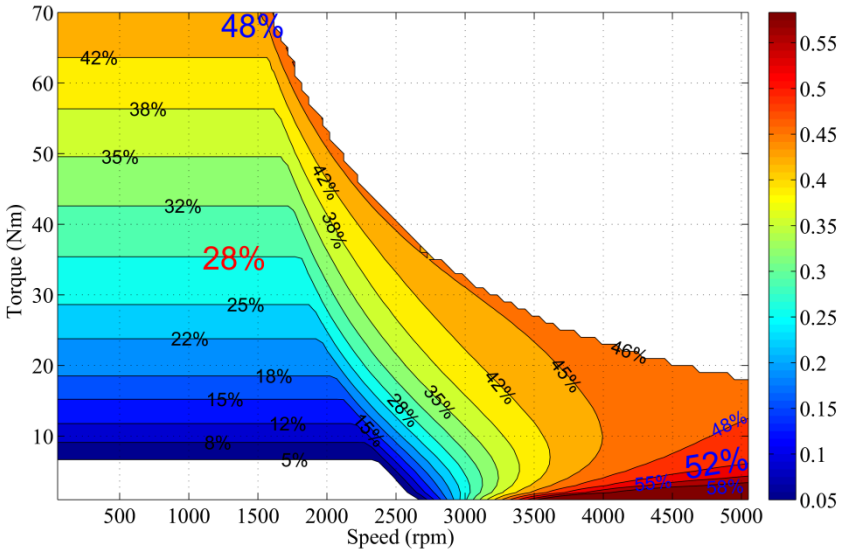

Figure 5.25 Percentages of reluctance torque with respect to the total torque over the torque-speed range

Figure 5.25 shows percentages of reluctance torque with respect to the total torque over the torque-speed range. It can be seen from the figure that the percentage of reluctance torque increases as the absolute value of total torque output increases. From the rated torque to the peak torque at the base speed, the percentage increases from around 30% to 50%. It is worthwhile to mention that the percentage also increases as the speed

increases. At low-torque maximum-speed region, the value reaches to 60%. The considerable contribution of reluctance torque indicates the torque capability at high speed field weakening region is greatly enhanced.

5.6.2.3 Efficiencies over driving cycles

Figure 5.26 plots the machine efficiencies over torque-speed range from 84% to 96%. The efficiencies were calculated without including iron loss building factor and converter losses. Since the machine efficiency is optimised against the NEDC driving cycle with frequent operations in the medium speed and low torque region, the machine exhibits efficiency above 94% over a wide speed range up to the maximum cruising speed 5050 rpm when torque is below 40 Nm. The maximum efficiency is 96.72% where the torque is 13 Nm, and speed is 2373 rpm.

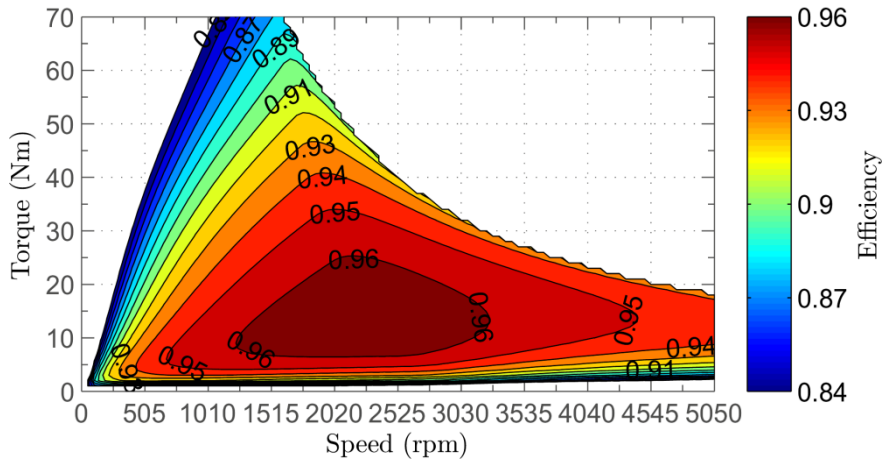

Figure 5.26 Efficiency map over torque-speed range

The efficiency distribution can be explained qualitatively by the nature of the machine design. Because of the high saturation with the IPM, the machine has large armature current and large copper loss at high torque, especially at the peak torque level, thus its efficiency is relatively low when torque is greater than 40Nm. However the efficiency over the continuous-power range when speed is above the base speed is as high as 94-96%. This is partly because the IPM machine has high field-weakening capability thus it needs relatively less current to maintain the voltage constraint at high speed. More importantly the designed machine benefits from the reluctance torque capability derived from the considerable saliency ratio feature. As a result, it relies on relatively low current to produce the required torque at high speed. Thirdly the low space harmonic-

content with the special 18-slot 8-pole winding configuration further reduces the rotor iron loss and rotor magnet loss.

Table 5.15 summarises the energy efficiencies and losses over two typical driving cycles: NEDC and Artemis, and over the combined Artemis and NEDC. The converter loss is included in the analyses. As seen in the table, either in the NEDC or in the Artemis, the copper loss is the major loss component, the iron loss weighing less, from around 21% of the total loss in the NEDC to 11% in the Artemis. Again the converter accounts for almost equal losses to the copper losses in the drive system during the driving cycles. Because high efficiencies up to 94% is achieved across a wide torque-speed region, the machine efficiencies during the three driving cycles are around 93-94%. The difference is the machine performs better in NEDC than in Artemis by 1.06% thanks to its high efficiency in the high-speed region.

Table 5.15 Loss break down and energy efficiencyover three typical driving cycles

	Unit	NEDC	Artemis	Combined
Mechanical output	kJ	1570.38	958.97	2529.35
Total loss	kJ	172.2168	129.2819	301.4887
Copper loss	kJ	67.1768	60.9019	128.0787
Iron loss	kJ	35.59	13.63	49.22
Magnet loss	kJ	0.29	0.06	0.34
Converter loss	kJ	69.16	54.69	123.85
Efficiency (w/o converter loss)	%	93.84%	92.78%	93.44%
Efficiency (with converter loss)	%	90.12%	88.12%	89.35%

5.6.3 Thermal performances

5.6.3.1 Cooling design

The cooling design for the machine is performed using Motor-CAD. Figure 5.27 (a) and (b) show the machine housing design in the axial view and 3D view, respectively. The machine is air-cooled. The stator housing contains 14 fins to increase convection area and facilitate heat transfer between the housing case and ambient.

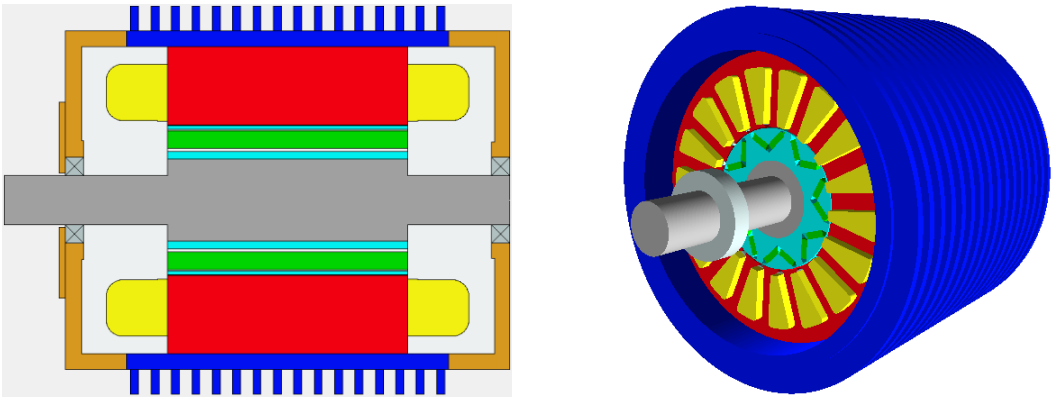

(a) (b)

Figure 5.27 (a). Axial view and (b). 3D view of the machine's cooling enclosure design

According to the geometry design of the machine and housing, and ambient conditions such as the ambient temperature and air velocity, Motor-CAD builds a lumper-parameter thermal model of the machine to predict temperatures of machine components. However in order to quickly assess the thermal behaviours over wide continuous operation region automatically, the simplified static thermal model illustrated in Chapter 2 is utilised. In addition, the transient state-space thermal model described in Chapter 4 is used to facilitate the machine's electro-thermal coupled simulations. The static and transient models are based on the thermal network generated in Motor-CAD.

5.6.3.2 Traction machine ambient convection analyses

In the thermal model, the convection resistance R_0 between the housing and ambient is a crucial component which greatly affects the accuracy of temperature predictions. The value R_0 is affected by the complicated fluid condition around the running vehicle especially inside the under-hood. In order to determine R_0, Centro Ricerche Fiat Srl (CRF) carried out fluid dynamic simulations at different vehicle speeds using CFD (Computational Fluid Dynamic) tool StarCCM+. Figure 5.28 shows the 3D structure of vehicle and under-hood used in the simulations. Figure 5.29 shows Air velocity distribution predicted in the simulation when the vehicle speed is 5km/h. Because the vehicle employs distributed traction system, air-flow conditions for the front motor and rear motor should be monitored. At 5 km/h, it is seen from Figure 5.29 that the air velocity around the front motor is 0.7-0.8 m/s, while the velocity around the rear motor is less than 0.1 m/s. Apparently, the rear motor is subject to more adverse cooling condition.

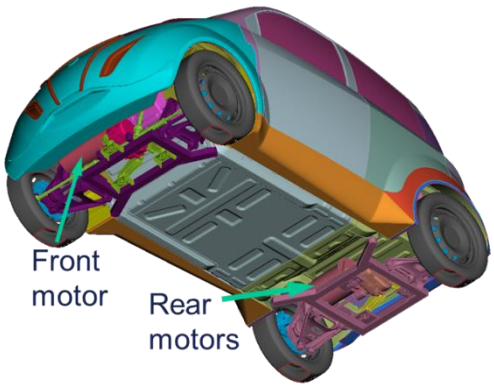

Figure 5.28 Vehicle and under-hood in the air fluid dynamic simulations

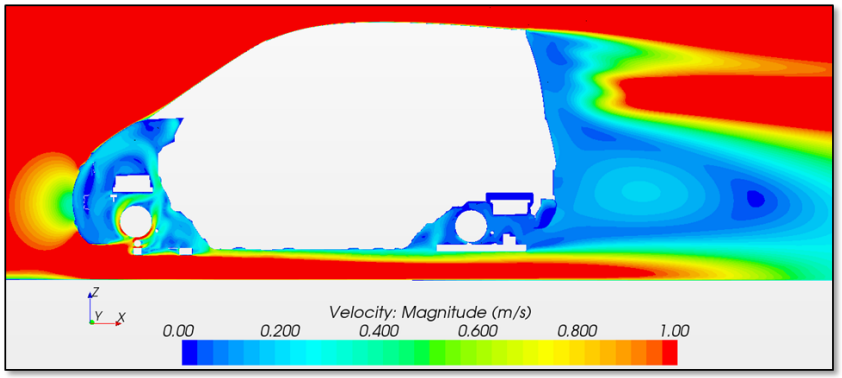

Figure 5.29 Air velocity distribution predicted in the simulation when the vehicle speed is 5km/h

In the simulations, heat flow Q and temperature difference ΔT between the traction machine and ambient are monitored. The heat exchange coefficient h and the convection resistance R_0 are captured at different speed using (5.8) and (5.9), where A is the machine surface area.

$$h = \frac{Q}{A \cdot \Delta T} \tag{5.8}$$

$$R_0 = \frac{1}{h \cdot A} \tag{5.9}$$

The estimated ambient convection resistance profile with variation of speed is then substituted into the detailed thermal model in Motor-CAD. By calibrating the ambient fluid coefficient set in Motor-CAD, the heat exchange coefficient profile estimated in CFD simulations can be closely followed in Motor-CAD. Figure 5.30 shows the Heat exchange coefficients with variation of machine speed in fluid simulations and in the

machine thermal models for the front and rear motors respectively. The heat exchange coefficients on housing also differ depending on different surfaces of the fins. As shown in Figure 5.27 (a) The fin sides are the surfaces of the fins that are perpendicular to the cylinder surface of the housing; while the fin tips are parallel to the cylinder surface.

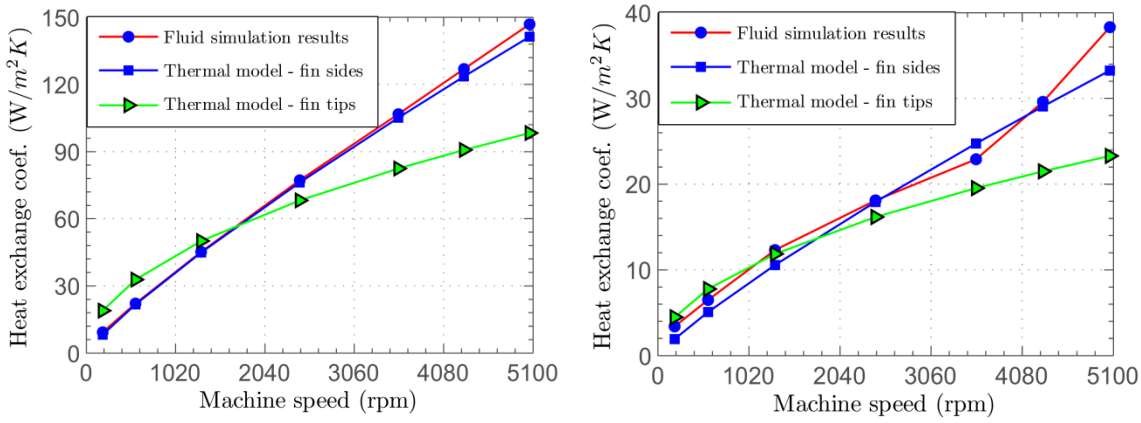

(a) (b)

Figure 5.30 Heat exchange coefficients with variation of machine speed in fluid simulations and in the machine thermal models for (a) the front and (b) rear traction machines

5.6.3.3 Steady-state thermal analyses

By using the static thermal model in Chapter 2 with the estimated ambient convection resistances and the ambient temperature set at 40°C, the temperature rises of the machine at arbitrary torque-speed operation points can be estimated. In the simulation, the vehicle velocity which determines the heat convection is linked to the motor speed at a given operating point. It should be noted that although in the previous section the heat transfer through convection is mainly considered, the heat conduction from the machine to the other parts in the vehicle is also considered in the simulation. Therefore by using using (5.8) and (5.9), the thermal resistance R_0 acquired from the simulation results and used in the analytical thermal model reflects the combined heat transfer of convection and conduction. Figure 5.31 and Figure 5.32 show the steady-state average temperature rises of the armature winding and magnets temperatures, respectively over the torque-speed envelope when the machine is mounted in the front.

It can be observed that within the continuous operation envelope, the estimated winding's temperatures are below 65°C, and magnet's temperatures are below 80°C.

The estimated temperatures are far below the design limits 120°C for windings or 150°C for magnets. Also it is found that over the continuous operation region, the worst steady-state temperature occurs at the continuous-power maximum-speed point T_{rm}. Table 5.16 summarises these worst temperatures at two different ventilation conditions:1) when the machine is mounted in the front axle; 2) when the machine is mounted in the rear; and 3) when the machine runs with only natural convection.

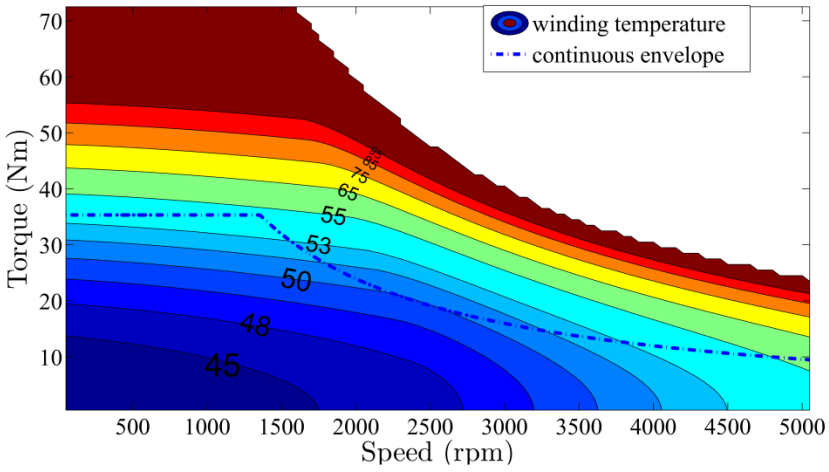

Figure 5.31 Steady-state average temperature rises of armature winding over torque-speed envelope predicted by the machine's static thermal model when the machine is mounted in the front

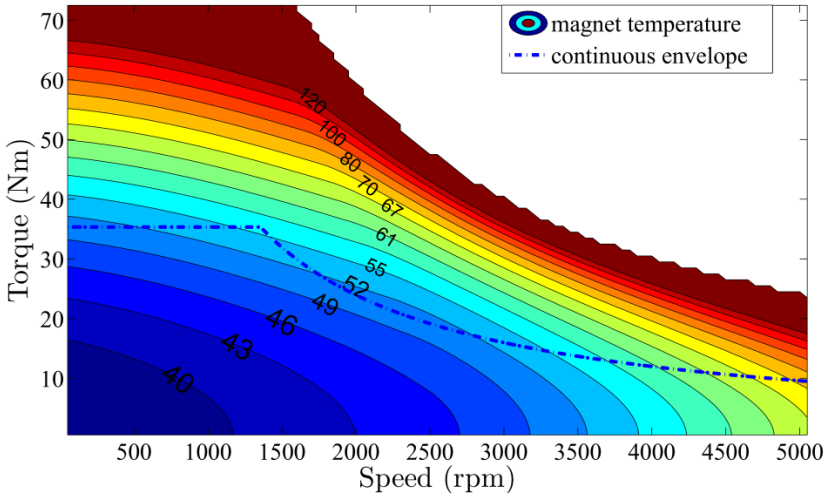

Figure 5.32 Steady-state magnet temperature rises over torque-speed envelope by machine's static thermal model when the machine is mounted in the front

Table 5.16 Steady-state temperature at maximum-speed continuous-power point

	Unit	Air-blown over(front)	Air-blown over (rear)	Natural convection
Winding	^{o}C	56.6	73.9	110.7
Magnet	^{o}C	70.1	87.2	127.6

5.6.3.4 Transient thermal analyses

By using the transient thermal model in Chapter 4 with the estimated ambient convection resistances, transient temperature curves are monitored while the vehicle runs through the driving cycles defined by CRF [131]. Since the driving cycles imitate real-world driving conditions, the simulation results are important indicators in judging machines' thermal performance. Ideally the temperature design limits and demagnetisation of permanent magnets should be checked against the maximum temperatures that occur when the machine reaches thermal periodic steady state during repetitive driving cycles.

Figure 5.33, Figure 5.34 and Figure 5.35 shows the temperature curves during Urban, Extra-Urban and Up-and-Down-Hill driving cycles respectively when the machine is mounted in the front axle. The starting temperature is set as the ambient temperature 40 ^{o}C. The driving cycles are repeated for 15 times in order for the machine to reach periodic steady state. It should be noted that although in the analytical thermal model, the thermal mass of the front and rear axles are not included, since the heat transfer coefficients are acquired from the thermal CFD simulation which considered the conduction between the machine and the surrounding parts in the vehicle, the analytical thermal model should be able reflect the transient thermal characteristics of the machine while running over driving cycles.

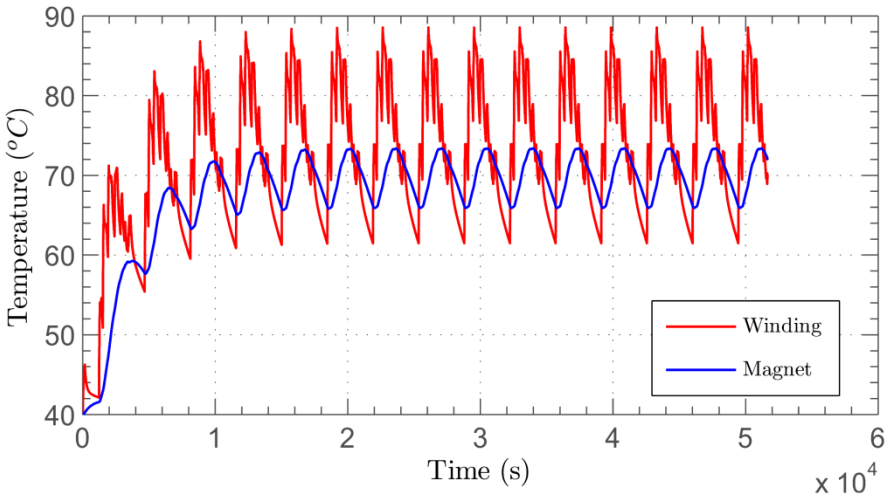

Figure 5.33 Machine temperatures over repeated Urban driving cycles predicted by transient thermal models when the machine is mounted in the front

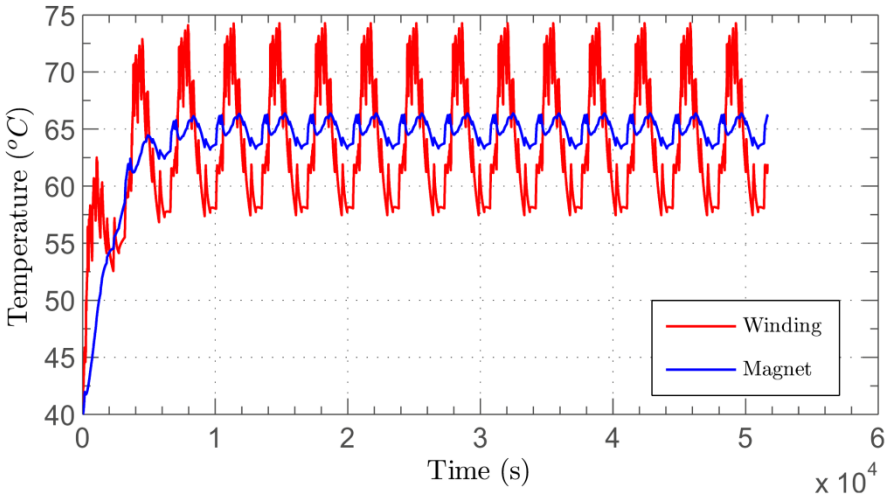

Figure 5.34 Machine temperatures over repeated Extra-Urban driving cycles predicted by transient thermal models when the machine is mounted in the front

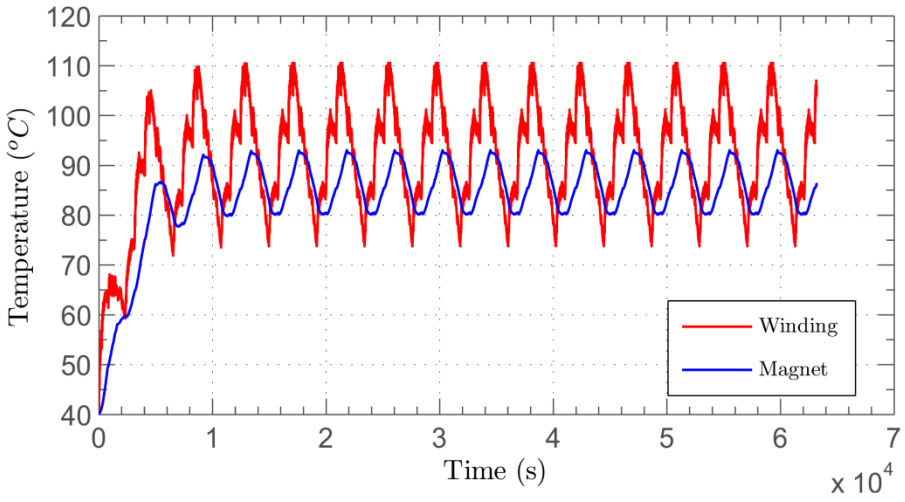

Figure 5.35 Machine temperatures over repeated Up-and-Down-Hill driving cycles predicted by transient thermal models when the machine is mounted in the front

As shown in the figures, in the periodic steady state, the temperatures vary between peaks and valleys by 10-30 ^{o}C due to torque and speed variations of the driving cycles. It is found that the maximum temperatures of magnets are always lower than that of windings. This is because high thermal masses of the stator and rotor act as filters for the transient loss variations during a driving cycle. This phenomenon is different from that observed in the steady-state results shown in Table 5.16, where the rotor magnet temperatures are higher than that of windings, since the heat on the rotor has to be dissipated through the stator.

Table 5.17 and Table 5.18 list the maximum winding and magnet temperatures respectively during the three driving cycles. While comparing the results among the three driving cycles, the temperatures of windings and magnets during Up-and-Down Hill are highest and the temperatures during Extra Urban are lowest. This is because Extra-Urban cycle represents high speed operations when the machine is more efficient while the cooling is also better.

The maximum temperatures of the windings and the magnets should be checked against the design limits as listed in Table 5.10. When the machine is mounted in the front, its maximum temperatures in the Up and Down Hill driving are 111^{o}C for windings and 93^{o}C for magnets. They are acceptable for the design limit. But when the machine is mounted in the rear, the temperatures are about 20-40^{o}C higher than those in the front. The temperatures in the rear during the Up and Down Hill driving are 153^{o}C for

windings and 133°C for magnets. It can be seen that the winding temperature in the rear during Up and Down Hill exceeds the design limit 120°C.

Table 5.17 Maximum winding temperatures over repeated driving cycles

Driving cycles	Unit	IPM motor mounted in front	IPM motor mounted in rear
Urban	°C	88	108
Extra Urban	°C	74	95
Up and Down Hill	°C	111	153

Table 5.18 Maximum magnet temperatures over repeated driving cycles

Driving cycles	Unit	IPM motor mounted in front	IPM motor mounted in rear
Urban	°C	73	98
Extra Urban	°C	66	83
Up and Down Hill	°C	93	133

5.6.3.5 Rotor lamination mechanical stress analyses

The mechanical stress in the rotor lamination is check at the speed 7575 rpm -- 1.5 times of the maximum speed. Using the analytical mechanical stress model illustrated in Chapter 2, the predicted maximum stress in the upper bridge is 42.11 MPa, and the predicted maximum stress in the middle bridge is 50.25 MPa. Therefore the maximum mechanical stress of rotor laminations which occurs in the middle bridge is far less than the constraint: 400 MPa. The mechanical stress analysis results are also examined using FE. Figure 5.36 shows the stress distribution contours at 7575 rpm calculated by FE. As predicted analytically, the highest stress predicted in FE occurs in the middle bridge, which is 49.03 MPa. The analytical result differs from the FE by 2.5%.

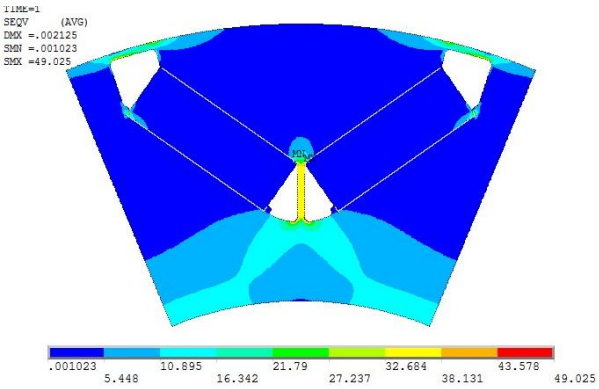

(a)

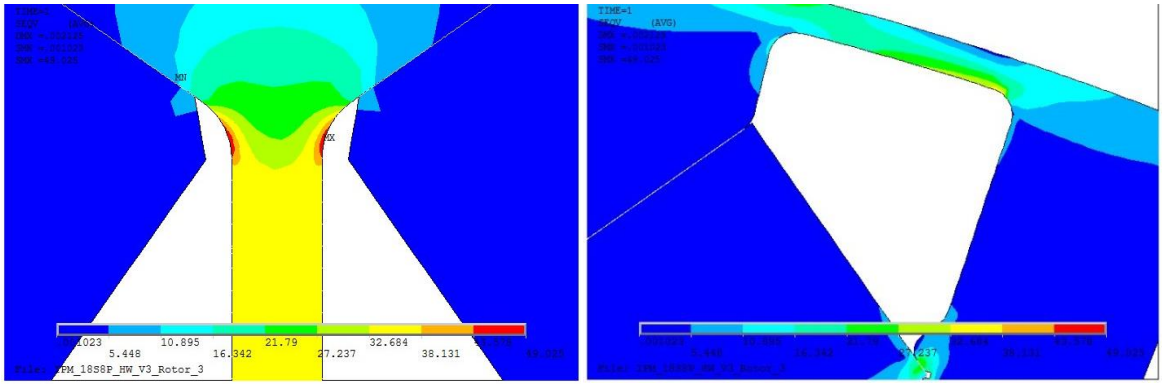

(b) (c)

Figure 5.36. Rotor stress distributions at 7575 rpm of (a) one pole, (b) the middle bridge, and (c) the upper bridge

5.7 The application of reduced dysprosium permanent magnets

5.7.1 Reduced dysprosium permanent magnets

Rare earth $Nd_2Fe_{14}B$ magnet such as the N35EH employed in the IPM machine studied above is one of the key materials for high performance PM machines, thanks to its high energy product. However, the volatile supply chain of heavy rare earth elements has made the magnets subject to massive price fluctuation and extremely high cost. This is especially the case for the Dysprosium (Dy), whose price is almost as 6 times high as the Neodymium (Nd) [120]. Since the operating temperatures of traction motors can reach 150^{o}C at which the coercivity (Hc) of pure $Nd_2Fe_{14}B$ magnets is too low, Dy plays an important role in the $Nd_2Fe_{14}B$ magnet as small addition of Dy substitutes the Nd to form $(Dy,Nd)_2Fe_{14}B$ which has a higher anisotropy field than $Nd_2Fe_{14}B$, thus can

significantly increase the Hc and elevate the temperature performance. On the other hand, due to antiferromagnetic coupling between Dy and Fe moments in $Dy_2Fe_{14}B$, Dy usage leads to a slight reduction in remanence and energy product [121]. Therefore reducing Dy content but maintaining its Hc enhancing effect is very desirable in terms of magnet's material cost and also its energy product.

In the context of volatile rare earth material supply, the application of a new type of sintered $Nd_2Fe_{14}B$ permanent magnets with reduced usage of Dy element in the developed IPM machine design is investigated. The new magnets are generated by a new Dy grain boundary diffusion process (GBDP) [122] in which Dy is diffused from the surface of an NdFeB magnet along NdFeB grain boundaries. Figure 5.37 shows the Energy Dispersive X-ray (EDX) spectroscopy image of the Dy rich shell around the edge of $Nd_2Fe_{14}B$ grains close to the surface of a processed magnet. The $Dy_2Fe_{14}B$ shell effectively shields the core of $Nd_2Fe_{14}B$, which contributes a high coercivity without significant reduction in remanence. The main advantage of the new magnets compared with magnet products of the conventional GBDP methods [123]-[126] is the great reduction of Dy usage. Figure 5.38 compares the properties of the new and conventional magnets. The two crossing lines in the figure shows the coercivity of magnets increases and the remanence (Br) decreases as more Dy is added to the $Nd_2Fe_{14}B$ base if following the conventional ways. In comparison, the new magnet contains 1.1 % by weight (wt%) Dy and has a coercivity equivalent to a conventional 4.4 wt% Dy magnet. In addition the remanence of the new magnets is 17% higher. As can be seen, there is an 81% reduction in Dy consumption with the new magnets which indicates significant machine cost saving. Although the weight percentage of Dy used in the $Nd_2Fe_{14}B$ product is quite low, considering the price of Dy is around 5 times higher than that of Nd, the 81% reduction of Dy consumption brought by the new Dy processing method means the $Nd_2Fe_{14}B$ product cost is reduced by 16.23% compared to the cost using the conventional method.

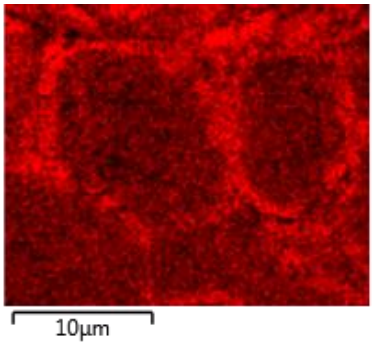

Figure 5.37. EDX image of counts per second of the Dy Mα line showing the Dy rich shell around the edge of $Nd_2Fe_{14}B$ grains close to the surface of a processed magnet

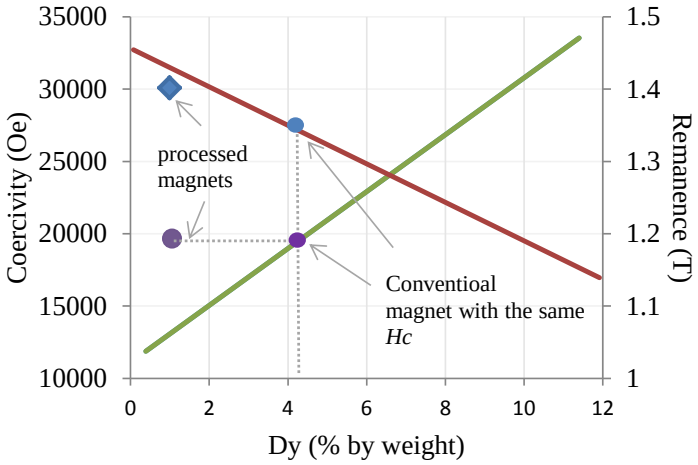

Figure 5.38. The relation of Dy usage percentage to conventional and new magnet properties

Table 5.19 Property comparison between N35EH and the Dy-reduced magnets

	Unit	N35EH	Dy-reduced magnets
Hc of magnets (150°C)	kA/m	744	446
Br of magnets (150°C)	T	1.00	1.20

The new Dy-reduced magnets are compared with the N35EH magnets in the properties of coercivity and remanence at 150°C in Table 5.19. Its remanence is about 20% higher, but its coercivity is -40% lower which is a considerable shortcoming. The new magnets were installed in the rotor of the IPM machine design with the identical geometry as

described in the previous section to form a new IPM machine. There are two research questions to be addressed in the new IPM machine. One is about the improvements of the machine's torque and efficiency compared to the case with N35EH magnets. Secondly, although carried with the merits of low rare-earth consumption and higher energy product, because of the lower Hc at high temperatures compared with conventional rare-earth magnets, the machine with the new magnets are subject to higher risk of demagnetization. Thus the new IPM requires particular examinations on the above two issues, especially over demanding driving cycles.

5.7.2 Performance comparisons

The performances of the machine with the new magnets (denoted as "Machine II" thereinafter) are assessed on typical operation points such as the rated torque, base speed point and the peak torque, base speed point as well as over driving cycles of NEDC and Artemis. Improvements of the torque capability and energy efficiencies are investigated when compared with the machine with N35EH (denoted as "Machine I" thereinafter).

5.7.2.1 Parameter comparison

Table 5.20 lists the basic machine parameters of Machine II at the three typical base-speed and high-speed points respectively and compares them with the parameters of Machine I. With around 20% higher Br, Machine II possesses 16%-19% higher magnet flux linkages and therefore exhibits 11%-14% higher torque constants at the two base-speed points. On the contrary, when it comes to high speed where the field weakening control mode is in use, for the same reason of higher magnet flux linkage, its torque constant is 6% lower because more negative current in the *d*-axis is needed to meet the voltage constraint. The torque constant parameters of Machine II suggest that it has different efficiency map compared with Machine I, which will be further examined below.

Table 5.20 Basic machine parameters of the Machine II

	Unit	Peak torque & Base speed	Rated Torque & Base speed	Continuous power & Max speed
$\psi_m * P$	Vs	0.251	0.294	0.313
$\psi_m * P$ increase	-	19 %	16 %	16 %
Torque constant: K_A	Nm/A	0.48	0.50	0.15

K_A increase	-	14 %	11 %	-6 %

* The parameter increase is compared against the machine with N35EH magnets

5.7.2.2 Energy efficiencies

Table 5.21 lists energy efficiency comparisons between Machine I and Machine II during NEDC and Artemis driving cycles as well as at the base-speed and maximum-speed points. Machine II exhibits 1.04%, 2.64% and 0.89% higher energy efficiency at the rated torque, peak torque points (both at base speed) and over Artemis respectively. This implies that a reduction of energy loss up to 10 - 20% is gained from the machine's better torque capability at low speed. On the other hand, Machine II's efficiencies at the continuous-power maximum-speed point and over the NEDC which features high speed operations are 92.6% and 93.4% respectively, being 0.5% lower and 0.4% lower respectively compared with Machine I.

The Machine II's overall efficiency performances could be clearly observed in efficiency maps over the torque-speed range shown in Figure 5.39, and its efficiency improvements over torque-speed range against Machine I is shown in Figure 5.40. In comparison, the new machine gains 0.5%-5% higher efficiency in the low-speed, medium-to-high-torque region, but exhibits 0.5%-5% lower efficiency in the low-torque and high-speed region due to high iron losses and high field-weakening currents.

Table 5.21 Energy efficiency comparisons between Machine I and Machine II

	Unit	Machine I	Machine II
Efficiency at rated point (base speed)	%	93.22%	94.26%
Efficiency at peak point (base speed)	%	86.63%	89.27%
Efficiency at continuous-power point (max speed)	%	94.11%	92.60%
Efficiency over NEDC	%	93.84%	93.41%
Efficiency over Artemis	%	92.78%	93.67%

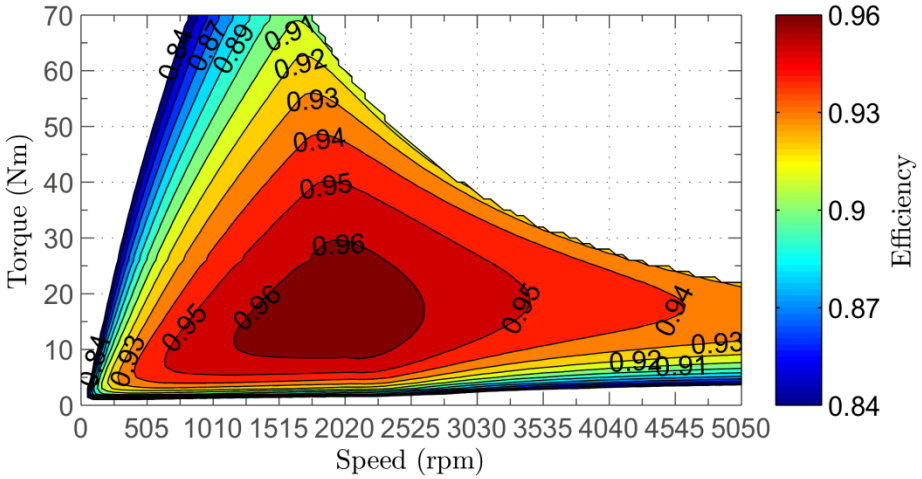

Figure 5.39. Efficiency map of the Machine II over torque-speed operation range

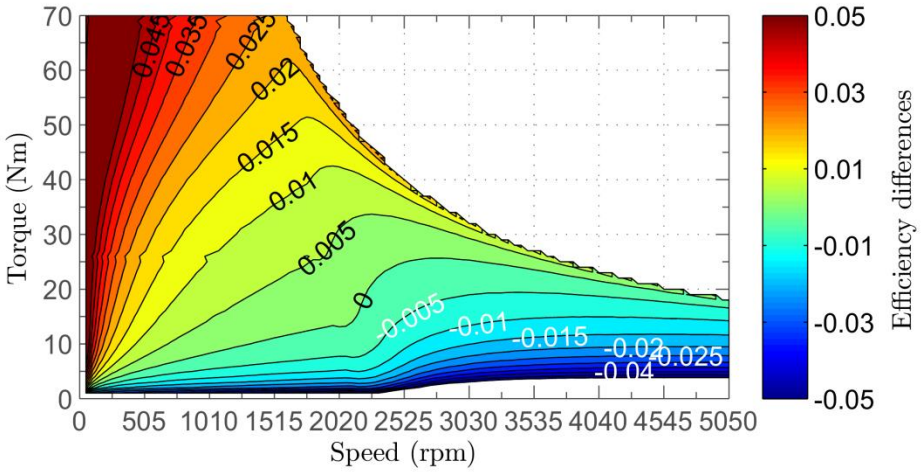

Figure 5.40. Efficiency improvements of Machine II (against Machine I) over torque-speed operation range

5.7.3 Thermal performance examination

Thermal performances of Machine II are evaluated following the same process as for Machine I which has been illustrated in Section 5.6.3. Table 5.22 summarises maximum temperatures that occur during the CRF three driving cycles. By way of example, Figure 5.41 shows the temperatures of the magnets and windings over the Up-and-Down-Hill driving cycle when the machine is front-mounted and rear-mounted respectively.

Similar to Machine I, driving cycles featuring high-torque low-speed operations such as Up-and-Down-Hill are more thermally demanding. Among all the evaluated cases,

when the machine is mounted in the rear and runs through Up-and-Down-Hill, it has the highest temperatures: 118 ^{o}C for the magnets and 132 ^{o}C for the windings. The maximum temperatures are below the design limits. They are indeed lower than that of Machine I due to improved torque capability at low speeds.

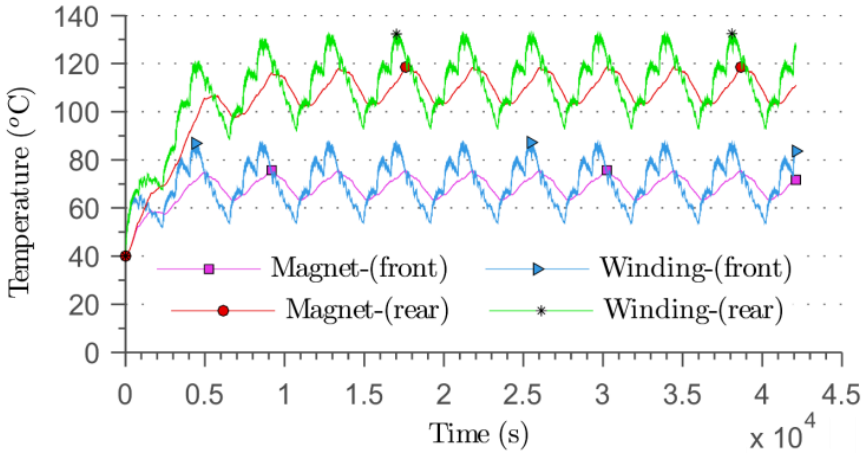

Figure 5.41. Temperature variations during 10 repeated Up-Down-Hill drive cycles when the motor is mounted in the front and in the rear of the vehicle respectively

Table 5.22 Maximum Temperatures over Repeated Driving Cycles

	Unit	Magnet/winding Temperature (motor in front)	Magnet/winding Temperature (motor in rear)
Up-and-Down Hill	^{o}C	76 / 87	118 / 132
Urban	^{o}C	62 / 76	87 / 98
Extra Urban	^{o}C	63 / 65	81 / 86

5.7.4 Demagnetisation examination

The magnet demagnetization withstand capability is checked on the worst condition where the magnet temperature is set at design limit 150^{o}C and the Machine II runs at the peak-torque base-speed point which has the highest demagnetizing *d*-axis current over the torque-speed range.

The time-step FE is used to evaluate the flux densities within magnets in each pole during an electrical cycle. To withstand the demagnetisation, the local "magnetisation-direction" flux density B_m needs to be above 0.6 T which is the knee point value of the new magnets at 150^{o}C. Figure 5.42 shows the flux lines within a magnet at a rotor

position of peak-torque point. As Figure 5.42 indicates, the magnetisation-direction flux density B_m is the projection vector of the local flux density $\boldsymbol{B}$ onto the magnet's magnetisation direction. Because 4 corner points of a magnet are usually paths for leakage flux through the rotor upper and middle bridges, they are positions most vulnerable to demagnetising field. B_m on these points (denoted as C1, C2, …, C8 for 2 magnets of one pole in Figure 5.42) should be particularly monitored.

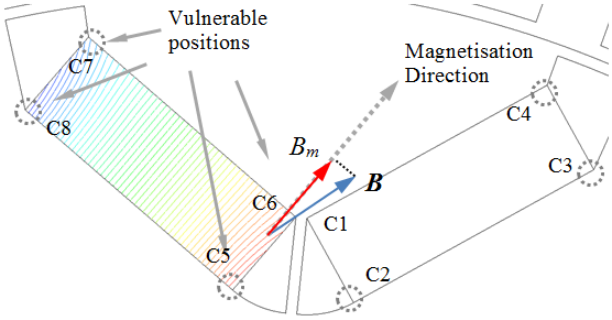

Figure 5.42. Flux lines within magnets indicating the magnetisation-direction flux density and corner points of magnets

Figure 5.43 shows the magnetisation-direction flux density variation curves on the 8 corner points of the 2 magnets of the second pole over an electrical cycle at the peak-torque base-speed point when the magnet temperature is 150 ^{o}C. It is shown in the figure that over a whole electrical cycle, due to the winding MMF harmonics and slots in the stator, B_m value of a given position keeps varying. And due to the geometric symmetry, two points which are symmetrical with respect to the centre d-axis have the same flux density variations, for example C1 and C6 or C2 and C5. Among the 4 pairs of points, C1 and C6 which face toward the rotor pole and are positioned near the middle bridge have the lowest flux density 0.53 T when the rotor rotates to mechanical degree 16.5^{o}.

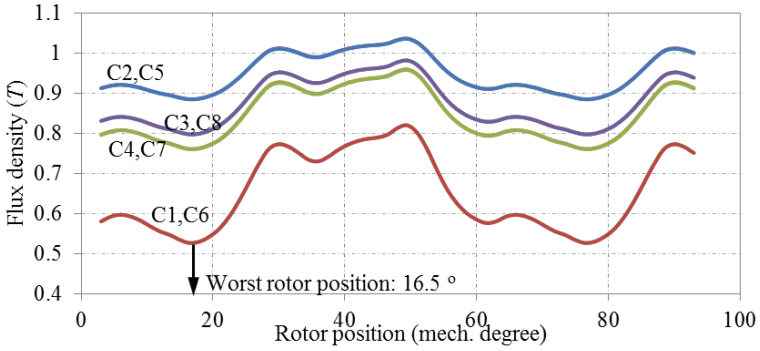

Figure 5.43. Magnetisation-direction flux density variation curves at the 8 corner points of one pole magnet over an electrical cycle when operating at the peak-torque base-speed and the magnet temperature is 150 ^{o}C

A close examination of the magnetisation-direction flux density distribution within the magnets at the worst rotor position 16.5^{o} is shown in Figure 5.44. The flux density shown in the figure ranges from 0.6T to the 1T. It is seen that the blank area of the magnets where the flux density is below the knee point 0.6 T are on the magnets corners. By calculation, the demagnetised areas are about 1.4% of the total magnet areas, which have a marginal effect on the machine performances.

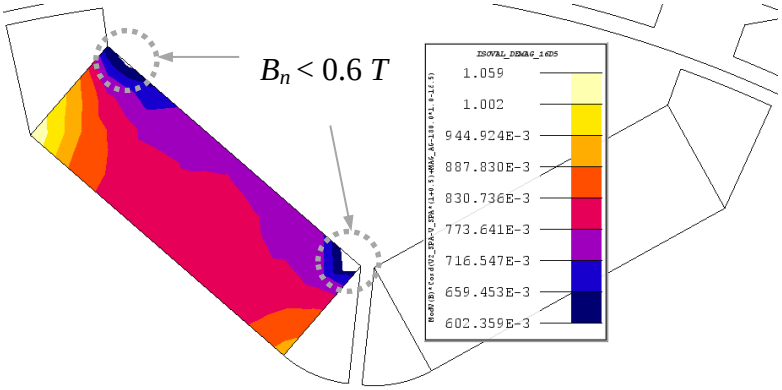

Figure 5.44. Magnetisation-direction flux density contour at the rotor position of 16.5 mechanical degrees when operating at the peak torque and base speed and the magnet temperature is 150 ^{o}C

5.8 Machine prototypes and experimental validations

Prototypes for Machine I and Machine II are built to measure the machine performances and to validate the analytical models proposed in Chapters 2, 3 and 4.

The two prototypes underwent various tests including no-load test, locked-rotor test, load test and transient thermal test in order to acquire their torque capabilities, efficiency and thermal behaviours.

Meanwhile the measured performance indicators are also predicted by employing the analytical models for comparison and validations. The models include the flux linkage/torque models, control-current model, iron loss model, and temperature-effect model. The accuracies of performance predictions by the models are checked in comparison with experimental results.

5.8.1 Machine prototypes

5.8.1.1 Laminations

Figure 5.45 shows the stator lamination sheet and rotor lamination sheet respectively. The silicon steel type M270/35 is used for the stator and rotor laminations which were fabricated by laser cut. It is known that the laser cutting will affect the magnetic property of the material in the regions close to the cutting edges [127]-[130]. The effect on the rotor lamination has two different trends. The laser cutting would deteriorate the permeability of laminations where it cuts through. For the stator tooth tips and the rotor surface, deterioration will equivalently increase the air gap length thus undermine the machine torque performance; however in the bridge parts of the rotor, it will decrease the leakage flux which in return increases the flux linkages of windings.

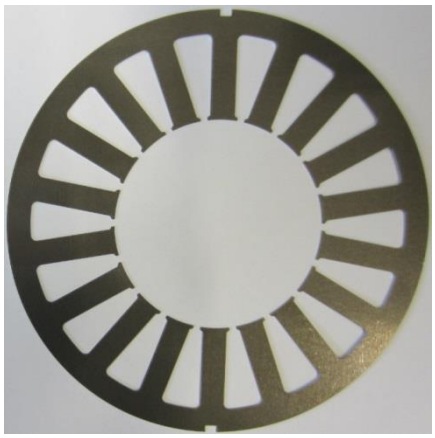

(a)

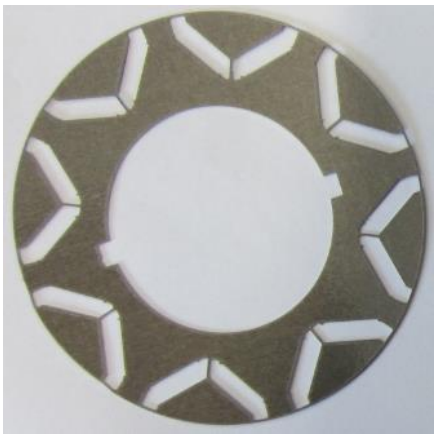

(b)

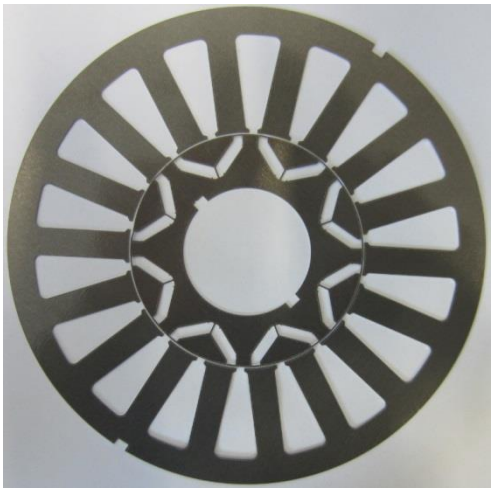

(c)

Figure 5.45. (a) stator lamination sheet, (b) rotor lamination sheet and (c) combined

5.8.1.2 Windings

Figure 5.46 shows the stator windings viewed from the front end and from the back end respectively. 5 thermal couplers are embedded in the windings to monitor the winding temperatures during the test. Three sensors are installed in the slot parts of phase A, B and C windings, respectively. Two other sensors are positioned in the front end winding and back end winding respectively.

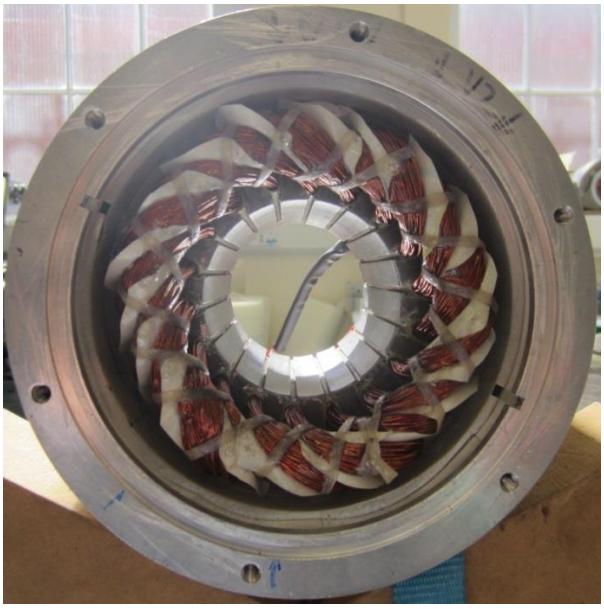

(a)

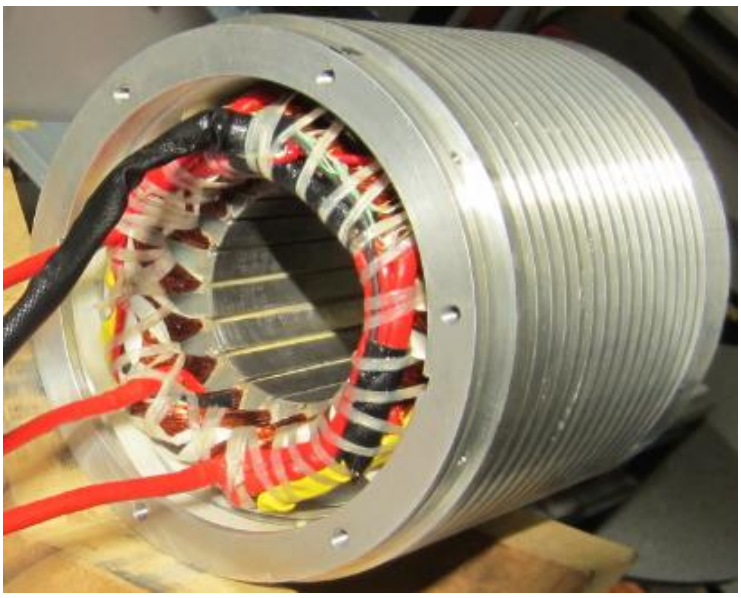

(b)

Figure 5.46. Stator windings (a) front view and (b) back view

5.8.1.3 New magnets for Machine II

Figure 5.47 shows the Dy-reduced magnets which are employed in Machine II. The magnets in each slot are segmented axially into three pieces to ease fabrication and assembly as the material is brittle. This also reduces eddy current loss in the magnets.

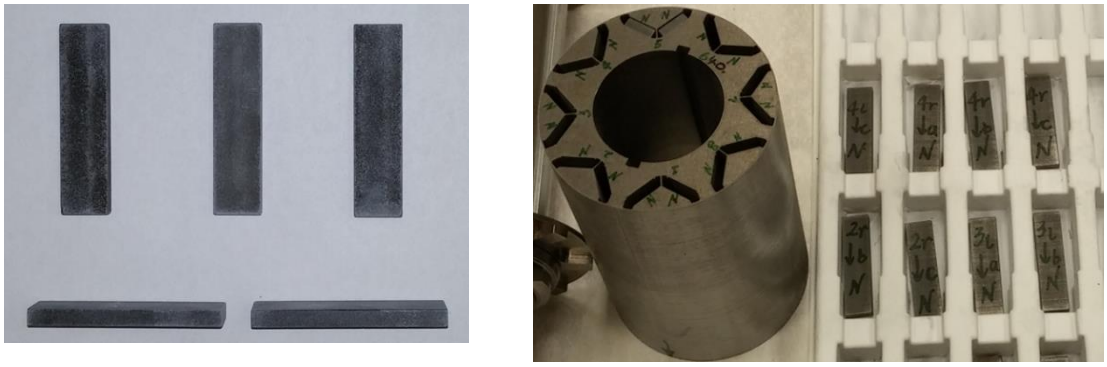

(a) (b)

Figure 5.47. Dy-reduced magnets (a) in front and side views, (b) in the process of being assembled into the rotor stack

5.8.1.4 Rotor stack and shaft

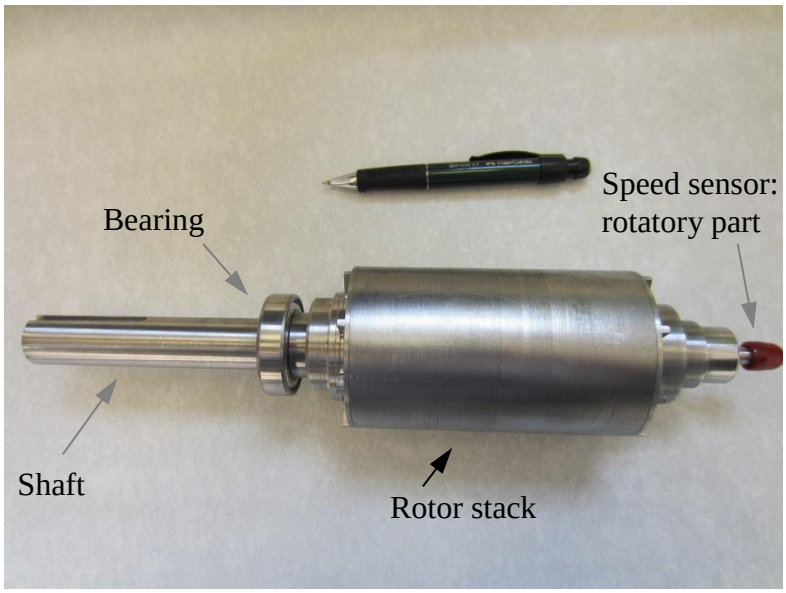

Figure 5.48. The rotor assembly

Figure 5.48 shows the rotor assembly with the rotor stack, shaft and bearings. No skew is employed for the rotor. The rotary part of a speed sensor (protected by the red cover in the figure) is installed in the back end of the shaft. The stator part of the speed sensor is installed in the back end plate fitted to the housing. The two parts together provide rotor position and speed information.

5.8.1.5 Motor assembly

(a)

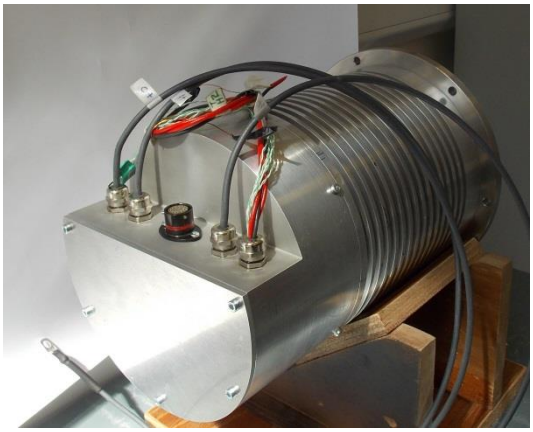

(b)

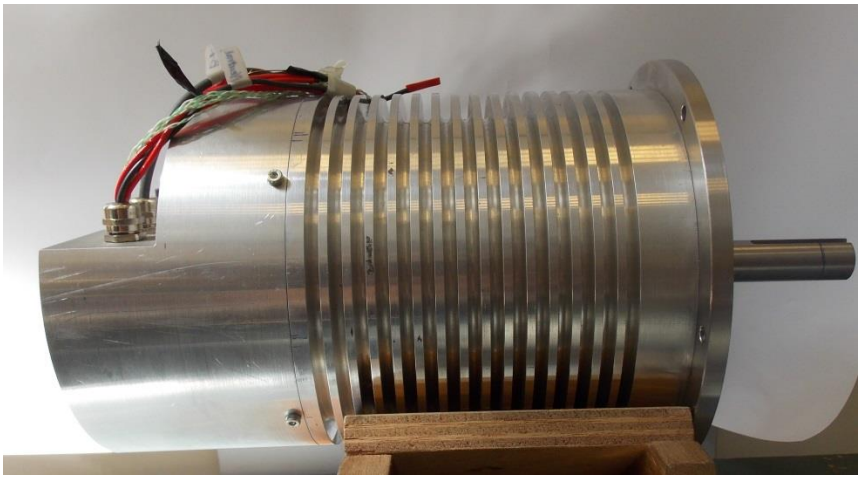

(c)

Figure 5.49. The machine housing of (a) the shaft side, (b) the connection box side, and

(c) the cooling fins

Figure 5.49 shows the machine assembly viewed in different angles. A connection box is attached to the back end of machine to provide an interface for the three phase cables, neutral point connection, rotor position signal wire and thermal sensor wires.

5.8.1.6 Test rigs

Initial no-load tests were performed on the test rig shown in Figure 5.50 in which the prototype machine is mechanically to the dynamometer via a high precision in-line torque transducer.

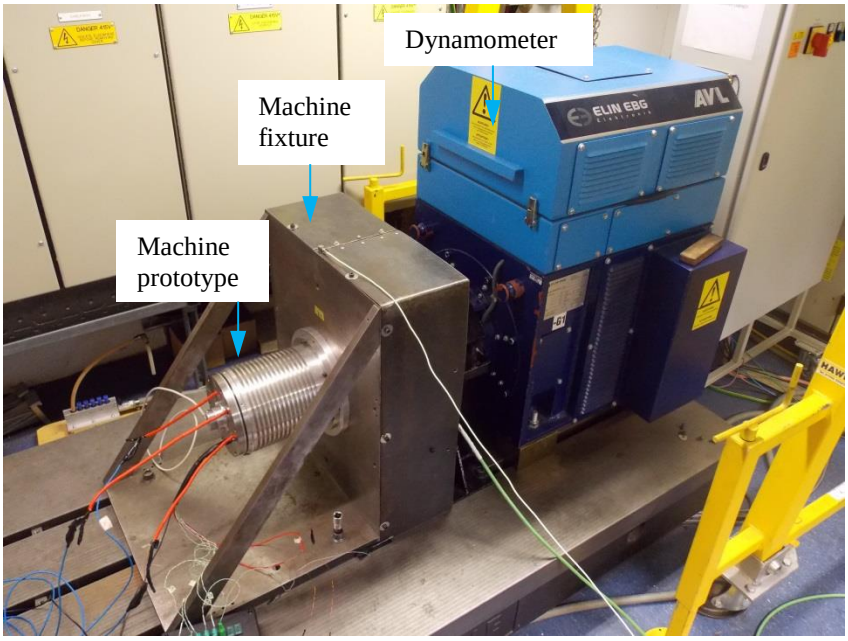

Figure 5.50. Test rig for machine no-load experiments

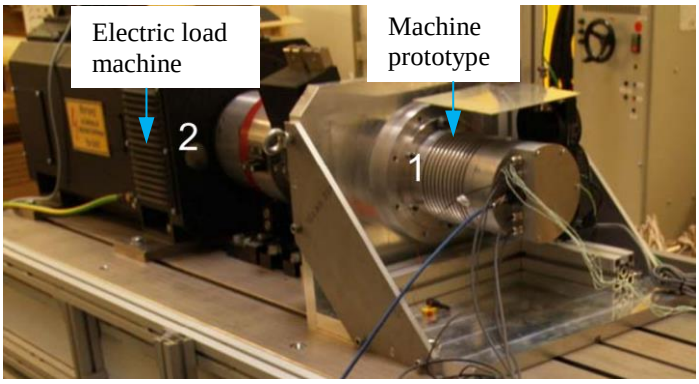

(a)

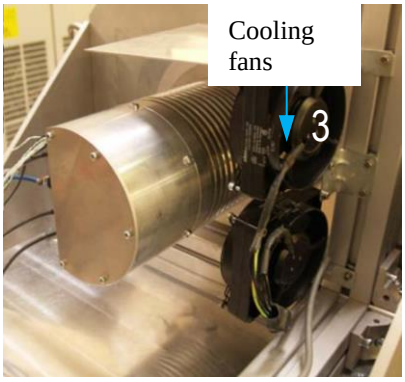

(b)

Figure 5.51. (a) Test rig for machine load experiments and (b) cooling sets

Figure 5.51 shows the second test rig and its cooling fans for load tests which were carried by in collaboration with Siemens Corporate Research in Erlangen, Germany. The test rig consists of an inverter (not shown in the figure) and a dynamometer which is able to run at speed as low as 3 rpm with in-line torque transducers and other measurement equipment.

5.8.2 Experiments for no-load characteristics

No-load tests for the prototypes Machine I and II are performed to acquire the machine no-load characteristics including the back-EMF and the no-load loss. Based on back-EMF test results, the remanence of permanent magnets is calibrated in the analytical modelling process to account the real properties of magnets and manufacture influence. Similarly, based on measured no-load loss, a building factor for iron loss is introduced in the analytical iron loss model to represent the effect of manufacture on the iron loss.

In the no-load test, the prototype machine is driven by the dynamometer at a constant speed. During the test the open-circuit line-to-line voltage is recorded by voltage probes, and the torque is measured by the torque transducer and will be used to calculate the power loss.

5.8.2.1 No-load back-EMF

Figure 5.52 shows the line-to-line back-EMF waveforms for Machine I at 1350 rpm from experiment. The predicted back-EMF using the analytical high-fidelity flux linkage model $\psi_d(i_d, i_q, \theta)$ and $\psi_q(i_d, i_q, \theta)$ in (4.4), (4.5) illustrated in Chapter 4 is compared with the measurements in Figure 5.52. The temperature effect model shown in Figure 4.11 in Chapter 4 is also used in the predictions to account the machine temperature of 50^{o}C during the test. It is seen from Figure 5.52 that the prediction agrees quite well with the measured back-EMF waveforms.

Figure 5.53 compares the harmonics of the back-EMF between the experiments and predictions. The predicted fundamental component is 68.6 V, which differs by 2.69% from the measurement of 66.8 V. Therefore, a calibrating factor of 1/1.269 for the remanence will be used in the analytical model to make the predicted fundamental back-EMF equal to the measurement. A very small second harmonic is also visible in the

measured back-EMF spectra, and this may be caused by manufacturing tolerances on each rotor pole and magnet property disparity.

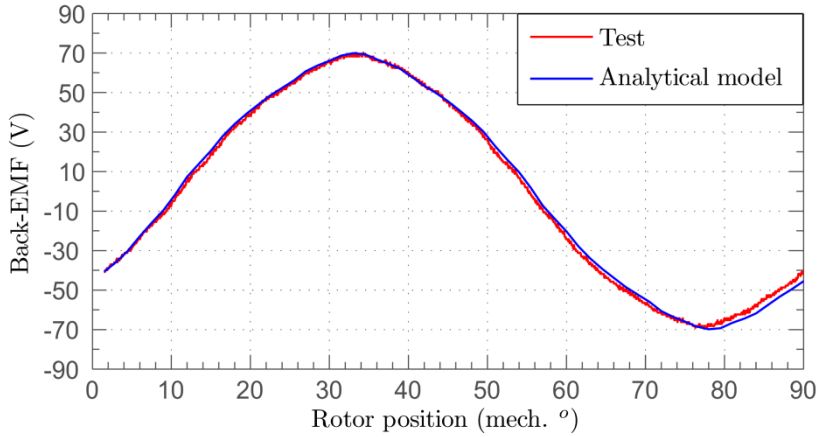

Figure 5.52. Machine I line-to-line back-EMF waveforms at 1350 rpm from experiment and analytical model

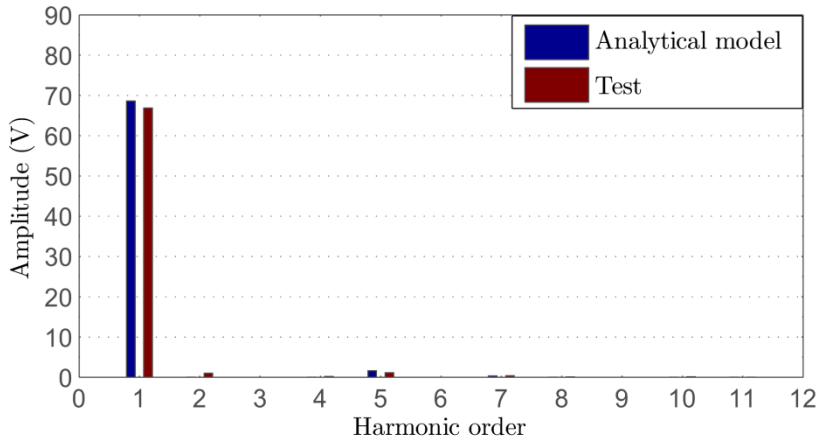

Figure 5.53. Harmonics of Machine I line-to-line back-EMF waveforms at 1350 rpm from experiment and analytical model

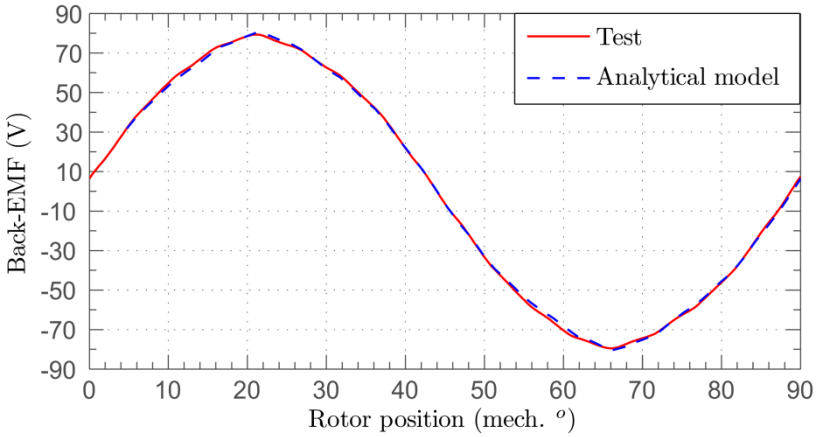

Figure 5.54. Machine II line-line back-EMF waveforms at 1350 rpm from experiment and analytical model

Figure 5.54 shows the measured and predicted line-to-line back-EMF waveforms for Machine II at 1350 rpm and Figure 5.55 shows the harmonics of the back-EMFs. For Machine II, the measured fundamental back-EMF is 77.7 V, which is 16.3% higher than that of Machine I. The predicted fundamental component of 79.1 V is1.8% higher compared with the measurement.

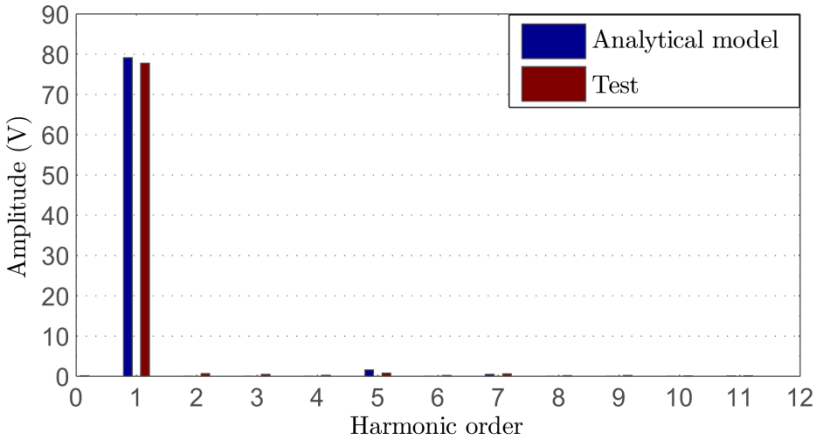

Figure 5.55. Harmonics of Machine II line-line back-EMF waveforms at 1350 rpm from experiment and analytical model

5.8.2.2 No-load loss test

In the no-load test when the machines were rotating at a given constant speed, the torque was measured and the no-load power loss variations with speed were calculated.

The measured no-load loss is separated into two parts: the iron loss P_{fe} and the friction & windage loss P_w. Idealy the friction and windage loss should be measured using the

rotor with the magnets before magnetisation then there would not be an introduction of the iron loss P_{fe} to the measurements. In the case of the prototype motor, for the reason of a limited access to the rotor before the manufacturing as the magnets were magnetised and installed into the rotor core by the manufacturers beforehand, a dummy rotor with the same size and similar weight as the real rotor has been used in the measurements of friction and windage loss. The measured friction and windage loss was scaled down according to the small weight reduction ratio of the dummy rotor due to the absence of the magnets.The no-load iron loss is calculated using the analytical model (2.18) developed in Chapter 2

Figure 5.56 shows the measured and predicted no-load loss variations with speed, including the predicted iron loss and measured friction and windage loss for Machine I. In order to account for the effect of manufacture process on the iron loss, a built factor k_b=1.75 is applied to the iron loss model in the form of $k_b \cdot P_{fe}$. As seen in Figure 5.56, after calibrating the iron loss, the predictions of total no-load loss match the measurements very well.

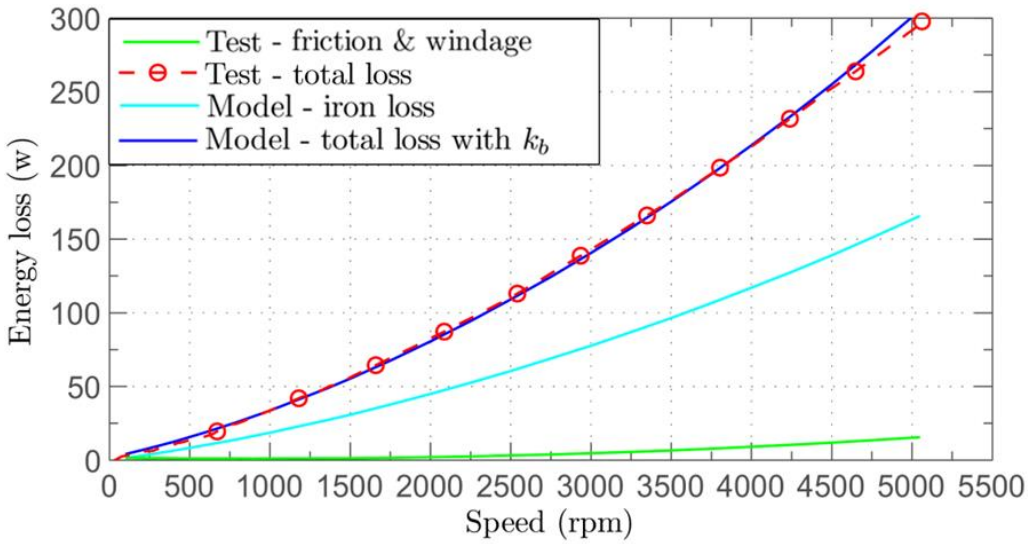

Figure 5.56. Measured and predicted no-load power loss variations with speed for Machine I

Figure 5.57 shows the measured and predicted no-load power loss for Machine II. The built factor k_b applied for Machine II is 1.89.

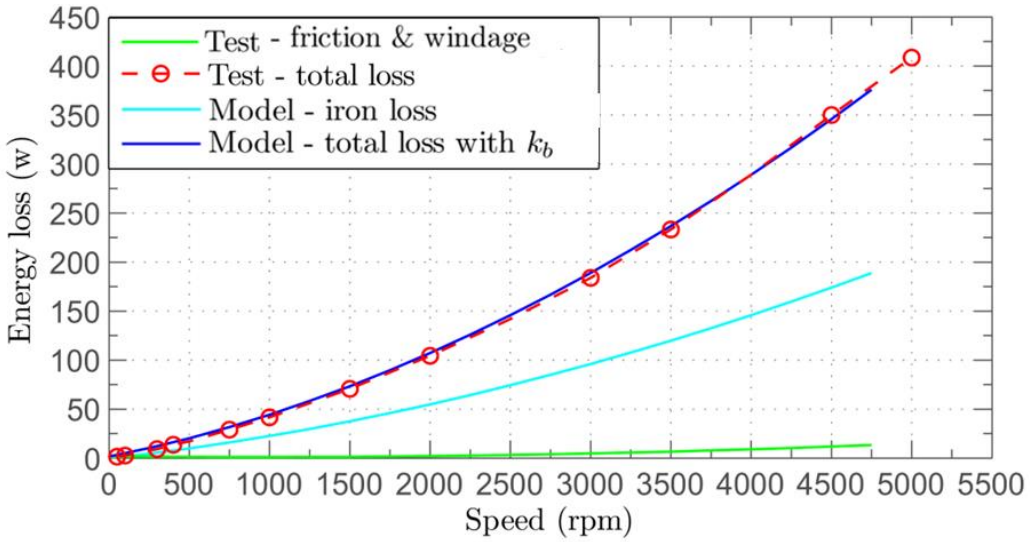

Figure 5.57. Measured no-load power loss with increasing speed and the predicted iron loss, windage loss and total no-load loss for Machine II

5.8.3 Experiments on torque capabilities

5.8.3.1 Locked rotor test

The locked-rotor test is designed to measure torque variation with rotor position with different levels of armature current. The test results provide means to examine the accuracy of the analytical flux linkage and torque models described in the Chapter 2. It should be not that the rotor is not physically locked during the test. It is instead driven at a very low speed smoothly by the dynamometer to ensure the machine reaches a steady state when the resultant torque at a given rotor position is measured.

5.8.3.1.1 Experiment method

In the test, the prototype machines are driven by the dynamometer for 2 mechanical revolutions at a very low speed of 3 rpm. DC currents are supplied to the three phase armature windings as shown in Figure 5.58, where two DC current sources are used to supply three-phase currents of which Phase A has positive current input i and Phase B and C have negative current -0.5i. When the rotor rotates, the equivalent i_d and i_q change with the rotor positions, and the torque at each position was measured by the torque transducer.

In the test, the prototypes were air-cooled by the fans. The machine temperature during the test was maintained around 50-60^{o}C which will be considered in the temperature effect model of the machines.

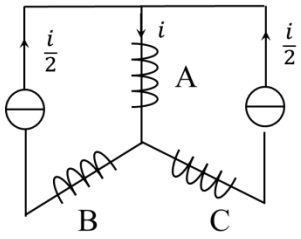

Figure 5.58. Winding connections in the "locked" rotor test

5.8.3.1.2 Experiment results

Figure 5.59 shows the torque variations with rotor position in one fourth of a mechanical revolution (one pole pair) for Machine I when fed by the current ranging from 20A to 120A. The torques predicted by the analytical model (2.3) in Chapter 2 at the same (i_d, i_q) combinations are shown for comparison.

As shown in the figure, when the rotor position is mech. 0^o, the current space vector is aligned with negative *d*-axis, thus full -i_d is applied, and i_q is 0. When the rotor rotates to mech. 22.5^o, the current space vector is aligned with positive *q*- axis, full i_q is applied, i_d is 0. Therefore the normal working area of currents for motoring operation should be between 0^o and 22.5^o, and the MTPA positions where the torque reaches the maximum value locate in this area. In the first half of the rotation, *q*-axis current is positive, thus torque recorded is also positive. In the rest half, the *q*-axis current and torque is negative.

It is seen from the figure, that from 20A to 60A, the torque predictions accurately follow the measured torque curves when the rotor position changes. However when the current is above 80A, the measured torque curves obviously deviate from the predictions. Taking the 80A curve for example, on the first half of rotation, the positive peak of the curve lags behind the predicted one while on the negative half, the negative peak leads ahead of the prediction. The lagging-leading trend becomes more pronounced when the current amplitude increases.

This can be explained by the method used in the test to calculate the rotor positions. It is assumed that the rotor speed is fixed by the dynamometer as 3 rpm during the test. This is not exactly the case when the torque produced by the prototype machine grows with increase in the current excitation. When the prototype torque is in the opposite direction as the dyno torque (in the first half), the speed of rotor actually is slightly lower. Thus, the estimated positions based on 3 rpm are behind the real ones. In contrast, in the case

of the second half of rotation, because the prototype torque is in the same direction as the dyno torque, the speed is slightly higher than 3rpm, resulting in the calculated position ahead of the real one. Of course, the above problem can be avoided should a separate rotor position sensor was used.

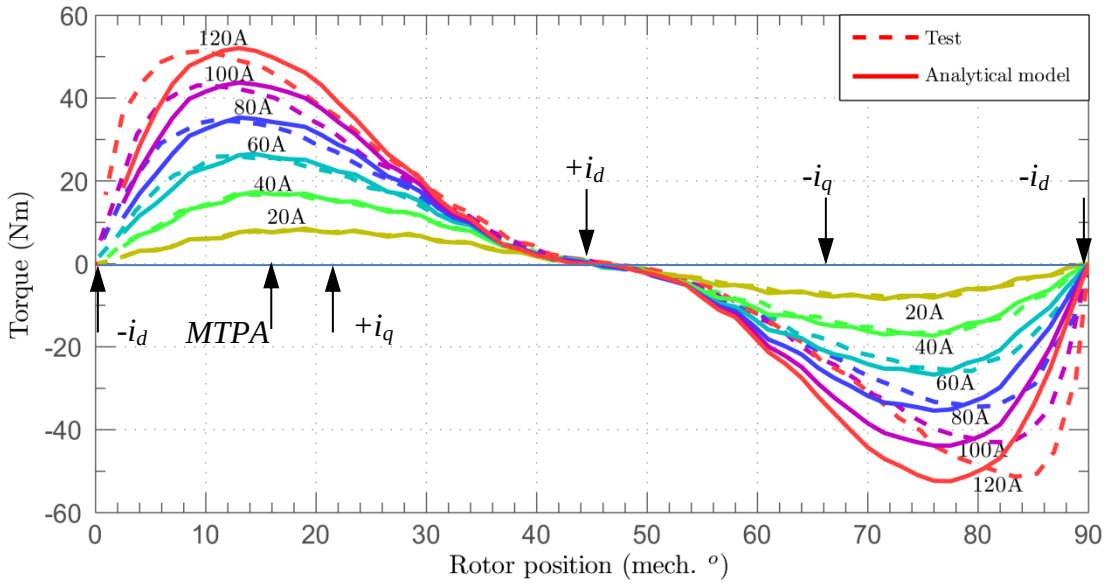

Figure 5.59. Measured and predicated torque variations with rotor position

Figure 5.60 shows the torque variations with the gamma angle (the current vector angle with respect to the q-axis, also known, torque angle) between 0^o and 90^o. It is seen that although the rotor positions in the locked rotor test have errors when the current amplitude is greater than 80A, the measured maximum torques show good agreements with those predicted by the analytical models. The torque characteristics with high current are more accurately captured with the rotor position information in of the subsequent experiments – load test with inverter. The measured torque curves in the load test exhibit good agreement with the predictions.

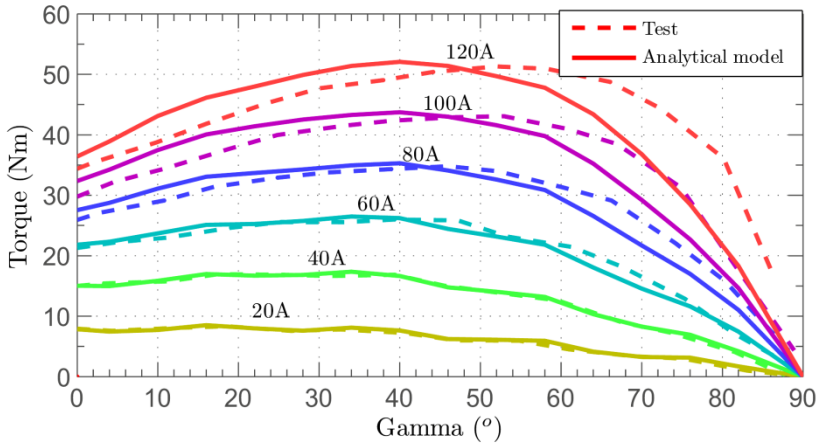

Figure 5.60. Measured and predicted orque variations with gamma angle between 0^o and 90^o

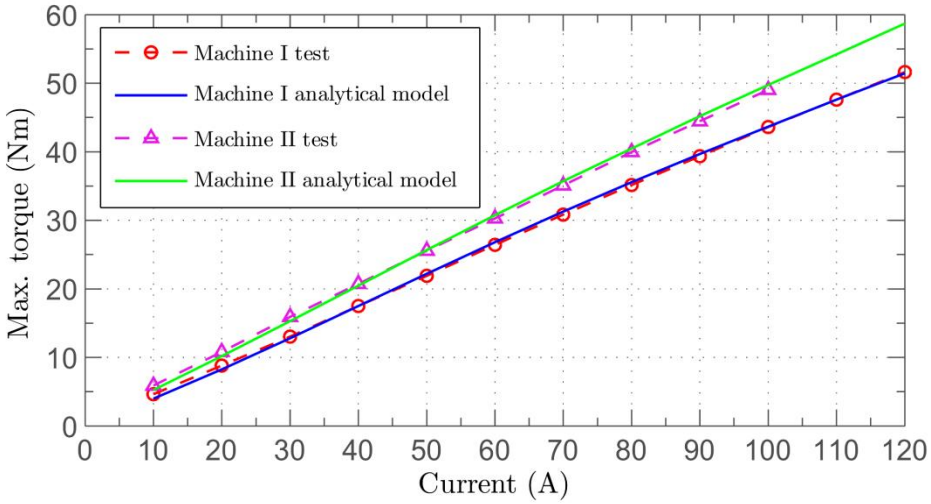

Figure 5.61. Measured and predicted maximum torque variations with current

Figure 5.61 shows the measured and predicted maximum torque variations with current amplitude for Machines I and II. It can be seen that there are very small errors between the the predictions and measurements. Table 5.23 lists the predicted and measure torque constants at 80A which is around the rated current for Machines I and II respectively. The predicted values have errors of 1.16% for Machine I and 1.35% for Machine II, compared with the measurements, respectively.

Table 5.23 Predicted and measured torque constant at 80A in the lock-rotor test for Machine I and II

	Unit	Machine I	Machine II
Measurements	Nm/A	0.445	0.499
Predictions	Nm/A	0.439	0.505
Errors	%	1.16	1.35

5.8.3.2 Cogging torque measurement

When the windings were not excited and the machines were driven by the dyno at a low speed of 6 rpm, the cogging torque for the prototypes were measured. The cogging torque can also be predicted using the analytical high-fidelity torque model illustrated in Chapter 4. Figure 5.62 shows the cogging torque in a 1/4 mechanical cycle measured for Machine I and compares it with the predicted values. From the test result, the 72th harmonic with respect to the mechanical period , which is the main harmonic component due to the least common multiple between the slot number and pole number, can be observed. The average peak-to-peak cogging torque value is 0.41 Nm, and the predicted value is 0.47 Nm.

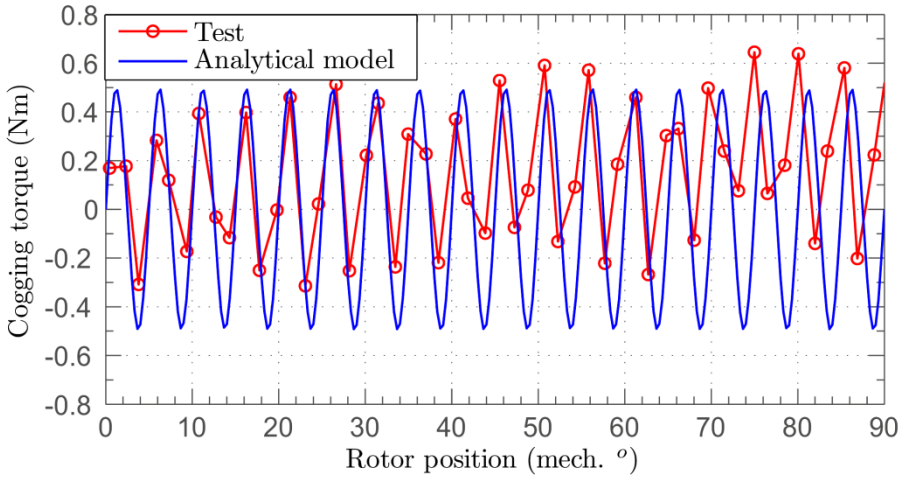

Figure 5.62. Measured and predicted cogging torque variations with rotor position in 1/4 mechanical cycle for Machine I

5.8.4 Experiments on energy loss and efficiencies on operation points

The load tests with inverter have been performed to measure the machine torque and efficiency under norminal load conditions and to validate the analytical models

including the torque model, control-current model, loss models and the temperature effect model proposed in the thesis.

In the tests, the prototypes were driven by an inverter in current-controlled mode. The shafts of the prototype machines were connected to the dynamometer machine via an in-line torque transducer. The dynamometer is speed-controlled to facilitate measurement at a given speed. The torque on the shaft is measured with the torque transducer. The prototypes were cooled with air, and operated in each operation point for a short time only.

5.8.4.1 The DC-link voltage

The inverter which drives the prototype machines is capable of 5kW continuously. The inverter's DC voltage input is provided directly by a DC voltage source of the test stand set at 120V, which is the design DC voltage of the prototype machines.

5.8.4.2 Rotor position signal

The control module of the inverter is established with the resolver interface to receive information of the rotor angular position. The position information is provided by the SLS RM44 magnetic encoder equipped on the prototype machines. Before the operation of control system of the inverter, the zero degree rotor position is detected from phase A back-EMF waveform and the measured rotor positions in the test. An offset is added to the measured rotor position coincides with the rotor angular displacement with phase A winding axis.

5.8.4.3 Test process

During the tests, the inverter operated in the current-controlled mode with *d*- and *q*- axis current i_d, i_q being controlled for given values and the machine speed was constant set by the dynamometer. The test consists of two steps. The first step is to find the MTPA points. During the tests, the current amplitude was varied from10A, 20A, …, to 100A in a step of 10A. For each amplitude, the gamma angle was varied between 10^o and 90^o, and the resultant *d*- and *q*-axis currents were tracked by the inverter. In the gamma scan process for each current amplitude, the MTPA (i_d, i_q) operation points which generates the maximum attainable torques are discovered. In the second step, voltages, currents, torques and power input and output are recorded at each of the MTPA points with increasing currents. The machine efficiencies with variable torques at a given constant speed are determined.

5.8.4.4 Test results

Figure 5.63 shows the measured torque variations with the gamma angle when the speed was 1350 rpm and the current amplitude was set at 80 A for Machines I and II, respectively. The torque predicted by the analytical model described in equation (2.3) with the same current is also shown for comparison. It is seen that the predictions agree with the test results. At the gamma angle 36^o which is the MTPA points at 80 A, the torque of Machines I and II is at their maximum value respectively. The prediction errors at the MTPA point are 3.8% for Machine I and 3.1% for Machine II, respectively. Frictional torque, which is not accounted in the model, may contribute in part to the errors. During the tests, the input powers to the motor were also measure using a high precision power analyser.

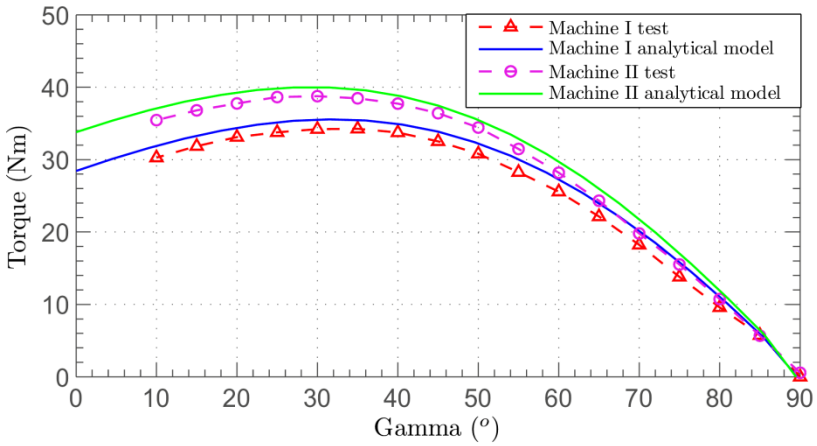

Figure 5.63. Measured and predicted torque variations with gamma angle at 80A and 1350 rpm

Figure 5.64 and Figure 5.65 show the measured efficiency variations with torque when operating at MTPA and the base speed 1350 rpm for Machines I and II respectively. By using the analytical model described in equation (2.18) with calibrated magnet flux linkages and iron loss built factors, the efficiency prediction results are given for comparison. The effect of the temperature which is ~50^{o}C during the experiments on the efficiency is considered in the analytical predictions using (4.14) and (4.15) proposed in Chapter 4.

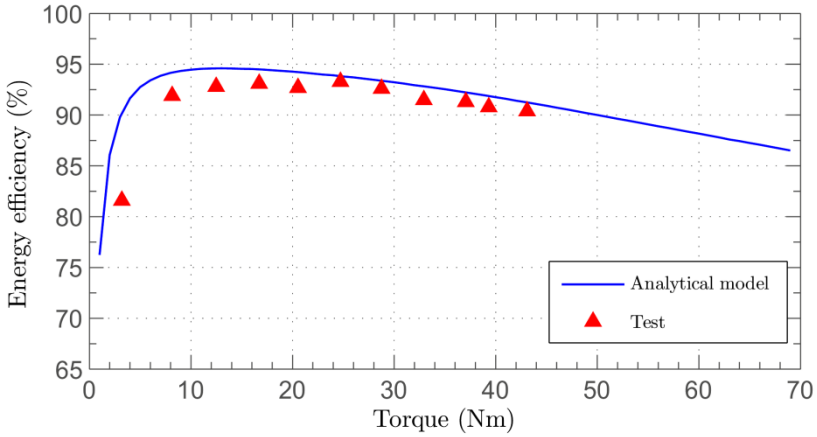

Figure 5.64. Efficiency variation of Machine I with torque at 1350 rpm

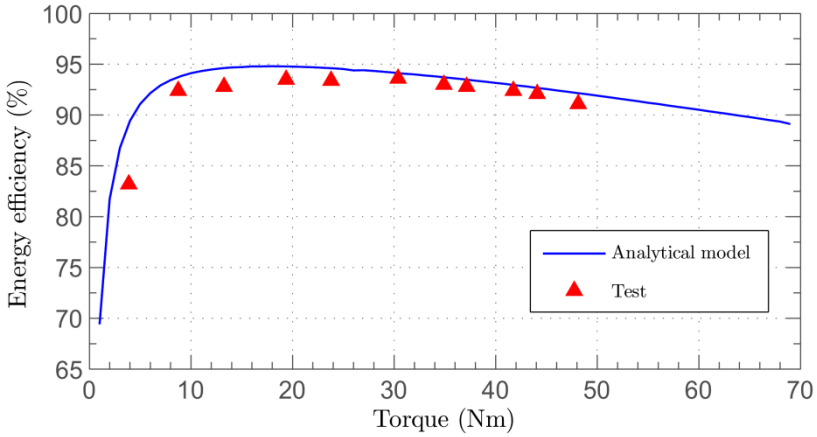

Figure 5.65. Efficiency variation of Machine II with torque at 1350 rpm

As for Machine I and II, when the torque is above 20 Nm, the efficiency predictions have errors around 1%. Table 5.24 lists the measured and predicted efficiencies and other performance indicated at the rated-torque base-speed points for the two machines, respectively. For the operating point of (37Nm, 1350rpm) of Machine I, the predicted (i_d, i_q) currents for the required torque are (-49.6A, 70.8A), being within 1A difference from the experimental currents (-50A, 70A). The predicted efficiency is 92.2%, which is 0.9% higher than the measured value of 91.3%. For the operating point of (35Nm, 1350rpm) of Machine II, the predicted (i_d, i_q) currents are (-36.1, 62.6), with ~3A error compared with the experimental currents (-40A, 60A). The predicted efficiency is 93.7%. Compared with the measured efficiency of 93%, the error is 0.7%. Given 0.2% accuracy in the torque transducer and the similar error in the power analyser, the efficiency measurement error at the rated condition may be in the region of 0.5%.

When the torque is below 10 Nm, the error between the measurement and prediction increases to 5%. This is because in the low-torque cases, the efficiency measurements are significantly affected by friction and torque measurement errors.

Table 5.24 Measured and predicted performances at the rated-torque base-speed point

	Unit	Machine I	Machine II
Speed	rpm	1350	1350
Torque	Nm	37	35
Predicted (i_d, i_q)	A	(-49.6, 70.8)	(-36.1, 62.6)
Measured (i_d, i_q)	A	(-50, 70)	(-40, 60)
Efficiency predictions	%	92.2	93.7
Efficiency measurements	%	91.3	93.0
Efficiency errors	%	0.9	0.7

5.8.5 Experiments on transient thermal performances

5.8.5.1 Experiment method

The continuous load tests were carried out to examine the transient thermal performances of Machines I and II and to verify the steady-state and transient thermal models used in the thesis.

The test uses the same settings as described in Section 5.8.4 including the inverter to drive the machines and the dynamometer to maintain the rotation speed. The two machines are controlled to operate at the rated-torque base-speed point.

During the experiments, the machines were cooled by air. As seen in Figure 5.51 (b), the cooling fans provide air flow at one the side of the machines with measured velocity in the region of 5-6 m/s, depending on the location of the sensor. The average velocity is used in the thermal steady-state and transient modelling process illustrated in Chapter 2 and Chapter 4 respectively to predict the transient and steady-state temperatures in the load test.

The load condition at the rated-torque and base-speed operation was kept for 2 hours and off for 40 minutes. The temperatures of the windings in the slots and the temperatures of the windings in the ends are recorded through the 5 thermal sensors

installed in the windings. The starting (ambient) temperatures of the machines were 23°C.

5.8.5.2 Experiment results

5.8.5.2.1 Temperatures of three phase windings

Figure 5.66 shows the measured temperatures of Machine I during the test. At the end of the two hour test, the machine reaches almost the steady-state temperature around 70°C. The winding temperatures in three phases shown are not exactly identical. For winding temperatures inside the slots, phase A temperature of 66.0°C and phase C temperature of 66.3°C are very close to each other, but phase B temperature of 63.25°C is ~3°C lower. This is probably because the thermal sensors in the slots of phases A and C were located in the machine side opposite to where the fan was installed, while the sensor of phase B was on the same side.

It is also shown in Figure 5.66 that the temperatures in the front and rear end-windings are also different. The temperature in the front end-winding of 63°C is 4°C lower than 67°C in the rear end-winding. The reason for this is the front end plate of the machine was in much contact with the mounting plate which acted as additional heat-sinker.

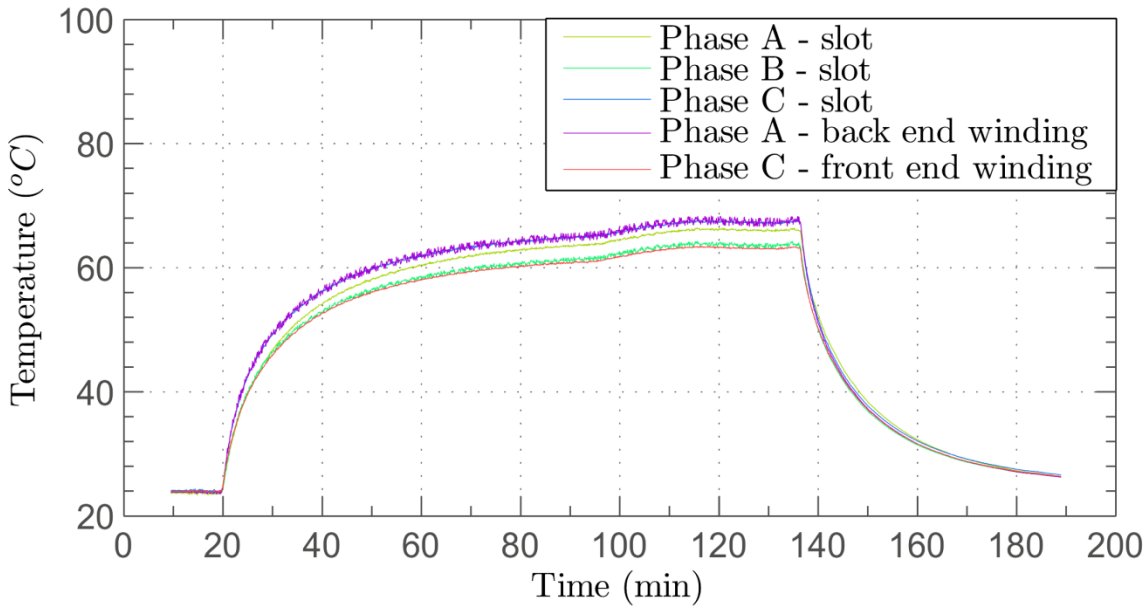

Figure 5.66. Temperature variations Machine I during the continuous load test at the rated-torque base-speed point

5.8.5.2.2 Comparison between the measurements and predictions

The temperatures in the magnets, in the slot-windings and in the end-windings predicted by the steady-state thermal model and transient model are shown in Figure 5.67 (for Machine I) and in Figure 5.68 (for Machine II) respectively, in comparison with the measured results. For the purpose of the comparison, the average temperatures in the slot-windings and in the end windings are used. From the figures it is seen that the transient predictions follow the test curves closely. At the end of the load test, the predicted temperatures lie within 2^{o}C compared with the measurements.

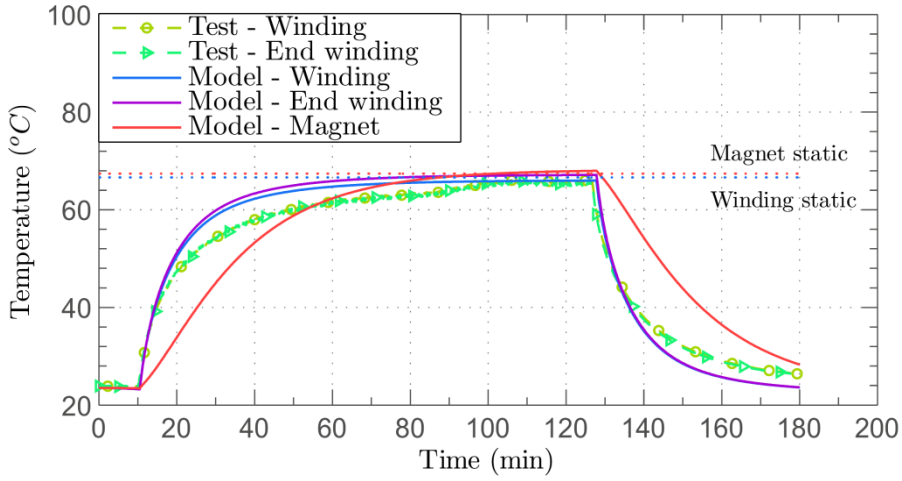

Figure 5.67. Comparison of measured and predicted temperatures during the continuous load test for Machine I

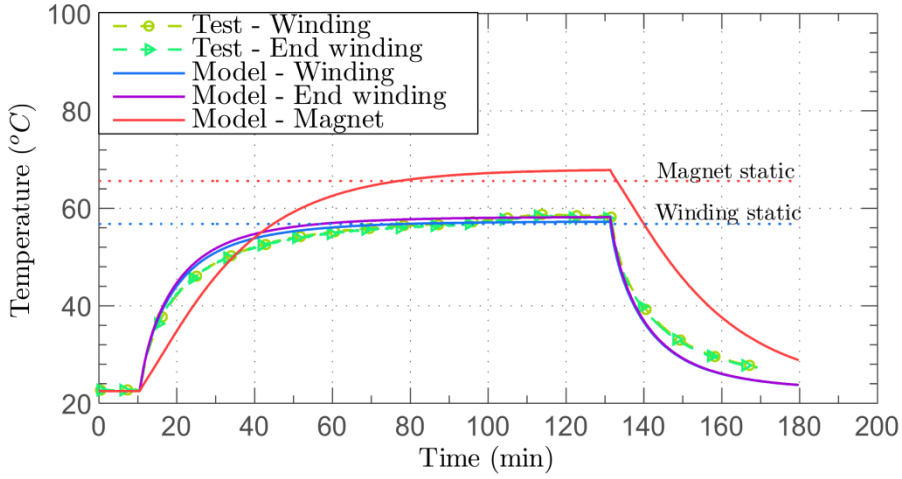

Figure 5.68. Comparison of measured and predicted temperatures during the continuous load test for Machine II

It should be pointed out that there is a noticeable difference in the measured and predicted winding temperatures during the transient. The measured transient temperatures of Machine I are lower than the predictions, and the machine exhibits larger thermal time constant. This may be caused by the additional thermal mass of the mounting plate. However, the difference in Machine II is less significant.

Table 5.25 and Table 5.26 list the detailed temperature values at the end of the rated-torque load test for Machine I and II respectively. For Machine I, the winding temperature predicted by the steady-state model is 66.6^{o}C, which is 0.4^{o}C higher than the transient predicted value, and 1^{o}C higher than the measured value. While in Machine II, the winding temperature predicted by the steady-state model is 56.8^{o}C, which is 0.4^{o}C lower than the transient predicted result, and 1.4^{o}C lower than the measured value. The steady-state winding temperatures of the two machines differ around 10^{o}C due to the higher copper loss in Machine I. While this effect is cancelled by the higher iron loss with Machine II, the predicted magnet temperatures between the two machines are similar within 2^{o}C difference.

It should be pointed out that there is a noticeable difference in the measured and predicted winding temperatures during the transient. The measured transient temperaures of Machine I are lower than the predictions, and the machine exhibits larger thermal time constant. This may be caused by the additional thermal mass of the mounting plate. However, the difference in Machine II is less significant.

Table 5.25 Predicted and measured temperatures at the end of the rated-torque load test for Machine I

	Unit	Steady-state predictions	Transient predictions	Measurements	Max. errors
Windings	^{o}C	66.6	66.0	65.6	1.0
End windings	^{o}C	-	67.1	65.2	1.9
Magnets	^{o}C	67.4	68.0	-	-

Table 5.26 Predicted and measured temperatures at the end of the rated-torque load test for Machine II

	Unit	Steady-state predictions	Transient predictions	Measurements	Max. errors

Windings	^{o}C	56.8	57.2	58.2	-1.4
End windings	^{o}C	-	58.2	57.7	0.5
Magnets	^{o}C	65.6	67.7	-	-

5.9 Conclusion

This chapter formulates a design process of permanent magnet machine for a light-duty electric vehicle traction system by using of proposed models, in which the benefits of advanced modelling techniques are exhibited. Employing the machine analytical models presented in the previous chapters, a computationally-efficient optimisation technique for EV traction machine design is developed; a wide range of PM machine topologies are optimised and assessed for EV traction system; optimisation of the selected 18-slot 8-pole IPM machine against a series of EV machine design criteria, the subsequent prototype building and test are implemented. Through the design process for the EV traction system and experiments, the effectiveness, computational efficiency, and accuracy of the proposed designing methods are exhibited and validated. Moreover, the validations provided by the experiments in return show strong supports for reliability of the work in terms of the machine topology comparison, geometry design/optimisations and simulations in the thesis.

CHAPTER 6 Design optimisation of EV traction machines for distributed power trains

Special issues on the machine designs for electric vehicle traction system including driving cycles and distributed traction systems are studied in this chapter. Distinctive torque-speed distribution characteristics of widely-used driving cycles are described and discussed. Optimisations of SPM and IPM machine designs as representative examples are implemented against different driving cycles to investigate the influences of the driving cycles on optimised designs in terms of geometry, losses and efficiency over torque-speed envelope. Distributed traction system is studied by employing a two-motor (front and rear) traction system as a generic example. Various machine topologies including SPM, IPM machines and SynRM or PMa-SynRM machines for the drive system, and optimal power split ratio between the two motors are investigated to improve the energy efficiency of the traction system.

6.1 Electric vehicle driving cycles and their influence on traction machine designs

6.1.1 Common electric vehicle driving cycles

The driving cycles are designed for vehicle test procedures to acquire vehicle exhaust gas emission performance, energy efficiency and other vehicle properties and performance indicators. High energy efficiency capability of traction machines over driving cycles is a crucial design objective for machine designers. Besides good thermal behaviour during driving cycles is also an important design goal. Therefore it is necessary to study the features of different driving cycles and their influences on the machine designs.

There are several commonly-used driving cycles among the regions such as Europe, USA and Japan. In Europe, the widely used driving cycles include New European Driving Cycles (NEDC), Common Artemis Driving Cycles and the Worldwide Harmonized Light Vehicles Test Procedure (WLTP). These driving cycles demand different torque-speed output from the traction machines, requiring low, middle or high level of torque-speed capabilities. Therefore, specifications of an EV traction machine should consider the requirements of driving cycles, and optimisations of machine design should target to maximise the energy efficiency during driving cycles while satisfying all other constraints. Consequently, the machine designs will be affected by driving cycles.

6.1.1.1 New European Driving Cycles

This is a combined chassis dynamometer test used for emission testing and certification in Europe. It is composed of four ECE Urban Driving Cycles, simulating city driving,

and one Extra Urban Driving Cycle (EUDC), representing highway driving conditions. The cold-start version of the test, introduced in 2000, is referred to as the New European Driving Cycle (NEDC) [23]. Because the NEDC has mild speed variations, it features low torque, middle-to-high speed requirements on traction machines. Figure 6.1 shows the vehicle speed profile of the NEDC cycle.

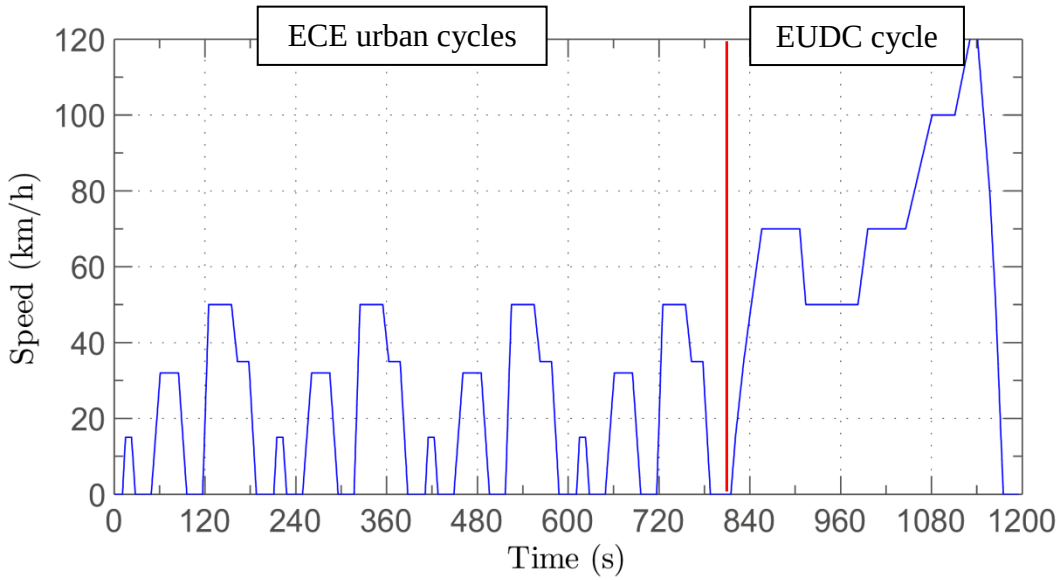

Figure 6.1. Vehicle speed during the NEDC cycle.

6.1.1.2 Common Artemis Driving cycles

The Common Artemis Driving Cycles (CADC) are chassis dynamometer procedures developed within the European Artemis (Assessment and Reliability of Transport Emission Models and Inventory Systems) project, based on statistical analysis of a large database of European real world driving patterns. The cycles include three driving schedules: (1) Urban, (2) Rural road and (3) Motorway. The Motorway cycle has two variants with maximum speeds of 130 and 150 km/h. For the Artemis Urban Driving Cycle (Artemis), the speed is maintained at low-to-middle level. But due to the frequent acceleration and deceleration, it has a high demand output torque from traction machines. Figure 6.2 shows the vehicle speed during the Artemis urban driving cycle.

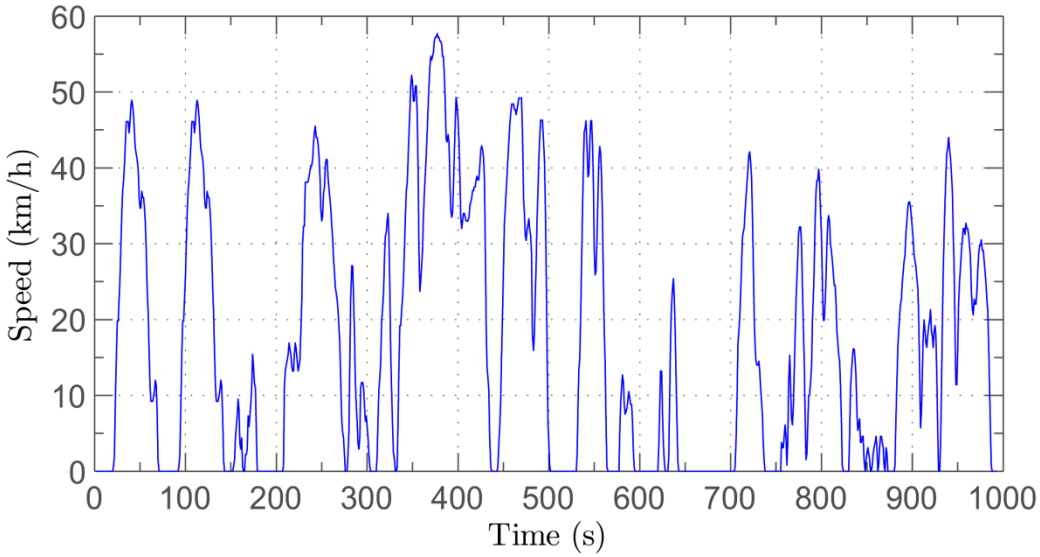

Figure 6.2. Vehicle speed during the Artemis urban driving cycle.

6.1.1.3 The worldwide harmonised light vehicles test procedure

The worldwide harmonized light vehicles test procedure (WLTP) is a chassis dynamometer test cycle for the determination of emissions and fuel consumption from light-duty vehicles. The test is being developed by the UN ECE GRPE (Working Party on Pollution and Energy) group. When finalized, the WLTP test is expected to replace the European NEDC procedure for type approval testing of light-duty vehicles.

The WLTP procedure includes three test cycles applicable to vehicle categories of different power-to-mass (PMR) ratio. The PMR parameter is defined as the ratio of rated power (W) / curb mass (kg). The curb mass means the “unladed mass” as defined in ECE R83. The cycle definitions may also depend on the maximum speed of the vehicle. For the power rating of the electric vehicles mainly studied in the thesis, the WLTP class 1 cycle with PMR<22 applies. Figure 6.3 shows the vehicle speed during a WLTP class 1 cycle. It can be seen from the figure that the cycle has similar low speed operations, but less frequent speed changes, compared to the Artemis. Thus it highlights moderate requirements of both torque and speed in between the NEDC and Artemis.

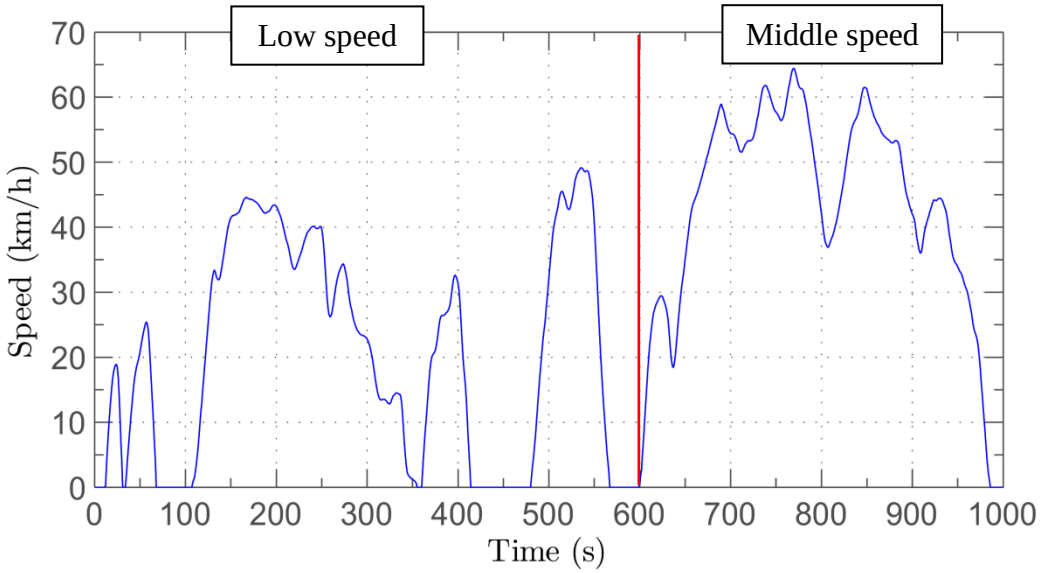

Figure 6.3. Vehicle speed during the WLTP class 1 cycle for light vehicles

6.1.1.4 On-road driving cycles developed in CRF

In the thesis, three other driving cycles are also made use of. They are based on measurement data of real driving, and defined in terms of different torque-speed requirements and air cooling conditions by Centro Ricerche Fiat Srl (CRF). Figure 6.4 shows the actual journeys for real-driving data collection of the mission profile.

Figure 6.4. Actual journeys for real-world gathering of mission profile by CRF

Figure 6.5 shows the machine speed during the three cycles calculated from the measured vehicle velocity data, the tyre size and the gear ratio of the transmission. As seen in Figure 6.5, the Urban and Extra Urban driving cycles features low torque, medium-to-high speed driving, while the Up-Down Hill cycle requires frequent high

acceleration/deceleration torque at low speed, and is therefore most demanding. Analysing the torque-speed characteristics of the three CRF driving cycles, the combination of the Urban and Extra Urban Driving cycles resembles the NEDC driving cycle, while the Up-and-Down Hill driving cycle is closer to the Artemis.

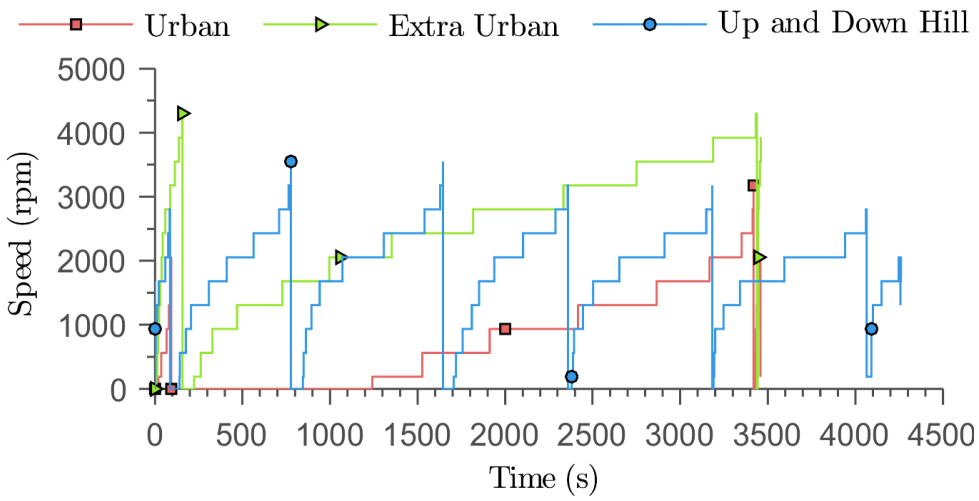

Figure 6.5. Machine speed of the three driving cycles derived from CRF

As discussed in the above, the NEDC and Artemis have distinct energy distribution on a machine's torque-speed operation range. These different torque-speed demands from the two cycles indicate very different loss characteristics in motors. Generally speaking, as for permanent magnet machines, iron loss and high-speed copper loss would be dominant in the total loss over the NEDC, while in the Artemis low-speed copper loss is the larger contributor. Thus the optimization aiming at the minimum losses over NEDC results in a machine design different from that of Artemis. Since the NEDC and Artemis shows two types of representative characteristics of driving cycles, in the following discussions, the two are taken as target driving cycles against which machine designs and optimisations are implemented.

6.1.2 Driving cycles application in machine design specifications

In order to determine the machine specifications of torque and speed, the requirements from driving cycles need to be considered.

According to the vehicle speed profiles during driving cycles, the required torque curves could be simulated using a vehicle dynamic model. A continuous torque envelope on traction machines can be designed, under which the vehicle can continuously operate during driving cycles. Apart from the continuous torque requirement, the peak torque

requirement needs to be typically more than 2 × continuous torque in order to satisfy the demand on acceleration and climbing capabilities. The maximum cruise speed of traction machine could be determined accordingly based on the maximum speed during driving cycles [16] or higher depending on manufacturer's requirement.

Traction machine studied in this section is designed for the distributed power train of a micro-size electric vehicle with front and rear wheel drives. The front and rear wheels are driven independently. A machine is mounted on the front axle with gear ratio of 4. Two identical machines with different design from the front one are mounted on the rear axle with gear ratio 7. The nominal power split ratios among the three machines are designed as 40% : 30% : 30%. Figure 6.6 shows the traction system.

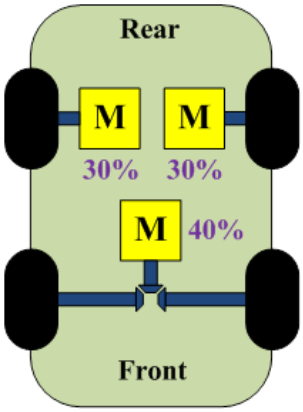

Figure 6.6. Three-motor traction system

Table 6.1 lists relevant physical parameters of the studied vehicle which are used to establish the vehicle dynamic model. The NEDC cycle is employed as a reference cycle together with requirements for peak acceleration and hill-climbing to define the traction machine's torque-speed specifications. Figure 6.7 shows the torque speed envelopes and the trajectory over NEDC. Table 6.2 lists the derived machine design specifications and constraints for the front motor in the drive system.

Table 6.1. Vehicle Data

Parameter (Unit)	Value
Tyre size	165/50 R15
Radius of wheels (m)	0.273
Vehicle mass (kg)	800
Gravitational acceleration (m/s^2)	9.807
Rolling resistance	0.007

Product of drag coefficient and front area (m^2)	0.35
Air density (kg/m^3)	1.25
Efficiency of differential	0.980

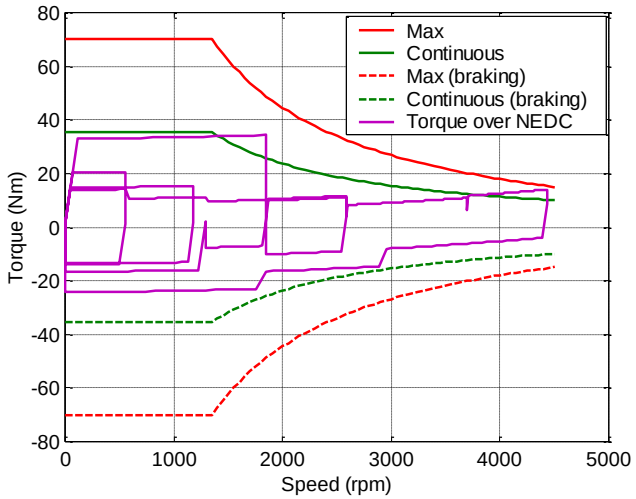

Figure 6.7 Torque speed envelope and trajectory over NEDC

Table 6.2 Front Motor design specifications and restrictions

Base speed	1350 rpm
Maximum cruise speed	4500 rpm
Maximum speed	5050 rpm
Peak torque below and at base speed	70 Nm
Continuous(rated) torque below and at base speed	35.5 Nm
Peak Power	9.9 kW
Continuous Power	5 kW
Peak Power at maximum cruise speed	7 kW
Continuous Power at maximum cruise speed	4.7 kW
Maximum current limit	170 A
Maximum current density limit (rms)	20 A/mm^2
Nominal DC link Voltage	120 V
Peak line-to-line voltage at maximum speed	<240 V
Stator outer diameter	150 mm
Stack length	118 mm
Ambient temperature	55 ^oC
Cooling	Air -cooled

As can be seen, the continuous and peak power ratings are 5 kW, and 9.9 kW, respectively. For ease of mechanical integration, stator outer diameter, shaft radius and stack length are kept constant. Likewise, current and voltage limits should be imposed together with thermal constrain during the design process.

6.1.3 Representative points derivation of driving cycles for machine designs

In order to minimize the EV traction motor loss over a driving cycle during a machine design process, the motor efficiency at each time instant of the driving cycle would have to be calculated for a given set of design parameters which satisfy all volumetric, electrical and thermal constraints. Taking the NEDC for an example, for a time interval of one second, the NEDC contains 600 operating points, excluding the repeat of ECE-15 city cycle. The computation time for the evaluation of motor energy efficiency of a single design over the driving cycle would reach 200 hours assuming 20 minutes for FE calculation of each operating points. Thus the entire optimization process requires enormous amount of time and effort.

Figure 6.8 shows the energy distribution of torque-speed operation points over NEDC and Artemis. By employing the representative points for the driving cycles [77], the energy centre-of-gravity points are calculated and shown in Figure 6.9 for the NEDC and Artemis. In this way, thousands of points in the time domain of the driving cycles are reduced into tens of characteristic torque-speed points. The resulting FE calculation time is drastically reduced while maintaining good accuracy for loss calculation (e.g. less than 3% error for the NEDC). As discussed in the above section, the NEDC, with less frequent acceleration/deceleration, has 12 representative points; the Artemis has 55 points Artemis with frequent and abrupt speed variations. Table 6.3 lists details of the 12 NEDC points including speed, torque, energy and duration.

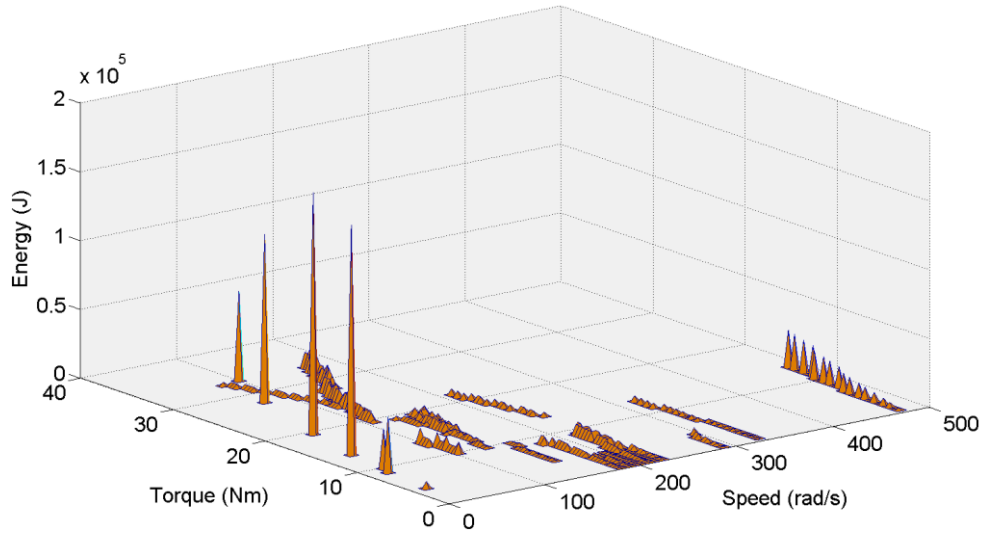

(a)

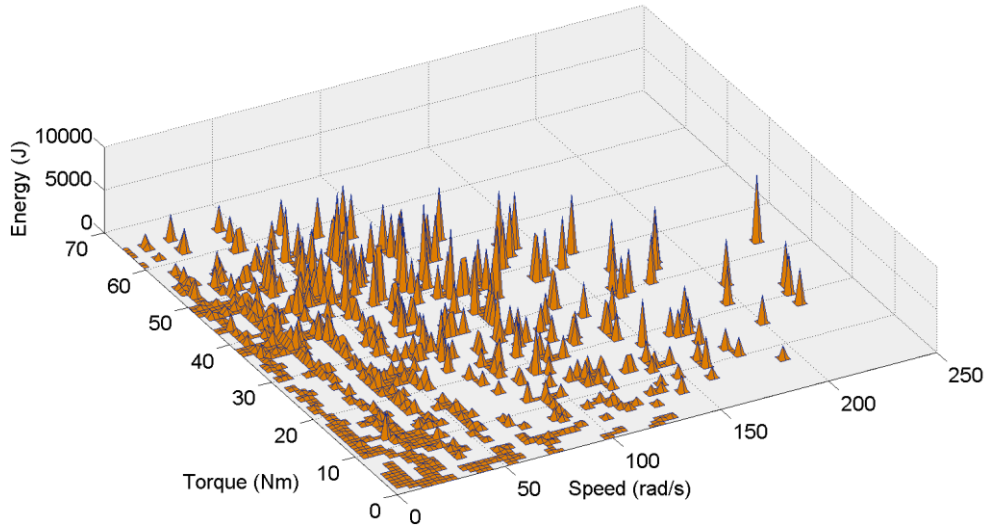

(b)

Figure 6.8. Energy distribution of torque-speed operation points over (a). NEDC and (b). Artemis

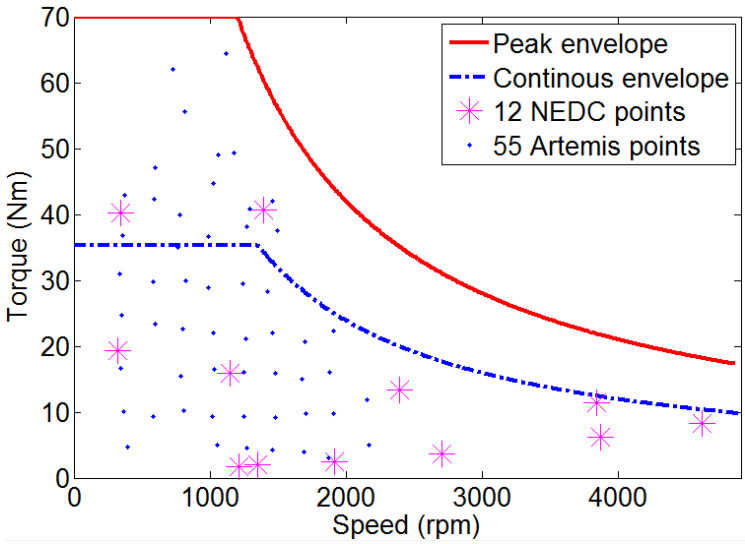

Figure 6.9. The NEDC and Artemis representative points within the continuous and peak torque-speed envelopes

Table 6.3 12 representative NEDC points

	Speed (rad/s)	Torque (Nm)	Duration (s)	Energy (kJ)	Normalized energy (%)
Low speed points	32.1	15.9	72	36.9	3%
	33.9	33.0	7	8.0	1%
	119.4	13.0	132	203.7	19%

	120.6	1.7	103	21.4	2%
	134.6	1.7	67	15.5	1%
	139.0	33.6	22	103.0	10%
	190.2	2.4	206	94.4	9%
High speed points	248.6	10.9	45	122.2	12%
	269.1	3.8	103	104.4	10%
	385.1	6.5	30	76.1	7%
	387.5	10.6	58	235.8	22%
	459.3	8.6	10	41.3	4%
		Total:	855	1062.7	100%

6.1.4 Influence of driving cycles on optimised SPM designs

The maximisation of energy efficiency over driving cycles is a key objective of design optimisations of electric vehicle traction machines. The distinct characteristic of representative torque-speed point distribution of a driving cycle will considerably affect the optimisation results. Therefore influences of driving cycles on machine optimisation results in terms of geometry parameters, energy losses and thermal behaviours are investigated on SPM machine in this section. An investigation on an IPM machine is illustrated in the next section.

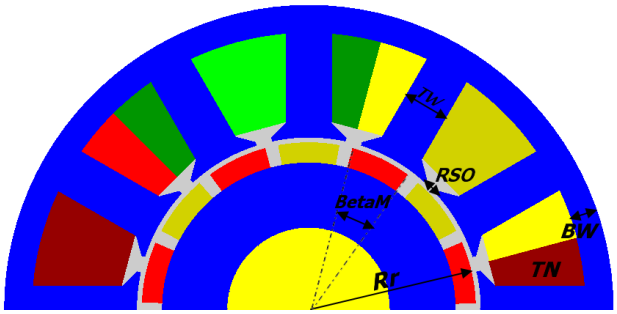

Figure 6.10. 12-slot 14-pole SPM topology and geometry parameters to be optimised

* TN is the number of turns in one coil

Without loss of generality, Figure 6.10 shows the 12-slot 14-pole SPM topology and six geometry parameters to be optimised. The SPM is optimised following the optimisation methodology, which is illustrated in Chapter 4. The design specifications and constraints to be satisfied in the optimisation processes are listed in Table 6.2. The optimisations are implemented, respectively, to maximise the energy efficiency of three driving cycles: the NEDC, Artemis and Combined Artemis-NEDC. Thereafter, the three

optimised designs (hereinafter referred to as the NEDC-optimised, Artemis-optimised and combined-optimised designs) are compared to assess the influence of the driving cycles on the design outcomes.

6.1.4.1 Efficiency performance differences

Figure 6.11 shows the outcome geometries after the three optimisations. Table 6.4 lists energy efficiency values over driving cycles of the initial and the optimised designs. For each driving cycle, the efficiency optimised against this cycle is shown as the reference, while the efficiencies of the machine optimised against other two driving cycles are also evaluated and their differences from the optimal one are shown in the table.

Besides the improvements by up to 0.7% on efficiencies obtained after optimisations on the initial design, clear efficiency differences among the optimised designs can be observed. The optimisations gain the optimal efficiency performances over their target driving cycles, but lose 0.7-0.9 % over the other driving cycles compared with the optimal values. For example, for the efficiency performances over the NEDC, the NEDC-optimised design has the highest value 95.16 %. In comparison, the Artemis-optimised design's efficiency is 0.93 % less, and the combined-optimised design's is 0.05 % less. On the other hand, for the NEDC-optimised design, its efficiency over the Artemis is 0.72% less compared with the Artemis-optimised design. The combined-optimised design shows performance in-between, with its NEDC efficiency quite close to the NEDC-optimised one, while its Artemis efficiency is not compromised by much.

It should be noted that even an increase in efficiency by only 0.5% can bring around 10% reduction of energy loss which is very significant. Therefore 0.7-0.9 % difference in efficiency, i.e. 14-18 % loss difference, among the optimisation results shows the selection of driving cycle as the target is important for machine optimisations.

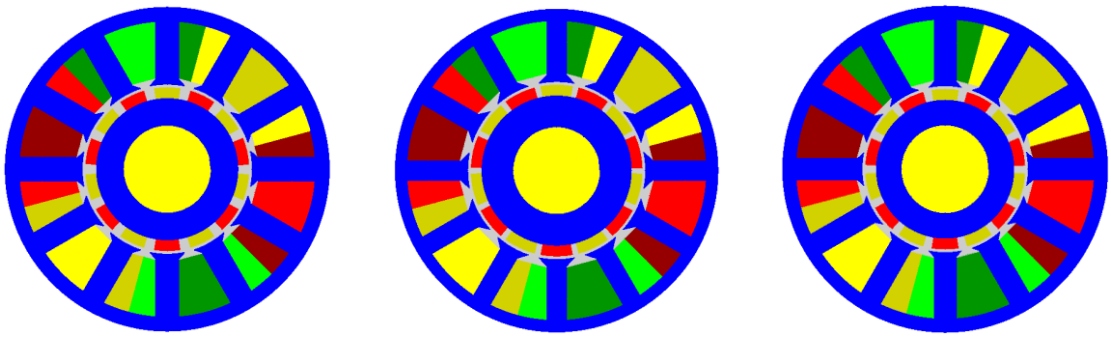

(a) (b) (c)

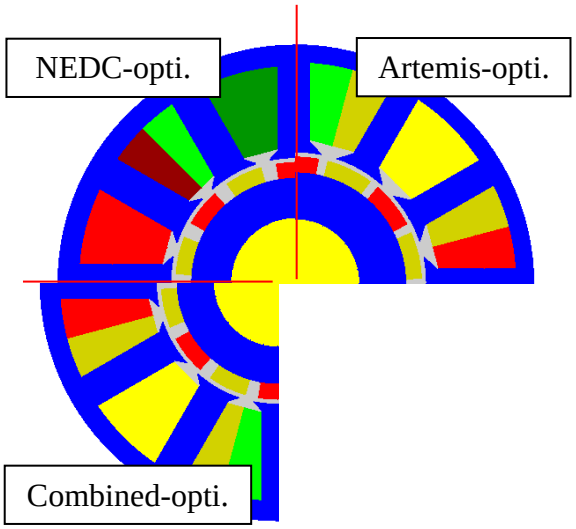

(d)

Figure 6.11. Optimised machine designs targeting (a) NEDC (b) Artemis (c) the combined cycle respectively; Geometry comparison among three optimised designs is shown in (d).

Table 6.4 The energy efficiencies over driving cycles of optimised machine designs

Optimised machine designs	Eff_{NEDC}	$Eff_{Artemis}$	$Eff_{combined}$
Initial design	-0.69%	-0.29%	-0.23%
Optimised for NEDC	95.16%	-0.72%	-0.07%
Optimised for Artemis	-0.93%	94.90%	-0.23%
Optimised for Combined (NEDC and Artemis)	-0.05%	-0.51%	94.77%

6.1.4.2 Geometry parameter differences

It can be seen from Figure 6.11 that the NEDC-optimised geometry has an apparently different set of parameters from the Artemis one. Table 6.5 compares the parameters of the three optimised designs. To minimise the discrete effect of number of turns, an integer plus half turn is allowed during the optimisation, and this can be realized by terminating a coil at different ends of the winding.

Table 6.6 illustrates the trend of the leading design parameter changes observed during the optimizing process for the purpose of reducing iron loss, high-speed copper loss and low-speed copper loss. Since the NEDC has a high energy distribution in high speed regions, this cycle requires its optimization to mainly aim at reducing iron loss and high-speed copper loss. Thus compared with the optimal design for the Artemis, BetaM and rotor radius are lower to reduce the permanent magnet field, and hence the flux

linkage due to the magnets, while the stator tooth width is increased to reduce flux density. The slot opening is reduced and the turn number is increased to increase the synchronous inductances and hence improve field-weakening capabilities. As for the Artemis, which needs high torque at low speeds, the reduction of low-speed copper loss is essential. Therefore, the rotor radius, BetaM and slot opening go up to increase magnet flux linkage, the tooth width goes down to increase copper area and the turn number goes down to decrease the phase resistance.

The optimisation trends of geometry parameters differ distinctly between the NEDC optimisation and the Artemis optimisation, leading to apparently different permanent magnet usage. As seen in Table 6.5, the NEDC-optimised design has 0.73 kg of permanent magnets which is 19% less than that of the Artemis-optimised design which is 0.9 kg. Besides the NEDC-optimised design also has 5% less copper usage than the Artemis one. Again compared with the two designs, the combined-optimised motor has the material usage in-between, with the permanent magnet usage closer to the NEDC-optimised one.

Table 6.5 Geometry parameters after optimisations

Motor geometry	TW (mm)	Rr (mm)	RSO (mm)	BetaM (deg)	TN (turn)	PM (kg)	Winding (kg)
Initial design	11.2	41.25	3.75	150	8	0.9	2.34
Optimised for NEDC	10.88	38	4.49	132.6	8.5	0.73	2.64
Optimised for Artemis	9	40	4.5	155	7.5	0.9	2.78
Optimised for Combined	10.25	37	4.5	140	8.5	0.75	2.78

Table 6.6 Parameter modification trends for minimization of losses

	Pfe	$Pcu_{(High\ Speed)}$	$Pcu_{(Low\ Speed)}$
TWS	Up	Up	Down
Rr	Down	Down	Up
BetaM	Down	Down	Up
RSO	Down	Down	Up
TN	Up	Up	Down

6.1.4.3 Loss differences

Two bar charts of Figure 6.12 show the motor loss components over the NEDC and Artemis, respectively. Three optimised machine designs are compared together in the figure. Table 6.7 lists loss values during the NEDC, and Table 6.8 lists the loss values

during the Artemis. In the figure and tables, high speed is defined as the speed above 2000 rpm when the machine operates in field weakening mode.

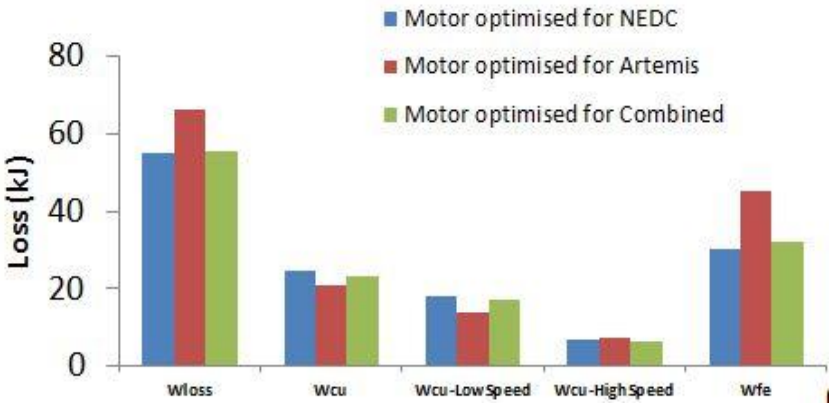

(a)

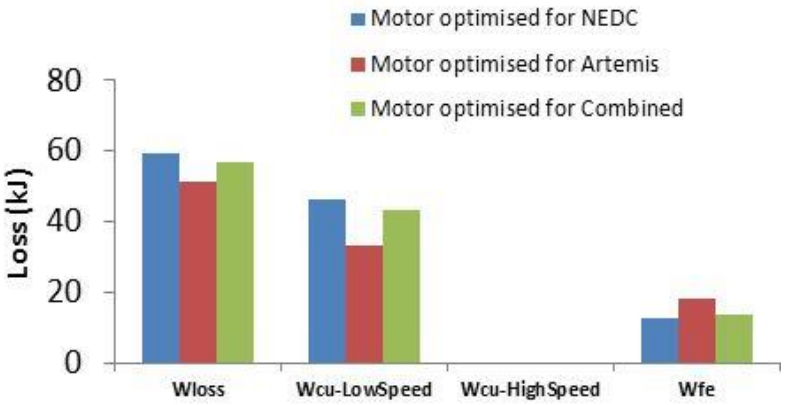

(b)

Figure 6.12. Loss components over (a). NEDC and (b). Artemis of the optimised motor designs for the NEDC, Artemis, and combined cycle, respectively.

Table 6.7 Losses over NEDC of the optimised machine designs

Designs optimised against-	Wcu-total	Wcu-LowSpeed	Wcu-HighSpeed	Wfe-total	Wfe-LowSpeed	Wfe-HighSpeed	Wcu/Wfe
NEDC	24.61	17.94	6.67	30.18	23.25	6.94	81.55%
Artemis	-14.95%	-23.70%	8.61%	49.45%	49.12%	50.55%	46.41%
Combined	-5.31%	-5.33%	-5.25%	6.50%	6.31%	7.13%	72.51%

Table 6.8 Losses over Artemis of the optimised machine designs

Designs optimised against-	Wcu-total	Wcu-LowSpeed	Wcu-HighSpeed	Wfe-total	Wfe-LowSpeed	Wfe-HighSpeed	Wcu/Wfe
NEDC	46.54	46.54	0	12.71	12.71	0	366%
Artemis	-28.67%	-28.67%	0	44.04%	44.04%	0	181%
Combined	-6.48%	-6.48%	0	6.27%	6.27%	0	322%

To compare the loss characteristics of designs clearly, in the loss values listed in the tables, the losses associated with the Artemis-optimised and the combined-optimised designs are shown as the differences in percentage referring to the values of the NEDC-optimised design.

Firstly as regards the loss characteristics of the driving cycles, the NEDC has iron loss as the major loss component, and the copper loss is only 40% ~80% of the iron loss. On the contrary the major loss in the Artemis is copper loss which is about 1.8 and 3.7 times higher than the iron loss.

Under the influences of driving cycles, the optimised designs exhibit explicitly different loss behaviours. Compared with the NEDC-optimised motor, the Artemis-optimised design greatly reduces the low-speed copper loss by about 25% in both cycles but generates about 45% higher iron loss and about 10% higher high-speed copper loss, thus has higher efficiency in the Artemis but lower efficiency in the NEDC. The motor optimised against the combined cycle tends to balance among the three loss components.

The contrasting loss behaviours lead to different thermal performances for the optimised designs albeit all the designs satisfy the thermal constraints. Compared with the Artemis-optimised design, the NEDC-optimised design has larger turn number and greater tooth width and, hence, slightly great phase resistance, stronger armature reaction and MMF harmonics. As a result, it has more iron loss and magnet eddy current loss in the rotor and larger copper loss at the rated operating point. Since the air gap, winding insulation and potting materials have poor conductivity, the higher rotor loss and higher copper loss with the NEDC-optimised design result in around 15 ^{O}C higher steady-state winding temperature at the rated condition.

6.1.4.4 Efficiency difference over torque-speed envelope

The performance differences of the optimised designs can also be seen from their efficiency maps in relation to the driving cycles. Figure 6.13 shows the efficiency map over the torque-speed range of the NEDC-optimised design.

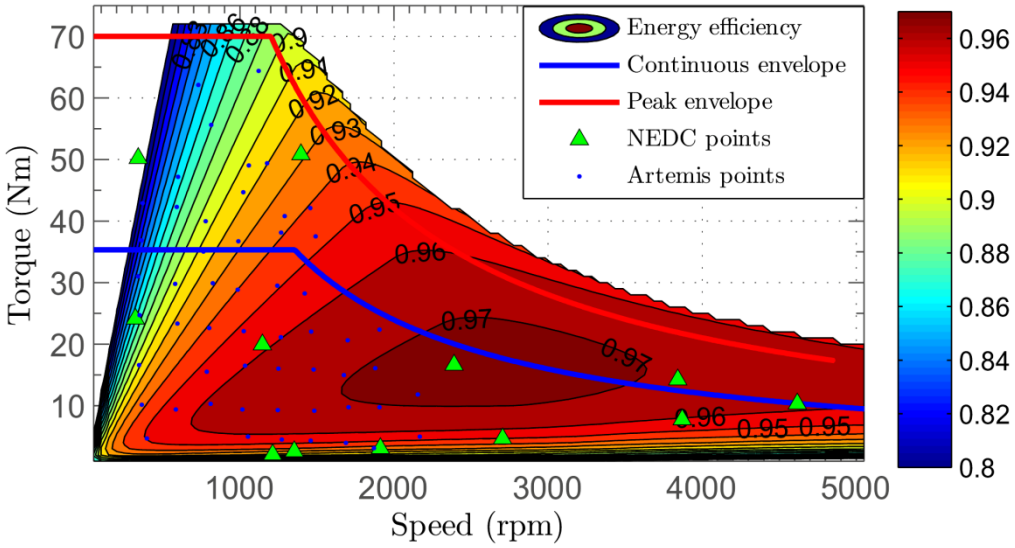

Figure 6.13. Efficiency map of NEDC-optimised motor

In order to compare the efficiencies of the design clearly, Figure 6.14 highlights high-efficiency regions of the three optimised designs, where the high-efficiency region is defined as the torque-speed operation region with efficiency greater than 94% and up to 97%. Furthermore, Figure 6.15 shows the efficiency difference map between the NEDC-optimised design and the Artemis-optimised one.

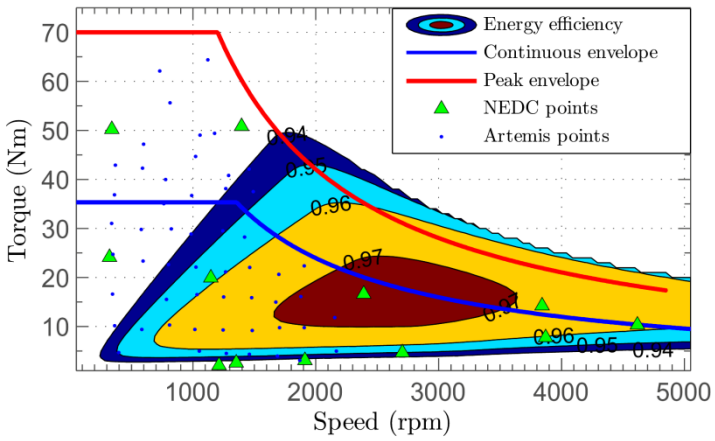

(a)

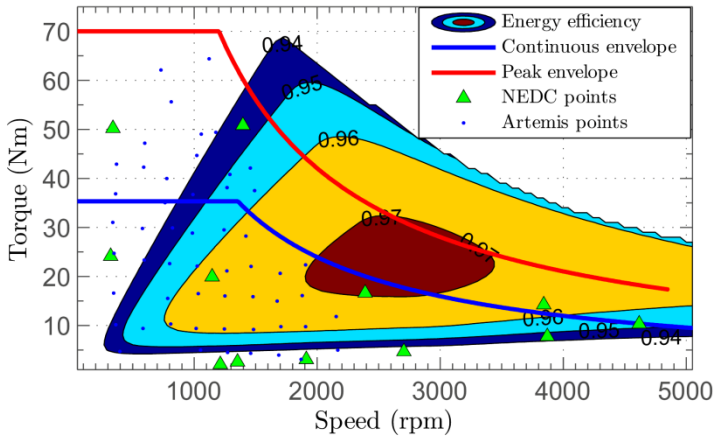

(b)

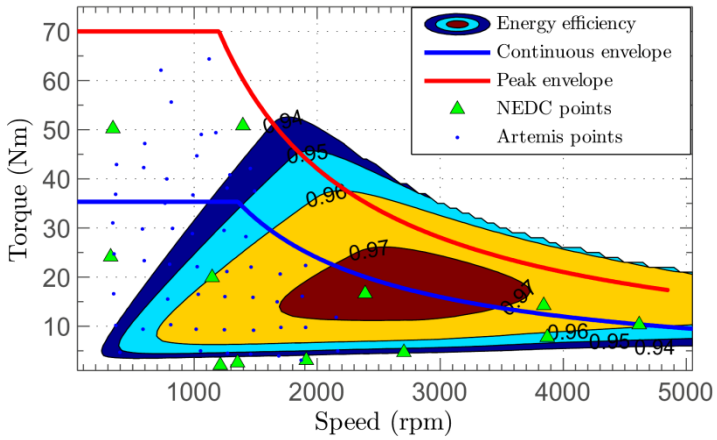

(c)

Figure 6.14. Comparison on high-efficiency region distributions among (a) the NEDC-optimised, (b) the Artemis-optimised, and (c) the combined-optimised designs.

From Figure 6.13 and Figure 6.14 (a), it can be seen that over a broad torque-speed operation area the NEDC-optimised design has high efficiency up to 97%. Its high-efficiency region is in the high speed, low torque region, and it covers most of the NEDC and Artemis representative points. Compared with the NEDC-optimised design, Figure 6.14 (b) shows that the high-efficiency region of the Artemis optimised design covers a broader area and extends to higher torque area, enclosing more Artemis points, but leaving low-torque NEDC points in a relatively low efficiency region. Again the area and location of the high-efficiency region of the combined-optimised design appear in between.

The high-efficiency distributions between the NEDC-optimised and the Artemis-optimised designs are further illustrated in Figure 6.15. On this efficiency difference

map, the negative percentage values indicate the NEDC optimised efficiencies are lower than that of the Artemis-optimised, and vice versa. It could be seen that 8 of the 12 NEDC representative operation points are located in the area where the NEDC-optimised design has higher efficiency up to 2.75% than that of the Artemis-optimised design. It shows that the optimisation trend correctly reflects the optimisation objective against the NEDC driving cycle.

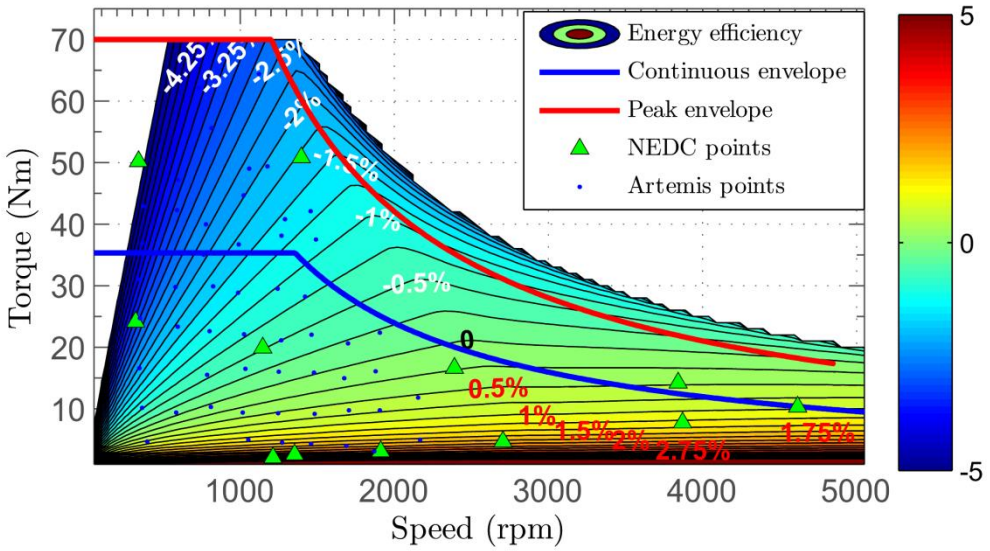

Figure 6.15 Map of efficiency difference between NEDC-optimised motor and Artemis-optimised motor

It follows that the energy distribution over torque-speed range of a driving cycle clearly influence the outcome of the design optimisation and, hence, the resultant geometry parameters, materials usage and cost.

The foregoing observations also suggest that the NEDC or the combined driving cycle might be a preferable optimisation target for a balanced performance over driving cycles. The efficiencies of the NEDC-optimised and combined-optimised designs over the Artemis driving cycle are ~ 94.5%, being still quite high, while they use less magnet materials (only 80% magnets of the Artemis-optimised design) and less copper which are conducive to lower cost.

6.1.5 Influence of driving cycles on optimised IPM designs

The influences of driving cycles on the optimisations of IPM designs are also investigated. Figure 6.16 shows the 18-slot 8-pole IPM topology and six geometry parameters to be optimised. Using the optimisation methodology illustrated in Chapter 4, and the design specifications and constraints listed in Table 6.2, the optimisations are performed, respectively, to maximise the energy efficiency against the two driving cycles: the NEDC and Artemis. Thereafter the two optimised designs are compared to analyse the influence of the driving cycles. Unlike the SPM optimisations described in the previous section, the total energy loss of converter-machine system is taken into account in the optimisations of the IPM machine.

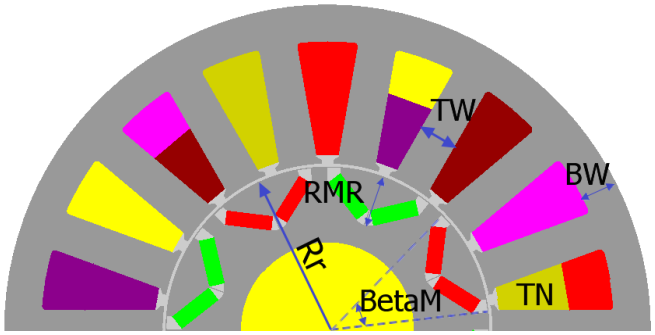

Figure 6.16. IPM geometry for optimization.

Figure 6.17 compares the geometries of the optimised designs. Table 6.9 lists the optimised parameter values. Table 6.10 lists the efficiencies at the rated torque, base speed point T_r and peak torque, base speed point T_{pk}, as well as over the driving cycles.

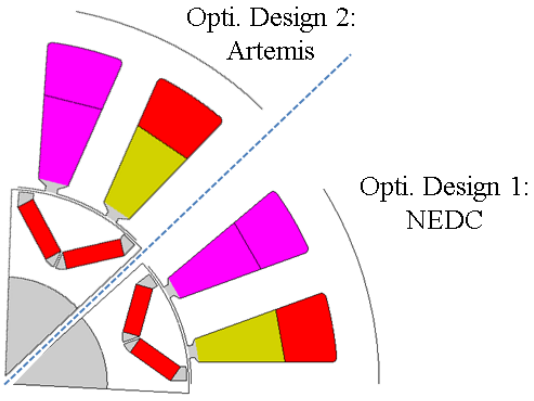

Figure 6.17. Geometries of Two Optimised Designs against NEDC and Artemis

Similar trends of optimised geometry parameters to that observed in the SPM machine optimisations can be seen in Table 6.9. Compared with the NEDC-optimised design, the

Artemis-optimised design has larger slot area, bigger rotor radius and wider magnet v-shape opening angle. As a result, the Artemis-optimised design requires 14% more copper and 20% more magnet materials than the NEDC-optimised design.

Table 6.9 Parameters of Two Optimised Designs against NEDC and Artemis

	Unit	Opti. for NEDC	Opti. For Artemis
Stator tooth width	mm	8.7	7.9
Stator back iron width	mm	8.4	7.0
Rotor radius	mm	36.5	37.7
Magnet opening angle	Deg.	147.8	161.8
Magnet depth	mm	8.3	10.1
Copper usage	kg	3.7	4.2
Magnet usage	kg	0.49	0.59

It should be noted that, although the IPM machines rely less on the permanent magnets since they have reluctance torque contributions from rotor saliency, magnet usage increase from the NEDC-optimised IPM design to the Artemis-optimised IPM design shown in Table 6.9 is still similar to that shown in Table 6.5 for the optimised SPM designs, and the copper usage increase (14%) in the IPM designs is even more in the than that (5%) observed in the SPMs. This is because the inclusion of the converter loss in the IPM optimisations demands the Artemis-optimised design to further increase the torque capability and further reduce the copper loss in order to minimise the total loss of the converter-machine system, resulting in higher magnet and copper usage than the optimisations without converter loss.

Table 6.10 Performances of Two Optimised Designs against NEDC and Artemis

	Unit	Opti. for NEDC	Opti. For Artemis
System efficiency at T_r	%	91.2	91.9
System efficiency at T_{pk}	%	85.6	86.2
System efficiency over NEDC	%	91.0	90.4
System efficiency over Artemis	%	89.3	89.9

Similar trends as seen with SPM optimised designs in efficiencies could be observed in Table 6.10 for the IPM designs. Compared with the NEDC-optimised design, the

Artemis-optimised design gains around 0.7% higher efficiency in low speed operations over the Artemis cycle, but loses 0.6% over the NEDC. However despite the relatively small efficiency differences, the two optimised designs both exhibit high efficiency over the NEDC and Artemis driving cycles.

Considering that NEDC-optimised design has advantages in terms of less magnet, less copper usage and high efficiencies over NEDC and Artemis, the NEDC driving cycle might also be a preferable target driving cycle in optimisations of IPM machines.

The foregoing analysis shows that the outcomes of the design optimisation is influenced by driving cycles irrespective of the PM machine topologies and whether the inverter loss is accounted or not.

6.2 Distributed traction system for electric vehicles

Distributed traction drive systems for electric vehicles employ two or more machines to provide traction forces. Compared with concentrated drive systems with a single traction machine, distributed traction systems benefit from improved traction control, operational efficiency and safety. The vehicle will have less tyre slip due to lower traction torque provided by the front and rear wheels than that of concentrated traction systems, and hence better efficiency performance. In term of safety concern, when one motor fails, with appropriate remedial actions, the remaining healthy motors can still provide traction forces and the vehicle is able to continue its operation, or at least stopped in a safe and controlled manner.

A further advantage of the distributed traction systems is that the torque from each wheel can be dynamically apportioned so that the vehicle may operate in high-efficiency regions over a wide torque-speed operation range.

For example, in the three-motor traction system shown in Figure 6.6 in Section 6.1.2, two identical motors on the rear wheels, each providing nominal 30% of the total traction power, and one motor on the front wheel having 40% nominally. Because the rear motor has a gear ratio 1:7, it operates at much high speed while its peak torque and peak current are relatively lower than that of the front motor. However, both the front and rear motors use the same converter configuration and rating, and their max current limits are set at 175 A. The resultant design specifications of the front and rear machines are listed in Table 6.11.

Table 6.11 Front and rear motor design specifications

	Front motor	Rear motor
Nominal power	5.0 kW	3.75 kW
Peak power	8.8 kW	6.6 kW
Gear ratio	4	7.0
Base speed	1350 rpm	2100 rpm
Max. Speed	4500 rpm	8200 rpm
Power split ratio	40%	2 x 30%
Continuous torque (base speed)	35 Nm	17 Nm
Peak torque (base speed)	70 Nm	30 Nm
DC Link Voltage	120 V	120 V
Current limit	175 A	175A

The front and rear motors could be designed purposely to locate their high efficiency regions in different areas within the torque-speed envelopes, as illustrated in Figure 6.18. The front motor has high efficiency at low-speed and high-torque operation regions, while the rear motor performs better in high-speed and low-torque region. It is reasonable to expect that the combined efficiency of the whole traction system would have higher efficiency over a wider torque-speed range, if the split ratios of the total traction power assigned to the front motor and to the rear motor are carefully selected on the basis of the real torque-speed load conditions rather than being kept constant. For example, in an operation condition with high speed and low torque, the front motor could share more torque/power, while the rear motors may contribute less or just being switch off. In this way, both of them would work in their best efficiency region, leading to a higher combined efficiency output from the traction system.

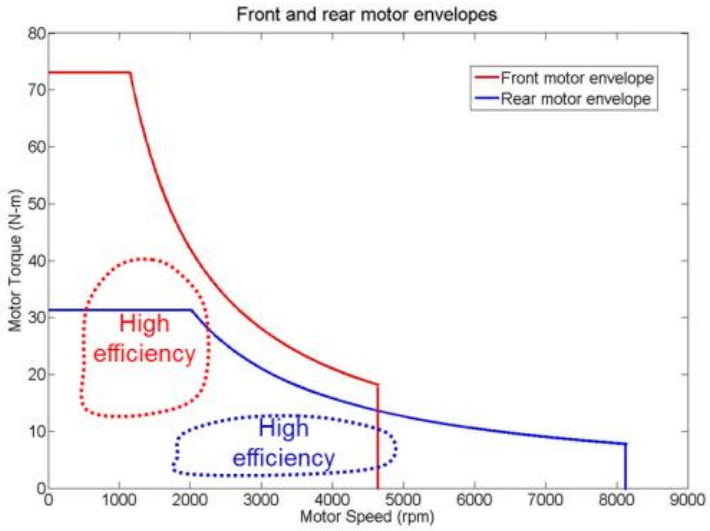

Figure 6.18 Co-working envelopes of two motors with different efficiency performances over torque-speed envelope

According to the work in [73], it is known that, in a traction system with front and rear axles coupled to two identical permanent magnet machines (PMM), the combined efficiency of the drive train with varying torque-split ratios would not be better than that with torque equal sharing, i.e., 50% to 50% split between the front and the rear because when one of the motor switches off with no power output, its iron loss which is significant at high speed still exists. Consequently, the combined efficiency will be lower. However, by employing PMa-SynRM (Permanent magnet assisted synchronous reluctance machine) for the rear traction motors, this limitation has been avoided since a PMa-SynRM has very low iron loss at high speed. In the studies described below, it is shown that in a distributed traction system with a PM machine and a PMa-SynRM cooperating under selected power split ratios, higher efficiency is achievable.

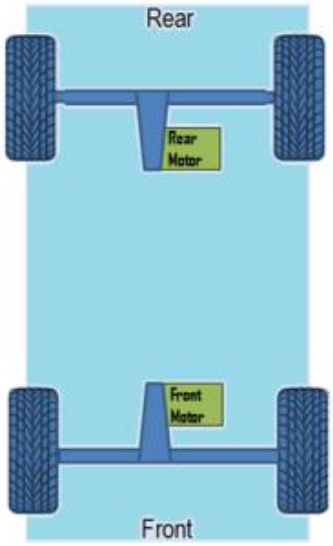

Figure 6.19. Two-motor traction system in the electric vehicle

Ideally, for a complete optimisation of the whole distributed traction system against various operation conditions, power split ratios for front and rear machines should be optimised together with geometric parameters at the same time. However, this very complex process requires 2 machine models to be evaluated simultaneously in optimisations, thus is difficult to realise using the current state-of-the art optimisation tool. In this section, studies on selection of appropriate power split ratios will be carried out after the optimisations of machine parameters to obtain basic knowledge on optimisations of electric vehicle traction systems with asymmetrical motor technologies.

In order to represent a generic application scenario, the traction system studied in this section is a two-motor power train employed in the same light-duty electric vehicle described in Section 6.1.2. As shown in Figure 6.19, the two motors provide the traction force to the front and rear axles via two differentials independently.

6.2.1 Candidate machine design combinations for the two-motor traction system

To assess the energy efficiency of the distributed traction system, various combinations of the front and rear motors using different machine topologies/technologies are investigated. As shown in Figure 6.20. (a), (b) and (c), a 12-slot 14-pole surface mounted permanent magnet machine (SPM), a 36-slot 6-pole interior permanent magnet machine (IPM) and an IPM with 18 slots 8 poles proposed in [105] are selected as the front motor. A 36-slot 4-pole PMa-SynRM which uses ferrite magnets in the rotor to improve the torque and a 36-slot 6-pole synchronous reluctance machine (SynRM), shown in Figure 6.20. (d) and (e) respectively, are considered for the rear axle traction. Table 6.12 lists six machine topology combinations for the front and rear motor and the variation range of the power split ratio between the two motors.

The front permanent magnet machines have high efficiency in the low-speed, high-torque region, while the rear motor has low idling loss thus high efficiency at low torque and high speed. The complementary characteristics of the front and rear motors could provide potential energy efficiency improvement for the vehicle traction system. This combination also uses less rare earth magnets and reduces the system cost.

Without loss of generality, the front and the rear motors are optimally designed with the same dimension and specifications listed in Table 6.2, to share equally the load, i.e. 50% : 50% power split ratio. The exception is that the 36-slot 6-pole SynRM has 30% extra stack length to meet the peak torque requirement. The representative points of the NEDC driving cycle are used in the evaluations of the traction systems with different machine combinations and power split ratios.

Table 6.12. Six combinations of front and rear motor topologies

Front motor	Rear motor	Original power split ratio (front power : rear power)	Power split ratio optimisation region (front power : rear power)
12s 14p SPM	36s 4p PMa-SynRM	0.5:0.5	from (0.3:0.7) to (1:0)
12s 14p SPM	36s 6p Syn-RM	0.5:0.5	from (0.3:0.7) to (1:0)
18s 8p IPM	36s 4p PMa-SynRM	0.5:0.5	from (0.3:0.7) to (1:0)

18s 8p IPM	36s 6p Syn-RM	0.5:0.5	from (0.3:0.7) to (1:0)
36s 6p IPM	36s 4p PMa-SynRM	0.5:0.5	from (0.3:0.7) to (1:0)
36s 6p IPM	36s 6p Syn-RM	0.5:0.5	from (0.3:0.7) to (1:0)

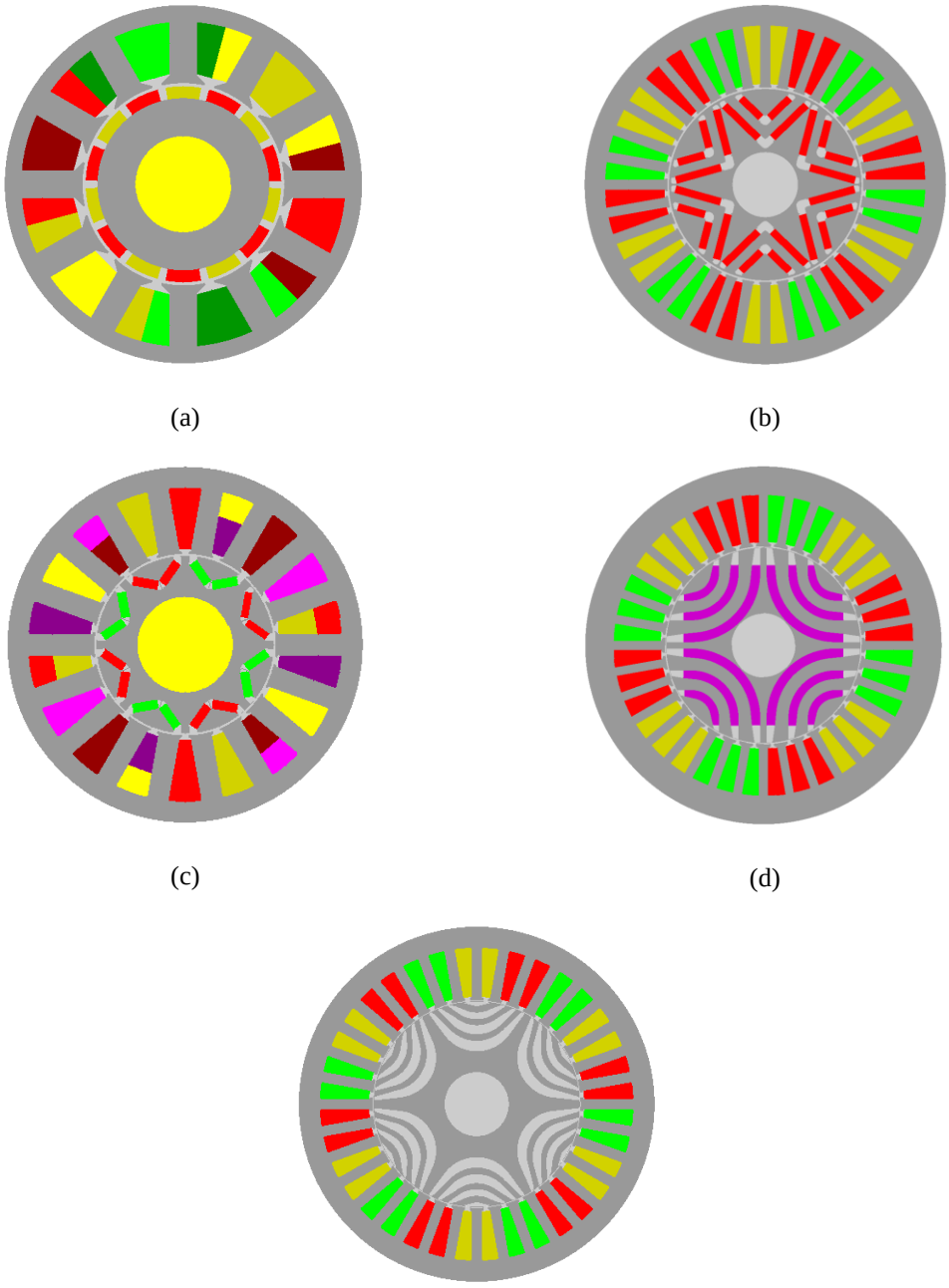

(a) (b) (c) (d) (e)

Figure 6.20. Machine topologies used in the traction system: (a). 12-slot 14-pole SPM; (b). 36-slot 6-pole IPM; (c). 18-slot 8-pole IPM; (d). 36-slot 4-pole PMa-SynRM; (e). 36-slot 6-pole SynRM

6.2.2 Energy efficiency performances of machine topologies

The 36-slot 6-pole IPM, and the 36-slot 6-pole SynRM are optimised, as in a conventional optimisation method, to have a high efficiency at the rated operation point, while the 12-slot 14-pole SPM, 18-slot 8-pole IPM and 36-slot 4-pole PMa-SynRM are optimised against the NEDC driving cycle following the optimisation strategy illustrated in Chapter 4. The characteristics of the machine topologies and the influence of the optimisation methods are reflected in the efficiency maps over the torque-speed envelope as shown in Figure 6.13, and Figure 6.21 to Figure 6.24.

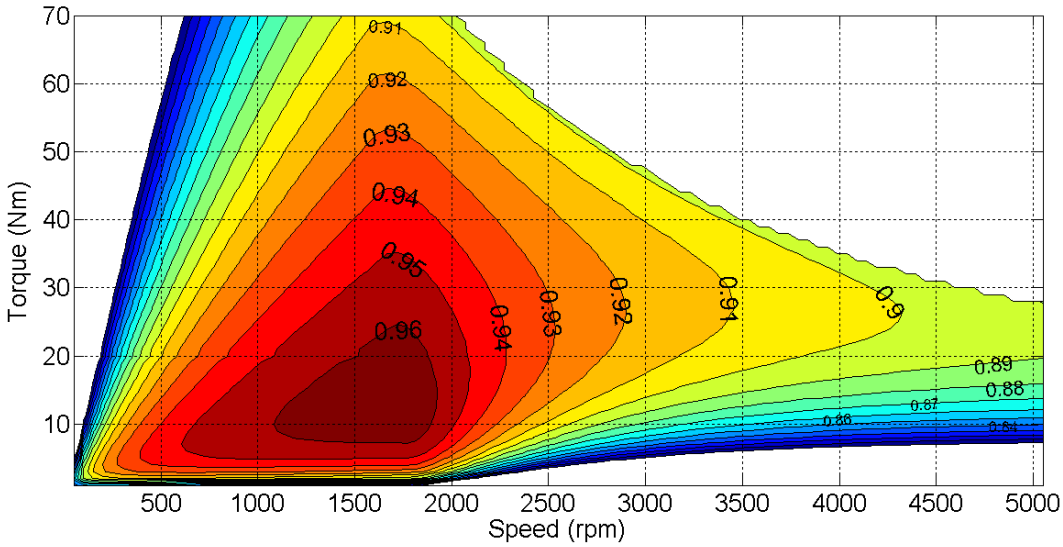

Figure 6.21. Efficiency map of 36-slot 6-pole IPM

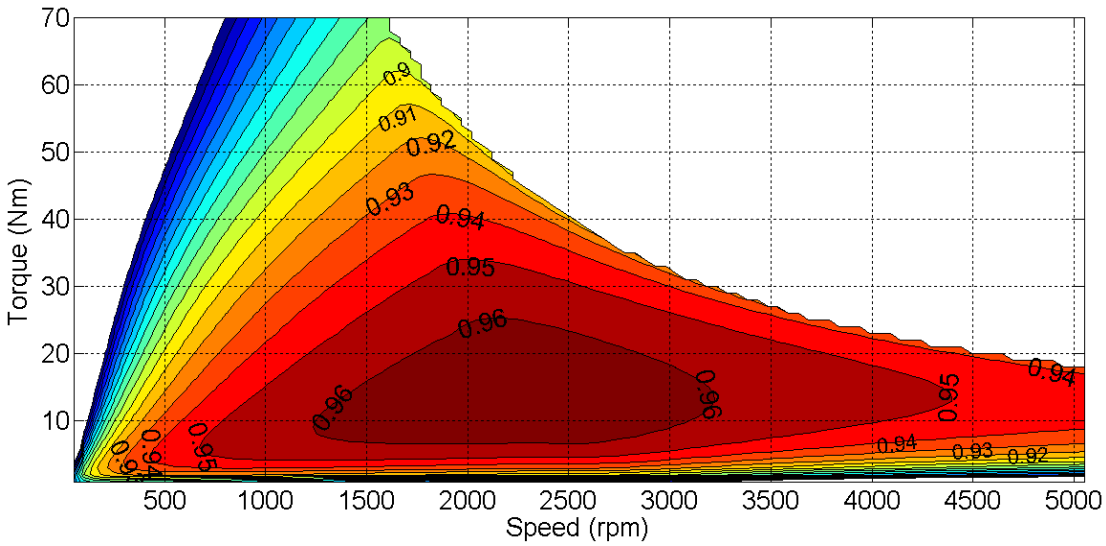

Figure 6.22. Efficiency map of 18-slot 8-pole IPM

The 36-slot 6-pole IPM has high efficiency at high torque, low speed, but clearly low efficiency at high speed because of high iron loss due to use of more rare-earth permanent magnets. Since the 12-slot 14-pole SPM and 18-slot 8-pole IPM are optimised against NEDC, their performance at high speed is greatly improved, thus resulting into high efficiency over a wide torque-speed range. The 18-slot 8-pole IPM, compared with the 12-slot 14-pole SPM, uses 40% fewer magnets due to a considerable amount of reluctance torque. Therefore although its efficiency at high torque is slightly lower than that of the SPM, it has higher efficiency over low torque and high speed region.

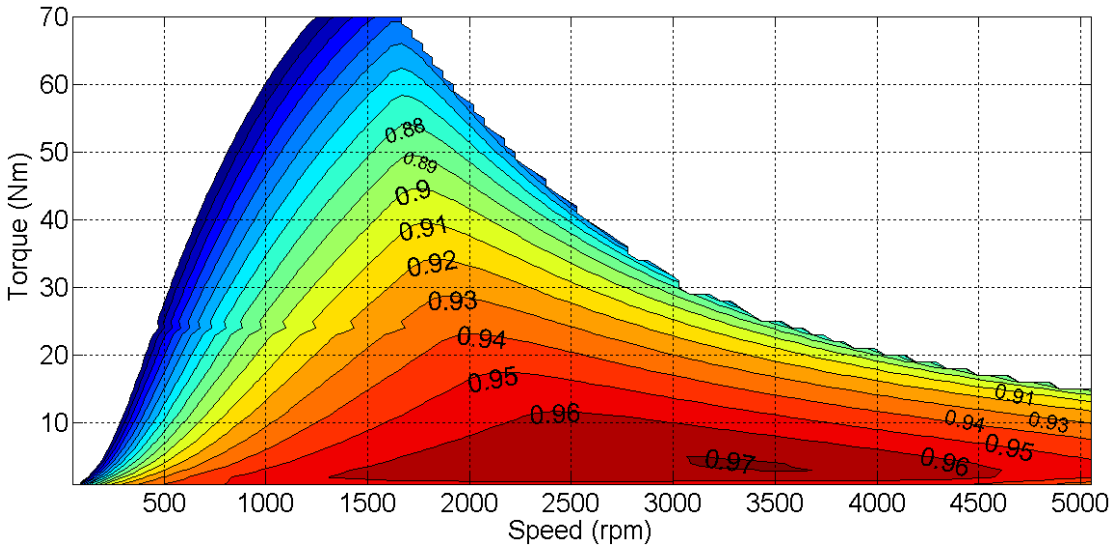

Figure 6.23. Efficiency map of 36-slot 4-pole PMa-SynRM

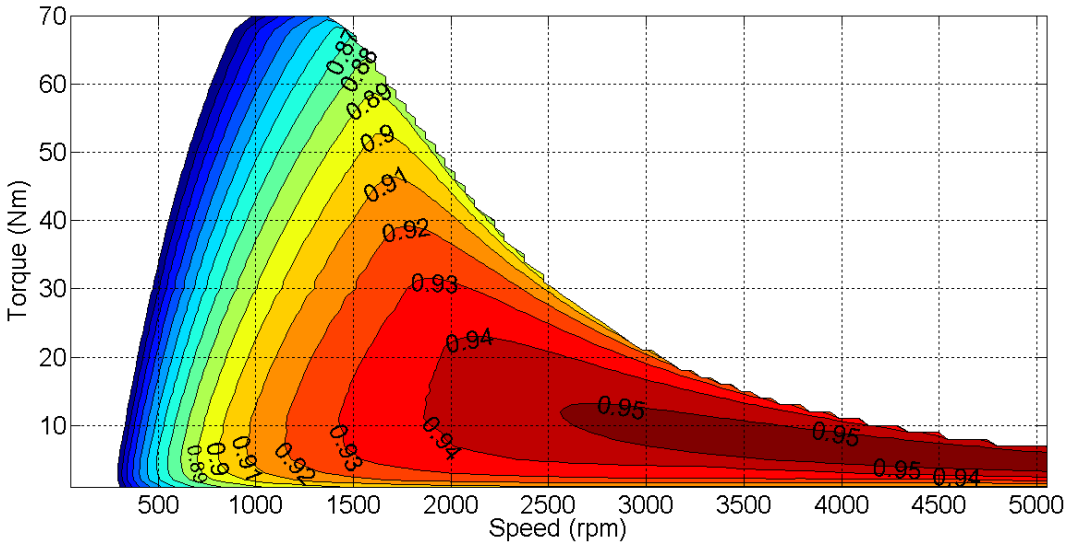

Figure 6.24. Efficiency map of 36-slot 6-pole SynRM

As for the PMa-SynRM and SynRM, they mainly rely on the reluctance torque and use only weak magnets or no magnets. Their efficiency in low speed region is around 2-3% lower than that of the SPM and IPM, but shows 2% higher efficiency in the high-speed region where the torque is less than 10 Nm, which is a complementary characteristic to permanent magnet machines.

6.2.3 Optimal power split ratios for the distributed traction system

To quantify the potential energy saving by dynamically apportioning the traction powers between the front and rear drives, the energy consumptions over the NEDC 12 points are considered. At each point, the power split ratios vary from 0.3 to 1.0 for the front motor, and from 0.7 to 0 for the rear motor.

Take the traction system with an SPM and a SynRM over the NEDC for example. Figure 6.25 and Figure 6.26 show the power loss variations of the system with the split ratio at a NEDC low-speed point of 16 Nm at 306 rpm, and high-speed point of 9 Nm at 4367 rpm, respectively. To obtain the minimum total loss of the traction system, the optimal power split ratios for the front motor are 0.85 and 0.92 respectively for the two points, which reduce the power loss by 22% and 28%, i.e. more than 1% higher in energy efficiency compared with the case using 0.5 as the power split ratio.

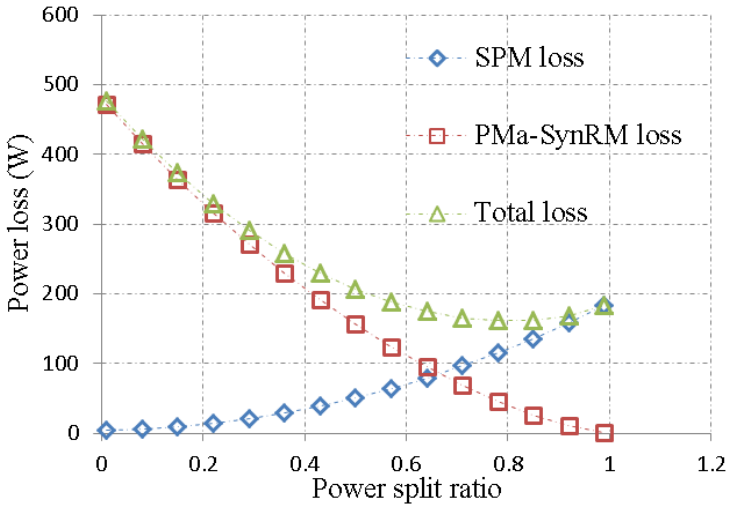

Figure 6.25. Power loss curves with varying power split ratios at 16 Nm 306 rpm

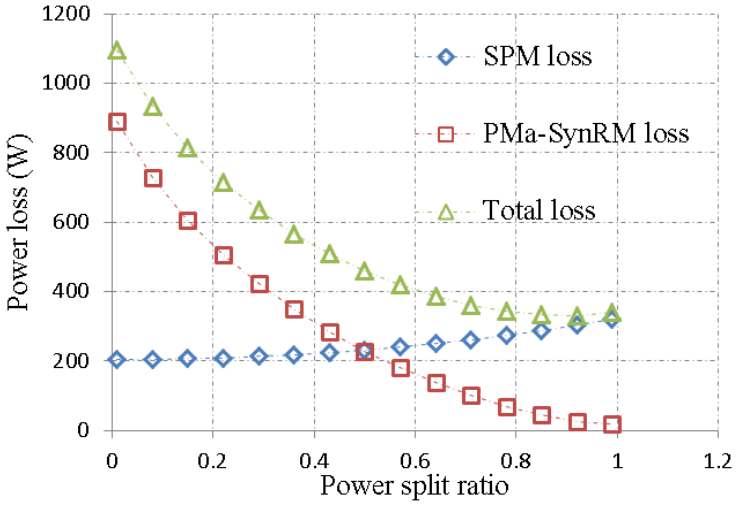

Figure 6.26. Power loss curves with varying power split ratios at 9 Nm 4367 rpm

In Figure 6.27, the optimal power split ratios of the front motor for all 12 NEDC points are marked with white circles on its efficiency map. Those with the power split ratio as 0.5:0.5 (equal sharing) are marked in black. It can be seen that the optimal split ratios moves 8 out of the 12 NEDC points to the motor's higher efficiency region. For the four points where the torque is less than 10 Nm, the optimal ratio for the front motor are close to 1.0, which implies that the rear PMa-SynRM motor is not active. This is the best choice since no-load iron loss of the PMa-SynRM is very low compared to that of the permanent magnet machine.

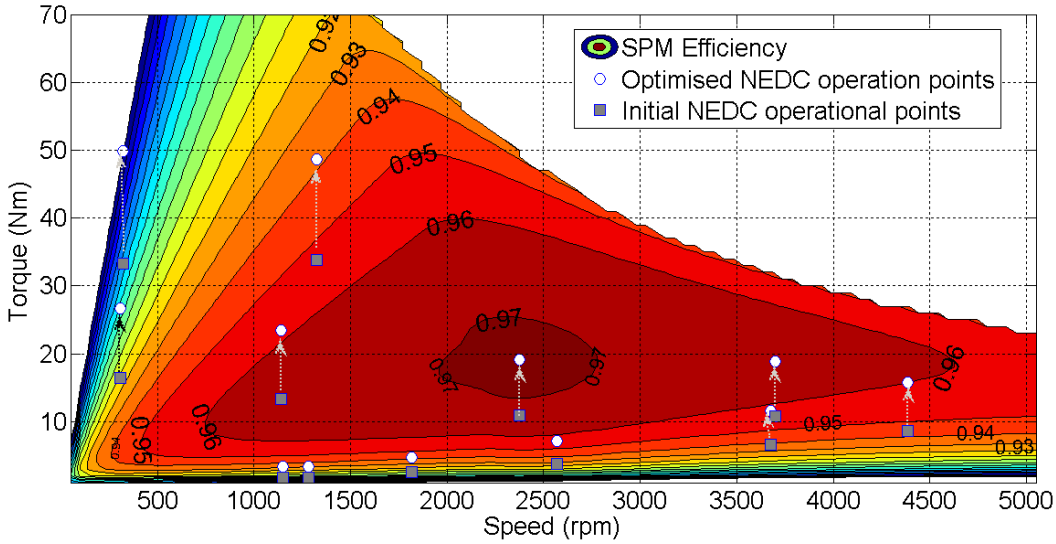

Figure 6.27. Efficiency map of 12-slot 14-pole SPM and its NEDC operation points with the initial power split ratios as 0.5:0.5 and with the optimal split ratios.

Table 6.13 lists NEDC cycle efficiencies for the 9 traction system options, employing fixed and optimal power split ratios. As can be seen, the efficiency could be increased by 1% to 2% or the loss reduced by 20% to 40% if the optimal split ratios are employed when compared with the equal sharing cases. It should be noted that because the SynRM has longer stack length, the traction system using the SynRM exhibits slightly higher efficiency than the system using the PMa-SynRM in the cases with optimal split ratios. It is also evident that both the PMM+PMa-SynRM combination and the PMM+SynRM combination yield better efficiency than the PMM+PMM combination when optimal power split ratios are employed, while their cost is lower.

Table 6.13. Energy efficiency of 9 distributed traction systems over the NEDC

	with two identical PM machines	with PMA		with SynRM	
		ratio=0.5	optimised ratio	ratio=0.5	optimised ratio
SPM	94.42%	93.98%	95.09%	94.13%	95.13%
18s-8p IPM	94.30%	93.93%	94.43%	94.07%	94.72%
36s-6p IPM	88.72%	91.07%	91.65%	91.21%	91.87%

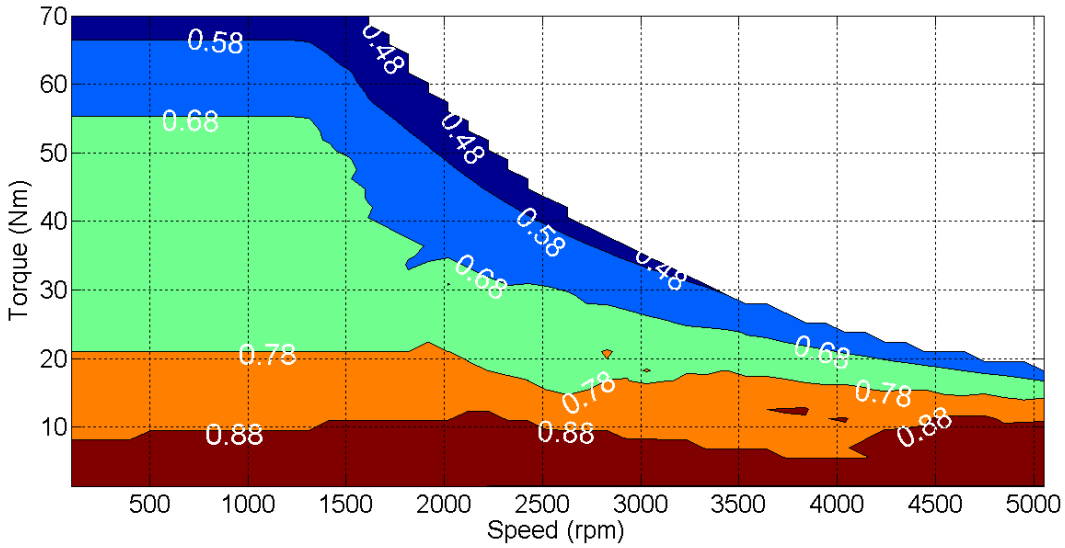

Figure 6.28. The map of optimal power split ratio for the front motor of the traction system using SPM + PMa-SynRM

Figure 6.28 displays the map of the optimal power split ratios for the front motor over whole torque-speed range for the SPM + PMa-SynRM traction system. It is clearly seen that over the low torque region, the optimal split ratio for the permanent magnet machine is above 0.8, which means the rear PMa-SynRM operates at quite low load or

in idle status. As the torque increases, the power split gradually approaches to equally sharing case. This implies that the PMa-SynRM is mainly used to boost the peak torque capability. It should also be noted that with the optimal power split ratios, the continuous power/torque rating of the front motor will be increased while that of the rear motor reduced. These changes will need to be incorporated in the design process to ensure that both machines have robust thermal performance.

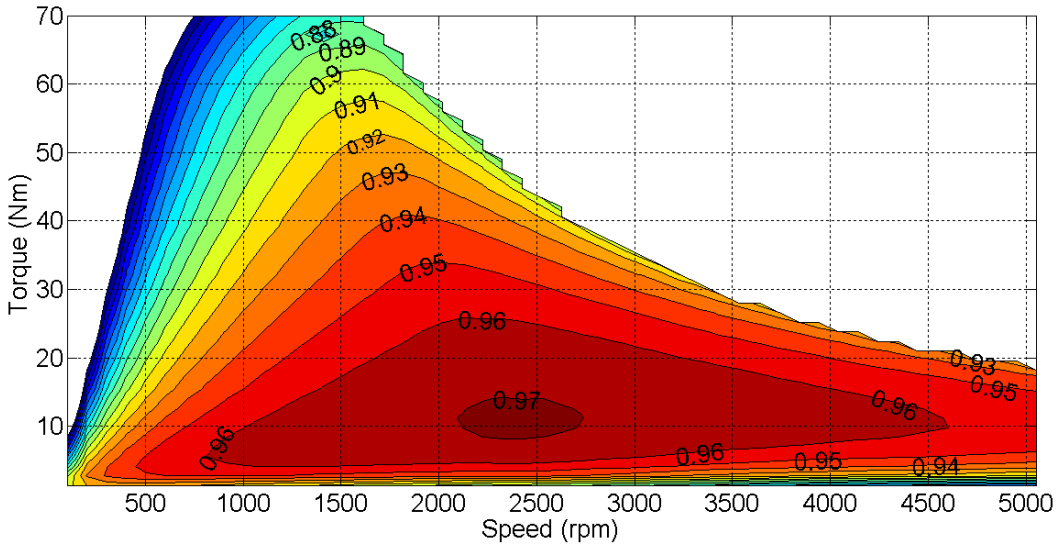

Figure 6.29. Efficiency map of the SPM + PMa-SynRM system with optimal power split ratios

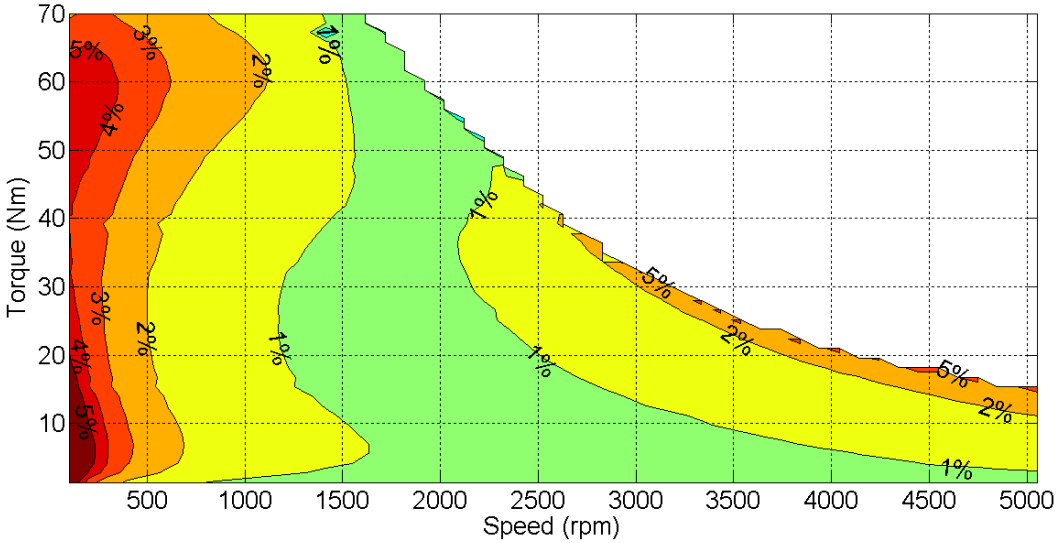

Figure 6.30. Efficiency difference map between optimal split ratio and equal split ratio in the SPM + PMa-SynRM system

Figure 6.29 shows the efficiency map of the SPM + PMa-SynRM system when optimal power split ratios are employed. Figure 6.30 shows efficiency difference map between the system using optimal split ratio and the system using equal split ratio. With the optimal ratios, the system's efficiency is increased 1-3% over a wide torque-speed range compared to the case with equal ratios.

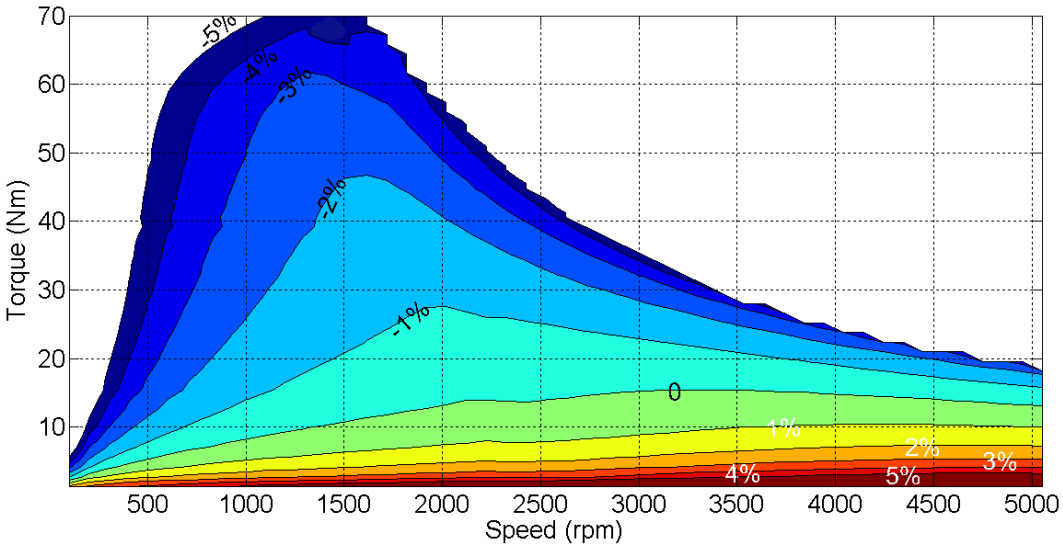

Figure 6.31. Efficiency difference map between split-ratio optimised SPM + PMa-SynRM system and SPM + SPM system

Figure 6.31 shows efficiency difference map between the SPM + PMa-SynRM system with the optimal power split ratios and SPM + SPM system with 0.5 : 0.5 ratios. The positive values indicate that the efficiency of the SPM+PMa-SynRM system is greater than that of the SPM+SPM. It can be seen that the SPM + PMa-SynRM system has the efficiency increased by 1-5% in the high speed region compared to the two SPM machine system. This is the reason why the NEDC efficiency of the SPM + PMa-SynRM system is 0.7% higher.

6.3 Conclusions

The influence of driving cycles and distribute traction systems on the design optimization of EV traction machines have been studied in this section.

By performing optimisations of candidate SPM and IPM machines against different driving cycles, it has been shown that driving cycles with distinctive torque-speed distribution characteristics have significant influence on the resultant optimal designs in terms of geometrical dimensions, losses and efficiency map over torque-speed envelope. In particular, among the optimised designs, the usage of permanent magnets and copper may vary by 10~20% and the efficiency over driving cycles differs by 0.7~1%,

depending on driving cycles used in the optimisation. The results suggest that the NEDC might be a preferable driving cycle against which design optimization is performed for balanced machine performances and cost.

A two-motor traction system as a generic example of distributed traction systems has been studied. Various machine topologies are considered for the distributed traction system which employs a SPM or IPM machine for the front axle traction and a SynRM or PMa-SynRM for the rear-axle drive. Optimal power split ratios are investigated to improve the energy efficiency of the traction system.

It has been shown that the system which employs a PM machine and PMa-SynRM or a PM machine and SynRM with the optimal power split ratios could benefit from complimentary characteristics of the high torque capability of the PM machines and the low idling loss of the PMa-SynRM or SynRM. By assigning more torque to the PM machines, the system efficiency in the low-torque, high-speed area is increased by 1-3%, and the efficiency over the NEDC can be improved by 1-2%, compared to the cases with equal split ratio, i.e., 50% to 50%. Besides, compared with the system using two identical PM machines, the asymmetric system with the optimal power split ratios leads to a better efficiency over the NEDC, and improved robustness and reduced cost.

It should be pointed out that before the optimisation of power split ratio, the geometry parameters of the machine designs are optimised assuming 50% to 50% power split ratio is used. Possible efficiency improvement of the whole distributed traction system could be expected if the geometry parameters of the machine designs and power split ratios are optimised together. This would be a subject for future research.

CHAPTER 7 Conclusions and recommendations for future work

7.1 Conclusions

In this work a set of modelling techniques for permanent magnet (PM) machines in electric vehicle traction applications has been developed, in order to establish a computationally-efficient yet accurate design and optimisation method for a PM machine, that entails comprehensive multi-physics performance assessments, various driving cycle operation requirements and distributed traction features. With the modelling techniques integrated together, a design/optimisation process for a PM machine in a distributed traction system, and subsequently the prototype building and experiments are fully described and presented. The effectiveness and accuracy of the designing methods are validated by the experiment results.

At first the computationally efficient modelling techniques that allow accurate multi-physics performance evaluations of PM machines in electric vehicle (EV) traction applications have been developed. It addresses multi-physics machine design issues against driving cycles, including inverter-machine system electromagnetic performance, energy efficiency, thermal behaviours and mechanical stress in rotor lamination.

Then the eddy current loss in the magnets of PM machines are particularly studied. An analytical method, based on the generalized image theory, has been proposed which enables fast and accurate prediction of 3-dimensional (3D) eddy current distributions in the magnets and the resultant eddy current loss.

Thirdly based on the aforementioned PM machine modelling method, high-fidelity computationally-efficient machine model that considers the effect of temperature variation on the electromagnetic behaviours of IPM machines has been proposed, and thereafter an electro-thermally coupled PM machine model has been achieved.

Following the establishment of the modelling methods, a design process of permanent magnet machine for a light-duty electric vehicle traction system has been formulated to exploit the benefits of advanced modeling techniques, which includes optimisation strategy and development of quantitative comparison among various PM machines, design/optimisation process of a selected 18-slot 8-pole IPM. And two prototype machines have been built and tested.

Finally, two special design issues for PM machines in an electric vehicle application have been studied based on different driving cycles widely used in vehicle test procedures. First, the influences of driving cycles on the machine designs including SPM and IPM are investigated in terms of geometry, losses and efficiency features respectively. Secondly, for an electric vehicle drive system which employs distributed traction system with two or more traction machines, combinations of candidate permanent magnet machine topologies, such as SPM, IPM, SynRM and PMa-SynRM, for the distributed traction as well as their torque/power split ratios have been investigated in order to improve the drive system energy efficiency.

The following conclusions can be made based on the work described in this thesis:

With the proposed FE-based analytical machine models, the evaluations of multiphysics performances of machine designs have been achieved with less computation effort without compromising evaluation accuracy compared with FE, facilitating greatly machine design/optimisations and subsequent machine simulations.

Validated by 3D time-stepped transient finite element analysis, the proposed analytical method for predicting 3D eddy current loss in magnets in PM machines has been shown to be extremely computationally efficient, accurate and widely adaptable to a variety of permanent magnet machines with due account of complex machine geometry, various winding configurations and magnetic saturation.

The developed model with temperature effect facilitates more accurate assessments of the electromagnetic and thermal performance of IPM machines, validated by measurements on the prototype IPM machine. The electro-thermal coupled model is shown essential in the related simulations. Simulation studies have shown that if the temperature effect on the machine is neglected, the temperatures of the windings and magnets may be underestimated by 10-20^{o}C, and the higher risk of partial demagnetization and reduced lifetime of windings might be expected.

The validation tests on the prototype 18-slot 8-pole IPM show good agreement with the predictions in various aspects, verifying high accuracy of the proposed analytical models. The 18-slot 8-pole IPM topology also exhibits very good overall performances in terms of high energy efficiencies over driving cycles and low permanent magnet usage.

By performing optimisations of candidate SPM and IPM machines against different driving cycles, it has been shown that driving cycles with distinctive torque-speed distribution characteristics have significant influence on the resultant optimal designs in terms of geometrical dimensions, losses and efficiency map over torque-speed envelope. In particular, among the optimised designs, the usage of permanent magnets and copper may vary by 10~20% and the efficiency over driving cycles differs by 0.7~1%, depending on driving cycles used in the optimisation. The results suggest that the NEDC might be a preferable driving cycle against which design optimization is performed for balanced machine performances and cost.

As for a distributed traction system employed in an electric vehicle, benefit of variable power split ratio can be seen. The optimal power split ratio always assigns more torque to the PM machine in the low torque region, thus increasing the system' efficiency in the low-torque high-speed area by 1-3%. By using optimal power split ratios, the traction system efficiency over the New European Driving Cycle can be improved by 1-2%, compared to the cases with equal split ratio, i.e., 50% to 50%. Besides, the combination of the PM machine with high torque capability and the PMA-SynRM or the SynRM with low idling loss and exploitation of the optimal power split ratios leads to a better efficiency than the system using a PM/PM combination, improved robustness, and reduced PM usage and cost.

7.2 Recommendations for future work

Based on the work that has been carried out on the subject of modelling and design optimisation of permanent magnet machines for electric vehicle traction applications, future work of values could be further going in a deeper and wider scale in the aspects of modelling and optimisation:

(1) While the high-fidelity PM machine model with thermal coupling has been shown effective in the thesis, further research could be carried out on how the model could be extended to predict the machine performances in the cases where the permanent magnets are partially demagnetised, and how the demagnetisation degree could be quantified.

(2) The analytical model of predicting the 3-D eddy current loss within permanent magnets based on generalised image method is applied in a SPM in the thesis. Further work is worthwhile to exploit the benefit of the model in calculating the eddy current loss for a variety of permanent magnet machine topologies such as

for IPM, flux switching machines and for the loss in the sleeve of SPM. Moreover, the eddy current reaction could be taken account of by coupling this model with a machine electromagnetic model in the cases where resistance-limited mode is not suitable anymore for high-frequency machines or for evaluating the effect of machine sources using pulse-width-modulation.

(3) While in the thesis, the power split ratio of the EV distributed traction system and the machine geometries are optimised separately, further energy efficiency improve can be reasonably expected if the machines and the power split ratios among them are optimised together. Therefore, the complete optimisation of EV distributed traction system is also worth the effort for engineers.

Appendix 1 Derivation of the Generalized Image Method for 3D Eddy Current Field in Rectangular Coordinate System

A1.1 Images for 3D eddy current field in two infinite conducting regions

Without loss of generality, consider two infinitely large conducting regions as shown in Figure 1.1 (a). Region 1 has conductivity σ_1 and occupies the space where $z > 0$ and the rest is denoted as region 2 with conductivity σ_2. A source of excitation $\boldsymbol{S}(x_1, y_1, z_1)$ is located in region 1.

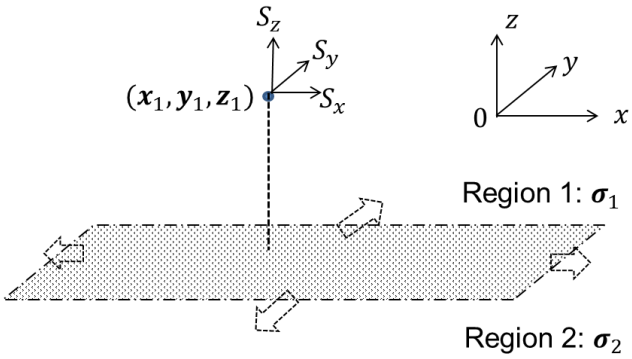

(a)

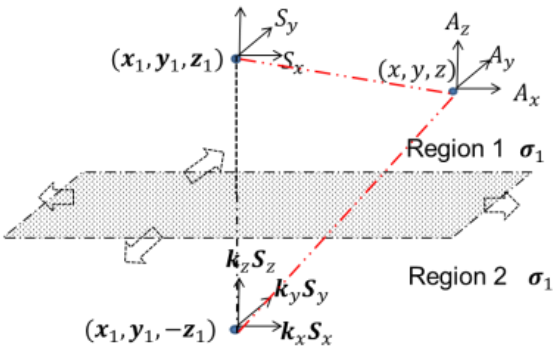

(b)

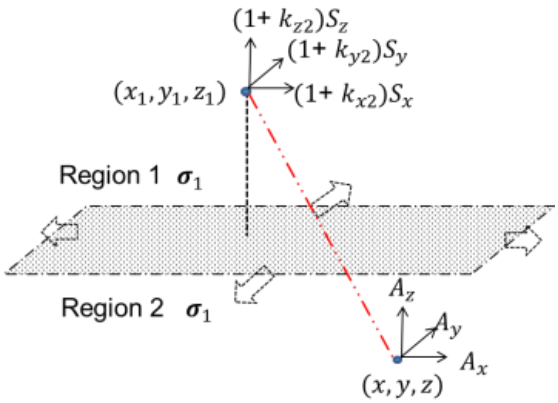

(c)

Figure 1.1. (a) Two semi-infinite conductors with sources in region 1; (b) equivalent image sources in region 2 for eddy current field in region 1; (c) equivalent image sources in region 1 for eddy current field in region 2.

To quantify the field distribution in region 1, the effect of the boundary conditions may be represented by the image, $\{k_x S_x(x_1, y_1, -z_1),\ k_y S_y(x_1, y_1, -z_1),\ k_z S_z(x_1, y_1, -z_1)\}$, in region 2 with its conductivity being set to σ_1, as shown in Figure 1.1 (b). Similarly, for the field distribution in region 2, the effect of the boundary conditions is represented by the image, $\{k_{x2} S_x(x_1, y_1, z_1),\ k_{y2} S_y(x_1, y_1, z_1),\ k_{z2} S_z(x_1, y_1, z_1)\}$, in region 1 with the conductivity in region 2 being set to σ_1 , as shown in Figure 1.1 (c). k_x, k_y, k_z and k_{x2}, k_{y2}, k_{z2} are image coefficients to be determined to satisfy the boundary conditions given in appendix A1.2.

Since the field region in Figure 1.1 (b) is now homogenous and extends to infinite, the current vector potential $\boldsymbol{A}$ which satisfies $\nabla^2 \boldsymbol{A} = -\sigma \boldsymbol{S}$ in region 1 can be obtained from the volume integration:

$$A_{1x} = \iiint \left(\frac{-\sigma_1 S_x}{4\pi r_1} + \frac{-\sigma_1 k_x S_x}{4\pi r_2}\right) \mathrm{d}x_1 \mathrm{d}y_1 \mathrm{d}z_1$$

$$r_1 = \sqrt{(x - x_1)^2 + (y - y_1)^2 + (z - z_1)^2} \tag{1.1}$$

$$r_2 = \sqrt{(x - x_1)^2 + (y - y_1)^2 + (z + z_1)^2}$$

$$A_{1y} = \iiint \left(\frac{-\sigma_1 S_y}{4\pi r_1} + \frac{-\sigma_1 k_y S_y}{4\pi r_2}\right) \mathrm{d}x_1 \mathrm{d}y_1 \mathrm{d}z_1 \tag{1.2}$$

$$A_{1z} = \iiint \left(\frac{-\sigma_1 S_z}{4\pi r_1} + \frac{-\sigma_1 k_z S_z}{4\pi r_2}\right) \mathrm{d}x_1 \mathrm{d}y_1 \mathrm{d}z_1 \tag{1.3}$$

The current vectors in region 2 are similarly derived as:

$$\boldsymbol{A_{2x}} = \iiint \left(\frac{-\boldsymbol{\sigma_1 S_x}}{\boldsymbol{4\pi r_1}} + \frac{-\boldsymbol{\sigma_1 k_{x2} S_x}}{\boldsymbol{4\pi r_1}}\right) \boldsymbol{\mathrm{d}x_1 \mathrm{d}y_1 \mathrm{d}z_1} \tag{1.4}$$

$$A_{2y} = \iiint \left(\frac{-\sigma_1 S_y}{4\pi r_1} + \frac{-\sigma_1 k_{y2} S_y}{4\pi r_1}\right) \mathrm{d}x_1 \mathrm{d}y_1 \mathrm{d}z_1 \tag{1.5}$$

$$A_{2z} = \iiint \left(\frac{-\sigma_1 S_z}{4\pi r_1} + \frac{-\sigma_1 k_{z2} S_z}{4\pi r_1}\right) \mathrm{d}x_1 \mathrm{d}y_1 \mathrm{d}z_1 \tag{1.6}$$

A1.2 Image coefficients satisfying boundary conditions

The interface conditions at the boundary between regions 1 and 2 that eddy current density $\boldsymbol{J}$ and electric field strength $\boldsymbol{E}$ must satisfy are given by:

$$\boldsymbol{J_{1z}} = \boldsymbol{J_{2z}} \tag{1.7}$$

$$E_{1x} = E_{2x} \tag{1.8}$$

$$E_{1y} = E_{2y} \tag{1.9}$$

which can be further expressed in terms of the current vector potentials as

$$\left(\frac{\partial \boldsymbol{A}_{y1}}{\partial x}-\frac{\partial \boldsymbol{A}_{x1}}{\partial y}\right)_{\mathrm{z=0}}=\left(\frac{\partial \boldsymbol{A}_{y2}}{\partial x}-\frac{\partial \boldsymbol{A}_{x2}}{\partial y}\right)_{\mathrm{z=0}} \tag{1.10}$$

$$\frac{1}{\sigma_1}\left(\frac{\partial \boldsymbol{A}_{z1}}{\partial y}-\frac{\partial \boldsymbol{A}_{y1}}{\partial z}\right)_{\mathrm{z=0}}=\frac{1}{\sigma_2}\left(\frac{\partial \boldsymbol{A}_{z2}}{\partial y}-\frac{\partial \boldsymbol{A}_{y2}}{\partial z}\right)_{\mathrm{z=0}} \tag{1.11}$$

$$\frac{1}{\sigma_1}\left(\frac{\partial \boldsymbol{A}_{x1}}{\partial z}-\frac{\partial \boldsymbol{A}_{z1}}{\partial x}\right)_{\mathrm{z=0}}=\frac{1}{\sigma_2}\left(\frac{\partial \boldsymbol{A}_{x2}}{\partial z}-\frac{\partial \boldsymbol{A}_{z2}}{\partial x}\right)_{\mathrm{z=0}} \tag{1.12}$$

The four partial differential terms in (1.10) are given by:

$$\left(\frac{\partial \boldsymbol{A}_{y1}}{\partial x}\right)_{\mathrm{z=0}}=\iiint\{\frac{1}{4\pi}\sigma_1\left(\boldsymbol{S_y}+k_{\boldsymbol{y}}\boldsymbol{S_y}\right)\times[(x-x_1)^2+(y-y_1)^2+(z_1)^2]^{-\frac{3}{2}} \times(x-x_1)\}\mathrm{d}x_1\mathrm{d}y_1\mathrm{d}z_1 \tag{1.13}$$

$$\left(\frac{\partial \boldsymbol{A}_{x1}}{\partial y}\right)_{\mathrm{z=0}}=\iiint\{\frac{1}{4\pi}\sigma_1(\boldsymbol{S_x}+k_{\boldsymbol{x}}\boldsymbol{S_x})\times[(x-x_1)^2+(y-y_1)^2+(z_1)^2]^{-\frac{3}{2}} \times(y-y_1)\}\mathrm{d}x_1\mathrm{d}y_1\mathrm{d}z_1 \tag{1.14}$$

$$\left(\frac{\partial \boldsymbol{A}_{y2}}{\partial x}\right)_{\mathrm{z=0}}=\iiint\{\frac{1}{4\pi}\sigma_1\left(\boldsymbol{S_y}+k_{\boldsymbol{y2}}\boldsymbol{S_y}\right)\times[(x-x_1)^2+(y-y_1)^2+(z_1)^2]^{-\frac{3}{2}} \times(x-x_1)\}\mathrm{d}x_1\mathrm{d}y_1\mathrm{d}z_1 \tag{1.15}$$

$$\left(\frac{\partial \boldsymbol{A}_{x2}}{\partial y}\right)_{\mathrm{z=0}}=\iiint\{\frac{1}{4\pi}\sigma_1(\boldsymbol{S_x}+k_{\boldsymbol{x2}}\boldsymbol{S_x})\times[(x-x_1)^2+(y-y_1)^2+(z_1)^2]^{-\frac{3}{2}} \times(y-y_1)\}\mathrm{d}x_1\mathrm{d}y_1\mathrm{d}z_1 \tag{1.16}$$

To satisfy (1.10) at *z=0*, the following relations must be true:

$$k_{\boldsymbol{x}}=k_{\boldsymbol{x2}}, k_{\boldsymbol{y}}=k_{\boldsymbol{y2}} \tag{1.17}$$

The four partial differential terms in (1.12) are expressed as

$$\left(\frac{\partial \boldsymbol{A}_{x1}}{\partial z}\right)_{\mathrm{z=0}}=\iiint\{\frac{1}{4\pi}\sigma_1(\boldsymbol{S_x}-k_{\boldsymbol{x}}\boldsymbol{S_x})\times[(x-x_1)^2+(y-y_1)^2+(z_1)^2]^{-\frac{3}{2}} \times(z_1)\}\mathrm{d}x_1\mathrm{d}y_1\mathrm{d}z_1 \tag{1.18}$$

$$\left(\frac{\partial \boldsymbol{A}_{z1}}{\partial x}\right)_{\mathrm{z=0}}=\iiint\{\frac{1}{4\pi}\sigma_1(\boldsymbol{S_z}+k_{\boldsymbol{z}}\boldsymbol{S_z})\times[(x-x_1)^2+(y-y_1)^2+(z_1)^2]^{-\frac{3}{2}} \times(x-x_1)\}\mathrm{d}x_1\mathrm{d}y_1\mathrm{d}z_1 \tag{1.19}$$

$$\left(\frac{\partial \boldsymbol{A}_{x2}}{\partial z}\right)_{\mathrm{z=0}}=\iiint\{\frac{1}{4\pi}\sigma_1(\boldsymbol{S_x}+k_{\boldsymbol{x2}}\boldsymbol{S_x})\times[(x-x_1)^2+(y-y_1)^2+(z_1)^2]^{-\frac{3}{2}} \times(z_1)\}\mathrm{d}x_1\mathrm{d}y_1\mathrm{d}z_1 \tag{1.20}$$

$$\left(\frac{\partial \boldsymbol{A}_{z2}}{\partial x}\right)_{z=0} = \iiint \{\frac{1}{4\pi}\sigma_1(\boldsymbol{S_z} + k_{\boldsymbol{z2}}\boldsymbol{S_z}) \times [(x-x_1)^2 + (y-y_1)^2 + (z_1)^2]^{-\frac{3}{2}} \times (x-x_1)\}\mathrm{d}x_1\mathrm{d}y_1\mathrm{d}z_1 \tag{1.21}$$

Equating the both sides of (1.22) gives:

$$1 - k_{\boldsymbol{x}} = \frac{\sigma_1}{\sigma_2}(1 + k_{\boldsymbol{x2}}) \tag{1.22}$$

$$1 + k_{\boldsymbol{z}} = \frac{\sigma_1}{\sigma_2}(1 + k_{\boldsymbol{z2}}) \tag{1.23}$$

Combining (1.17) and (1.22), we get

$$k_{\boldsymbol{x}} = k_{\boldsymbol{x2}} = \frac{\sigma_2 - \sigma_1}{\sigma_2 + \sigma_1} \tag{1.24}$$

Application of the same process to (1.11) leads to

$$k_{\boldsymbol{y}} = k_{\boldsymbol{y2}} = \frac{\sigma_2 - \sigma_1}{\sigma_2 + \sigma_1} \tag{1.25}$$

k_z and k_{z2} that satisfies (1.35) is not unique but it is convenient to set $k_{\boldsymbol{z}} = -k_{\boldsymbol{z2}}$, which results in:

$$k_{\boldsymbol{z}} = -k_{\boldsymbol{z2}} = \frac{\sigma_1 - \sigma_2}{\sigma_1 + \sigma_2} \tag{1.26}$$

When region 2 is non-conductive, $\sigma_2 = 0$, then

$$k_{\boldsymbol{x}} = k_{\boldsymbol{y}} = -1, \qquad k_{\boldsymbol{z}} = 1 \tag{1.27}$$

In summary, to represent the effect of an infinite boundary at $z = 0$ on the eddy current field, the boundary may be removed and an extra image source is placed in the symmetrical position with respect to the boundary plane in non-conducting region 2. The three components of the image vector have the same amplitude. The z component has the same sign as the source, while the x and y components whose directions are in parallel with the boundary plane have the opposite signs to the source.

A1.3 Solutions to the Eddy Current Functions in Rectangular Coordinate System

The coefficients, $c_{(m,n,k)}$, $d_{(m,n,k)}$, $e_{(m,n,k)}$, $h_{(m,n,k)}$, $q_{(m,n,k)}$ for the current vector potential and eddy current densities, and $p_{1(m,n,k)}$ - $p_{5(m,n,k)}$ for the eddy current loss are defined as follows:

$$\text{Let } M^2 = (m\frac{\pi}{L_x})^2 + (n\frac{\pi}{L_y})^2 + (k\frac{\pi}{L_z})^2 \tag{1.28}$$

$$c_{(m,n,k)} = \sigma \cdot \frac{a_{(m,n,k)}}{M^2} \tag{1.29}$$

$$d_{(m,n,k)} = \sigma \cdot \frac{b_{(m,n,k)}}{M^2} \tag{1.30}$$

$$e_{(m,n,k)} = \sigma \cdot \frac{-b_{(m,n,k)}(k\frac{\pi}{L_z})}{M^2} \tag{1.31}$$

$$h_{(m,n,k)} = \sigma \cdot \frac{a_{(m,n,k)}(k\frac{\pi}{L_z})}{M^2} \tag{1.32}$$

$$q_{(m,n,k)} = \sigma \cdot \frac{b_{(m,n,k)}\left(m\frac{\pi}{L_x}\right) - a_{(m,n,k)}(n\frac{\pi}{L_y})}{M^2} \tag{1.33}$$

$$p_{1(m,n,k)} = {b_{(m,n,k)}}^2 \cdot \left[\frac{\left(k\frac{\pi}{L_z}\right)}{M^2}\right]^2 \cdot \frac{\sigma L_x L_y L_z}{8} \tag{1.34}$$

$$p_{2(m,n,k)} = {a_{(m,n,k)}}^2 \cdot \left[\frac{\left(k\frac{\pi}{L_z}\right)}{M^2}\right]^2 \cdot \frac{\sigma L_x L_y L_z}{8} \tag{1.35}$$

$$p_{3(m,n,k)} = {b_{(m,n,k)}}^2 \cdot \left[\frac{\left(m\frac{\pi}{L_x}\right)}{M^2}\right]^2 \cdot \frac{\sigma L_x L_y L_z}{8} \tag{1.36}$$

$$p_{4(m,n,k)} = {a_{(m,n,k)}}^2 \cdot \left[\frac{\left(n\frac{\pi}{L_y}\right)}{M^2}\right]^2 \cdot \frac{\sigma L_x L_y L_z}{8} \tag{1.37}$$

$$p_{5(m,n,k)} = -2a_{(m,n,k)}b_{(m,n,k)} \cdot \left(m\frac{\pi}{L_x}\right)\left(n\frac{\pi}{L_y}\right) \cdot [\frac{1}{M^2}]^2 \cdot \frac{\sigma L_x L_y L_z}{8} \tag{1.38}$$

List of tables

Table of figures

Bibliography

[1]. EU energy, transport, and greenhouse gas emissions trends to 2050 (2013). [Online] Available: ec.europa.eu/energy/en/statistics/energy-trends-2050

[2]. Energy 2020: A strategy for competitive, secure, and sustainable energy (2010). [Online] Available: ec.europa.eu/energy/en/topics/renewable-energy

[3]. State of the Art on Alternative Fuels Transport Systems in the European Union (July, 2015). [Online] Available: ec.europa.eu/transport/themes/sustainable/index_en.htm

[4]. International Energy Agency (IEA), World Energy Outlook (2008). [Online] Available: www.iea.org.

[5]. C. C. Chan, "An overview of electric vehicle technology", in Proc. IEEE, vol.81, no.9, pp.1202-1213, Sep. 1993.

[6]. C. C. Chan, "The State of the Art of Electric, Hybrid, and Fuel Cell Vehicles," Proc. IEEE, vol. 95, pp. 704-718, 2007.

[7]. Z. Q. Zhu, C.C. Chan, "Electrical machine topologies and technologies for electric, hybrid, and fuel cell vehicles" in *Proc. IEEE VPPC Conf.*, pp.1-6, Sept. 2008.

[8]. Z. Q. Zhu, and D. Howe, "Electrical Machines and Drives for Electric, Hybrid, and Fuel Cell Vehicles", Proceedings of the IEEE, Vol. 95, No. 4, April 2007, pp. 746-765.

[9]. T. M. Jahns, G. B. Kliman, and T. W. Neumann, "Interior Permanent-Magnet Synchronous Motors for Adjustable-Speed Drives," IEEE Trans. Ind. Appl., vol. IA-22, pp. 738-747, 1986.

[10]. N. Bianchi and S. Bolognani, "Magnetic models of saturated interior permanent magnet motors based on finite element analysis," in Industry Applications Conference, 1998. Thirty-Third IAS Annual Meeting. The 1998 IEEE, 1998, pp. 27-34 vol.1.

[11]. K. T. Chau, C. C. Chan, C. Liu, "Overview of permanent-magnet brushless drives for electric and hybrid electric vehicles", IEEE Trans. Industrial Electronics, vol.55, no.6, pp.2246-2257, Jun. 2008.

[12]. S. Kreuawan, F. Gillon, and P. Brochet, ''Comparative study of design approach for electric machine in traction application'', International Review of Electrical Engineering, vol. 3, no. 3, pp. 455–465, June 2008.

[13]. G. Pellegrino, A. Vagati, B. Boazzo, and P. Guglielmi, "Comparison of Induction and PM Synchronous Motor Drives for EV Application Including Design Examples," IEEE Trans. Ind. Appl., vol. 48, pp. 2322-2332, 2012.

[14]. H. Neudorfer, N. Wicker, and A. Binder, "Comparison of Three Different Electric Powertrains for the Use in Hybrid Electric Vehicles", IET conference on Power Electronics, Machines and Drives, 2008, pp. 510-514

[15]. J. de Santiago, H. Bernhoff, B. Ekergå andrd, S. Eriksson, S. Ferhatovic, R. Waters, and M. Leijon, "Electrical motor drivelines in commercial all-electric vehicles: a review," IEEE Transactions on Vehicular Technology, vol. 61, no. 2, pp. 475 –484, Feb. 2012.

[16]. P. Morrison, A. Binder and B. Funieru, "Drive train design for medium-sized zero emission electric vehicles", in Proc. EPE'09 Conf., pp. 1-10, Sept. 2009

[17]. N. Phi Hung, E. Hoang, and M. Gabsi, "Performance Synthesis of Permanent-Magnet Synchronous Machines During the Driving Cycle of a Hybrid Electric Vehicle," IEEE Trans. Veh. Technol., vol. 60, pp. 1991-1998, 2011.

[18]. S. Kreuawan, F. Gillon, and P. Brochet, ''Comparative study of design approach for electric machine in traction application'', *International Review of Electrical Engineering*, vol. 3, no. 3, pp. 455–465, June 2008.

[19]. E. Sulaiman, T. Kosaka, and N. Matsui, “Design and Performance of 6-slot 5-pole PMFSM with Hybrid Excitation for Hybrid Electric Vehicle Applications”, *International Power Electronics Conference*, 2010, pp. 1962-1968.

[20]. L. Chen, J. Wang, P. Lombard, P. Lazari and V. Leconte, "Design optimisation of permanent magnet assisted synchronous reluctance machines for electric vehicle applications," *Electrical Machines (ICEM), 2012 XXth International Conference on*, Marseille, 2012, pp. 2647-2653.

[21]. P. Lazari, J. Wang and L. Chen, "A computationally efficient design technique for electric vehicle traction machines," *Electrical Machines (ICEM), 2012 XXth International Conference on*, Marseille, 2012, pp. 2596-2602.

[22]. P. Lazari, J. Wang and L. Chen, "A Computationally Efficient Design Technique for Electric-Vehicle Traction Machines," in *IEEE Transactions on Industry Applications*, vol. 50, no. 5, pp. 3203-3213, Sept.-Oct. 2014.

[23]. Driving cycles (Oct. 2015). [Online] Available: https://www.dieselnet.com/standards/cycles/

[24]. N. Bracikowski, D. Ilea, F. Gillon, M. Hecquet, and P. Brochet, "Design of permanent magnet synchronous machine in order to reduce noise under multi-physic contraints," in Electric Machines & Drives Conference (IEMDC), 2011 IEEE International, 2011, pp. 29-34.

[25]. Z. Q. Zhu, D. Howe and C. C. Chan, "Improved analytical model for predicting the magnetic field distribution in brushless permanent-magnet machines," in *IEEE Transactions on Magnetics*, vol. 38, no. 1, pp. 229-238, Jan 2002.

[26]. Jiabin Wang, Zhen Ping Xia and D. Howe, "Three-phase modular permanent magnet brushless Machine for torque boosting on a downsized ICE vehicle," in *IEEE Transactions on Vehicular Technology*, vol. 54, no. 3, pp. 809-816, May 2005.

[27]. P. Kumar and P. Bauer, "Improved Analytical Model of a Permanent-Magnet Brushless DC Motor," in *IEEE Transactions on Magnetics*, vol. 44, no. 10, pp. 2299-2309, Oct. 2008.

[28]. L. J. Wu, Z. Q. Zhu, D. Staton, M. Popescu and D. Hawkins, "Analytical prediction of electromagnetic performance of surface-mounted PM machines based on subdomain model accounting for tooth-tips," in *IET Electric Power Applications*, vol. 5, no. 7, pp. 597-609, August 2011.

[29]. L. J. Wu and Z. Q. Zhu, "Analytical investigation of open-circuit eddy current loss in windings of PM machines," *Electrical Machines (ICEM), 2012 XXth International Conference on*, Marseille, 2012, pp. 2759-2765.

[30]. L. J. Wu, Z. Q. Zhu, D. Staton, M. Popescu and D. Hawkins, "Analytical Model for Predicting Magnet Loss of Surface-Mounted Permanent Magnet Machines Accounting for Slotting Effect and Load," in *IEEE Transactions on Magnetics*, vol. 48, no. 1, pp. 107-117, Jan. 2012.

[31]. L. J. Wu, Z. Q. Zhu, D. Staton, M. Popescu and D. Hawkins, "Analytical Model of Eddy Current Loss in Windings of Permanent-Magnet Machines Accounting for Load," in *IEEE Transactions on Magnetics*, vol. 48, no. 7, pp. 2138-2151, July 2012.

[32]. L. J. Wu, Z. Q. Zhu, D. Staton, M. Popescu and D. Hawkins, "Analytical modeling of eddy current loss in retaining sleeve of surface-mounted PM machines accounting for influence of slot opening," *Industrial Electronics (ISIE), 2012 IEEE International Symposium on*, Hangzhou, 2012, pp. 611-616.

[33]. A. Rahideh and T. Korakianitis, "Analytical Armature Reaction Field Distribution of Slotless Brushless Machines With Inset Permanent Magnets," in *IEEE Transactions on Magnetics*, vol. 48, no. 7, pp. 2178-2191, July 2012.

[34]. K. Yoshida, Y. Hita, K. Kesamaru, "Eddy-current loss analysis in PM of surface-mounted-PM SM for electric vehicles," *IEEE Trans. Magnetics*, vol.36, no.4, pp. 1941-1944, Jul. 2000

[35]. N. Zhao, Z. Q. Zhu, W. Liu, "Rotor eddy current loss calculation and thermal analysis of permanent magnet motor and generator," *IEEE Trans. Magnetics*, vol.47, no.10, pp.4199-4202, Oct. 2011

[36]. H. V. Xuan, D. Lahaye, M. J. Hoeijmakers, H. Polinder, J. A. Ferreira, "Studying rotor eddy current loss of PM machines using nonlinear FEM including rotor motion," in *Proc. XIX International Conference on Electrical Machines (ICEM), 2010*, pp.1-7, Sept. 2010

[37]. L. Chen, J. Wang, " Evaluation of rotor eddy current loss in permanent magnet machines employing fractional-slot windings with low space harmonics", in *Proc. IEEE International Magnetics Conference, Intermag Europe 2014,* Dresden, Germany, May 4-8, 2014

[38]. J. Wang; K. Atallah; R. Chin, W. M. Arshad, H. Lendenmann, "Rotor Eddy-Current Loss in Permanent-Magnet Brushless AC Machines," *IEEE Trans. Magnetics*, vol.46, no.7, pp.2701-2707, July 2010

[39]. A. Rahideh, T. Korakianitis, "Analytical magnetic field distribution of slotless brushless permanent magnet motors – Part 1. Armature reaction field, inductance and rotor eddy current loss calculations,", *IET Electric Power Applications*, vol.6, no.9, pp.628-638, November 2012

[40]. K. Yamazaki, Y. Fukushima, "Effect of Eddy-Current Loss Reduction by Magnet Segmentation in Synchronous Motors With Concentrated Windings," *IEEE Trans. Industry Application*, vol.47, no.2, pp.779-788, March-April 2011

[41]. P. Sergeant, Van Den Bossche, "Segmentation of Magnets to Reduce Losses in Permanent-Magnet Synchronous Machines," *IEEE Trans. Magnetics*, vol.44, no.11, pp.4409-4412, Nov. 2008

[42]. O. de la Barrière, S. Hlioui, H. Ben Ahmed and M. Gabsi, "An Analytical Model for the Computation of No-Load Eddy-Current Losses in the Rotor of a Permanent Magnet Synchronous Machine," in *IEEE Transactions on Magnetics*, vol. 52, no. 6, pp. 1-13, June 2016.

[43]. P. Arumugam, T. Hamiti and C. Gerada, "Estimation of Eddy Current Loss in Semi-Closed Slot Vertical Conductor Permanent Magnet Synchronous Machines Considering Eddy Current Reaction Effect," in *IEEE Transactions on Magnetics*, vol. 49, no. 10, pp. 5326-5335, Oct. 2013.

[44]. F. Dubas, A. Rahideh, "Two-Dimensional Analytical Permanent-Magnet Eddy-Current Loss Calculations in Slotless PMSM Equipped With Surface-Inset Magnets," *IEEE Trans. Magnetics*, vol.50, no.3, pp.54-73, March 2014

[45]. Y. Amara, P. Reghem, G. Barakat, "Analytical Prediction of Eddy-Current Loss in Armature Windings of Permanent Magnet Brushless AC Machines," *IEEE Trans. Magnetics*, vol.46, no.8, pp.3481-3484, Aug. 2010

[46]. K. Yamazaki, Y. Kanou, "Rotor Loss Analysis of Interior Permanent Magnet Motors Using Combination of 2-D and 3-D Finite Element Method," *IEEE Trans. Magnetics*, vol.45, no.3, pp.1772-1775, March 2009

[47]. T. Okitsu, D. Matsuhashi, Yanhui Gao; K. Muramatsu, "Coupled 2-D and 3-D Eddy Current Analyses for Evaluating Eddy Current Loss of a Permanent Magnet in Surface PM Motors," *IEEE Trans. Magnetics*, vol.48, no.11, pp.3100-3103, Nov. 2012

[48]. J. D. Ede, K. Atallah, G. W. Jewell, J. B. Wang, D. Howe, "Effect of Axial Segmentation of Permanent Magnets on Rotor Loss in Modular Permanent-Magnet

Brushless Machines," *IEEE Trans. Industry Application*, vol.43, no.5, pp.1207-1213, Sept.-oct. 2007

[49]. Y. Aoyama, K. Miyata, K. Ohashi, "Simulations and experiments on eddy current in Nd-Fe-B magnet," *IEEE Trans. Magnetics*, vol.41, no.10, pp.3790-3792, Oct. 2005

[50]. K. Yamazaki, A. Abe, "Loss Investigation of Interior Permanent-Magnet Motors Considering Carrier Harmonics and Magnet Eddy Currents," *IEEE Trans. Industry Application*, vol.45, no.2, pp.659-665, March-April 2009

[51]. K. Yamazaki, M. Shina, Y. Kanou, M. Miwa, J. Hagiwara, "Effect of Eddy Current Loss Reduction by Segmentation of Magnets in Synchronous Motors: Difference Between Interior and Surface Types," *IEEE Trans. Magnetics*, vol.45, no.10, pp.4756-4759, Oct. 2009

[52]. S. Ruoho, T. Santa-Nokki, J. Kolehmainen, A. Arkkio, "Modeling Magnet Length In 2-D Finite-Element Analysis of Electric Machines," *IEEE Trans. Magnetics*, vol.45, no.8, pp.3114-3120, Aug. 2009

[53]. W.-Y. Huang; A. Bettayeb, R. Kaczmarek, J. C. Vannier, "Optimization of Magnet Segmentation for Reduction of Eddy-Current Losses in Permanent Magnet Synchronous Machine," *IEEE Trans. Energy Conversion*, vol.25, no.2, pp.381-387, June 2010

[54]. M. Mirzaei, A. Binder, C. Deak, "3D analysis of circumferential and axial segmentation effect on magnet eddy current losses in permanent magnet synchronous machines with concentrated windings," in *Proc. XIX International Conference on Electrical Machines (ICEM), 2010*, Sept. 2010

[55]. M. Mirzaei, A. Binder, B. Funieru, M. Susic, "Analytical Calculations of Induced Eddy Currents Losses in the Magnets of Surface Mounted PM Machines With Consideration of Circumferential and Axial Segmentation Effects," *IEEE Trans. Magnetics*, vol.48, no.12, pp.4831-4841, Dec. 2012

[56]. J. Pyrhonen, H. Jussila, Y. Alexandrova, P. Rafajdus, J. Nerg, "Harmonic Loss Calculation in Rotor Surface Permanent Magnets—New Analytic Approach," *IEEE Trans. Magnetics*, vol.48, no.8, pp.2358-2366, Aug. 2012

[57]. B. Aslan, E. Semail, J. Legranger, "Analytical model of magnet eddy-current volume losses in multi-phase PM machines with concentrated winding," in *Proc. Energy Conversion Congress and Exposition (ECCE), 2012 IEEE* , pp.3371-3378, Sept. 2012

[58]. Sang-Yub Lee; Hyun-Kyo Jung, "Eddy current loss analysis in the rotor of permanent magnet traction motor with high power density," in *Proc. Vehicle Power and Propulsion Conference (VPPC), 2012 IEEE* , pp.210-214, Oct. 2012

[59]. Peng Zhang; G. Y. Sizov, Jiangbiao He; D. M. Ionel, N. A. O. Demerdash, "Calculation of magnet losses in concentrated-winding permanent magnet synchronous machines using a Computationally Efficient - Finite Element method," in *Proc. Energy Conversion Congress and Exposition (ECCE), 2012 IEEE* , pp.3363-3370, Sept. 2012

[60]. B. Aslan, E. Semail, J. Legranger, "General Analytical Model of Magnet Average Eddy-Current Volume Losses for Comparison of Multiphase PM Machines With Concentrated Winding," *IEEE Trans. Energy Conversion*, vol.29, no.1, pp.72-83, March 2014

[61]. T. Lubin, S. Mezani, A. Rezzoug, "2-D Exact Analytical Model for Surface-Mounted Permanent-Magnet Motors With Semi-Closed Slots," *IEEE Trans. Magnetics*, vol.47, no.2, pp.479-492, Feb. 2011

[62]. B. Hannon, P. Sergeant, L. Dupré, "2-D Analytical Subdomain Model of a Slotted PMSM With Shielding Cylinder," *IEEE Trans. Magnetics*, vol.50, no.7, pp.1-10, July 2014

[63]. B. N. Cassimere, S. D. Sudhoff, D. H. Sudhoff, "Analytical Design Model for Surface-Mounted Permanent-Magnet Synchronous Machines," *IEEE Trans. Energy Conversion*, vol.24, no.2, pp.347-357, June 2009

[64]. B. M. Ma, Y. L. Liang, J. Patel, D. Scott and C. O. Bounds, "The effect of Fe on the temperature dependent magnetic properties of $Sm(Co,Fe,Cu,Zr)_z$ and $SmCo_5$ sintered magnets at 450°C," in *IEEE Transactions on Magnetics*, vol. 32, no. 5, pp. 4377-4379, Sep 1996.

[65]. P. Bretchko and R. Ludwig, "Open-loop pulsed hysteresis graph system for the magnetization of rare-earth magnets," in *IEEE Transactions on Magnetics*, vol. 36, no. 4, pp. 2042-2051, Jul 2000.

[66]. L. Jahn, R. Schumann and V. Ivanov, "Investigation of the thermal remagnetization in sintered hard magnets," in *IEEE Transactions on Magnetics*, vol. 37, no. 4, pp. 2506-2508, Jul 2001.

[67]. M. Rosu, J. Saitz and A. Arkkio, "Hysteresis model for finite-element analysis of permanent-magnet demagnetization in a large synchronous motor under a fault condition," in *IEEE Transactions on Magnetics*, vol. 41, no. 6, pp. 2118-2123, June 2005.

[68]. W. Yi, D. M. Ionel, and D. Staton, "Ultrafast steady-state multi-physics model for PM and synchronous reluctance machines," in *Proc. IEEE Energy Conversion Congress and Exposition (ECCE), 2014*, pp. 5152-5159, 2014,

[69]. A. Sarikhani and O. Mohammed, "A multi-physics multi-objective optimal design approach of PM synchronous machines," in *Proc. 2014 International Conference on Electrical Machines (ICEM)*, pp. 968-974, 2014,

[70]. S. A. Semidey, D. Yao, J. R. Mayor, R. G. Harley, and T. G. Habetler, "Optimal Electromagnetic-Thermo-Mechanical Integrated Design Candidate Search and Selection for Surface-Mount Permanent-Magnet Machines Considering Load Profiles," *IEEE Trans. Industry Application*, vol. 47, pp. 2460-2468, 2011. (Finite difference method)

[71]. Ruoho, S.; Kolehmainen, J.; Ikaheimo, J.; Arkkio, A., "Interdependence of Demagnetization, Loading, and Temperature Rise in a Permanent-Magnet Synchronous Motor," *IEEE Trans. Magnetics*, vol.46, no.3, pp.949-953, March 2010

[72]. Wenying Jiang; Jahns, T.M., "Development of efficient electromagnetic-thermal coupled model of electric machines based on finite element analysis," in *Proc. 2013 IEEE International Electric Machines & Drives Conference (IEMDC)*, pp.816-823, 12-15 May 2013

[73]. X. Yuan, J. Wang and K. Colombage, "Torque Distribution Strategy for Front and Rear Wheel Driven Electric Vehicle", *Vehicular Technology, IEEE Transactions on*, vol.61, no.8, pp.3365-3374, Oct. 2012

[74]. N. Mutoh, Y. Takahashi and Y. Tomita, "Failsafe Drive Performance of FRID Electric Vehicles With the Structure Driven by the Front and Rear Wheels Independently," in *IEEE Transactions on Industrial Electronics*, vol. 55, no. 6, pp. 2306-2315, June 2008.

[75]. M. Terashima, T. Ashikaga, T. Mizuno, K. Natori, N. Fujiwara and M. Yada, "Novel motors and controllers for high-performance electric vehicle with four in-wheel motors," in *IEEE Transactions on Industrial Electronics*, vol. 44, no. 1, pp. 28-38, Feb 1997.

[76]. Y. Hori, "Future vehicle driven by electricity and Control-research on four-wheel-motored "UOT electric march II"," in *IEEE Transactions on Industrial Electronics*, vol. 51, no. 5, pp. 954-962, Oct. 2004.

[77]. P. Lazari, Jiabin W.W. Jiabin, and C. Liang, "A Computationally Efficient Design Technique for Electric-Vehicle Traction Machines," *Ind. Appl., IEEE Transactions on*, vol. 50, pp. 3203-3213, 2014.

[78]. J. Wang, V. I. Patel, W. Wang, "Fractional-Slot Permanent Magnet Brushless Machines with Low Space Harmonic Contents," *Magnetics, IEEE Transactions on*, vol.50, no.1, pp.1,9, (Jan. 2014)

[79]. X. Chen, J. Wang, B. SEN, P. Lazari, T. Sun, "A High-Fidelity, Computationally Efficient Model for Interior Permanent Magnet Machines Considering the Magnetic Saturation, Spatial Harmonics and Iron Loss Effect," *IEEE Trans. Ind. Electron.*, vol.62, no.7, pp.4044-4055, July 2015

[80]. Gyselinck, J.; Vandevelde, L.; Melkebeek, J.; Dular, P.; Henrotte, F.; Legros, W., "Calculation of eddy currents and associated losses in electrical steel laminations," in Magnetics, IEEE Transactions on , vol.35, no.3, pp.1191-1194, May 1999

[81]. Ionel, D.M.; Popescu, M.; Dellinger, S.J.; Miller, T.J.E.; Heideman, R.J.; McGilp, M.I., "On the variation with flux and frequency of the core loss coefficients in electrical machines," in Industry Applications, IEEE Transactions on , vol.42, no.3, pp.658-667, May-June 2006

[82]. Jang-Ho Seo; Sang-Yeop Kwak; Sang-Yong Jung; Cheol-Gyun Lee; Tae-Kyung Chung; Hyun-Kyo Jung, "A Research on Iron Loss of IPMSM With a Fractional Number of Slot Per Pole," in Magnetics, IEEE Transactions on , vol.45, no.3, pp.1824-1827, March 2009

[83]. Eggers, D.; Steentjes, S.; Hameyer, K., "Advanced Iron-Loss Estimation for Nonlinear Material Behavior," in Magnetics, IEEE Transactions on , vol.48, no.11, pp.3021-3024, Nov. 2012

[84]. Lavers, J.D.; Biringer, P.; Hollitscher, H., "A simple method of estimating the minor loop hysteresis loss in thin laminations," in Magnetics, IEEE Transactions on , vol.14, no.5, pp.386-388, Sep 1978

[85]. Atallah, K.; Zhu, Z.Q.; Howe, D., "An improved method for predicting iron losses in brushless permanent magnet DC drives," in Magnetics, IEEE Transactions on , vol.28, no.5, pp.2997-2999, Sep 1992

[86]. Shimizu, T.; Iyasu, S., "A Practical Iron Loss Calculation for AC Filter Inductors Used in PWM Inverters," in Industrial Electronics, IEEE Transactions on , vol.56, no.7, pp.2600-2609, July 2009

[87]. Yamazaki, K.; Fukushima, N., "Iron-Loss Modeling for Rotating Machines: Comparison Between Bertotti's Three-Term Expression and 3-D Eddy-Current Analysis," in Magnetics, IEEE Transactions on , vol.46, no.8, pp.3121-3124, Aug. 2010

[88]. Steentjes, S.; von Pfingsten, G.; Hombitzer, M.; Hameyer, K., "Iron-Loss Model With Consideration of Minor Loops Applied to FE-Simulations of Electrical Machines," in Magnetics, IEEE Transactions on , vol.49, no.7, pp.3945-3948, July 2013

[89]. P. H. Mellor, R. Wrobel, and D. Holliday, “A computationally efficient iron loss model for brushless ac machines that caters for rated flux and field weakened operation”, In Proc. IEEE Int. Electric Machines and Drives Conf. IEMDC ’09, pages 490-494, 2009

[90]. Mickael Kremer, Damien Flieller, Jean Merckle , Guy Sturtzer, " Investigation of an axial flux machine for hybrid and electric cars regarding magnet losses and protecting against thermal demagnetization", IEEE International Magnetics Conference, Intermag Europe 2014, Dresden, Germany, May 4-8, 2014, ISSN 0018-9464

[91]. Jiabin Wang and Howe, D., "Design optimization of radially magnetized, iron-cored, tubular permanent-magnet machines and drive systems," Magnetics, IEEE Transactions on , vol.40, no.5, pp.3262,3277, Sept. 2004

[92]. M. Klohr and A. Binder, "Design of carbon fiber bandages for high speed permanent magnet rotors", *Proc. SPEEDAM*, pp. B7/13-B7/18, 2002

[93]. A. Binder, T. Schneider and M. Klohr, "Fixation of buried and surface-mounted magnets in high-speed permanent-magnet synchronous machines," in *IEEE Transactions on Industry Applications*, vol. 42, no. 4, pp. 1031-1037, July-Aug. 2006.

[94]. A. Borisavljevic, H. Polinder and J. A. Ferreira, "Enclosure design for a high-speed permanent magnet rotor," *Power Electronics, Machines and Drives (PEMD 2010), 5th IET International Conference on*, Brighton, UK, 2010, pp. 1-6.

[95]. Motor-CAD. [Online]. Available: www.motor-design.com/

[96]. H. Bolton, "Transverse Edge Effect in Sheet-rotor Induction Motors," in Proceedings of the Institution of Electrical Engineers, vol.116, no.5, pp.725-731, May 1969

[97]. T. W. Preston, A. B. J. Reece, "Transverse Edge Effects in Linear Induction Motors," in Proceedings of the Institution of Electrical Engineers, vol.116, no.6, pp.973-979, June 1969

[98]. Ranran Lin, A. Arkkio, "Calculation and Analysis of Stator End-Winding Leakage Inductance of an Induction Machine," IEEE Trans. Magnetics, vol.45, no.4, pp.2009-2014, April 2009

[99]. Dong Li, Weili Li, Xiaochen Zhang, Jin Fang, Hongbo Qiu, Jiafeng Shen, Likun Wang, "A New Approach to Evaluate Influence of Transverse Edge Effect of a Single-Sided HTS Linear Induction Motor Used for Linear Metro," IEEE Trans. Magnetics, vol.51, no.3, pp.1-4, March 2015

[100]. L. J. Wu, Z. Q. Zhu, D. Staton, M. Popescu, D. Hawkins, "Analytical prediction of electromagnetic performance of surface-mounted PM machines based on subdomain model accounting for tooth-tips," IET Electric Power Applications, vol.5, no.7, pp.597-609, August 2011

[101]. P. Hammond, "Electric and magnetic images," in Proc. the IEE - Part C: Monographs , vol.107, no.12, pp.306-313, September 1960

[102]. C. J. Carpenter, "The application of the method of images to machine end-winding fields," in Proc. the IEE - Part A: Power Engineering, vol.107, no.35, pp.487-500, October 1960

[103]. B. Hague, The Principles of Electromagnetism Applied to Electrical Machines, Dover, 1962

[104]. K. J. W. Pluk, T. A. van Beek, J. W. Jansen, and E. A. Lomonova, " Modeling and Measurements on a Finite Rectangular Conducting Plate in an Eddy Current Damper," IEEE Trans. Ind. Electron., vol. 61, no. 8, pp. 4061–4072, August 2014

[105]. J. Wang, V. I. Patel, W. Wang, "Fractional-Slot Permanent Magnet Brushless Machines with Low Space Harmonic Contents," IEEE Trans. Magnetics, vol.50, no.1, pp.1-9, Jan. 2014

[106]. Chen, X.; Wang, J.; SEN, B.; Lazari, P.; Sun, T., "A High-Fidelity, Computationally Efficient Model for Interior Permanent Magnet Machines Considering the Magnetic Saturation, Spatial Harmonics and Iron Loss Effect," *IEEE Trans. Ind. Electron.*, vol.62, no.7, pp.4044-4055, July 2015

[107]. P. H. Mellor, R. Wrobel, and D. Holliday, "A computationally efficient iron loss model for brushless ac machines that caters for rated flux and field weakened operation", in *Proc. IEEE International Electric Machines and Drives Conference (IEMDC '09),* pages 490-494, 2009

[108]. Mickael Kremer, Damien Flieller, Jean Merckle , Guy Sturtzer, " Investigation of an axial flux machine for hybrid and electric cars regarding magnet losses and protecting against thermal demagnetization", *IEEE International Magnetics Conference (Intermag) 2014*, Dresden, Germany, May 4-8, 2014, ISSN 0018-9464

[109]. MotorDesignLimited. (2015). *Motor-CAD v8.3.8*. Available: http://www.motor-design.com/motorcad.php

[110]. P. Lazari, J. Wang, L. Chen, X. Chen, "Design optimisation and performance evaluation of a rare-earth-free Permanent Magnet Assisted Synchronous Reluctance Machine for electric vehicle traction," in Proc. 7th IET International Conference on Power Electronics, Machines and Drives (PEMD 2014), pp.1-6, 8-10 April 2014

[111]. K. T. Chau, C. C. Chan, and L. Chunhua, "Overview of Permanent-Magnet Brushless Drives for Electric and Hybrid Electric Vehicles," Industrial Electronics, IEEE Transactions on, vol. 55, pp. 2246-2257, 2008.

[112]. X. Wei, et al., "Flux-switching permanent magnet machine drive system for plug-in hybrid electrical vehicle," in Universities Power Engineering Conference (AUPEC), 2010 20th Australasian, 2010, pp. 1-6.

[113]. F. Weizhong, P. C. K. Luk, S. Jian Xin, X. Bin, and W. Yu, "Permanent-Magnet Flux-Switching Integrated Starter Generator With Different Rotor Configurations for Cogging Torque and Torque Ripple Mitigations," Industry Applications, IEEE Transactions on, vol. 47, pp. 1247-1256, 2011.

[114]. V. I. Patel, Jiabin Wang, Weiya Wang, Xiao Chen, "Six-phase fractional-slot-per-pole-per-phase permanent-magnet machines with low space harmonics for electric vehicle application," IEEE Trans. Industry Applications, vol.50, no.4, pp.2554,2563, July-Aug. 2014

[115]. Peng Zhang, G. Y. Sizov, Muyang Li, D. M. Ionel, N. Demerdash, S. J. Stretz, A. W. Yeadon, "Multi-Objective Tradeoffs in the Design Optimization of a Brushless Permanent-Magnet Machine With Fractional-Slot Concentrated Windings," Industry Applications, IEEE Transactions on , vol.50, no.5, pp.3285,3294, Sept.-Oct. 2014

[116]. G. Y. Sizov, Peng Zhang, D. M. Ionel, N. Demerdash, M. Rosu, "Automated Multi-Objective Design Optimization of PM AC Machines Using Computationally Efficient FEA and Differential Evolution," Industry Applications, IEEE Transactions on , vol.49, no.5, pp.2086,2096, Sept.-Oct. 2013

[117]. L. Jolly, M. A. Jabbar, Qinghua Liu, "Optimization of the constant power speed range of a saturated permanent-magnet synchronous motor," Industry Applications, IEEE Transactions on , vol.42, no.4, pp.1024,1030, July-Aug. 2006

[118]. Do-Kwan Hong, Byung-Chul Woo, Dae-Hyun Koo, Do-Hyun Kang, "Optimum Design of Transverse Flux Linear Motor for Weight Reduction and Improvement Thrust Force Using Response Surface Methodology," Magnetics, IEEE Transactions on, vol.44, no.11, pp.4317,4320, Nov. 2008

[119]. Got-It. [Online]. Available: www.cedrat.com

[120]. http://www.metal-pages.com/metalprices/rareearths/

[121]. G. Bai, et al, "Study of high-coercivity sintered NdFeB magnets," Journal of magnetism and magnetic materials, vol. 308, no. 1, 2007, pp. 20-23.

[122]. Liang Chen, D. Hopkinson, Jiabin Wang, A. Cockburn, M, Sparkes, W. O'Neill, "Reduced Dysprosium Permanent Magnets and Their Applications in Electric Vehicle Traction Motors," IEEE Trans. Magnetics, vol.51, no.11, pp.1-4, Nov. 2015

[123]. K. T. Park, K. Hiraga, and M. Sagawa, “Effect of metal-coating and consecutive heat treatment on coercivity of thin Nd-Fe-B sintered magnets,” in Proc. 16th Workshop Rare-Earth Magnets and Their Applications, Sendai, 2000, pp. 257-264.

[124]. Fukunaga, Hirotoshi, et al, "Coercivity enhancement of Dy-coated Nd-Fe-B flakes by crystallization," Journal of Applied Physics, vol. 109, no. 7, 2011, 07A701.

[125]. H. Sepehri-Amin, T. Ohkubo, and K. Hono, "Grain boundary structure and chemistry of Dy-diffusion processed Nd–Fe–B sintered magnets," Journal of Applied Physics, vol. 107, no. 9, 2011, 09A745.

[126]. K. Hirota, et al, "Coercivity enhancement by the grain boundary diffusion process to Nd-Fe-B sintered magnets," IEEE Trans. Magnetics, vol. 42, no. 10, 2006, pp. 2909-2911.

[127]. P. Lazari, K. Atallah and J. Wang, "Effect of Laser Cut on the Performance of Permanent Magnet Assisted Synchronous Reluctance Machines," in *IEEE Transactions on Magnetics*, vol. 51, no. 11, pp. 1-4, Nov. 2015.

[128]. R. Siebert, J. Schneider and E. Beyer, "Laser cutting and mechanical cutting of electrical steels and its effect on the magnetic properties", *IEEE Trans. Magn.*, vol. 50, no. 4, 2014

[129]. E. G. Araujo, J. Schneider, K. Verbeken, G. Pasquarella and Y. Houbaert, "Dimensional effects on magnetic properties of Fe-Si steels due to laser and mechanical cutting", *IEEE Trans. Magn.*, vol. 46, no. 2, pp. 213-216, 2010

[130]. A. Schoppa, J. Schneider and C.-D. Wuppermann, "Influence of the manufacturing process on the magnetic properties of non-oriented electrical steels", *J. Magn. Magn. Mater.*, vol. 216, pp. 74-78, 2000

[131]. Report for HIWI project: Materials and Drives for High & Wide Efficiency Electric Powertrains”